The new mineralogy of the outer solar system and the high-pressure behaviour of methane

Helen E Maynard-Casely

A thesis submitted in fulfilment of the requirements
for the degree of Doctor of Philosophy
to the
University of Edinburgh
2009

Abstract

This thesis will introduce the study of methane as a mineral. Along with ammonia and water, methane is one of the main planetary-forming materials in the outer solar system. The topic of 'new mineralogy of the outer solar system' is outlined and introduced, and previous studies in the area are discussed. This review identifies a lack of high-pressure structural knowledge on methane when compared to ammonia and water. The significance of this knowledge for the study of the planets Neptune and Uranus is discussed.

The crystal structures of methane above 5.2 GPa were, prior to this thesis, unknown. To tackle this long-standing problem an integrated approach of high-pressure diffraction techniques had to be used. The dominance of hydrogen within the structures of methane necessitated the use of neutron diffraction. The difficulties and limitations of high-pressure neutron powder diffraction are presented. It will be shown that the complexity of the subsequent structures required the use of single-crystal x-ray diffraction. Using a combination of x-ray and neutron diffraction the structures of methane phase A (5.2 - 10 GPa) and B (10 - 25 GPa) were solved.

The structure of phase A, was shown to conform to an indexing from literature [Nakahata 99] of a rhombohedral unit cell with $\alpha \approx 89.3°$ and $a \approx 8.6$ Å. Powder data were insufficient to determine atomic positions for this phase, and a single-crystal x-ray diffraction study was undertaken. The process of growing samples for this study is described as well as data collection. As a result of these studies the carbon atoms were located within methane phase A, and the density of the structure confined. The heavy atom structure, of phase A, was refined against neutron powder diffraction data, enabling positions of hydrogen atoms to be found.

Preliminary powder diffraction studies of methane phase B found that the structure did not conform to the unit cell described within the literature. The phase was instead assigned to a cubic unit cell with $a \approx 11.73$ Å. Similarly to the studies of phase A, a single-crystal x-ray diffraction study was undertaken. This was complicated by the presence of a contaminant within the sample area. This contaminant was shown to have no effect on the structural results. From a single-crystal study the heavy atom

structure of phase B was found. The thesis charts the attempt, but ultimate failure, to obtain neutron powder diffraction on this phase. Comparisons of phase B with the higher pressure phase HP (25 GPa +) led to the conclusion that there would still be some disorder within the hydrogen atoms of phase B.

Other studies have been carried out on the methane phase diagram. A Raman spectroscopy study, in the literature, on the low-temperature and high-pressure region of the phase diagrams (20 K up to 30 GPa) had suggested the existence of 3 additional phases of methane. A low-temperature, high-pressure neutron diffraction experiment was undertaken to try and characterise these phases. It was found that the phase A structure persisted under all conditions (to 20 K and 5 GPa) throwing the original results into question. During the growth of single-crystals for the above studies on phase A and B, a high-temperature solid-solid phase transition was observed. This transition line was mapped out and the phase resulting from it characterised with high-temperature single-crystal x-ray diffraction.

Declaration

I do hereby declare that this thesis was composed by myself and that the work described within is my own, except where explicitly stated otherwise.

Helen E Maynard-Casely
February 2009

Acknowledgements

The work of this thesis was funded by a studentship from EPSRC.

My first personal thanks go to my supervisors. It seems a long time now since I first met Dr John Loveday and Prof Richard Nelmes at ISIS in November 2004. I can remember being overwhelmed by the surroundings, but excited at the opportunities that a move to Edinburgh presented. I thank John and Richard for taking me on, and introducing me to the wealth of opportunities that high-pressure science brings.

I believe that much of the success of my PhD overall is down to the excellent group structure that I became part of. The high-pressure physics group is an excellent melting pot of experimental minds and I feel privileged to have been part of this. The entire group; John, Richard, Prof Malcolm McMahon, Dr Eugene Gregoryanz, Dr Ingo Loa, Dr Olga Degtyareva, Dr Lars Lundegaard, Dr Craig Bull, Dr Malcolm Guthrie, Dr Christophe Guillaume, Dr John Procter, Dr Miriam Marques, Dr Chrystèle Sanloup, Dr Graham Stinton, Dr Simone Magni, Dr. Kazuki Komatsu, Shaun Evans and Jenny Jeppsson should be recognised for providing this.

Specific thanks need to go to; Lars, who patiently taught me how to load a diamond anvil cell, fielded my (endless) question and let me borrow his international tables. Eugene, who presided over the cryogenic loadings and gave me my first proper nickname - Beakie. Prof Malcolm, who let me use his beamtime at 9.5, 9.8 and ESRF. Craig for being a rock during the neutron experiments. Olga, for helping me through my first steps of crystallography and putting up with me at 2 in the morning. Graham, Lars, Shaun, Olga, Miriam and Jenny all had the misfortune to share an office with me.

I would also like to acknowledge Dr Stefan Klotz and Julian Philippe of IMPMC, Paris, who were instrumental in the success of the low-temperature neutron diffraction experiment. I also learnt much from my time spent with Stefan and Dr Thierry Strässle on early ISIS beamtime.

I must also acknowledge the beamline scientists who maintain and run the central facilities instruments that I have used. Thomas Hansen, D20, ILL; Michael Hanfland, ID09A, ESRF; Alistair Lennie, 9.5, SRS; John Warren, 9.8, SRS; Matt Tucker and Bill Marshall who maintain PEARL, ISIS. All of these facilities are supported by STFC.

On an incidental note I'd like to acknowledge the people who make Innocent smoothies, as they came up with their Veg Pot just in time for me to not have to resort to Pot Noodles during writing up.

I lastly would like to thank my parents for their encouragement, and my grandparents for inspiring me. And most of all to Andy, for being there.

"I call myself Wonko the Sane to re-assure people. Wonko was what my mother called me when I was a clumsy kid, knocking things over. Sane is what I intend to remain and the angels with golden beards, green wings and orthopaedic sandals agree with me"
"And they visit when?"
"Weekends mostly - on scooters. They are great machines."
"I see....."
"Look I'm not trying to prove anything here, I'm a scientist, I know what constitutes proof. I use my childhood name to remind myself that a scientist must also be like a child. If he sees a thing he must say that he sees it weather it was what he was expecting to see or not. Otherwise he'll only see what he's expecting"

So Long, and Thanks for All the Fish Douglas Adams, 1984.

Contents

Chapter 1

Introduction and outline of thesis

The Oxford English dictionary defines a mineral as 'a solid, naturally occurring, usually inorganic substance with a definite chemical composition and characteristic physical structure and properties (such as crystalline form)'. This definition is interpreted to refer to a naturally occurring terrestrial substance formed through geological processes. On Earth the largest and most important group of rock-forming minerals is the silicates. However, when examining the composition of the outer solar system (i.e. planetary bodies beyond the orbit of Jupiter) a very different suite of minerals dominate. In this region, simple molecular species, such as methane, water and ammonia, become the dominant planet-forming materials [dePater 01, Stevenson 82, Guillot 99]. These systems are rarely thought of as minerals, but are key to understanding geological phenomena occurring in the outer solar system.

The dynamics of Earth's interior constrain geological phenomena such as tectonics and volcanism, which constantly shape the surface of the planet. Dynamical properties such as thermal conductivity, thermal diffusivity and rheology of the interior of the Earth are determined by its silicate mineralogy. Knowledge of the mineralogy of Earth's interior is critically important to constraining processes that occur within the planet, affecting Earth's ability to sustain life. Current knowledge of the composition of outer solar system bodies, namely Jupiter, Saturn, Uranus, Neptune and their moons, is constrained by chemical evolution models. These models are confirmed to an extent by spectroscopic observations of the surfaces and atmospheres of these planets. Visual observations from satellites (such as Voyager 1 and 2, Galileo and the recent Cassini) have revealed a diverse suite of geological phenomena that these planets' moons exhibit. The task now is to approach the mineralogical questions in the same way to that has been done for the interior of Earth; to match the mineralogy to the geological phenomena that are observed.

To achieve these aims the physical properties of constituent materials must be

tightly constrained; more so than for those found on Earth. From Jupiter outwards, as already stated, planet-forming materials are simple molecular systems. For Jupiter and Saturn, the materials are hydrogen and helium, whereas methane, water and ammonia make up a bulk of Uranus and Neptune. The Galilean moons of Jupiter have a mineralogy based around salt hydrates. The moons of Saturn, Uranus and Neptune have mineralogy that is dominated by water, methane and ammonia. Understanding the transformations and interactions that methane undergoes in its solid form can lead to improved modelling of the interiors of planets in the outer solar system. This knowledge could provide better explanations of the observed phenomenon on the giant planets, such as their luminosity and magnetic fields.

The study of methane structures is also motivated from a more fundamental viewpoint. Recent calculations on methane's analogue, silane (SiH_4), suggested this compound could, under pressure, initiate superconductivity in its hydrogen [Feng 06]. Comparisons between methane, silane and also germane (GeH_4) would provide insight into the proposed process of 'chemical pre-compression' of hydrogen.

In the context of this thesis, the author would wish to define water ammonia and methane and mixtures between these as 'the new mineralogy of the outer solar system'. Although within the systems of the outer solar system methane is unlikely to exist as a separate species, knowledge of its crystalline form under a variety of conditions would have implications for interior modelling of planets within the outer solar system.

As the scope of this thesis is a little varied, it is hoped that the outline that follows in this chapter will serve to guide the reader through the work. Chapter 2 was written to set the context of the studies that are described in Chapters 4, 5 and 6, with Chapter 3 detailing the methods used to carry out these studies.

1.1 Chapter 2 - The new mineralogy of the solar system

Chapter 2 reviews the constituent mineralogy of the outer solar system, methane, ammonia and water systems, and then sets out how this body of work on methane will contribute to this. Further knowledge on the high-pressure behaviour of methane would have the most impact on the 'icy' giants Uranus and Neptune, and these planets are discussed specifically. The first task of the review is to set out what is known of the interiors of Uranus and Neptune, and how this knowledge came about. This is summarised with an objective that states the conditions under which the behaviour of methane must be known to complete interior modelling of Uranus and Neptune.

Next, the review turns to previous work on the pure phases; water and methane, before briefly reviewing work upon binary mixtures between these. The focus of each topic is two-fold; firstly, previous studies of the solid high-pressure crystalline behaviour

of each substance will be discussed. Then, where appropriate, studies of each substance under more extreme environments will be reviewed.

To illustrate the effect that high-pressure crystallographic studies can have on the development of models for planetary interiors, a case study on Titan is described. Here, the discovery of methane hydrate existing beyond 2 GPa revolutionised the picture of Titan's interior evolution. The detailed model that prevailed as a result of these studies is discussed.

1.2 Chapter 3 - Experimental techniques

Chapter 3 outlines the principles and experimental techniques that are employed within this thesis. It is all encompassing, describing all the methods of experimental work undertaken. The first section outlines diffraction, applicable to both x-rays and neutrons with focus on the elements that are of relevance to the solution of crystal structures. Scattering induced by an x-ray photon or a neutron is introduced. This is followed by an overview of crystallography, included for clarity in later sections. A description of the underlying principles of diffraction analysis is then progressed, with the introduction of the 'phase problem' for crystal-structure solution.

The more practical aspects of diffraction analysis are then reviewed. The choice between powder and single-crystal data collection is put forward and the strengths and weaknesses of each method outlined. From this the differing benefits of neutron and x-ray diffraction will be discussed, with reference to the former's advantages for the study of hydrogen dominated systems. After these discussions, the section continues to explain the corrections that are needed to raw data intensities. Lastly the section outlines the processes of crystal structure refinement.

Next, the focus of the chapter switches to the high-pressure equipment used during these studies. This begins with a general comment on generating pressures in excess of 1 GPa, before focusing on opposed anvil devices. Included in this section is an explanation of pressure calibration. Two high-pressure devices are discussed in detail, the Merrill-Bassett type diamond anvil cell and the Paris-Edinburgh press. Within discussions of the Merrill-Bassett cell is a description of the new Böhler-Almax seats, and the advantages that they bring to single-crystal diffraction. For the Paris-Edinburgh press, there is an overview of the motivation for its design and a discussion of how it has been adapted.

The chapter then introduces the specific high-pressure diffraction instruments that were used for data collection during this thesis. This section is divided into three main parts. The first of which describes the neutron powder diffraction instruments used; PEARL/HiPr at the ISIS facility, UK and D20 at the Institut Laue-Langevin, France.

Each instrument is described with reference to the quality of data that can be collected from each. This is followed by a description of the corrections that have to be applied to high-pressure neutron powder data. The second part of this section describes x-ray powder diffraction instruments. During these studies x-ray powder diffraction data were only collected at station ID09a at the European Synchrotron Radiation Facility (ESRF), France. The station is described and the methods of correcting the diffraction intensities obtained from ID09a explained. The last part describes the x-ray single-crystal instruments used. The section describes the in-house APEX II diffractometer used for preliminary studies as well as stations 9.8 and 9.5 at Synchrotron Radiation Source (SRS), UK and station ID27 and ID09a at ESRF, France. The section then explains the stages of data reduction before refinement can progress.

The last section describes the processes of synthesis and growth used to prepare samples for these studies. There are descriptions two the methods from cryogenic gas loading (for Merrill-Bassett and Paris-Edinburgh pressure cells) with reference to some of the problems that were encountered. As a wider demonstration of techniques learnt during this thesis, two methods of clathrate synthesis used for studies described in Appendix A are explained. Lastly the methods of crystal growth are described, along with the development of equipment and techniques to achieve this.

1.3 Chapter 4 - Studies of methane, phase A

Methane solidifies at room temperature at a pressure of 1.3 GPa to a face centred cubic structure designated phase I. Because the molecule in this phase is completely rotationally disordered, comparisons of phase I have been made to the rare gas solids (argon, neon, etc.). Methane phase A forms from phase I at room temperature and a pressure of 5.2 GPa. The first section of this chapter is a review of the development of the methane phase diagram at high-pressure and discussion of previous studies on phase A. The similarity of the methane molecule to the rare gases had led to an expectation that methane would show a similar structural progression with pressure; face centred cubic to hexagonal close packing.

The next section presents a powder diffraction study using archive data. From this study the need for a single-crystal study is established. Before this single-crystal study is described, the chapter will outline a validation study that was undertaken. This was to verify that valid results could be achieved from the small high-pressure samples of weakly scattering methane. The validation study was carried out on the preceding low pressure methane phase I. The study results of the validation study enabled the author to comment on the validity of calculated scattering factors for a rotationally disordered methane molecule.

The subsequent single crystal study is described, with specific mention to adaptations made to the methods of crystal growth. From the data collected from subsequently crystals the carbon structure of methane phase A could be determined. Two, related, structures were found to fit the diffraction data. These are both discussed, but only one is used for further refinement. The structure was refined against a separate data set. The molecular structure is discussed, with reference to its departure from the expected packing regime.

The next section of the chapter presents the neutron powder diffraction data collected on phase A. Subsequently these data were used, with the structure from the preceding single-crystal study, to determine hydrogen positions within phase A. The author believes that some of the hydrogen in the structure are disordered, and evidence for this is presented.

1.4 Chapter 5 - Studies of methane, phase B

Similarly to the chapter on phase A, this chapter begins by outlining previous characterisation of phase B's structure. Like phase A, speculations on the structure of phase B in the literature had centred about the expectation for methane to take up hexagonal close packing.

The resultant study of phase B progressed in a similar way to that of phase A. The characterisation of the phase started with a powder diffraction study, the results of which dispute the previously determined unit cell of phase B. Using the collected powder diffraction data the symmetry of the structure is confined to a body centred cubic cell. Again, the structure was determined to be too complex to be solved from powder diffraction data alone.

The results from the powder diffraction study are used to progress a single-crystal study of phase B. From the resultant data the carbon structure of phase B was determined with Fourier difference methods. The structural result was complicated by the presence of nitrogen contamination within the pressure cell. When compared to other cell loadings, it was justified that the presence of the contaminant was having no effect on the structure of methane. Similarly to phase A, the resultant carbon structure was refined against a separate data set and the molecular arrangement discussed.

Because of the contamination effects, the very existence of phase B was called into question. Its continued existence as a distinct phase of methane was justified by a short study showing a transition between phase B and the proceeding phase HP at 23 GPa. The last section in this chapter charts the attempts to obtain neutron diffraction data from this phase.

1.5 Chapter 6 - Further studies of the phase diagram

To facilitate improved modelling of methane behaviour, its solid phases must be characterised at all conditions that can currently be obtained by experiment. As a contribution to this, Chapter 6 describes two studies undertaken to determine the structure of methane at conditions never before accessed by diffraction experiments.

The first study describes a low-temperature, high-pressure neutron diffraction study of methane. Using a specially adapted Paris-Edinburgh press, the unit cell of methane was assigned at temperatures to 20 K and pressures to 5 GPa. This section includes an account of the difficulties preparing this experiment and the practicalities of analysis.

The second study that this chapter describes is a collection of investigations undertaken as a result of observations made during the growth of single crystals. Reproducibly, a transformation was observed occurring within the sample at temperature of $\sim$430 K and above pressures of 5 GPa. This section will account the attempts to characterise the resultant phase from this transformation with high temperature single crystal diffraction.

1.6 Chapter 7 - Conclusions

The conclusions comment genrally on the results and implications of this thesis. The trend of methane structures solved by this thesis has been to depart, from the expected, to be complex multi-site crystals. This result calls into question many studies that have assumed a single-site model for methane at high-pressure.

Chapter 2

The new mineralogy of the outer solar system

It is the intention of this review to introduce a new way of regarding high-pressure studies of methane. Together with water and ammonia, methane is a planetary forming 'mineral' of the outer solar system. As such, understanding of these molecules behaviours at the conditions of planetary interiors will facilitate modelling. This could lead to explanations for phenomena that have been observed in this region of the solar system. Experimental studies of pure methane, water and ammonia are most applicable to the icy gas giants, Uranus and Neptune. In particular these compounds are thought to make up the 'hot ice' layer, comprising of over two thirds of each planet's mass. The interior conditions of Uranus and Neptune are presently inaccessible for experimental studies. Instead computer simulations have to be relied on. Thorough understanding of the structures and behaviour of methane, ammonia and water at accessible experimental conditions, such as high pressures, could vastly improve the accuracy of calculations. This review will discuss methane, water and ammonia, as well as binaries between these, as minerals would draw attention to the wealth of studies that still need to be completed.

2.1 How do we know anything about the interiors of Uranus and Neptune?

Earth and space based spectroscopy have given insights into the atmospheric compositions of Uranus and Neptune. Direct sampling of the interiors of these planets is impossible. Instead models of the interiors of Uranus and Neptune have been built from coupling exterior observations with fundamental knowledge. The first of these

'building blocks' are constraints from models of the formation of the solar system.

Elemental abundance of our star, the Sun, gives an overall picture of the elements present within the proto-planetary nebula, from which the planets would have evolved. Hydrogen is the most abundant element by far (75%), then helium (23%). But, the next most abundant elements are oxygen, carbon and nitrogen (0.9% 0.3% and 0.1%) [dePater 01]. The evolution of these elements into molecular species was a complex process which varied with time and distance from the sun within the proto-planetary disk. The key point of note is where the temperature of the proto-planetary disk dropped below 500 K. At this point water could begin to condense directly from the nebula. This occurred beyond the 'ice line', 4 AU in our solar system, and enabled rapid core formation. This led to run-away accretion forming the giant planets; Jupiter, Saturn, Uranus and Neptune - a model consistent with current observations.

The gravity field of a symmetric and spherical planet only reveals one piece of information: the body's mass. However, and fortunately for the planetary science community, all the planets rotate and consequently oblate in a way which is constrained by their interiors. If hydrostatic equilibrium is assumed the external gravitational potential, Φ, of a uniformly rotating body can be expanded with even Legendre polynomials to Equation 2.1.

$$\Phi = -\frac{GM}{r}\left[1 - \sum_{i=1}^{\infty}\left(\frac{R_e}{r}\right)^{2n} J_{2n} P_{2n}(\cos\theta)\right] \tag{2.1}$$

Where G is the gravitational constant, M is the planetary mass, R_e is the equatorial radius, θ is the angle between the rotation axis and the radial vector $\mathbf{r}$. P_{2n} are Legendre polynomials and the dimensionless J_{2n} are the gravitational moments. The rotation of each planet causes obliquity, expressed as $\epsilon \equiv (R_e - R_p)/R_e$ where R_p is the polar radius. This in turn can be expressed as gravitational potentials, Equation 2.2.

$$\epsilon \simeq \frac{1}{2}\left(3J_2 + \alpha\right)\left(1 + \frac{3}{2}J_2\right) + \frac{5}{8}J_4 \tag{2.2}$$

Here, α is related to the mass, equatorial radius, the planetary angular rotation and obliquity; all measurable quantities.

It is these gravitational moments, J_2 and J_4, that can be calculated from observations. They can be derived from natural satellites and directly by artificial satellites. The gravitational moments are characteristic to the density distribution of each planet. There are also other, less direct, observational constraints upon a planets interior; the magnetic field and the internal heat flux. Both of these can indirectly provide information on the interior of the planet and as such are reviewed in the discussions below.

Table 2.1: Summary of gravity fields and radii for the gas giants, values taken from [Guillot 05]. M is the mass of the planet, R_e is its equatorial radius, R_p is its polar radius, with $\overline{R}$ the average radius. $\overline{\rho}$ is the average density, J_2, J_4 and J_6 are the gravitational moments. C is the value of axial moment of inertia, as it is less than that of a sphere with uniform density this implies a dense central region for all the gas giants. Uranus and Neptune have no values for J_6 as no spacecraft has passed close enough to observed this.

	Jupiter	Saturn	Uranus	Neptune
M $\times 10^{-29}$ [g]	18.986112(15)	5.684640(30)	0.8683205(34)	1.0243542(31)
$R_e \times 10^{-9}$ [cm]	7.1492(4)	6.0268(4)	2.5559(4)	2.4766(15)
$R_p \times 10^{-9}$ [cm]	6.6854(10)	5.4364(10)	2.4973(20)	2.4342(30)
$\overline{R} \times 10^{-9}$ [cm]	6.9894(6)	5.8210(6)	2.5364(10)	2.4625(20)
$\overline{\rho}$ [g cm^{-3}]	1.3275(4)	0.6880(2)	1.2704(15)	1.6377(40)
$J_2 \times 10^2$	1.4697(1)	1.6332(10)	0.35160(32)	0.3539(10)
$J_4 \times 10^4$	-5.84(5)	-9.19(40)	-0.354(41)	-0.28(22)
$J_6 \times 10^4$	0.31(20)	1.04(50)	...	...
C/MR_e^2	0.258	0.220	0.230	0.241

It was the grand tour of the outer solar system by the Voyager 2 spacecraft that revealed most of what is known about Uranus and Neptune. The values that characterise the gravity fields of Uranus and Neptune can be seen in Table 2.1, including values from Jupiter and Saturn for comparison. The first observation is the large differences in their polar and equatorial radii. This is caused by the very fast rotational period, about 17 hours, for both Uranus and Neptune.

$$\overline{\rho} = M / \frac{4}{3}\pi s_0^3 \tag{2.3}$$

The biggest constraint on Uranus' and Neptune's interior composition is the average density, calculated with Equation 2.3, and displayed in Table 2.1. Compared with that of the Earth (5.15 g cm^{-3}), the low average density confirms that the majority of these planets will be composed of materials lighter than silicates and possibly gaseous in state. This first approximation gives a remarkable insight. In Figure 2.1, it is shown that hydrogen must be the dominant composite of Jupiter and Saturn as it is the least dense material. Additionally it is observed that the the smaller Saturn has a greater departure from a uniform cosmic mixture, indicating that a larger fraction of helium must be present at depth. In contrast the average densities of Uranus and Neptune show greater affinity to the ice isentrope. By 'ices' the planetary science community refer to 'volatile species that under conditions within the outer solar system become planetary forming materials' [Hubbard 95]. In particular for the giant icy planets, Uranus and

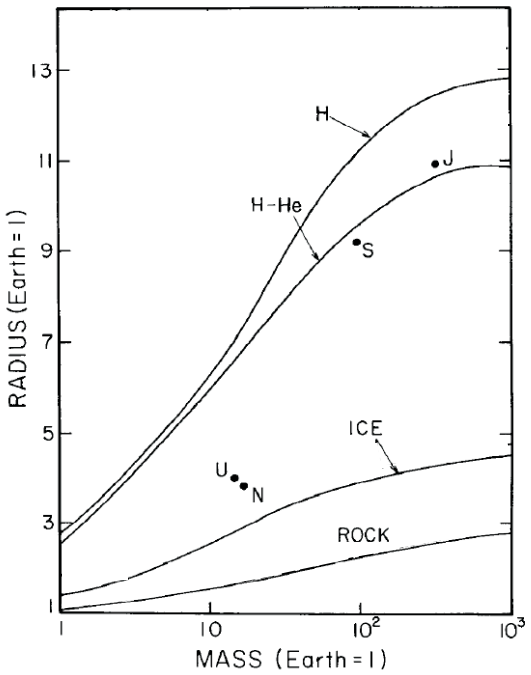

Figure 2.1: The mass-radius relationships for self-gravitating bodies of idealised compositions [Stevenson 82] of pure hydrogen, pure helium and an 'ice' and 'rock' composition taken from [Hubbard 80]. The positions of the giant gas planets on this plot are marked with J for Jupiter, S for Saturn, U for Uranus and N for Neptune.

Neptune, the literature refers [Hubbard 80, Stevenson 82, Guillot 05, Oganov 05] to a mixture of H_2O - CH_4 - NH_3 in solar abundance. This mixture is calculated to make up to 70% of the planets' composition.

For an interior model to be valid, its density distribution must conform to the observed gravitational moments. The density of a material under non-ambient conditions can be calculated with an equation of state. However, the conditions, temperature and pressure profiles, for gas giants can only be assumed from the density distributions. Hence, many differing interior models can be fitted to the gravitational moments which leads to an ambiguity as to the relative fractions of atmosphere, ice and rock. But, the relative fractions are limited by what could have been amassed during accretion, and any model must realistically reflect this. The ambiguities in relative mass fractions in addition to those inherent within the equation of state calculations and both of these problems must be kept in mind. From the observed J_2 and J_4 components, a common three layer model has been constructed for Neptune and Uranus. The density profiles that fit the observational constraints are shown in Figure 2.2. The value of J_4 is thought to require a central core of an Earth mass, accompanied by an atmospheric enhancement in volatiles of about 20 times the solar values [Podolak 91]. Alternatively,

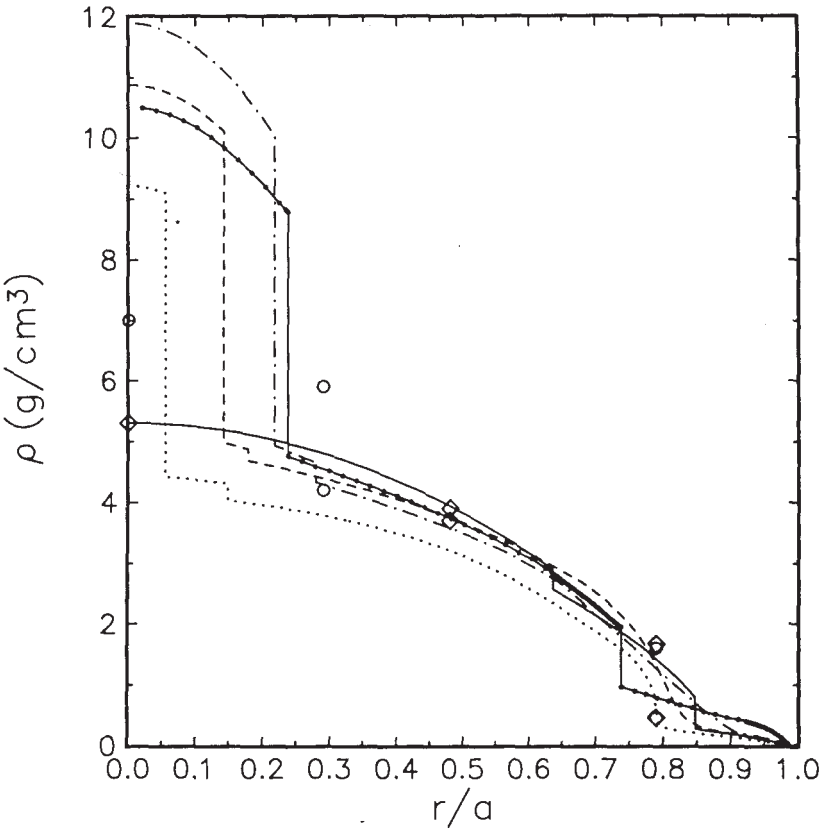

Figure 2.2: Comparison of four modelled density profiles of Neptune and one for Uranus (the light dashed line) taken from [Hubbard 80]. All the models have been determined by fitting of the observed J_2 and J_4 parameters. All profiles are for models of Neptune, except the light dashed line which is calculated for Uranus. The Uranian profile shows systematically lower densities because of its smaller mass. With the exception of the solid line (representing a core-less profile for Neptune [Podolak 90]) all the profiles exhibit the same features. The most prominent feature, in the profiles including a core, is the large discontinuity density at about 0.15-0.25 Neptune radius and 0.5 Uranus radius. This boundary is assumed to be between the atmosphere and 'hot ice' layer. The open symbols are from a separate model, [Zharkov 91] and show general agreement with the other models presented here.

it is possible that a one layered interior of hydrogen, helium and rock mixture could fit the gravitational moments. Other evidence, such as the 30 times enrichment of methane in the Neptune and Uranus atmospheres and the observed magnetic fields, further validate the assumption of a hot 'ice' layer [Hubbard 95].

Unlike terrestrial planets, the giant planets have a large intrinsic heat flow that can be measured by remote sensing. This is because of both the larger values of heat flow these planets exhibit and lower background, being further from the sun. Table 2.1 gives the observed heat flow parameters for each of the giant planets. Comparing the internal power per unit mass (parameter 4, Table 2.1) to the value from a carbonaceous chondrite [0.4×10^{-11} W kg^{-1}] (taken to be characteristic of radioactive decay) we see that Neptune's heat flow is too large to be described by this process alone. Current models suggest that the large internal heat flux from the giant planets is primarily a remnant from the accretion process [Hubbard 80]. The internal power per unit mass of Neptune is in stark contrast to the value exhibited by Uranus, which is particularly low. This has been interpreted to show that the remnant heat of Uranus is trapped beneath a non-conductive layer [Guillot 95].

A further observational constraint upon Uranus and Neptune is their magnetic fields, illustrated in Figure 2.3. Both of these bodies exhibit magnetic fields that are anomalous to those observed elsewhere in the solar system. Unlike the fields of Earth, Jupiter and Saturn; Uranus and Neptune's fields are not dipolar or axial symmetric. It was suggested [Hubbard 95] that to generate fields of this nature a new type of thin-shell dynamo would need to arise.

It was unclear whether or not a magnetic field generated by a thin-shell dynamo would be sustainable on long enough time scales to explain the fields of Uranus and Neptune. Recent calculations have shown that this is possible [Stanley 04]. For this to be accomplished a convective region in the interior must arise. This is at odds to models previously introduced in Figure 2.2, which assumed a purely conductive interiors for Uranus and Neptune. Whilst the previous models explain the present-day luminosity they imply that the interiors would be stratified compositionally and unable to convect. The stark differences between Uranus and Neptune's heat flow was thought to arise from small differences in their interior stratification [Guillot 95]. Herein lies one of the key issues for further constraining Uranus and Neptune's interiors; to unite the models that explain the observed heat flow (implying a stratified interior) with those that explain the generated magnetic fields (convecting interior). To achieve this detailed knowledge on the behaviour of each layer's constituents is vital. To model properly and characterise the hot ice layer within Uranus and Neptune the physical properties of water, ammonia and methane must be accurately constrained.

Parameter	Jupiter	Saturn	Uranus	Neptune
(1)Effective temperature (K)	124.4(3)	95.0(4)	59.1(3)	59.3(8)
(2)Energy balance	1.67(9)	1.78(9)	1.06(8)	2.61(28)
(3)Internal energy flux (W m^{-2})	5.44(43)	2.01(14)	0.042(47)	0.433(46)
(4)Internal power/unit mass (10^{11} W kg^{-1})	17.6(14)	15.2(11)	0.392(441)	3.22(34)

Table 2.2: Heat flow parameters for the giant planets taken from [Hubbard 95]. The effective temperature is the total infrared energy flux from the planet, including the contribution from sunlight. The energy balance is the ratio of the infrared energy flux to the value for thermalised sunlight alone. The average internal energy flux is the total value from their interior, with the last parameter being the average of this per unit mass.

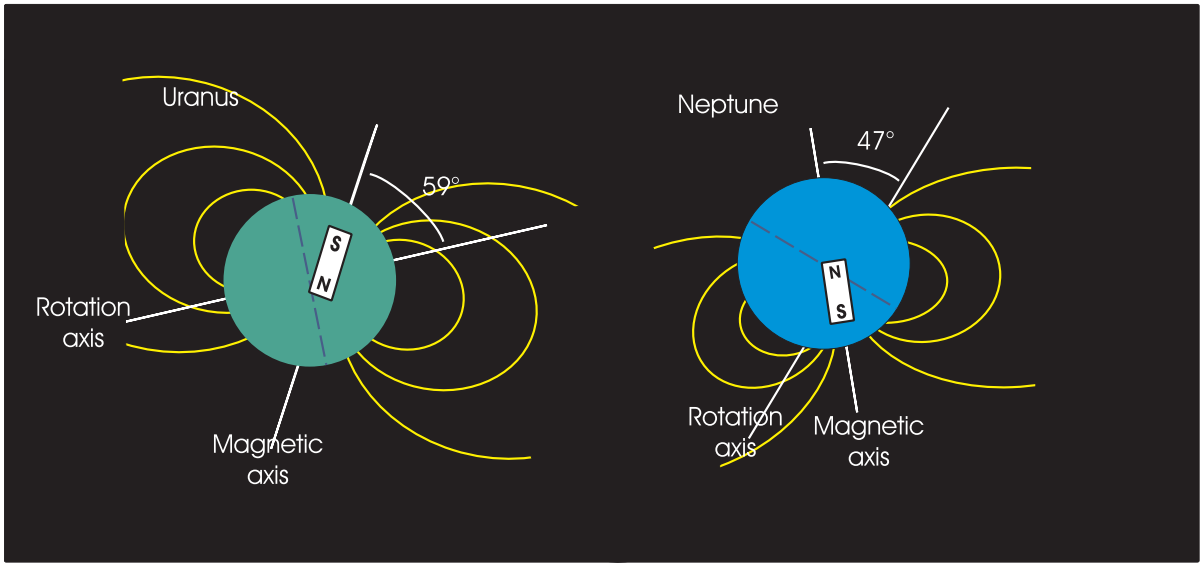

Figure 2.3: The anomalous magnetic fields of Uranus and Neptune. The yellow lines indicated the magnetic force lines and the blue dashed line indicates the equator (perpendicular to the rotation axis) of each planet. Unlike the other planets in the solar system with magnetic fields, their rotation axes and magnetic axes have a abnormally large angular separation, and the magnetic field has a non-centred dipole.

2.2 Objective

There is no method of directly sampling the interiors of planets in the outer solar system. Instead, relevant experimental studies must be carried out within the constraints put forward by the observations and subsequent models that have been outlined. To fully understand the interiors of the icy gas giants, Uranus and Neptune, experiments on water, ammonia and methane under the conditions of the hot ice layer would need to be carried out. These conditions are presented in Figure 2.4. The boundaries of this layer are accepted to be from 10 GPa and 2000 K to a maximum of 800 GPa and 8000 K, although the precise position of this lower boundary is highly subjective [Hubbard 95].

Despite the similarities between Uranus' and Neptune's interior structures, inferred by the gravitational moments, it is important to keep in mind that the realities may be very different. The difference in heat flow (Table 2.1) between Uranus and Neptune indicate that these simplistic models must only be used as a guide and that only through detailed knowledge of the constituent components can all the observed phenomena be explained.

To re-create the interior conditions of the gas giants experimentally is extremely challenging. The majority of experiments that will be discussed that were undertaken at

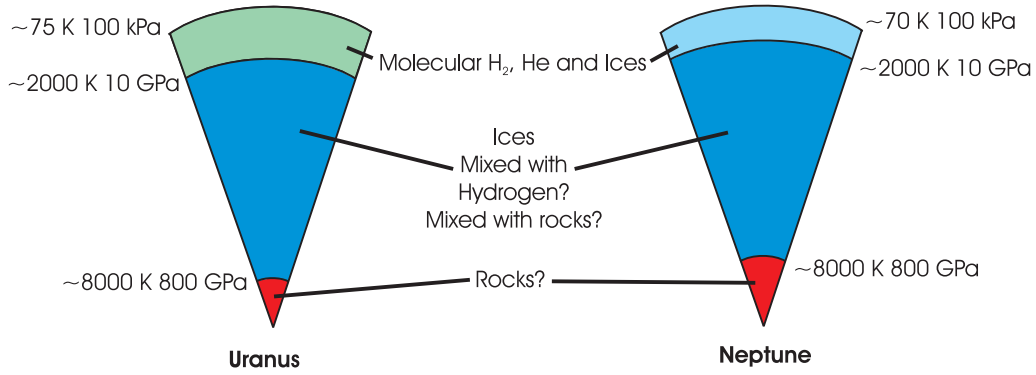

Figure 2.4: Illustrating the 3-layer interior models of Uranus and Neptune after [Guillot 99], showing the range of temperatures and pressures that define each layer.

giant planet conditions come from the dynamic high-pressure (shock-wave) community. Increasingly, with improved equipment and methods, this will not always be the case and static high-pressure experiments at Uranus and Neptune conditions will become more viable.

All conditions can be simulated computationally. But constraints on potentials derived from experiments are crucial to the accuracy of theoretical predictions. Accurate determination of structures at lower pressures and temperatures with experiments are vital grounding for computational studies. An understanding of fundamental properties can significantly influence the accuracy and interpretation of the computational results generated.

2.3 Water

The complexity of water under pressure was one of the first great discoveries of high-pressure science. P.W. Bridgman, the only worker in the field to have received a Nobel prize, was a pioneer of this investigation [Bridgman 37]. He found that upon compression at room temperature water freezes to tetragonal ice VI at 0.9 GPa and alters to cubic ice VII at 2 GPa. Figure 2.5 is of the current high-pressure phase diagram of water, and labels the principal phases of interest to this review.

In both ice VI and VII the orientation of the water molecule is disordered. At each molecular site the oxygen atom remains fixed, but the orientation of the hydrogen atoms may not replicated at an identical site elsewhere in the structure. This can be visualised as the hydrogen atoms being free to 'flip' about, explained by the 'half hydrogen model' for ice Ih proposed by Pauling [Pauling 39]. In this model the oxygen in tetrahedrally co-ordinated with hydrogen atoms, but each hydrogen is only half occupied.

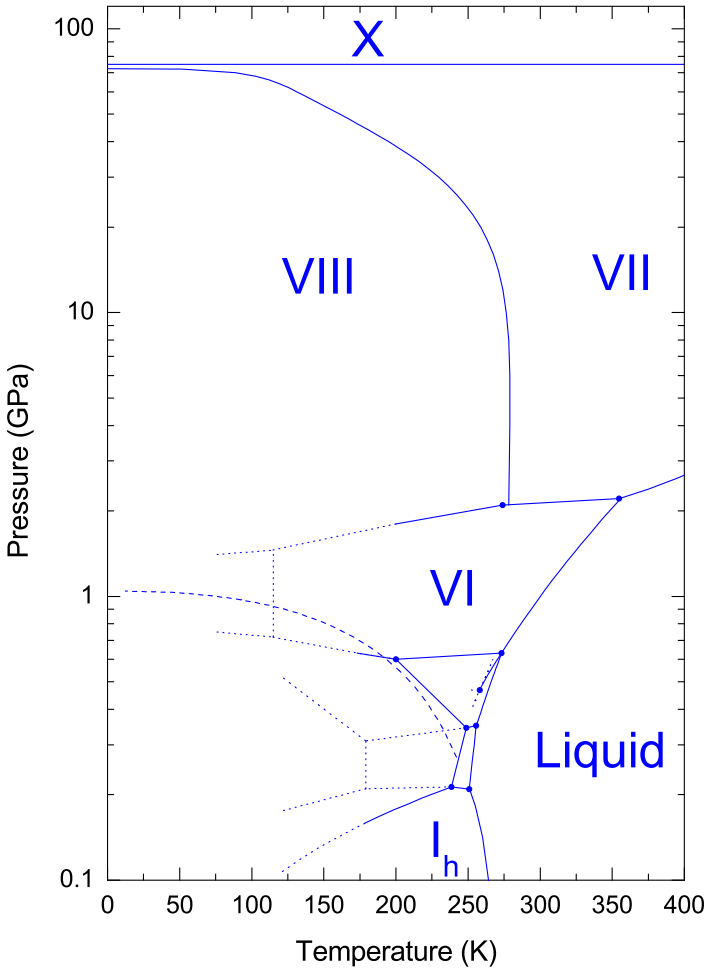

Figure 2.5: The phase diagram of water ice with the principal phases discussed in this review labelled. The dotted line is a projection of the negative melting line to low temperatures.

Ice Ih, the ambient pressure form of ice, forms a tetragonal network with the central oxygen atom connected to two of its nearest neighbours. This is achieved by donating forming hydrogen bonds to two other molecules, and then accepting hydrogen bonds from two other molecules. Because of the disorder, a time averaged structure of ice Ih will show only two hydrogen atoms for each O $\cdots$ O bond, but with a 50% chance of finding an atom at this site at any time, Figure 2.6.

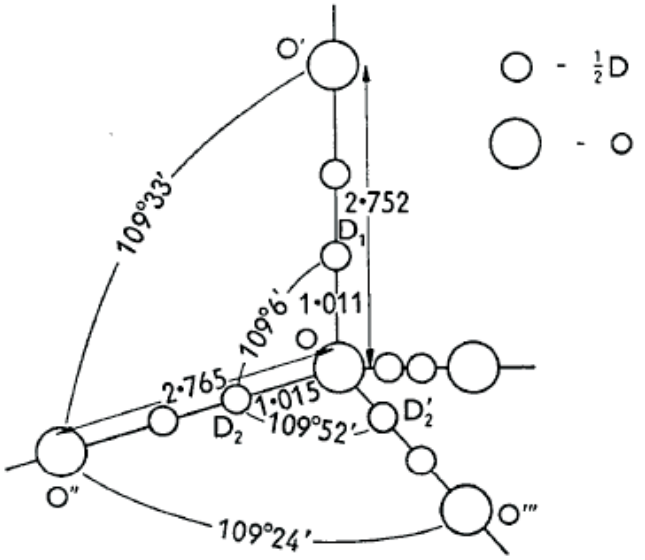

Figure 2.6: Structural relationships in one tetrahedron of the ice Ih structure. The distances and angles are those at 223 K [Peterson 56].

At lower temperatures and sufficient time the hydrogen 'flipping' will slow and the molecules become fixed, forming an ordered crystal. Ice Ih will transform to an ordered form, ice XI, at 72 K but at these temperatures the molecules are effectively immobile. This inhibits long range ordering within laboratory time-scales. Ice XI can be obtained by doping ice Ih with KOH [Tajima 82], by introducing ionic defects. Recently two new phases ice, phases XIII and XIV, were discovered by ordering ice V and XII respectively by doping with HCl [Salzmann 06]. Within Ganymede and Callisto, given appropriate conditions, these ordered ices may be the dominant interior phases.

Between 2 and 60 GPa there exist only two structures of ice, VII and VIII, both of which can be visualised as inter-penetrating hydrogen bonded networks of the cubic ice Ic. Like ice Ih and XI, ice VIII is the ordered form of ice VII. Cubic ice VII will transform to tetragonal, ordered, ice VIII at 3 GPa at $\sim$273 K. However, increasing the pressure from 3 GPa, the ice VII to VIII transition drops in temperature. Ice is, in this high-pressure regime, favouring disorder.

In both the ice VII and VIII structures, oxygen atoms are surrounded by eight nearest neighbours but only bonded, tetrahedrally though hydrogen bonds, to four of these. In ice VII multi-site disorder is observed in oxygen as well as hydrogen atoms [Nelmes 98]. Ice VII transforms, at pressures approaching 60 GPa, to 'symmetric' ice X. In ice X the hydrogen atoms are located in central and ordered positions between the oxygen atoms replacing the previous hydrogen bonds, demonstrated in Figure 2.7.

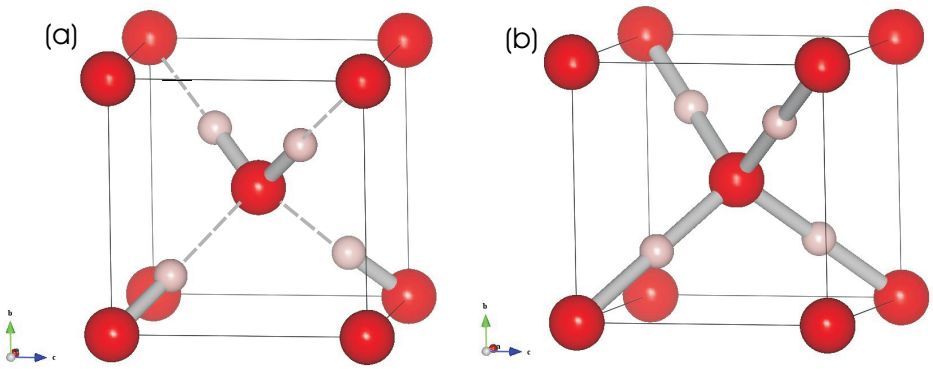

Figure 2.7: Crystal structures of ice VII (a) and ice X (b) with the red spheres representing oxygen atoms in a bcc lattice and the smaller pink spheres hydrogen. (a) exhibits how ice VII can be viewed as a intermediate step towards ice X. Each hydrogen is only bonded to one oxygen, but is hydrogen bonded to a separate molecule. As the hydrogen in ice VII are disordered, and will only have 50% of being found in a particular site, the oxygen are effectively tetrahedrally co-ordinated. (b) shows that in iceX the hydrogen atoms become protons each bonded to two oxygen. The hydrogen are situated in the midpoints between oxygen and create an interpenetrating network throughout the structure.

Studies of water within the conditions of the ice layer of Neptune and Uranus have thrown up a multitude of inconsistencies. Still, to date, there is little consensus on the behaviour of the water molecule at these extremes. Before any studies commenced, it was generally believed that under extremes of temperature and pressure, of order of those found in the gas giants, the molecular nature of water would break down. Any production of charged ions and change in transport properties could begin to explain the formation of the giant and unusual magnetic fields that Uranus and Neptune exhibit. Initial shock-wave experiments charting the conductivity of water under pressure showed that it increases exponentially until a plateau between 30 and 60 GPa at 20 $(\Omega^{-1}cm)^{-1}$ [Hamann 69]. Later developments of simultaneous Raman

spectroscopy with shock experiments enabled the nature of the water molecule itself to be investigated [Holmes 85]. This investigation showed no evidence for H_3O^+ and OH^- ions that were expected, instead pointed to a mechanism that formed H^+ and OH^- ions. The Raman spectroscopy also showed a decrease in the hydrogen bonding, tending to zero at 26 GPa the maximum pressure achieved in this experiment.

The results of conductivity measurements were later confirmed by theoretical means [Cavazzoni 99], where calculations showed agreement with the results from the previous shock-wave experiments, Figure 2.8. Further to this, Cavazzoni *et al* proposed a super-ionic phase which exists above the stability field of ice VII. They charted the progress of water molecules (all initially as ice) at various fixed pressures, starting at 30 GPa, up to temperatures of 3500 K. In each of these experiments two forms of 'melting' were observed, the first leaving the oxygen sub-lattice intact and the second marked when this disintegrated. Between these 'meltings' the ice phase is thought to consist of fast-conducting protons diffusing through an oxygen lattice.

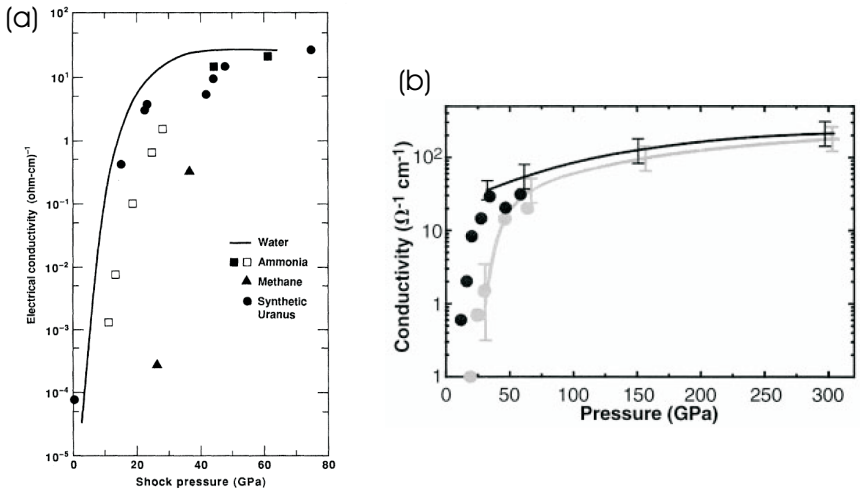

Figure 2.8: (a) taken from [Nellis 88], shows the ionic conductivity of water (solid line) measured along the planetary isentrope of Neptune, compared with conductivity results from shock-wave experiments on ammonia, water and methane. (a) also compares results from a similar study on a 'synthetic Uranus' composition; a solution of water, ammonia and isopropanol. (b) is taken from [Cavazzoni 99] and charts a similar investigation though this time from a theoretical study. The solid lines have been calculated for water (black) and ammonia (grey). The circles are values from the shock-wave experiments for comparison.

There have been a number of claims from static high-pressure experiments to have observed the super-ionic phase of ice. These have been determined from evidence

of a 'kink' in the melting curve thought to indicate a triple point in the ice phase diagram. Lin *et al* reported a discontinuous change in the melting curve at 35 GPa and 1040 K [Lin 05]. They charted this by noting a significant shift in the O-H Raman stretch. The melting curve that was measured subsequent to this point was much steeper than previously predicted, an extrapolation of which would intersect the Neptunian and Uranian isentropes at 50 GPa. The steepness of the melting line also indicated a large change in the physical properties of ice at this point. The authors suggest that this perhaps could be the super-ionic phase predicted by Cavazzoni *et al*. [Cavazzoni 99]. The claim was further supported by *in situ* x-ray diffraction, which showed the persistence of the oxygen sub-lattice under these conditions.

A further study [Goncharov 05] has reiterated the possibility of a solid super-ionic phase intercepting the Neptune planetary isotrope. This study was combined with molecular dynamics to investigate the nature of the super-ionic phase. Goncharov *et al* found a different point of discontinuity in the melting curve, proposing a triple point at 47 GPa and 1000 K. They also propose a new phase of 'disordered' ice VII that exists beyond the inflection but at lower temperatures to the super-ionic phase discussed by Cavazzoni *et al.* They reported that the difference between these phases is characterised by the mobility of the protons. The protons are more constrained and localised in the lower temperature disordered ice VII, before becoming more mobile and delocalised in the super-ionic phase [Goncharov 05].

Schwager *et al.* [Schwager 04] report a change in the melting slope of water at a similar pressure to Goncharov *et al* but at significantly higher temperature, 43 GPa and 1600K. They used a different method of noting melting, relying on visual observations. All of the above studies are contrary to Dubrovinskaia and Dubrovinski's findings which report the melting line of Ice VII to 50 GPa with no observation of a change of slope [Dubrovinskaia 04].

The lack of consensus on the location and existence of a further triple point in the ice phase diagram is a key issue for any progression of the interior modelling for Uranus and Neptune. The possibility of the ice melting curve intersecting the icy gas giants isentrope would mean that the assumptions taken to construct the models in Figure 2.4 would have to be re-assessed. The differing views of the static community on this issue demonstrates the difficulty of these experiments. This strengthens the scientific case for accurate calculations, which can only be improved with full experimental characterisation of the water molecule at easily accessible conditions.

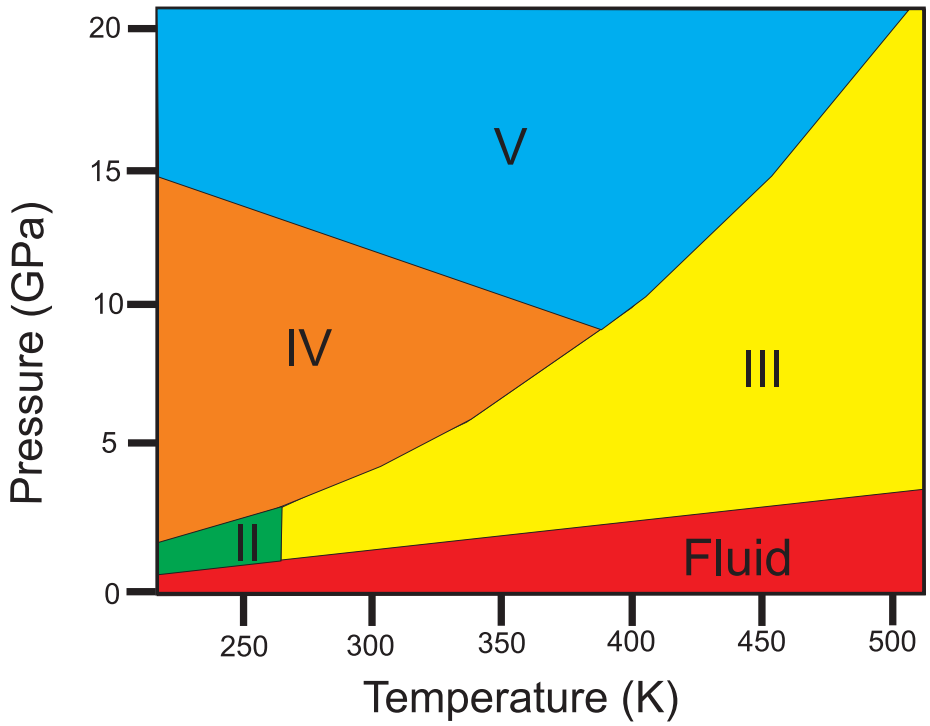

Figure 2.9: Showing the phase relations of four of the current known phases of ammonia [Ninet 08].

2.4 Ammonia

Like water, the structures of ammonia within its solid forms are governed by hydrogen bonds. Compared to water, this is a weaker effect and ammonia perhaps can be thought of as an intermediary between water and methane (which has no hydrogen bonds). Despite the weaker hydrogen bond behaviour, ammonia has been included in the speculations of a super-ionic phase under high-pressure and high-temperature conditions. The molecular nature of ammonia at extreme conditions is thought to break down, and nitrogen networks develop with protons (hydrogen) diffusing between them [Cavazzoni 99].

High-pressure studies on ammonia have been limited. Presently, ammonia is thought to take up six distinct crystalline phases. Part of the current phase diagram of ammonia is illustrated in Figure 2.9. At room temperature the first phase to crystallise from fluid at 1 GPa is phase III, a face centred cubic phase - which is rotationally disordered. Upon further compression at 3.5 GPa this transforms to phase IV [Gauthier 88].

Phase IV was the centre of some debate as to its structure, concluding with a departure from expected behaviour. Originally, x-ray diffraction suggested it adopted hexagonal close packing with space-group $P6/mmc$ and two molecules within the unit cell [Mills 82]. This would be in line with expectations of rare-gas like structure evolution, which discussed in detail for the case of methane below. However, this was later shown to be inconsistent with spectroscopic data [Gauthier 88] which required four molecules within the cell to explain the observed modes. Neutron powder diffraction data from ND_3, suggested that the structure is in fact orthorhombic, with $P2_12_12_1$ symmetry, but the nitrogen atoms adopt a pseudo-closed packed arrangement [Loveday 96]. Later x-ray single crystal data collection [Datchi 06], confirmed that this structure held for hydrogenous ammonia as well.

Phase V was originally reported by Gauthier *et al.* [Gauthier 88], and thought to be cubic from spectroscopic evidence. The single crystal diffraction work of Datchi *et al.* [Datchi 06] observed a reproducible crystal splitting at the location of the transition to phase V, along with a kink in the c/a ratio. However, the resultant crystallites still indexed to the same $P2_12_12_1$ symmetry of phase IV up to 123 GPa.

Hydrogen bond centring in ammonia has fuelled further discussions within the literature. This transition, analogous to that seen between ice VII to X transition, was first reported to occur at 60 GPa [Gauthier 88] from Raman spectroscopy. Similar to ice, hydrogen bond symmetrisation in ammonia was thought to force a structural transitions. As discussed above, the current picture of ammonia structures is that phase VI is maintained into the megabar pressure range. The iso-symmetric transition

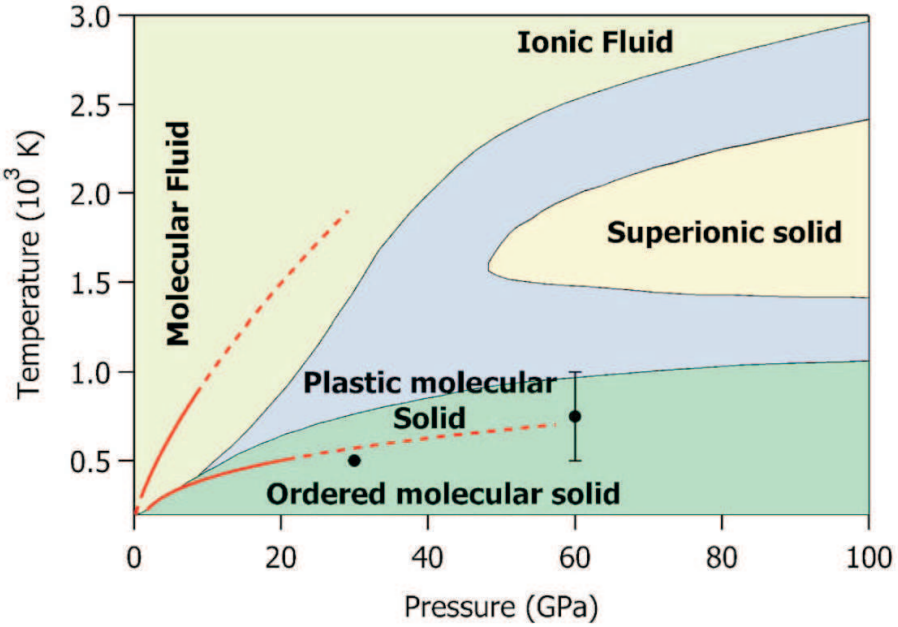

Figure 2.10: Taken from [Ninet 08] this figure compares the computational phase diagram of [Cavazzoni 99] to the melting curve determined in [Ninet 08] (red solid lines, dashed lines extrapolations). The top line is the melting line of ammonia that they observe (the bottom line being the phase III to IV transition). The blue area marks the uncertainty in transitions within the computational study.

reported previously to be to phase V, is now believed to a result of differing hydrogen arrangements [Datchi 06], the nitrogen atoms maintaining their pseudo-closed packed arrangement. Datchi *et al* also raised the possibility, from conflicting evidence in the spectroscopy, that hydrogen bond symmetrisation could occur in in some bonds, and not others at this point. This would later progress to all bonds at higher pressures [Datchi 06]. This hypothesis is at odds with calculations of ammonia phase IV that show that hydrogen bond symmetrisation would not occur to pressures approaching 1-2 TPa [Fortes 03].

Recent work by Ninet and Datchi [Ninet 08], Figure 2.10, charted the melting curve of ammonia to 900 K and found no evidence of a kink similar to that discussed for water. In fact, they report an affinity of the melting line to that extrapolated for methane, suggesting that the single hydrogen bond has little effect on melting in ammonia. The work of Ninet and Datchi [Ninet 08] is compared in Figure 2.10 to Cavazzoni *et al*'s phase diagram. Figure 2.10 shows that the experimental study has a much steeper melting curve to that previously calculated. This is projected to intersect the Uranian and Neptunian isentropes [Ninet 08].

2.5 Methane

Unlike water and ammonia, methane's room-temperature high-pressure structures remain unsolved. Figure 2.11 details the current high-pressure phase diagram of methane, setting out its eight high-pressure forms [Bini 97]. There has been some debate as to the numbering and relation of many of these phases. Of all the eight phases, only three of these have resolved structures with atomic co-ordinates, phases I, II and III.

A point to be considered about the methane molecule is its geometry: a carbon atom surrounded by a tetrahedral arrangement of four hydrogen atoms. This means that at lower pressures its structures can be compared to the more spherical noble gas solids. The comparison is maintained by methane's similar size and neutral charge. On compression along the room temperature isotherm, liquid methane solidifies at 1.3 GPa to a face-centred cubic structure, similar to the rare gas solids [Press 72].

Phase I, which can also be formed by cooling methane at ambient pressure below 140K, has been studied with both x-ray diffraction and Raman spectroscopy. It is known to have $Fm3m$ space group, with all four molecules able to freely rotate [Press 72]. Further cooling at ambient pressure, below 27 K, a second order phase transition occurs, instigated by the partial ordering of some of the molecules. This, Phase II, also has a cubic structure but with a unit cell containing 32 molecules [Press 72]. Within the primitive cell, six of the eight molecules are ordered with local

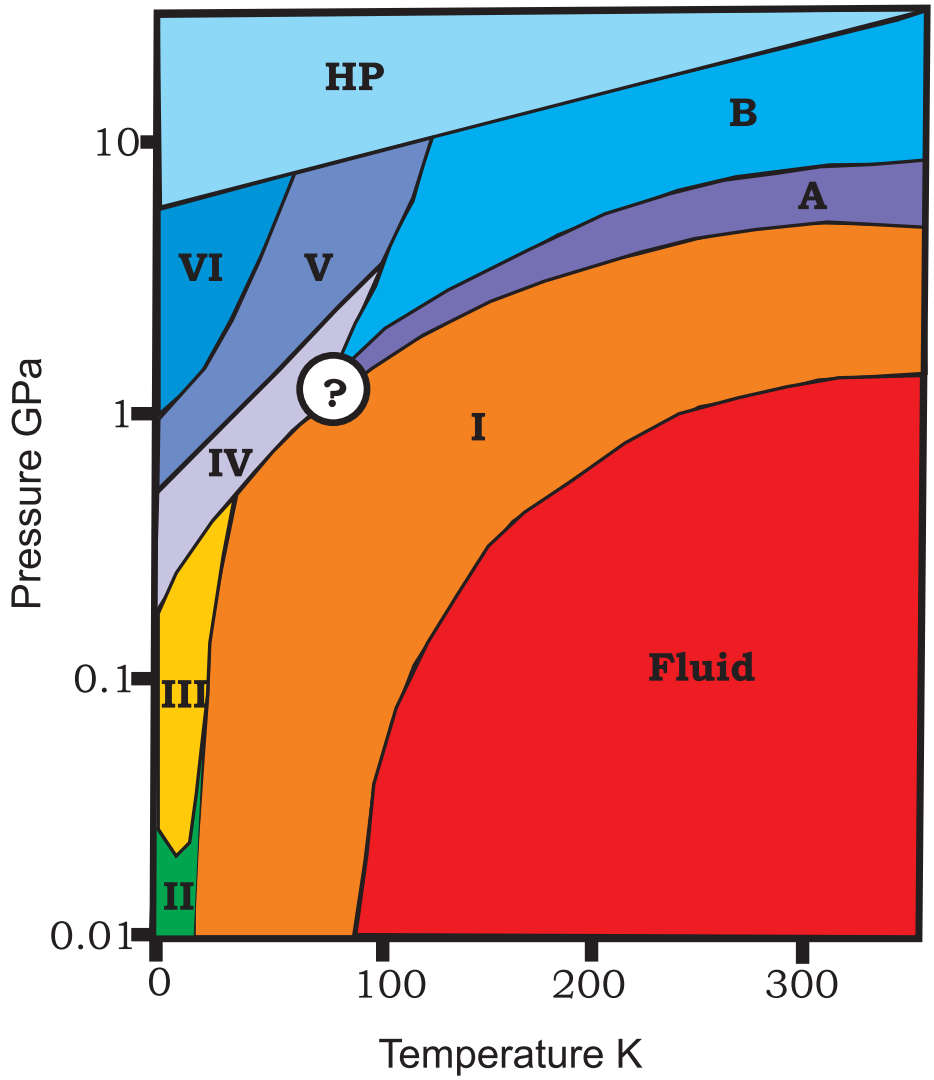

Figure 2.11: Current phase diagram of methane after [Bini 97], with the phase boundaries proposed by them. The area marked with the question mark indicates where the boundaries have not yet been determined.

symmetry of ($\bar{4}2m$). The remaining two molecules are spherically disordered, as those in phase I. This arrangement is less symmetric than phase I, resulting in space group $Fm3c$. Application of low pressure ($\geq$200 bar) to methane at temperatures below 20 K, forms phase III. The structure of phase III is closely related to that of II, but is orthorhombic with space group *Cmca* [Neumann 03]. Unlike the previous two phases, the hydrogen positions of methane phase III are fully ordered.

Compressing along the room temperature isotherm at 5.2 GPa, methane transforms to a new orientation, the nomenclature of which has been subject to some debate. Originally this was named phase IV and was thought to be iso-structural with a phase found at low temperatures [Hebert 87]. Subsequent workers separated the low and room temperature phase IV and renamed the room temperature form phase A [Bini 97]. Further compression at room temperature revealed another more sluggish phase transition, the onset of which begins at 9 GPa. This new phase was originally named VII [Hebert 87], but has subsequently been changed to B [Bini 97]. To date these phases (henceforth referred to as A and B for distinction) have not been subject of a comprehensive structural study. At present the unit cell of A has been found to be rhombohedral with $\alpha = 89.5^\circ$ and $a = 8.7$ Å [Nakahata 99], the with same group proposing that phase B is cubic with a lattice parameter of $a = 7.914$ Å [Umemoto 02]. Previous investigations of phases A and B will be discussed in more detail in Chapters 4 and 5 respectively.

Like water and ammonia, methane has been subject of a number of theoretical and shock experiment investigations that have probed its behaviour under more extreme conditions. These were motivated by preliminary results from hydrocarbons [Block 70] that indicated that this class of material would decompose under high pressure and temperatures to form condensed carbon and hydrogen. Shock-wave experiments [Nellis 81] suggested that methane decomposes into a mixture of condensed carbon (diamond) and hydrogen at pressures greater than 23 GPa and $\sim$2000 K. These conclusions were arrived at from theoretical assumptions on fitting the measured Hugoniot. Above 23 GPa the experimental Hugoniot pressures became less than those predicted by theory, which suggested the dissociation. Chemical equilibrium calculations also showed that other gaseous species of C, H, CH_2, CH_3 and C_2H_2, would also be present in the shocked samples.

First-principles molecular dynamics were employed to investigate methane up to 300 GPa, 5000 K [Ancilotto 97]. In their first experiment to 100 GPa and 4000 K they did not observe dissociation into condensed carbon and hydrogen. Instead Ancilotto *et al* report that methane dissociated to form saturated hydrocarbons of higher molecular weight, such as ethane (C_2H_6) and butane (C_3H_8). They re-interpreted the discontinuity observed by [Nellis 81] to be the onset of dissociation to the heavier

hydrocarbons. Under these temperatures and pressures, which correspond to the centre of the hot-ice layer of Uranus and Neptune, the neutral molecules produced would have no influence on the magnetic field. Ancilotto *et al.* found that the complete dissociation of methane to condensed carbon and hydrogen does not become energetically favourable until at least 120 GPa. They state that low-temperature dissociation would not occur until 300 GPa. Despite these conclusions a surprising experimental report later claimed that methane dissociates to condensed carbon and hydrogen at 10-50 GPa 2000-3000 K [Benedetti 99]. This was observed using a laser-heated diamond anvil cell and taking Raman measurements. However, these observations have not been repeated subsequently.

Methane is an analogue of silane (SiH_4) and germane (GeH_4). In these systems chemical pre-compression of the heavier element on hydrogen is calculated to initiate superconductivity under high-pressure [Feng 06]. This is perhaps contrary to other theoretical studies probing the metallisation of methane under pressure. Here it has been predicted that metallisation would not occur until 520 GPa, corresponding to a compression factor of $\sim$7.5 [Martinez-Canales 06]. Martinez *et al.* conclude that in these circumstances methane would not be a good candidate for a super conductor. However, the starting structure for both these studies were based on speculative structures of SiH_4 and GeH_4, only incorporating 3 to 4 molecules within the unit cell. Methane could be a structural analogue for these systems, which are extremely difficult to study experimentally.

2.6 Mixed-phased studies

The Earth exhibits a wide variety of geochemistry. A consequence of this is the varied and complex geological processes that are observed. In contrast, the composition of the Saturnian, Neptunian and Uranian systems are thought to be much simpler, dominated by water, ammonia and methane. As well as understanding the behaviour of these materials in their pure forms, binary and ternary mixtures should be investigated to fully re-create these planetary systems.

Under more moderate pressure and temperature conditions there has been a wealth of studies within the binary systems of methane-water and ammonia water. These can have had direct impact upon interior modelling of the moons in the outer solar system. One particular example, of relevance for Saturn's moon Titan, will be discussed in the last section of this chapter.

2.6.1 Methane hydrates

On compression with water, methane forms a clathrate hydrate, where the methane molecules are guests within cages formed of water hosts. There are currently three known clathrate structures varying in the size and number of cages that they contain, sI (seen in Figure 2.6.1) and sII which are cubic and sH which is hexagonal [Kirchner 04]. At relatively low pressure, methane and water mixtures transform to methane hydrate I (MHI) adopting a sI type clathrate.

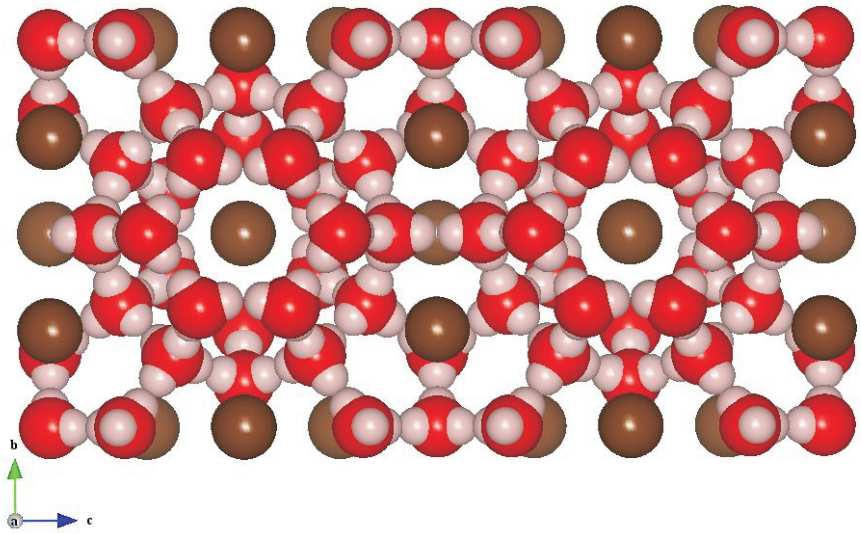

Figure 2.12: Diagram of the clathrate sI structure, with the brown atoms representing carbon at the centre of each methane molecule, and the red and pink atoms representing the water molecules. The water molecules are hydrogen bonded together to form two sizes of cadges.

Initial high-pressure diffraction studies suggested that MHI would progressively decompose into water (high-pressure ice), and methane between 1 and 2 GPa [Hirai 00a, Hirai 00b]. These experiments observed the production of ice VI at 1.5 GPa, progressing to the production of solid methane at 2.1 GPa. These conclusions were later revealed to be incorrect, with methane hydrate undergoing phase transitions and persisting to high-pressures along the room temperature isotherm. Currently three distinctive high-pressure structures of methane hydrate are known to be stable. The cubic methane hydrate I (MHI) is stable to 0.9 GPa, where it transforms to the sH hexagonal structure clathrate, methane hydrate II (MHII) [Loveday 01c]. At pressures exceeding 2 GPa a 'filled ice' methane dihydrate (MHIII) is formed [Loveday 01b]. This dihydrate (not

clathrate) structure is unusually stable with pressure and has yet to be observed to decompose under pressure, though it is calculated to do so at pressures approaching 100 GPa [Iitaka 03]. Recent work suggests that a further phase transition occurs at about 40 GPa [Machida 06]. This has been interpreted to be a result of hydrogen bond centring in the water cages.

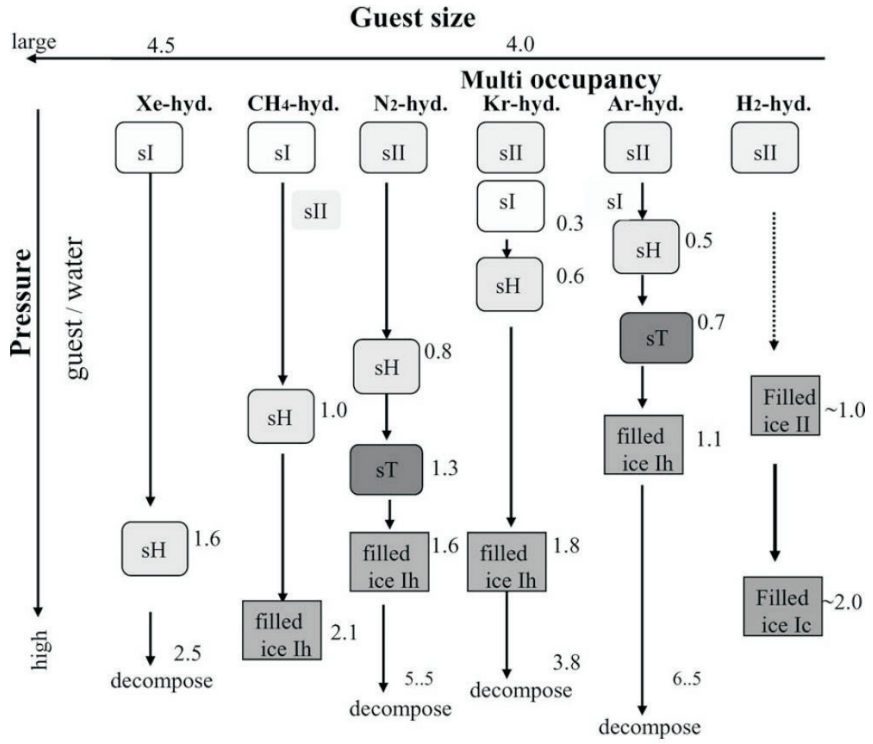

Figure 2.13: Stability and transitions of a selection of gas hydrates with pressure and decreasing (from left to right) guest size, taken from [Hirai 04]. Each of them form a clathrate structure, which is sustained beyond ambient pressures. Of interest are the two gas hydrates that have not be observed to decompose with pressure, methane hydrate and hydrogen hydrate.

The stability of this structure over such a wide range of pressure is surprising when compared to other gas hydrates. Figure 2.13. The larger noble gases xenon and krypton, along with nitrogen transform in similar sequence to that of methane, although xenon does not form a filled ice phase. However, unlike methane hydrate, all three of these have been observed to decompose under 6 GPa. Machida *et al.*, [Machida 05] have proposed an explanation for the anomalous stability of MHIII from Raman spectroscopy. They show substantial softening and splitting of vibrational modes of methane hydrate, indicating increasing intermolecular interactions between the host and guest upon increasing pressure.

2.6.2 Ammonia hydrates

There are three types of ammonia hydrate increasing in water content: ammonia hemihydrate ($2NH_3.H_2O$), ammonia monohydrate ($NH_3.H_2O$) and ammonia dihydrate ($NH_3.2H_2O$). The ammonia hydrates are the simplest molecular systems to contain mixed hydrogen bonding, O-H $\cdots$ N and N-H $\cdots$ O, and hence enable fundamental studies on the nature of these bonds to be carried out. More specifically to this project, ammonia hydrates occur widely in the solar system and are major 'rock forming' minerals in the icy satellites of Saturn, Uranus and Neptune. Both the ammonia monohydrate (AMH) and ammonia dihydrate (ADH) systems have been studied under pressure and at low temperature but a great deal is still unknown on phase stability. Both AMH and ADH have been revealed to have complex phase diagrams.

Seven separate phases of AMH have been identified, the structures of which are largely unknown. At ambient pressure, AMH takes an orthorhombic structure, space group $P2_12_12_1$ with dimensions of $a = 4.511$ Å, $b = 5.586$ Å and $c = 9.714$ Å at 110 K [Loveday 04]. One of the few high-pressure AMH phases that have been fully solved is AMH VI, which was found to be a new class of material: a hydrogen bonded molecular alloy [Loveday 99]. This phase is stable at room temperature above 6.5 GPa, and in contrast to other high-pressure AMH phases has a simple diffraction pattern comprising of one dominant peak and four accessory small peaks. This is indexed with a body centred cubic unit cell, $a = 3.37$ Å. AMH VI has been shown to be substitutionally disordered, a property that seems to be unique within H-bonded systems.

On compression at room temperature, liquid with composition of ADH forms into high pressure ice and AMH phases [Boone 91]. However, more recent studies have shown that compressing ADH at low temperatures, $\sim$170 K, and then warming back up to room temperature revealed new solid phases with ADH composition [Fortes 04]. These phases may prove to be stable within icy satellite interiors as the experimental pressure-temperature path taken to form them may be similar (but on a much faster time scale) to that of planetary accretion. This path opened up a whole phase diagram to study, currently five high-pressure polymorphs of ADH have been identified [Fortes 04].

2.7 Case study - Titan

High-pressure crystallographic studies can have significant implications for the understanding of the interiors of planetary bodies. This has been the case for Titan, the largest moon of Saturn. Like other satellites within the region it has a low overall density (1.88 g cm$^-$3), indicating a large compositional fraction of water. Its position

in the solar system also dictated that a suite of materials, ammonia and methane hydrates, would have initially formed the moon's interior [Lunine 87]. Titan has a substantial atmosphere a unique feature among the moons of the solar system. Like our own atmosphere it is mainly composed of nitrogen, but contains up to 5% methane [Kuiper 44]. This relative high percentage of methane presented a challenge to planetary scientists. The photo-chemistry of the stratosphere of Titan is such that the present amount of methane would be removed within a few million years [Yung 84]. The implications of this were that the atmospheric methane must be being replenished.

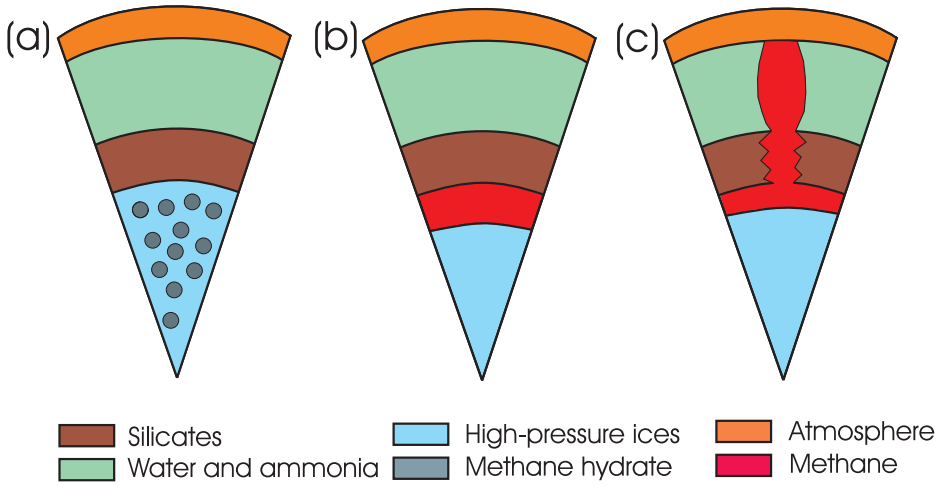

Figure 2.14: Series of internal evolution models of Titan before the discovery of MHIII after [Lunine 87]. (a), shows the interior of Titan just after accretion, with a rocky carapace overlying a mixture of high-pressure ice and methane clathrate. Under the pressure and gradual warming of the proto-core the methane hydrate dissociates resulting in (b), with a layer of free methane. The vastly more buoyant methane ruptures the rocky carapace, initiating core overturn. As this methane is half as dense as the ammonia-water it rises rapidly to reach the atmosphere, (c).

Methane would have initially accreted into Titan in the form of methane hydrates, along with ice, ammonia monohydrate and rock from the solar nebular [dePater 01]. It is thought that the beginning internal stratification resulted in a rocky carapace overlying a mixture of methane clathrates, ice and ammonia hydrates, Figure 2.14. As discussed in the previous section the original assumption was that methane clathrate structures would dissociate under moderate pressure. With this knowledge, the rising temperatures and pressures of this proto-core would cause the methane clathrate to dissociate creating a layer of free methane. The methane would rupture the overlying rocky carapace initiating core overturn (the denser rock differentiating to the centre of the body). The free methane, which is half as dense as the water and ammonia ocean, would rise rapidly towards the atmosphere, as illustrated in Figure 2.14. As

already pointed out, methane would only have a very limited life-span within Titan's atmosphere, being lost because of gravitational or photo-chemistry effects. The original source of methane replenishment was thought to be from oceans of simple hydrocarbons (methane, ethane) or from a methane saturated regolith that would exist on the surface of the moon [Lunine 87].

The realisation that solid methane hydrate persisted beyond 2 GPa had a profound effect on models of the interior evolution of Titan. If methane did not dissociate before core overturn then there would be no layer of free methane. Instead methane within the proto-core could exist as at MHIII [Loveday 01b]. Upon core overturn the MH III could back transform to MH II and MH I - coexisting with ammonia hydrates. A layer of methane hydrates up to 100 km thick would be present within the interior. A methane hydrate layer would be a more plausible repository of methane than surface storage. Tectonic and volcanic activity could provide a mechanism for the methane hydrate to reach the surface and dissociate [Loveday 01b].

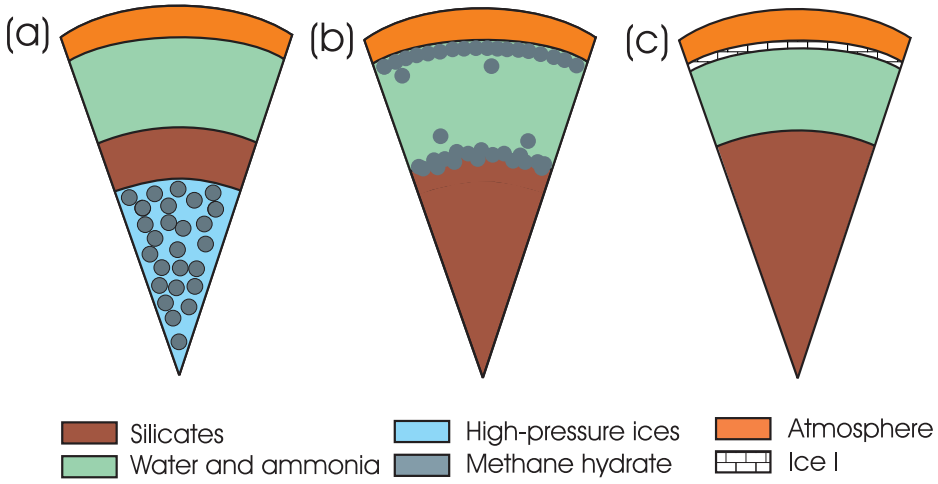

Figure 2.15: . Current model of the internal evolution of Titan after [Tobie 06]. Stage (a) is the same as in Figure 2.14. As the methane clathrate would not have dissociated the core overturn is a less dramatic process with the core methane unable to escape towards the surface. This gradual process would result in episodes of methane outgassing throughout Titans history. The first would result from the methane clathrate that could rise to the surface at core overturn. This would come form the layer in (b) that is close to the surface and be relatively prolonged. The second from the onset of convection within the silicate core. The core-methane hydrate boundary would subsequently heat up and initiate dissociation, resulting in a subsequent rise to the surface. The third occurs with onset of convection and crystallisation of a ice I layer just under the surface (c)

The current picture of Titan interior evolution is slightly more complex than originally set out by Loveday *et al* [Loveday 01b]. In their recent paper, Tobie *et*

al [Tobie 06], set out that methane out-gassing into the atmosphere has been confined to three discrete periods in Titans history. Their model has been confined by structural information on ammonia and methane hydrates from [Loveday 03] and [Loveday 01b] respectively. Summarised in Figure 2.15, the first methane out-gassing event occurs at core overturn with the dissociation of methane hydrate forced to the surface as part of the overturning process. This would result, as shown in Figure 2.15(b), in a layer of methane hydrate close to the surface. As it is exposed to the surface, the clathrate structure would decompose and release methane into the atmosphere. The amount and rate of this out-gassing would be determined by the quantity of methane hydrate within the proto-core. The second event would arise at the onset of convection within the silicate core. This would warm the layer of methane hydrate at the core-mantle boundary, Figure 2.15(b) and cause it to dissociate. The methane could then rise through the saturated ocean to the surface. Again this would be controlled by the initial amount of methane hydrate, but also reflect the efficiency of convection within the silicate core. The third event, and last according to the authors, occurs with the onset of convection and ice I crystallisation in Titan's outer layers. Methane clathrate, still recumbent in the subsurface, is brought towards the surface by icy plumes and would dissociate at $\sim$1 km.

The prolonged existence of methane clathrates within Titan's interior was recently supported by observations from the Cassini spacecraft. No evidence of methane lakes was discovered but methane rainfall was apparent, indicating a saturated atmosphere [Elachi 05]. In addition spectroscopic measurements point to the origin of Titan's nitrogen from ammonia [Waite 05], supporting the transport of substances from the interior.

2.8 Chapter summary

This review set out to introduce the 'new mineralogy' of the outer solar system, namely water, methane and ammonia and the compounds formed between them. These materials are major constituents within the planets Uranus and Neptune, as well as the satellites that surround them. The introduction was qualified by a explanation of the observational constraints that have provided the current information on the planets interiors. From this an objective was constructed of what knowledge is needed to further qualify these interior models. The behaviour of water, ammonia and methane under the extremes of pressure and temperature found in Uranus and Neptune's interior's must be constrained. Once this is known, accurate models re-creating the observed phenomena can be constructed. The following sections set out what high-pressure experimental and theoretical work has already been completed, reviewing work on

water, ammonia, methane, methane hydrates and ammonia hydrates. Lastly, as a case study, the progress of internal evolution models of Titan was discussed. Here a high-pressure crystallographic study had direct implications on understanding of Titan's interior. Data determined from structural studies was used directly to construct a detailed model, charting the out-gassing of methane into Titan's atmosphere.

It was the author's wish to point out that further studies of the extreme high pressure and temperature behaviour of water, ammonia and methane are still very much in their infancy. Static experiments are very challenging under these regimes, and the data often quite unreliable. Theoretical investigations are limited by the characterisation of the molecular potentials under these conditions. Hence, detail structural knowledge of these systems under more accessible conditions are key to progressing the subject. It is hoped that it has been shown that for water and ammonia such information is reasonably well progressed, whereas in contrast the equivalent structures in methane are still unknown. This therefore sets out the need for the main study conducted for this thesis, determining detailed structural knowledge on methane at conditions where reliable results can be achieved.

Chapter 3

Experimental techniques

3.1 Diffraction

3.1.1 Scattering

The modern science of crystallography was pioneered first by M. von Laue [Laue 13], and refined by W.H. and W.L. Bragg [Bragg 13], for which they respectively won the 1914 and 1915 Nobel prizes in Physics. Since then 20 further Nobel prizes have been won using crystallography as a technique. The strengths of crystallography and diffraction are that direct information can be obtained on molecular configuration and atomic positions from a large number of independent observations. Further to this is that the rules of symmetry mean that models of crystal structures can easily be calculated and compared to observations.

The response of a charged particle to a plane of monochromatic radiation was first described by J.J. Thomson [Thomson 10]. The electric field of the radiation exerts a periodic force $\mathbf{F} = e\mathbf{E}_i$ upon the particle. Where e is the charge of the particle and $\mathbf{E}_i$ is the value of the of the electric vector at position x and time t. This periodic force induces oscillatory motion and subsequent acceleration. A charged particle with accelerated motion is, itself, a source of radiation. This 'scattered' radiation will have the same wavelength as the original incident radiation. The intensity of the scattered radiation is described by Equation 3.11 below.

$$I_{\mathrm{eTh}} = I_i \frac{e^4}{m^2 r^2 c^4} \sin^2 \varphi \tag{3.1}$$

I_{eTh} is the intensity of the scattered radiation, I_i is the intensity of the incident radiation, m the mass of the particle, r its radius, e is the particles electric charge, c is the speed of light and ψ is the direction between the acceleration of the electron and the direction observation. Equation 3.11 excludes neutrons from being Thomson

scatterers, as they have no electric charge. The process of inducing scattered intensity from interaction of a charged particle with an incident radiation forms the underlying mechanism for x-ray diffraction. X-rays are the best choice for crystal lattice diffraction as their characteristic wavelengths are of the same approximate value to plane spacing of atoms in most solids. Characteristic wavelengths of x-rays used in diffraction studies are typically between 0.4 Å and 2.5 Å.

The picture described in the preceding text is an idealised situation. In addition to Thomson scattering, the incident photon can undergo an inelastic collision with an electron. Part of the photon's energy is transferred to the electron before it is deflected from its original path. This results in a difference in energy between the incident and scattered radiation, which is related by Equation 3.2 below.

$$\Delta\lambda(\text{Å}) = 0.024(1 - \cos 2\theta) \tag{3.2}$$

This effect is named Compton scattering [Compton 23]. The change in wavelength ($\Delta\lambda$) has no dependance on the incident wavelength, instead $\Delta\lambda$ is dependent on the angle of observation. Thomson and Compton scattering illustrate the wave-particle duality nature of electromagnetic radiation.

When electrons collectively scatter from an atom this can be described by an atomic scattering factor or form factor; denoted f_a. Contributions from both the core and valence electrons are summed to obtain this, as explained in Figure 3.1.

Thermal neutrons, typically with velocities of 2.20 kms^{-1}, are able to diffract from crystalline lattices as their de Broglie wavelengths are within the same order as inter-atomic distances within solids. Neutrons, as already mentioned have no charge and subsequently interact with crystalline matter differently to x-rays. Their zero charge enables them to by-pass the Coulomb barriers of the electrons and scatter directly from the nucleus. This also brings an additional benefit, of relevance to this thesis, as it results in a penetrating ability which is much greater than that of x-rays. The significance of this is discussed further later in the chapter. Instead of a form factor, nuclei scatter neutrons with a characteristic scattering length, b. Unlike the atomic scattering factor, b is independent of Z, the number of electrons, values can vary greatly even from adjoining elements. The significance of this for the present study, is that hydrogen can strongly scatter neutrons whilst being nearly transparent to x-rays.

3.1.2 Diffraction conditions

Before describing how crystalline diffraction occurs, a brief explanation of how a crystal is constrained is needed. By crystalline this thesis describes a solid with a long range order and translational symmetry. Within the structure the long range order can be

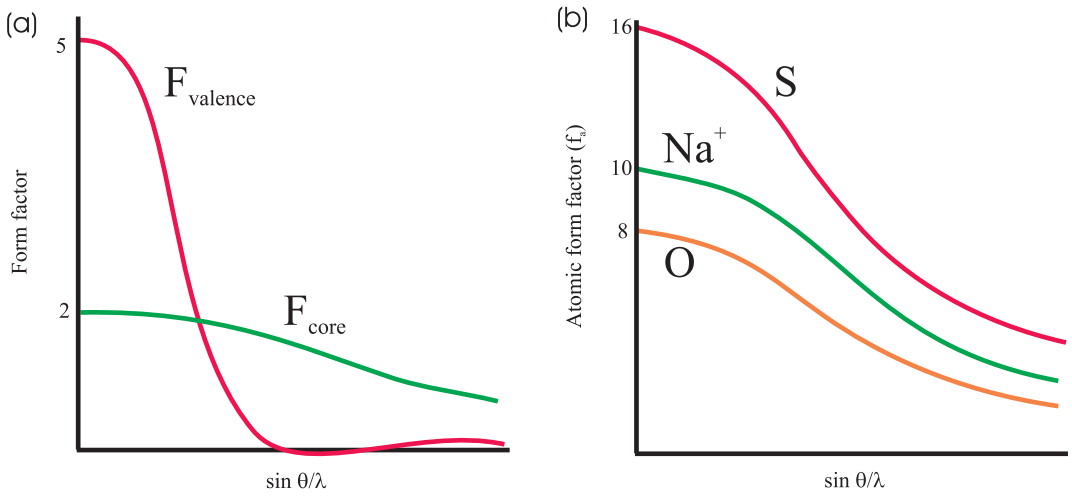

Figure 3.1: Two diagrams showing the scattering response of atoms as a function of $\sin\theta/\lambda$. All show a maximum at $\sin\theta/\lambda = 0$, where the value is equal to Z, the number of electrons. (a), shows the contributions from both core and valence electrons within a nitrogen atom. The valence electrons only scatter at low angles, with the core electrons contributing more significantly at higher angles. (b), shows the consequent shape of both of core and valence contributions for: sulphur, S, sodium ion, Na^+ and oxygen, O.

identified with identical points which make up a lattice. The atoms that surround these identical points are known as the basis and are the building blocks of the crystal structure. To compete the crystal structure a basis is placed on each of the lattice points. A 2-dimensional illustration of these points can be see in Figure 3.2.

The translational symmetry of the crystalline state is described by defining an arbitrary unit cell between the lattice points. The choice of this is, as already stated, arbitrary, but the convention is to choose a unit cell with the smallest area. Within 3-dimensions there are seven crystal systems defined by the dimensions of unit cell; a, b, c axis and α, β and γ angles as defined in Figure 3.3. It is sometimes more convenient to choose a non-primitive unit cell, like that shown in Figure 3.2(d)(i). The extra, non-primitive unit cells, are classed within the seven crystal systems, but together with the primitive unit cells make up the 14 Bravis lattices. A crystalline structure is further constrained in that there is 230 space groups to which the symmetry of atoms within the unit cell can be assigned. The first stage of crystal structure solutions is to determined the lattice, and from this a unit cell which contains the structure.

A further important explanation is how a plane of atoms within a structure are described. Three integer values h, k, and l of a plane are defined on where it intersects the unit cell's axes, a, b and c at $a/h, b/k$ and c/l.

The phenomenon of crystalline diffraction (common to x-rays and neutrons) occurs

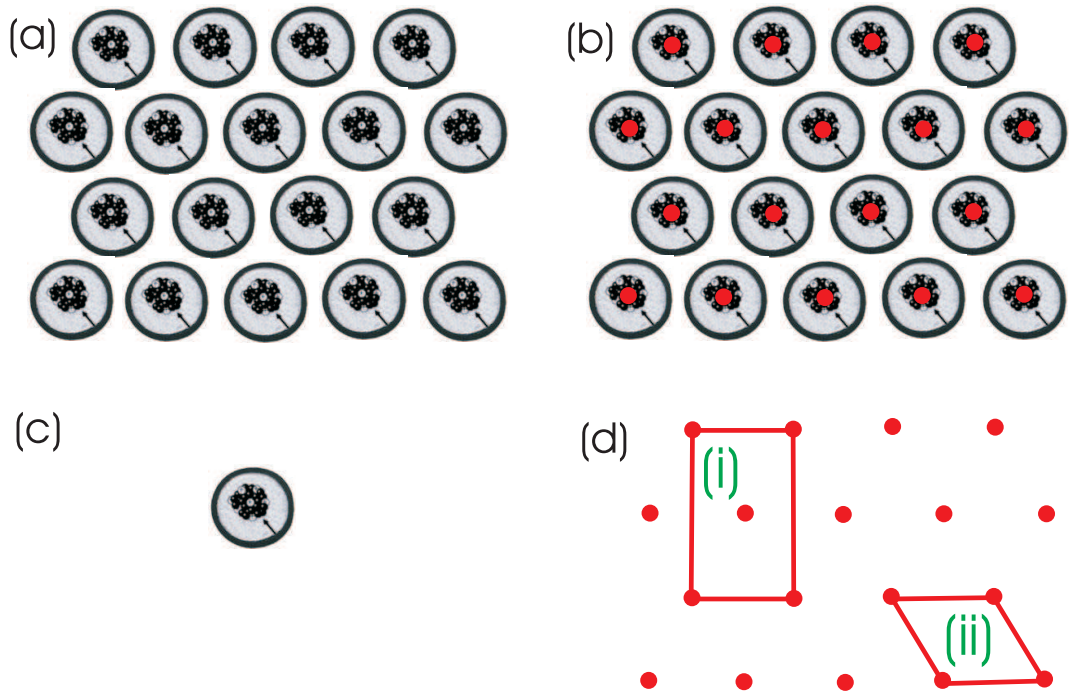

Figure 3.2: (a), shows a simple pattern with translational symmetry. To this pattern an arbitrary point has been chosen, and a subsequent lattice has been build. The relation of the this to the pattern is shown in (b) where the red dots are the lattice to build a lattice, (b). (c), is the basis of the pattern. Placing the basis at each lattice point will build the complete pattern. (d), illustrates the choice of a unit cell. (i), is a non-primitive cell as it contains more that one lattice point; (ii), is a primitive unit cell only containing one lattice point.

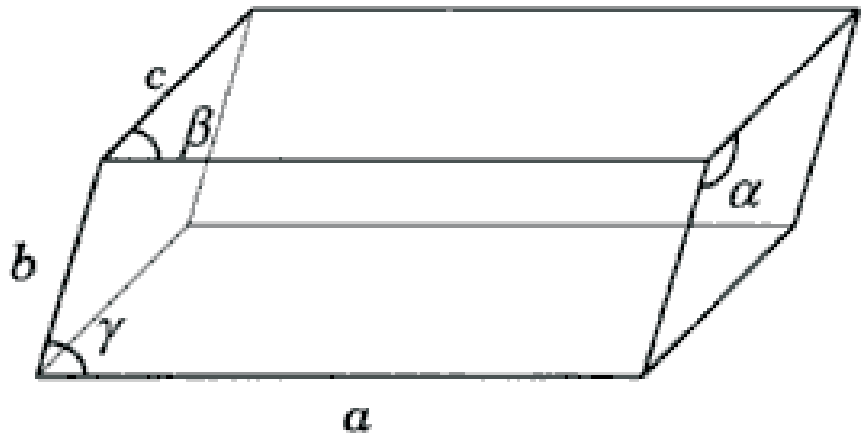

Figure 3.3: The notation for an unit cell, taken from [Wilson 00].

when an incident beam scatters in phase from a plane of atoms. The beam combines constructively with scattered radiation from other planes in the same family and result in a scattered beam which has measurable intensity. The conditions for this are set out in Equation 3.3.

$$n\lambda = 2d\sin\theta \tag{3.3}$$

Equation 3.3, is the Bragg equation, where λ is the wavelength of the incident radiation, d is the inter-planner spacing, θ is the angle between the radiation and the plane and n the order of the reflections obtained. If the difference in path length between two planes, $2d\sin\theta$, is a multiple of λ the waves will combine with the maximum positive interference.

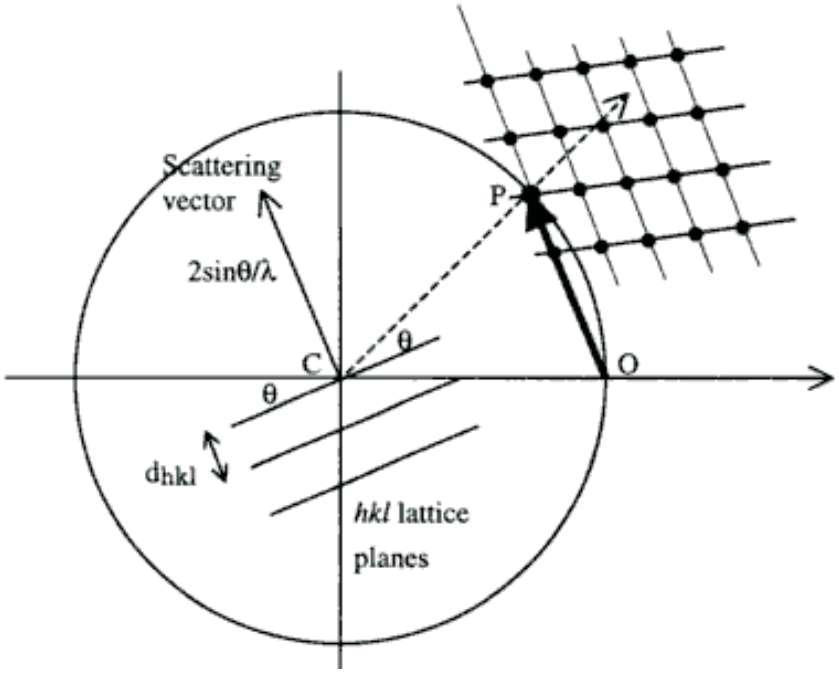

Figure 3.4: Ewald circle (sphere) construction illustrating reflection conditions taken from [Wilson 00]. The radius of the sphere is $1/\lambda$ of the incident radiation, centred on C where the crystal lattice is positioned. A reciprocal lattice with its origin at O is constructed. Observation of the reciprocal lattice will only occur when reflection conditions are met. This occurs when the reciprocal lattice point intersects with the Ewald sphere. This construction is a useful visualisation tool, and will be referred to later in the chapter.

Reflection conditions can be further visualised with an Ewald sphere construction, illustrated in 2-dimensional form in Figure 3.4. The circle (sphere) is of radius $1/\lambda$ and is centred at point C, where the crystal is located. Point O is the origin of the

reciprocal lattice. Diffraction will occur when the scattering vector length is equal and in the same direction to that from the origin to the reciprocal lattice point. The Bragg condition is only satisfied when points from the reciprocal lattice intersect the circle (sphere). Each reflection is incident from a family of planes described by their Miller indices, (hkl), with the spacing between them being $d_{(hkl)}$.

3.1.3 Diffraction analysis

The contribution of an individual atom to the the total amplitude of an refection, F_a when located in a (hkl) plane is given by Equation 3.4. Here f_a is the scattering factor of an atom, x_a, y_a and z_a denotes its position within the unit cell.

$$F_a = f_a \exp[2\pi i(hx_a + ky_a + lz_a)] \tag{3.4}$$

The total scattering from a plane is the sum of the contributions of each atom located within it:

$$\mathbf{F}(hkl) = \sum_{a=1}^{s} f_a \exp[2\pi i(hx_a + ky_a + lz_a)] \tag{3.5}$$

$\mathbf{F}(hkl)$ is the structure factor and has both amplitude and phase. The electron density, $\rho(xyz)$ of a crystal structure can be obtained from the Fourier transform of the structure factor, Equation 3.6.

$$\rho(xyz) = \frac{1}{V} \sum_{h,k,l} \mathbf{F}(hkl). \exp[-2\pi i(hx + ky + lz)] \tag{3.6}$$

$\mathbf{F}(hkl)$ can be expanded to express both the phase and amplitude:

$$\rho(xyz) = \frac{1}{V} \sum_{h,k,l} \mid F(hkl) \mid . \exp[i\phi_{(hkl)}]. \exp[-2\pi i(hx + ky + lz)] \tag{3.7}$$

Equation 3.7 separates $\phi_{(hkl)}$, the intrinsic phase of each reflection. When conducting a diffraction experiment only the amplitudes of the reflections can be measured. This is from measurement of reflection intensities, $I(hkl)$, which are proportional to $\mathbf{F}(hkl).\mathbf{F}^*(hkl) = F^2(hkl)$. The phases, ϕ, of the reflections relative to each other cannot be determined from a diffraction experiment. Consequently the direct summation of Equation 3.6 cannot be obtained from an experiment to give $\rho(xyz)$, the crystal structure.

3.1.4 Solving the phase problem

When attempting structure solution from diffraction data the determination of phases presents the biggest obstacle. There are three principal techniques to approach this, the 'phase problem', each involves a method of initially estimating the intrinsic phases $\phi_{(hkl)}$. Once the phases are estimated a model can be constructed which is then refined against the data to improve the structural result.

The first method is to take a known part of the structure and to calculate residual electron density from a diffraction data set, Equation 3.8.

$$\Delta\rho(x,y,z) = \frac{1}{V}\sum_{h}\sum_{k}\sum_{l}\{\mid F_{obs}(hkl)\mid - \mid F_{calc}(hkl)\mid\}\exp[i\phi_{calc(hkl)}].\exp[-2\pi i(hx+ky+lz)] \tag{3.8}$$

The residual electron density, $\Delta\rho$, will represent any electron density that is not accounted for in the original model. This is an effective method to determine whether or not a complete model has been reached. The technique, know as difference Fourier, is also often used to find hydrogen atom positions from neutron data if the other atomic positions are known (for example from x-ray diffraction).

The second method is Patterson synthesis [Patterson 34], which is a Fourier synthesis that can be calculated directly from experimental intensities (i.e. without any part of the structure needing to be defined). This method takes the average product of densities over the unit cell and sets all phases to zero, Equation 3.9.

$$P(u,v,w) = \frac{2}{V_c}\sum_{h}\sum_{k}\sum_{l}\mid F_{obs}(hkl)\mid^2 \cos[2\pi(hu+kv+lw)] \tag{3.9}$$

u, v and w are coordinates that specify the roving vector. The peaks in the Patterson synthesis do not represent electron density, but instead each maximum corresponds to a vector between significant concentrations of electron density. For example, every pair of atoms in the structure with coordinates (x_1, y_1, z_1) and (x_2, y_2, z_2) will create a peak in the Patterson synthesis at $(x_1 - x_2, y_1 - y_2, z_1 - z_2)$. The objective is to work out atom coordinates by only knowing the differences in positions between them. All Patterson maps will have the largest peak at the origin, corresponding to the self vectors between each atom and itself. If n is the number of atoms in the unit cell then the Patterson synthesis will have $n^2 - n$ peaks. The Patterson unit cell is the same size and shape as the original cell, and to accommodate many more peaks there is a large amount of peak overlap. Patterson synthesis is particularly useful for solving structures with a small number of heavy atoms within a majority of lighter atoms. As each peak is proportional to the product of the two atomic numbers, Z, of its constitute atoms

prominent heavy-heavy atom vectors can usually be identified.

The last method, Direct methods or phase probability techniques, arose from the desire to have a way of phase determination that was independent of trial structures. The amplitude and phase of a structure factor are linked through a knowledge of electron density. Direct methods of structure determination exploits this link, by applying constraints from the electron density to the structure factors. Direct methods work by first normalising structure amplitudes, Equation 3.10, where **h** is a reciprocal lattice vector, F_{obs} is the observed amplitudes, ϵ is a factor accounting for the effect of space group symmetry and f_a is the atomic form factor.

$$\mid E_{\mathbf{h}} \mid^2 = \mid F_{\text{obs}}\mathbf{h} \mid^2 / \epsilon_{\mathbf{h}} \sum_{i=1}^{N} f_a^2 \tag{3.10}$$

Normalising the structure amplitudes removes the atomic 'shape' from them, meaning that the resultant normalised structure factor, E, values more closely reflect the Fourier coefficients of a point-atom structure. This ensures that the resultant electron density map is made up of discrete atoms, the application of a known constraint. Direct methods then use a random atomic arrangement to determine initial phases. A subset of $\mid E \mid$s are used for phase determination, based on the accuracy that the value has been determined and the presence in a maximum of phase relations. This subset is usually from the strongest reflections, making these the most important inputs for Direct method structure determination. Phases are then assigned to each of the other reflections, which are then refined via calculated figures of merits. The figures of merit assess the quality of the phase set before an electron density map is calculated for interpretation.

3.2 Practical diffraction

The aim of this section is to build upon what has been explained in the previous section, but show how it is used in experimental practise.

3.2.1 Single crystal and powder techniques

One of the first choices when developing a diffraction experiment will be the form of the sample to be used; a single crystal or a ground powder. This choice influences the geometry of the diffraction equipment, the time taken to complete the experiment and the amount of information collected.

Single crystal techniques involve diffraction from one crystallite of the sample. The principles of this method are demonstrated well by the Ewald sphere construction shown

in Figure 3.4. As reflection conditions are met, a reciprocal lattice is constructed, which has its origin at point O. Observation will only occur when the detector and reciprocal lattice intersect the Ewald sphere.

There are two main variables for single-crystal data collections. For the first, the sample is fixed and the wavelength of the incident radiation is varied. Known as the Laue technique, the volume of reciprocal space that can be accessed is controlled by the range λ_{min} to λ_{max}. This can be visualised as the change in radius of the Ewald sphere ($\mathbf{r} = 1/\lambda$). Laue techniques, in conjunction with synchrotron radiation, provides a fast, efficient method of recording data. Unfortunately Laue techniques have only limited applications for high-pressure diffraction because of background and occlusion from the sample environment. The second variable for single crystal data collection is to use monochromatic radiation and to rotate the sample. Changing the geometry of the crystals lattice, means that the reciprocal lattice is also rotated, and intersect with the Ewald sphere as reflection conditions are met. This is the most common technique for data collection, owing to the wide availability of monochromatic laboratory x-ray sources.

As techniques powder and single crystal data collections are very complementary, and during this study both have been used. Figure 3.5 illustrates a progression from a single crystal to a powder sample, as viewed by an area detector.

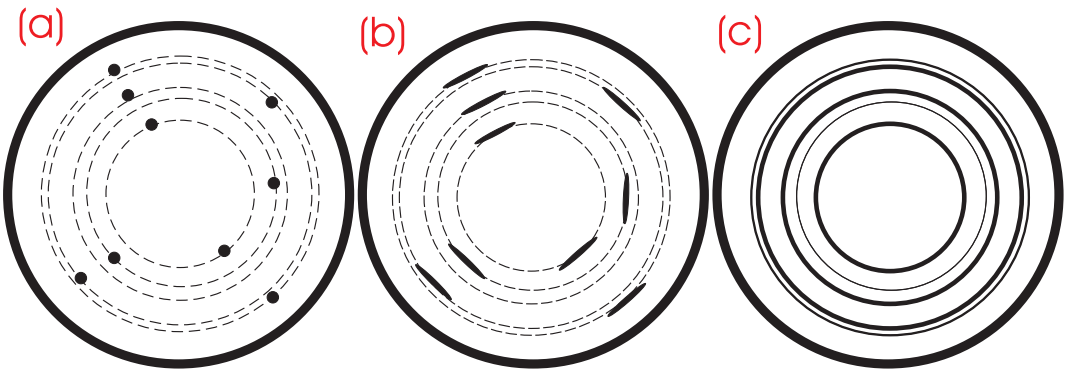

Figure 3.5: All three images represent characteristic area detector images. (a) shows diffraction from an orientated single crystal with the dashed lines indicating the d spacing of each sample spot. (b) from a bad quality single crystal, with its intensity spread into the Debye-Scherer rings. (c) a pattern from a polycrystalline (powder) sample.

An ideal sample for powder data collection will contain a large amount of randomly orientated crystallites. Instead of discrete reflections, the sample generates 'cones' of diffracted intensity, that emanate from the sample position. On an area detector perpendicular to the sample, as shown in Figure 3.5(c), the pattern will appear as a

series of concentric circles with their centre the origin of reciprocal space. The usual procedure for powder data from this point is to integrate the rings to a single line which records the 2θ angle of diffraction and the intensity at that point, as described in Figure 3.6. This profile can then be refined against a structural model. The small sample required by high-pressure equipment means that powder diffraction data from these samples can only be collected on high-flux central facility sources.

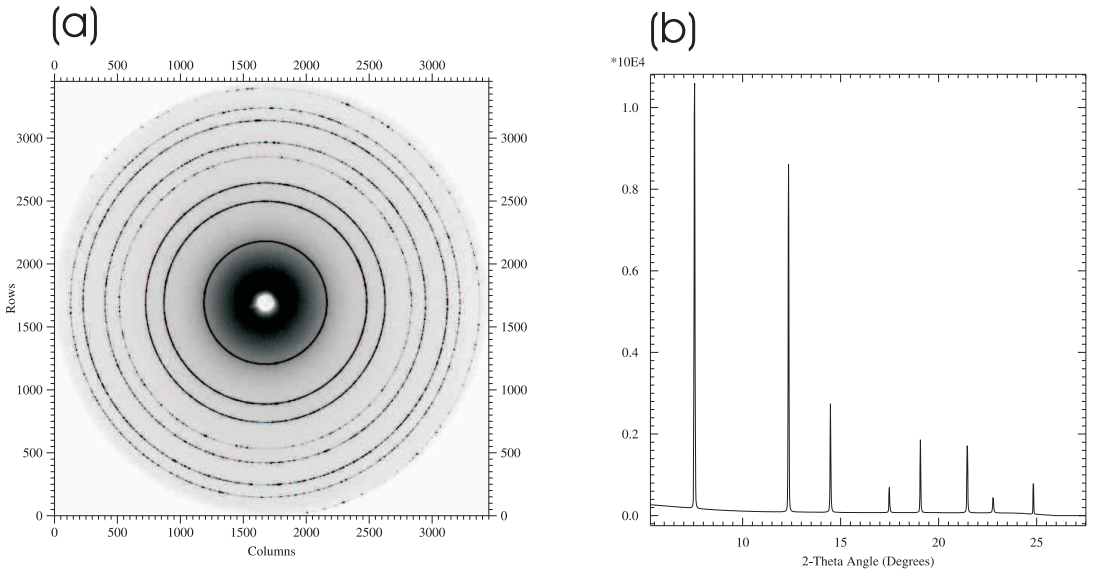

Figure 3.6: A typical powder collection from ID09a, ESRF, Grenoble. (a) shows the raw data image, a series of concentric Debye-Scherer rings. The quality of the powder sample can be gauged from the completeness of the rings, and the absence of any 'spottiness'. Once the instrument is calibrated; sample detector, wavelength and pixel centering of the image place, is set the raw data image can be integrated to form (b). The profile in (b) is typical output for powder data experiments. The peaks positions are indicative of the unit cell of the material, whilst the relative intensities are a result of the unit cell contents. The peak width will give information to the strain and stress which the crystallites are under.

Each technique, single crystal and powder diffraction, has its merits. Of the two, single-crystal diffraction far outstrips powder diffraction in the amount of independent information obtained. Every reflection from single crystal data collection has a unique *(hkl)* index with a integrateable intensity and error upon that value. But with single crystal collection data is acquired from just one crystal. Any defects or impurities within this crystal will be transposed to the final data. The single-crystal sample could

also be twinned, either as a result of growth or a symmetry effect. This can vastly complicate interpretation and indexing of the data. Collections of single crystal data invariably involves a multi-step procedure, taking time to be collected and a large amount of computer storage space. Corrections have to be applied to every step of data collection, which can result in many more errors. Powder diffraction, in contrast, is a 'one shot' collection and is a quicker method of data collection. As a result it can be applied to more dynamic studies; phase change, time resolved, crystallisation processes. Because resultant diffraction in powder samples is from many crystallites, the effect of impurities can be less severe on the final result.

During this thesis for all types of diffraction, single-crystals and powders, with x-ray and neutron diffraction, an area detector has been used. Area detectors vastly speed up collection times, allowing large areas of reciprocal space to be sampled at a time. The disadvantages of using area detectors with high-pressure, specifically the diamond anvil cell, are discussed in a later section.

3.2.2 Comparing neutrons and x-rays

To date the intensity of available x-ray sources, both in house and from synchrotron sources, have far outstripped that of neutron sources. In-house x-ray diffractometers are a common feature in all crystallographic laboratories, whereas neutron diffraction is only available at central facilities. This immediately limits the access to neutron diffraction. It is not then surprising that x-rays have become the more 'usual' diffraction technique.

One context of this thesis is the study of hydrogenous systems under pressure. As previously described, x-ray diffraction occurs when incident radiation interacts with the electron cloud of an atom. In contrast, neutron diffraction does not interact with the electron cloud, but with the nucleus itself. This results in a very different distribution of scattering cross sections across the periodic table, illustrated in Figure 3.7. Where the scattering cross section with x-rays is dependent on the number of electrons, this is not the case for neutron diffraction where the value varies randomly. This brings a wealth of advantages to neutron diffraction over x-ray diffraction. The first of these is for diffraction from hydrogen atoms. X-ray diffraction from hydrogen, having only one electron, is very weak. This severely limits x-ray diffraction for positioning hydrogen within a structure. This is not the case for neutron diffraction, where hydrogen scatters strongly enough for anisotropic thermal parameters to be refined. There is a caveat, because of spin effects the hydrogen nuclei have a large incoherent scattering length, which results in a large background on measurement. This does not occur with deuterium (a heavier isotope of hydrogen) so the usual procedure is to use deuterated

samples, such as CD_4, instead of hydrogenous ones. Figure 3.7 shows that the neutron scattering cross section of a deuterium is orders of magnitude larger than its x-ray hydrogen equivalent.

The 'random' variation of neutron scattering cross section with atomic number means that adjacent elements can be distinguished. For example, iron and manganese atoms cannot be distinguished with x-ray diffraction, but with neutrons they can be, Figure 3.7. This random variation also has very practical uses. The neutron scattering cross section of vanadium is very close to zero and so it is used as a sample container for neutron scattering studies. Similarly the variation of neutron scattering lengths can be used to engineer a material that does not scatter. This is the case for an titanium-zirconium (Ti:Zr) metal alloy, titanium has a negative scattering length and zirconium a positive one. When mixed in a approximately 2:1 ratio the scattering lengths cancel out, effectively producing a null scattering material. Ti:Zr alloy is a tough material that is used as gasket material for the Paris-Edinburgh press.

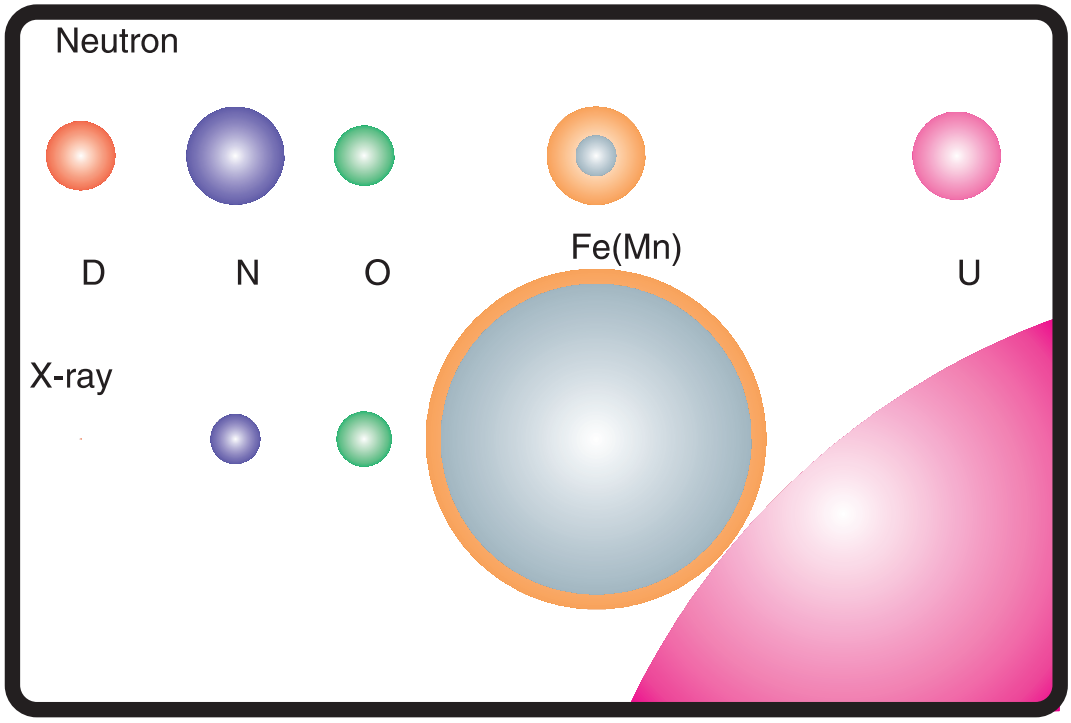

Figure 3.7: A comparison of the neutron and x-ray scattering cross sections for a selection of elements. As previously described for x-rays the scattering cross section is proportional to the number of electrons contained in each element. For neutron diffraction the interaction is directly with the nucleus, and the resultant scattering does not vary with atomic number. Hence neutron diffraction has advantages over x-ray diffraction such as hydrogen (deuterium) will scatter much stronger and elements such as iron and manganese can be identified apart.

When diffracting with neutrons the nucleus can be considered a point source. This removes the scattering dependance on $\sin\theta/\lambda$ and is illustrated in Figure 3.8. The removal of form factors from neutron scattering means that, in principal, far higher resolution data can be collected with neutrons compared to x-rays. This facilitates the refinement of subtle effects on diffraction patterns, such as thermal motion and disorder. The lack of a form factor in neutron diffraction is also an advantage for high-pressure diffraction, where the choice of detector angle has to be mainly influenced by the pressure cell, and not always the optimal geometry for scattering.

Neutrons, because of their neutral nature, are highly penetrating, a property not shared by x-rays. This is a further advantage for high-pressure diffraction as it means that complex sample environments can be constructed (see Figure 3.18 later) and refineable data still collected.

Increases in x-ray source brightness has outstripped even that of computer speed since 1955 [Jordan-Sweet 00], but the same cannot be said for neutron sources. Current synchrotrons can deliver a 10^5 increase in flux to that of neutrons facilities. This limits the sample size for neutron diffractions to $\sim$50 mm^2. This, in turn, imposes restrictions on the pressures that can be achieved. Development of the Paris-Edinburgh press will be described later, but to date high-pressure neutron diffraction is limited to 30 GPa.

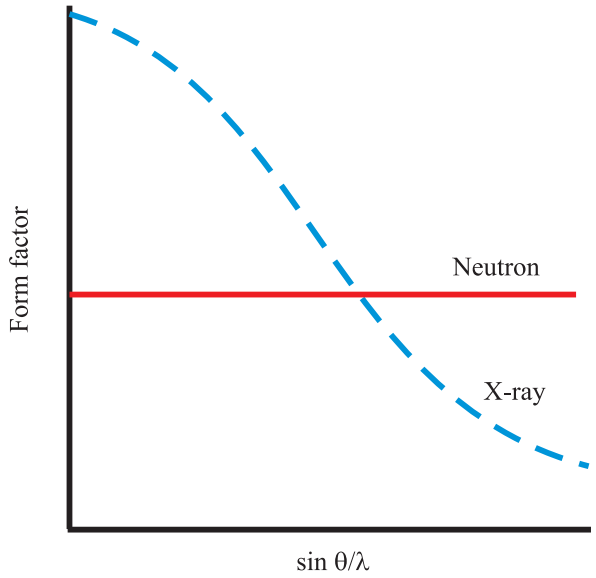

Figure 3.8: Contrasting the scattering as a function of $\sin\theta/\lambda$ for neutrons and x-rays. As previously shown in Figure 3.1 x-ray diffraction exhibits a dependence on $\sin\theta/\lambda$ because of the interaction with the electron cloud. Neutrons, in contrast, interact directly with the nucleus of an element, which is a point source of diffraction. This results in no $\sin\theta/\lambda$ dependance on scattering.

It is with sample size that x-ray diffraction techniques at high-pressure come into their own. The higher flux lets smaller samples be accommodated, and means that the study of matter with x-ray diffraction is only limited to the diamond anvil cells capability of 400 GPa. With free electron lasers and the integration of shock techniques, this could be pushed much higher. 'In house' lab sources also enable single-crystal data to be collected from pressure cells, but for powder studies and more detail single-crystal data sets synchrotron sources of x-rays have to be used. The use of low wavelength, high-flux radiation and angular dispersive data collections increase the reciprocal space that can be accessed. This is an advantage for high-pressure cells, where much of the diffraction can be obscured by the cell body.

3.2.3 Correction to intensities

The output from a diffraction experiment is intensities, $I(hkl)$. For structure solution and crystal refinement these raw intensities from the detector need to be converted to the amplitude of structure factors, $F(hkl)$. Diffraction intensity for a given reflection is proportional to the square of the modulus of the structure factor, Equation 3.11. To these measured intensities, a series of geometric and crystal corrections need to be applied. A general form of the corrections is described in Equation 3.11 including the most common corrections to be accounted for:

$$I_{hkl} = cL(\theta)p(\theta)A(\theta)E(\theta)d(t)m \mid F_{hkl} \mid^2 \tag{3.11}$$

The brackets in Equation 3.11 indicate if the correction is angle dependent (θ) or time dependent (t). The first, c, is a scaling factor. The next, $L(\theta)$, is the Lorentz correction, which accounts for some lattice planes being measured longer than others. This is dependent on the data collection, how the crystal lattice rotates relative to the detector. $p(\theta)$, the polarization correction accounts for partial polarization in both the incident and diffracted beams. The polarization correction is dependent on the nature of the monochromator crystal. The polarization and Lorentz corrections are geometrical, whereas the remaining corrections are sample dependent. The first of these is an absorption correction, $A(\theta)$. All samples will absorb x-rays at a certain level depending on the absorption coefficient, μ, the x-ray wavelength, λ and the path length through the crystal. For high-pressure diffraction this is a particularly important consideration as the incident beam will, at times, pass through the sample environment. Absorption of x-rays is greater at longer wavelengths, so for high-pressure diffraction there is a real advantage to using very small wavelengths. $E(\theta)$ is an extinction correction accounting for diffracted beams interacting with other planes in the crystal. This is normally accounted for as a variable in structural refinement. Some samples, such as proteins

and organics, will decay with time in the beam, as such a decay correction, $d(t)$, will correct for this. Lastly there is a multiplicity correction, m, which is only applicable for powder diffraction data. This accounts for peak overlap, but is automatically corrected for by powder refinement packages.

In practice the correction to the observed intensities will be particular to the instrument used. As such difference correction procedures will be applied depending on the type (powder or single crystal) of data collected and where it was observed (instrument). Detailed descriptions of the corrections applied at each diffraction instrument are included in the section discussing them, Section 3.4

3.2.4 Crystal structure refinement

The output from solving the 'phase problem' will only indicate initial positions and atom assignments within a unit cell. The structural solution output is most often just the starting point for crystal structure refinement. To determine correct and accurate crystal structures many other quantities; such as hydrogen atoms, thermal parameters and atomic positions, need to be refined directly against the experimental data. Structure refinement is particularly important for high-pressure data sets as the restricted reciprocal lattice access could skew the output from solving the phase problem. These studies used both single-crystal and powder refinement techniques, and both are described below.

Single crystal refinement

Once difference Fourier has located any 'missing' electron density then least squares refinement can proceed. It is a common method in physical sciences to compare a given set of experimental observations with a parametrically constrained model. From a starting point the parameters of the model can be adjusted to best fit the observations. Consequently the validity of the model, in light of the data, can be assessed.

For single crystal refinement the large number of $\mid F_{\mathrm{obs}} \mid$, observed structure factors are obtained. An initial structural model is used to calculate $\mid F_{\mathrm{calc}} \mid$ for comparisons with the observations. Parameters of the initial model, such as atomic positions and thermal parameters, are then refined to minimise the difference between $\mid F_{\mathrm{obs}} \mid$ and $\mid F_{\mathrm{calc}} \mid$. A number of constraints and restraints can be applied to this refinement. Constraints are quantities that must be satisfied by the refined model, such as a required bond length. Whereas restraints are less harsh and are approximations that can be used to bring about convergence. An example of this is to constrain the U_{iso} shifts of identical environment carbons to the same amount.

The fit of a crystal model to the data is quantified through residual factors or R-factors. These should converge to a minimum during refinement. Three most commonly used are expressed in Equations 3.12, 3.13, 3.14. The most popular of these, and the most readily quoted, is the unweighted R-factors calculated from the structure factor, **F**, Equation 3.12.

$$R = \frac{\sum || F_{\text{obs}} | - | F_{\text{calc}} ||}{\sum | F_{\text{obs}} |} \tag{3.12}$$

The weighted R-factor, Equation 3.13 is calculated with F^2. The weighting factor is calculated from the standard uncertainties of the measured reflections. As high-pressure diffraction collections are restricted data sets this value will be high, and not representative of the model's fit. wR will not be quoted during this thesis.

$$wR = \left[\frac{\sum w(F^2_{\text{obs}} - F^2_{\text{calc}})^2}{\sum w F^2_{\text{obs}}} \right]^{1/2} \tag{3.13}$$

Lastly there is the goodness of fit, GooF, denoted in the SHELX program as S, which is calculated with Equation 3.14.

$$S = \left[\frac{\sum w(F^2_{\text{obs}} - F^2_{\text{calc}})^2}{(N_R - N_P)} \right]^{1/2} \tag{3.14}$$

Two single crystal refinement packages have been used during this thesis, SHELX [Sheldrick 08] and CRYSTALS [Betteridge 04]. CRYSTALS was used because of its graphical user interface. This user friendly interface applies refinement shifts and q peaks from Fourier refinement directly to a displayed crystal structure. This feature greatly facilitated the solution of the phase B structure.

Powder data refinement

Rietveld refinement [Rietveld 69] has lead to the wide spread use of powder diffraction, as it enables structural models to be refined directly against powder data. The powder pattern is expressed in terms of y_{obs} the intensity at a given value of 2θ. Each point along the profile, y_{calc}, is determined using three components: the structural model, a model to describe the variation of peak widths over 2θ and a model for the background. y_{calc} is determined for each experimental point of 2θ.

Then, similar to single crystal refinement methods, least squares methods are used to adjust structural parameters to minimise the difference between y_{obs} and y_{calc}. The quality of the fits are assessed with the expressions in Equations 3.15 to 3.17. In each of these equations n is the number of observations, p the number of parameters, w_i is a weighting factor. R_{wp} directly represents the minimised quantity and χ^2 compares

R_{wp} to the statistically expected value R_{exp}. All these quantities can sometimes give misleadingly low values, especially with data that has a high background. Often the best indication of the quality of the refinement is visual inspection of the fit and the difference profile.

$$R_{\mathrm{wp}} = \left\{ \frac{\sum_i w_i [y_i(\mathrm{obs}) - y_i(\mathrm{calc})]^2}{\sum_i w_i [y_i(\mathrm{obs})]^2} \right\}^{1/2} \tag{3.15}$$

$$R_{\mathrm{exp}} = \left\{ \frac{(n-p)}{\sum_{i=1}^{n} w_i y_i^2} \right\}^{1/2} \tag{3.16}$$

$$\chi^2 = \frac{R_{\mathrm{wp}}}{R_{\mathrm{exp}}} \tag{3.17}$$

Rietveld refinements also allow for multi-phase pattern fitting. For high-pressure powder neutron diffraction, where the sample is surrounded by powdered sintered diamond or tungsten carbide anvils, this is an essential feature. It also allows for quantitative analysis of other components, such as lead, which can be used as pressure calibrants.

There is a second type of refinement procedure that can be applied to powder profiles, LeBail refinement. In contrast to Rietveld refinement, LeBail refinements do not require a structural model. Instead, LeBail refinement uses the unit cell size, shape and symmetry to determine relative intensities, and apply a constant peak width across the 2θ range. If peaks are not fitted during a LeBail refinement, this indicates an incorrect indexing or space group determination. It is also a useful routine for discovering the best fit that can be achieved with the model-dependent Rietveld method.

There are a variety of Rietveld refinement packages freely available for use. During this study GSAS [Larson 94], JANA2000 [Petricek 00] and Fullprof [Rodriguez-Carvajal 93] have all been used, each having slight advantages for different types of refinement. GSAS is the only one of these to read time of flight neutron powder data, as recorded from ISIS. For consistency, all of the neutron data were refined with this package. JANA2000 was used for analysis of the x-ray diffraction data. This was because at the time none of the structures were determined and the LeBail refinement of Jana is much more stable than that of GSAS. The Fullprof package was used for its 'simulated annealing' capabilities, in an attempt to solve phases A and B from powders.

3.3 High-pressure Equipment

The simplest device for generation of pressure is a piston cylinder device. Although there have been many design modifications and adaptations these are intrinsically limited to pressures approaching 3 GPa [Eremets 96]. The generation of pressures beyond 3 GPa has its roots within the diamond synthesis process, developing from the first belt and girdle device [Hall 54] to the large variety of cells used today. The first opposed anvil device was developed by Bridgman in 1951 [Bridgman 52]. Essentially all modern high-pressure techniques are footnotes to the pioneering work of this Nobel laureate.

This review of high-pressure equipment will focus on opposed anvil devices used for the studies contained in this thesis. In particular the review will focus on the Merrill-Bassett type diamond anvil cell and the Paris-Edinburgh press, discussing the use and adaptations of these high pressure devices.

A natural modification to Bridgman's opposed tungsten carbide anvil device was the insertion of gem anvils which allowed optical and radiation access to the sample. Indeed diamond, being the hardest substance know to man, as well as transparent, is analogous to the babel fish [Adams 79] in its usefulness to this end. The very first diamond anvil cell was developed in 1958 in NBS laboratories, Washington [Weir 59]. Widespread use of this techniques was stalled by pressure calibration until 1975, when the ruby pressure scale was developed.

The diamond anvil cell soon superseded Bridgman's cell as the work horse of high-pressure research. Compared to Bridgman's apparatus, the diamond anvil cell was adaptable and easy to use. The adaptability of the diamond anvil cell stems from the simple principals that it operates on, a pair of diamond anvils squeezing a metal gasket which contains a hole to be the sample chamber, Figure 3.9. Using this simple basis the diamond anvil cell currently can obtain quasi-hydrostatic pressures to 400 GPa. Pressure is determined principally from the ruby fluorescence [Mao 78]. Alternatively, pressures can be obtained in diffraction studies with powder patterns of markers, such as the metal gasket itself. The optical access of the diamonds allow for a wide range of experiments to be accomplished, only limited by the sample volume. With ever more powerful sources of radiation and more sensitive detectors, measurements are constantly improved. There exists a multitude of designs of the diamond anvil cell each optimised for specific purposes.

As already mentioned, pressure calibration within the sample chamber of a diamond anvil cell stalled progress of the technique for many years. In 1975 the ruby pressure gauge was developed [Piermarini 75] which led to an explosion in the use of the diamond anvil cell. The gauge makes use of the characteristic fluorescence spectra of Cr doped

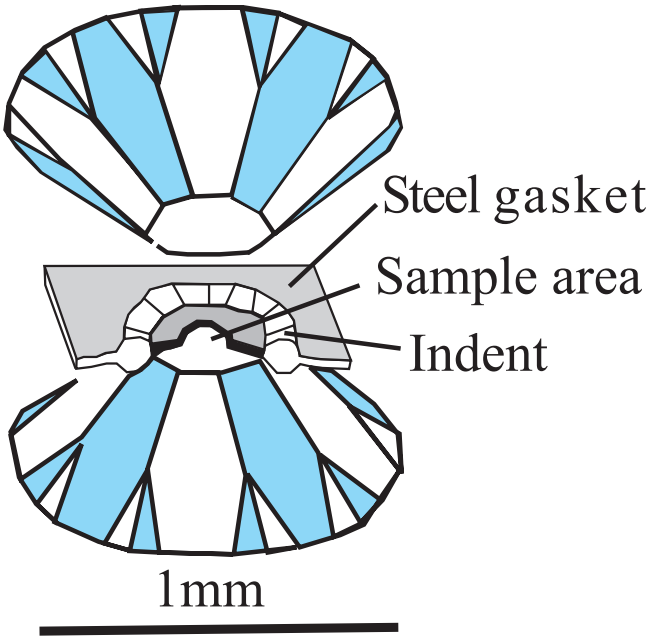

Figure 3.9: The arrangement of components in a diamond anvil cell, with a cross section through the gasket. Although the gasket in this image has been indicated as steel; tungsten and rhenium are also commonly used to contain the sample.

α-Al_2O_3, also known as ruby. This could easily be observed through the diamond anvils, with a conventional Raman spectroscopy set up. The ruby fluorescence is a characteristic doublet in the spectra, labelled R_1 (larger and at higher wavelength) and R_2 shown in Figure 3.10. The doublet shifts $\sim$7 nm under 20 GPa of pressure. This shift ($\Delta\lambda$) is approximately 12 times the full width half maximum of the R_1 line at 300 K. This shift is approximately linear until 50 GPa. The ruby pressure scale has been extensively extended from this point into a non-linear regime and was recently revised [Syassen 08]. For consistency this study will use the pressure scale determined by Mao *et al* [Mao 78] throughout. This scale was determined from calibration with specific volume measurements of 4 metals from shock-wave experiments for, 0.06 to 1 Mbar. This scale is used as it encompasses the full range of pressures measured during these studies, and is in close agreement below 20 GPa to the original work of Piermarini *et al* [Piermarini 75].

$$P(GPa) = (19.04/5)\left\{\left[\frac{(\lambda_0 + \Delta\lambda)}{\lambda_0}\right]^5 - 1\right\} \tag{3.18}$$

On sample loading a small (1-2μm) piece of ruby dust or sphere is placed within the gasket hole. In ideal conditions the R_1 of the ruby under ambient conditions (i.e. before the anvils are close) is taken to be used in later calculations. It will be explained

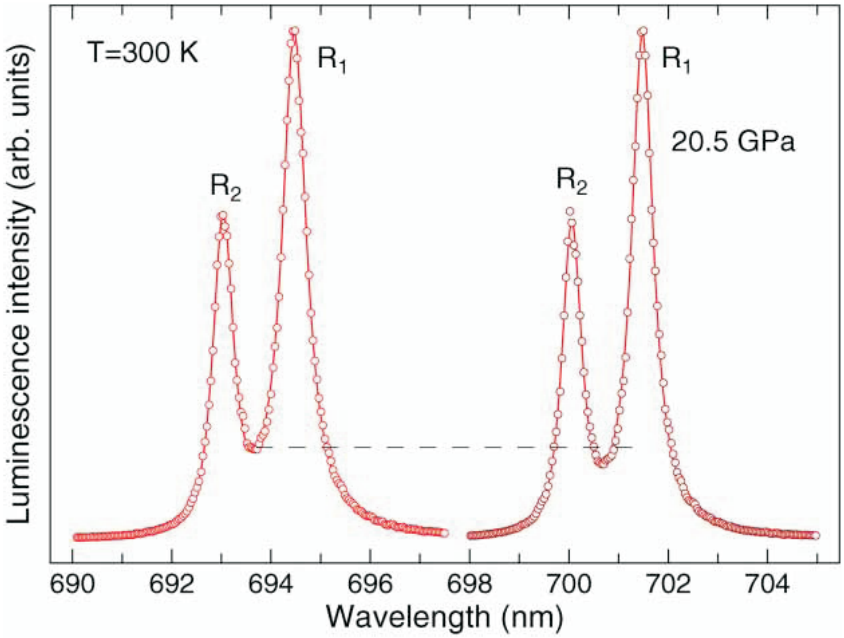

Figure 3.10: The shift of the R_1 (and R_2) lines under 20.5 GPa of pressure taken from [Syassen 08]. Total shift of about 7 nm is ∼12 times the full width half maximum of the R_1 line at ambient pressure and at a temperature of 300 K.

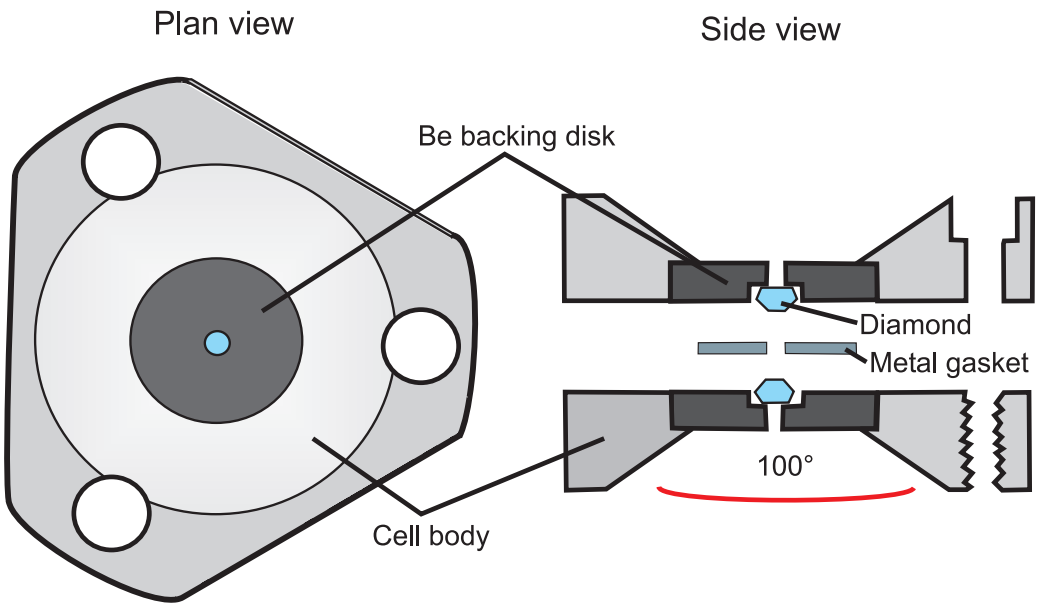

Figure 3.11: Views of the Merrill-Bassett cell [Merrill 74]. The simplicity of the design, and the maximum diffraction access that is the defining feature of this cell. The use of beryllium backing disks enables the 100° access angle for the incident radiation. The cell body is normally manufactured from hardened steel and the pressure is applied using screws which force the two parts of the cell together. The metal gasket that is used to contain the sample needs to be pre-indented prior to loading.

later that this is not always possible for complex loadings and in these cases a standard value of $\lambda_0 = 694.32$ nm was used. After pressure application the R_1 is measured again and the pressure calculated with Equation 3.18 [Mao 78] to an accuracy of $\pm 6\%$.

3.3.1 The Merrill-Bassett cell

The wide spread use of high-pressure techniques have stemmed from the development of simple and adaptable diamond anvil cells. One of these, and the most relevant for this thesis, is the Merrill-Bassett cell [Merrill 74]. It was developed to optimise the incident radiation access to the sample for single crystal diffraction and is illustrated in Figure 3.11.

One of the main advantages of this cell is that it is light enough to be mounted on a conventional goniometer head and be small enough to fit in a standard diffractometer. Mounting the diamonds on Be plates, which are transparent to the incident x-rays, enables a large opening angles of $\pm 50°$. A 1.0 mm diameter hole is drilled into the Be backing disks to allow optical access to the diamond, for alignment and monitoring of the sample chamber. The force is generated by tightening conventional screws, this limits the pressure to 30 GPa. The designers, Merrill and Bassett, originally reported

concerns of the presence of diamond reflections in single crystals data sets but noted criteria for identifying them i) they are usually much greater in intensity and ii) the 2θ positions can later be indexed to diamond.

Access to reciprocal space, as will all high-pressure techniques, is limited by occultation from the cell body. The maximum volume of reciprocal space that can be accessed by the Merrill-Bassett cell is calculated with Equation 3.19. Here ϕ quantifies the orientation of the crystal plane, $\mathbf{r}$ is the reciprocal lattice vector with $\mathbf{r_l}$ denoting the limit of this, α is half the opening angle of the cell and ω is the rotation of the cell.

$$V_m = 2\int_0^{2\pi}\int_0^{\alpha}\int_0^{rl} r^2 \cos\phi \; d\mathbf{r} \; d\phi \; d\omega \tag{3.19}$$

It follows from Equation 3.20 that increasing the opening angle, α, will increase the amount of reciprocal space that can be accessed. The limiting reciprocal lattice vector is given by Equation 3.19 below.

$$\mathbf{r}_l = [2\sin(\alpha - \phi)/\lambda)] \tag{3.20}$$

The characteristic wavelength of a diffraction instrument at a synchrotron facility is much smaller than a conventional lab-based instrument. This, and the ability to change wavelength, means that the access to reciprocal space can be optimised for each cell. Logically for a Merrill-Bassett type cell the smallest wavelength possible would enable you to maximise the volume of reciprocal space, but with the fall off of intensity with $\sin\theta/\lambda$, this may not be appropriate for every sample.

When originally designed, the beryllium backing disks supporting the diamonds were seen as a advantageous design feature. Beryllium is a strong material that is highly permeable to x-rays. The Merrill-Bassett cell was designed to be mounted upon an instrument with a point detector. This would enable contributions from the backing disks to be collimated out. Reflections that had passed through the backing disks would have to be corrected for absorption at the data reduction stage. As the use of area detectors became more popular, powder lines from the backing disks became more of a problem as illustrated in Figure 3.12(a).

This problem has been alleviated by the use of the Böhler-Almax (BA) design of diamonds with tungsten carbide backing disks (seats) [Böhler 04]. This new arrangement can be seen alongside the old Be backing disks in Figure 3.13. The large, unoccluded opening angle was in fact a happy by-product of the seats, which had been designed to give better support to the diamonds. The original design of the BA diamonds and seats used asymmetric diamonds to maximised the pressures that could be reached. A small adaptation, making the diamonds symmetric [Moggach 08],

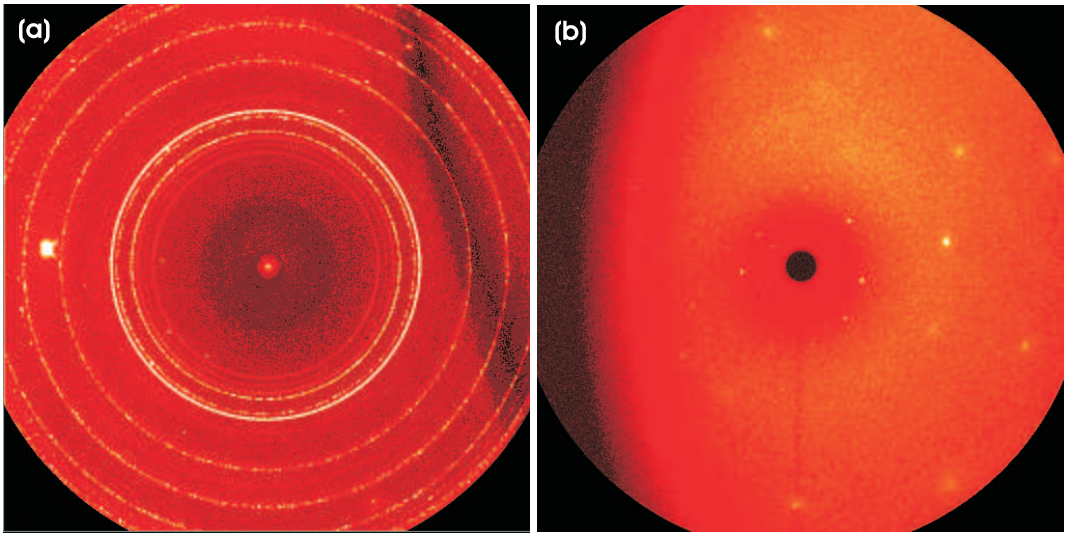

Figure 3.12: Images from 9.5, SRS, data collection with (a) from a cell with beryllium backing disks and (b) from one with Böhler-Almax (BA) seats. (a), shows contamination from the gasket, backing disk and diamond peaks which subsequently made integration of the diffraction spots very challenging. (b), with none of the contamination stated previously, shows the result of using a focused small wavelength beam. Diamond peaks are still apparent in this image but these rarely interfere with the integration process.

enabled crystallographers to fully take advantage of this innovation. The Merrill-Bassett cell can now be easily be adapted for beryllium free diffraction, Figure 3.12(b), and potentially higher pressures.

A further source of background contamination occurs when the incident beam diffracts off the gasket material. This is unavoidable on lab-based diffractometers where the incident beam cannot be collimated to be smaller than the gasket hole (200-50 μm). However, incident beams from synchrotrons can be focused to this size, further cutting the observed background, Figure 3.12(b).

3.3.2 The Paris-Edinburgh press

One of the limitations of diamond anvil cells (which could be seen as an advantage when obtaining very high pressures) is the very small sample volume. Unfortunately, this excludes them for use with neutron diffraction studies where, because of the relatively low flux of neutrons, a sample volume of $\sim$50 mm^2 is needed. The Paris-Edinburgh press [Besson 92] Figure 3.14, was developed to address this, and now *in situ* studies of up to 30 GPa can be achieved. Although other similar cells had been developed for neutron diffraction, the key difference of the Paris-Edinburgh press was the incorporation of a

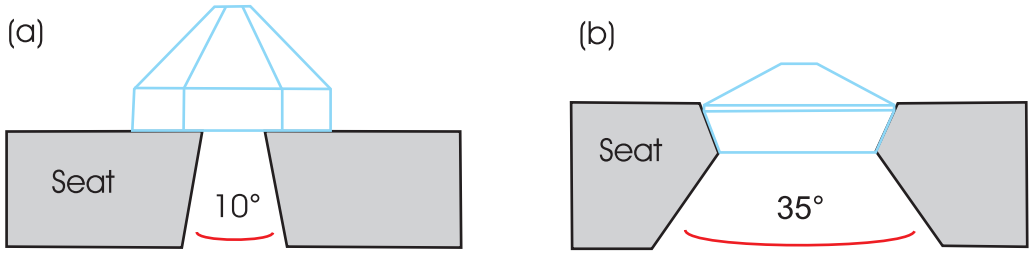

Figure 3.13: Comparing the original beryllium backing disks, (a), to the new Böhler-Almax design, (b). The larger opening angle allows for uncontaminated diffraction images.

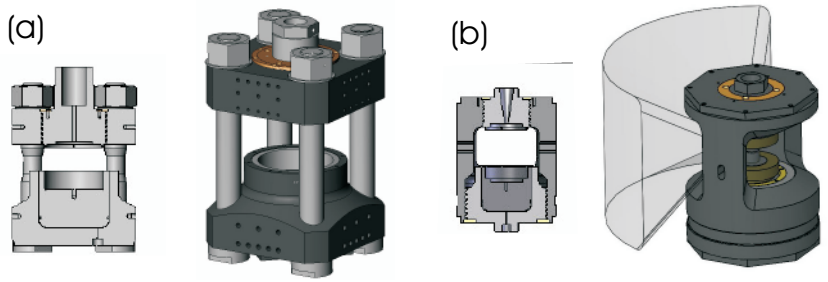

Figure 3.14: Images of the two types of Paris-Edinburgh cell used during this thesis, (a) the V3 cell and (b) the VX5 cell.

hydraulic ram. The design of this was calculated to provide compensation of strain with negligible deformation. The result was a 250 ton press weighing 60 kg, making it uniquely portable for a press of its rating.

The Paris-Edinburgh press is, like the diamond anvil cell, an opposed anvil device with the construction of the anvils taken from Bridgman [Bridgman 52]. Bridgman's original configuration was to use relatively large flat-tipped tungsten carbine anvils with pyrophyllite to contain a sample within a solid pressure transmitting medium. This arrangement is limited by the lack of lateral support from the pyrophyllite gasket and consequently has a 10 GPa pressure limit [Eremets 96]. As already stated research interest in the Bridgman cell dissipated after the invention of the diamond anvil cell. This was revived in latter years with the increased availability of sintered diamond anvils, pushing the pressure limit of the Bridgman cell to 40 GPa. Despite these advances, most of the investigations that utilise the Bridgman anvil arrangement probe electrical resistance of materials. This is because of the limited sample volumes that

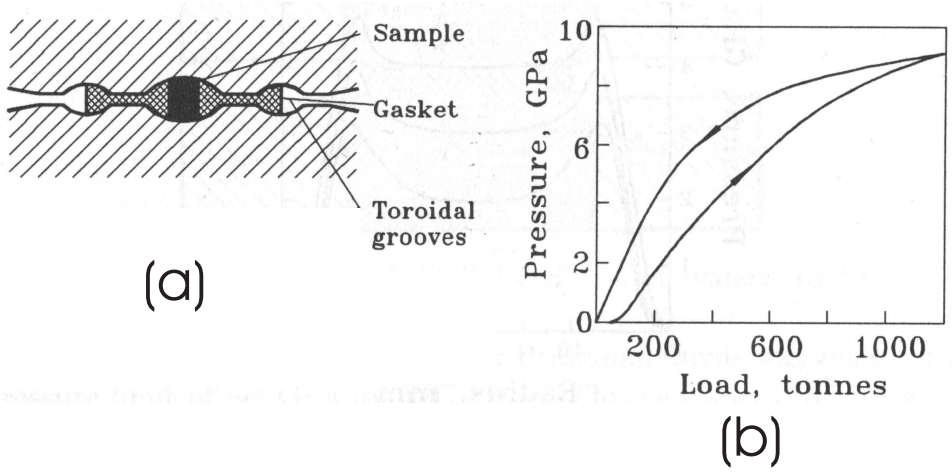

Figure 3.15: The toroidal anvil geometry used within a Paris-Edinburgh press taken from [Eremets 96]. The diagram at the top of (a) shows the arrangement of sample and gasket upon loading. The gasket compressed by the toroidal geometry provides additional support for the sample and allows for higher pressures to be obtained. (b) is the expected shape of a load/pressure graph upon upstroke and downstroke when using toroidal anvils.

can be pressurised.

Cupped anvils were originally designed to counteract the deformation inherent within the Bridgman anvils [Ivanov 60], but were later deepened to allow for larger sample volumes. But, the profiling of anvils in this way leads to limitations in the obtainable pressures to 4-5 GPa. The development of toroidal anvils [Khvostantsev 77] was in a bid to retain the pressure performance of the Bridgman anvils but with larger sample volumes of cupped anvils. The toroidal anvils are constructed from a smaller cupped centre surrounded by toroidal groves outside of this, Figure 3.15. The toroidal anvils provide support to the gasket, but also crucially allow it to flow when subjected to plastic deformation. Toroid grooves provided a pressure distribution similar to the bevelled diamonds, allowing for higher pressures to be achieved. Toroidal anvils have been used throughout this thesis. In some cases, double toroidal profiled anvils were used to attain a higher pressure performance.

The standard gaskets for use with the Paris-Edinburgh press is a small metal ring (preferably non-absorbing to neutrons) which sits in the toroid grove to contain the sample Figure 3.16(b). Metal gaskets are used because of their plastic deformation which increases the support of the sample area. The type of gasket chosen when using the Paris-Edinburgh press depends greatly on the substance to be investigated. For the current studies, a SME encapsulated gasket was used to achieve near-hydrostatic conditions in the sample environment [Marshall 02] and to adequately contain the

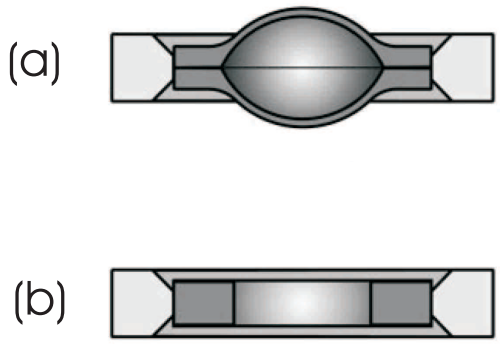

Figure 3.16: Illustrations of (a) the SME gasket compared to (b) a standard metal gasket used in the Paris-Edinburgh press, taken from [Marshall 02].

(initially) fluid samples. SME gaskets are constructed with the TiZr alloy that was introduced in Section 3.2.2. The complete assembly of a SME gasket is show in Figure 3.16(a). It is made up of three components, an outer ring which is designed to fit inside the toroidal groove and two cups to constrain the sample in the anvils. Conventionally a powder sample is piled into the bottom cup before a pressure transmitting medium is added. Then the top cup is placed on the powder sample. For cryogenic loadings, when the gasket is sealed within the press this confines the liquid.

Direct gas loading of the press is not achievable at present and remains one of the goals of the Edinburgh-CSEC group. Instead gases need to be loaded cryogenically, a process that is explained later in this Chapter, Section 3.5.1.

16 years after the original design the Paris-Edinburgh press had been widely adapted to accommodate both high and low temperatures. In 2004 the press underwent a re-design resulting in the VX variant [Klotz 04] Figure 3.17(b). The VX press was developed to optimise angular access to the sample. The original press design, Figure 3.14(a), has four supporting tirods (rods of hardened steel). The tirods on some instruments occluded the incident radiation and contributed to the background. During these current studies both the V and VX variants of the Paris-Edinburgh press were used.

With sintered diamond and tungsten carbide anvils there is no optical access to the sample area. Hence, the ruby pressure scale described above cannot be used. Instead pressure calibration within the Paris-Edinburgh press is achieved with diffraction markers. Pre-determined equation of states for common metals (usually from diamond anvil cell studies) can be used with diffraction patterns generated by placing some of the metal within the sample space. Refinement of the volume of the metal used can give pressures accurate to $\pm$ 0.2 kbar. The pressure calibrant used during these studies

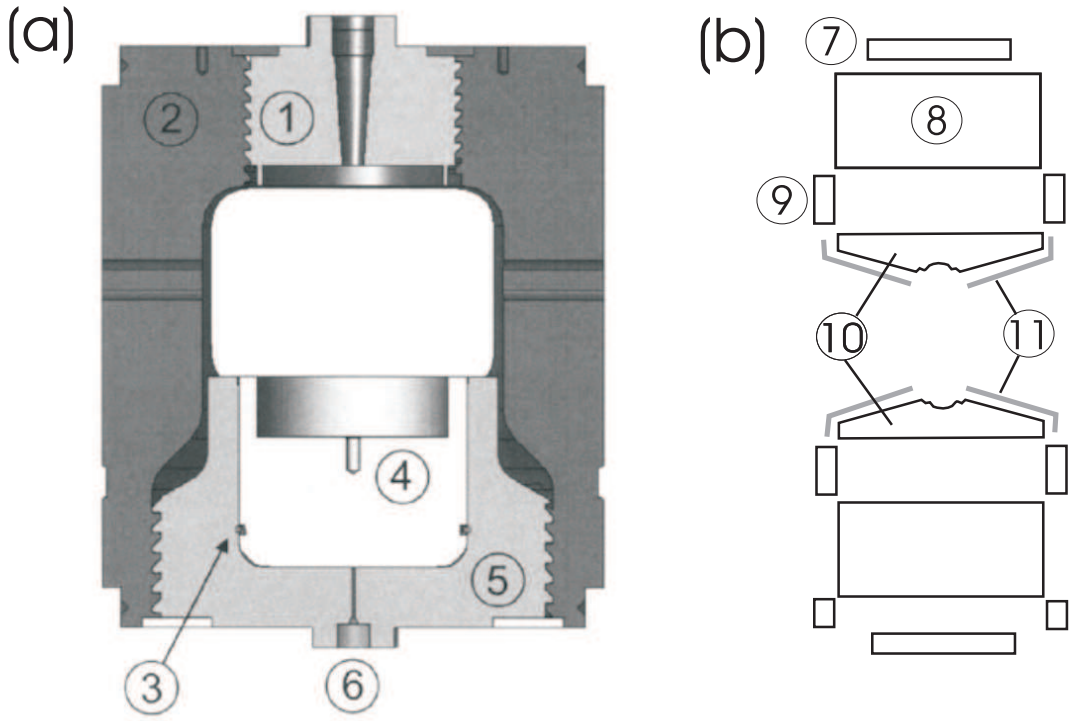

Figure 3.17: Two cross sectional diagrams of the internal components of a Paris-Edinburgh press (in this case the VX type) - (a) the press and (b) the cell assembly. 1, breech; 2, body; 3, O-ring seal; 4, piston; 5, cylinder; 6, hydraulic fluid inlet; 7, backing disk; 8, seat; 9, Al centering rings; 10, anvils; 11, Cd shielding.

was lead, usually cut to be a curl of 0.08g. Its main diffraction peak, d_{111} is located about 2.8 Å, and usually does not obscure the experimental pattern. Pressure was calculated with an equation of state for lead [Mao 90] and corrected for low and high temperatures with the universal equation of state [Vinet 87].

3.4 High-Pressure diffraction instruments

To place a high-pressure cell upon a diffraction instrument two considerations must be made. Firstly, does the cell fit safely onto the diffractometer? Secondly, is the radiation of significant flux to collect meaningful data? Diamond anvil cells usually pass the first consideration. As illustrated in Figure 3.11, the size of these cells means that use on most conventional diffractometers only requires minor adaptations. However, the small sample sizes inherent with diamond anvils cells effectively exclude powder data collection from anywhere other than synchrotron sources. It is possible to collect meaningful data with a diamond anvil cell from a laboratory single crystal x-ray diffraction machine. But, an additional consideration for this study has been the low scattering power of methane. This effectively rules out using a x-ray laboratory source beyond crystal quality checking and indexing. Data from synchrotron sources, ESRF and SRS, were far superior and revealed the detailed structural information desired.

The two questions posed above have particular relevance for high-pressure neutron studies. The lower flux available from current neutron facilities means that a large ($\sim$50 mm^3) sample is needed to collected refineable diffraction data. This need fuelled the development of the Paris-Edinburgh press, as outlined above. Despite being 'compact' the Paris-Edinburgh press still weighs 60 kg and measures 20 $\times$ 30 cm, many more considerations need to be made when mounting this upon an instrument.

This study has required the use of a variety of central facility instruments for data collection. Within this section the different instruments used will be be outlined.

3.4.1 Neutron powder diffraction instruments

Data were collected for this study at both the ISIS neutron and muon facility, Didcot, UK and Institut Laue-Langevin (ILL), Grenoble, France. At ISIS the PEARL/HiPr instrument has been used extensively, for the study discussed within the thesis on methane and for those discussed within Appendix A on ammonia hydrates and carbon dioxide hydrate. D20, at the ILL, was used to complement the work from ISIS on methane, and for the low-temperature neutron diffraction experiment described in Chapter 6.

PEARL/HiPr, located on beam line S9 of the ISIS facility, is a medium-resolution

high flux diffractometer that has been optimised for use in conjunction with the Paris-Edinburgh press, Figure 3.18. The motivation behind the construction of the instrument was to study the often dramatic changes in the physical properties of condensed matter. PEARL originally had only half of its operational time given for high-pressure research, with the other half used for engineering applications. With the building of ENGINX, a dedicated engineering beamline, PEARL became HiPr, a dedicated high-pressure beamline at ISIS.

ISIS is a spallation neutron source, fed by a 800 MeV proton synchrotron. From this a beam of protons is extracted, at 50 Hz, which is directed at a tantalum target, and a pulse of neutrons are produced radially from this point. The neutrons then pass through a moderator; for PEARL/HiPr this is a methane moderator at 100 K. The moderator stops some of the highest energy neutrons, and spreads the rest of the neutrons in energy. These neutrons are then channelled into guides to reach the sample in pulse. The faster more energetic neutrons reach the sample first, and travel to a detector at a fixed distance. This technique, known as time of flight neutron diffraction, is ideally suited to high-pressure diffraction. The fixed detector simplifies shielding to remove contribution from the cell and its surrounding material.

Data can be collected on PEARL/HiPr in two geometries, transverse and longitudinal. The transverse geometry, which is being illustrated in Figure 3.18(a), has the neutrons reaching the sample through the breach and the anvils. The cross section of the V3 cell in Figure 3.14(a) shows a hole through the breach, which is then continued through the backing disk, seat and the anvil. This feature maximises the number of neutrons that can reach the sample. In the transverse geometry the main detector bank is fixed and covers $83^\circ < 2\theta < 97^\circ$ and allows data to be collected between 0.5 and 4.1 Å d-spacing, with a resolution ($\Delta d/d$) of 0.8%. The longitudinal banks consists of two modules of detectors, the first $20^\circ < 2\theta < 40^\circ$ with a $\Delta d/d$ of 1.5% and the second $100^\circ < 2\theta < 120^\circ$ with a $\Delta d/d$ of 0.7%. In this geometry d-spacings of up to 10 Å can be measured, but with a compromise in resolution. During this study only the transverse geometry was used, as the phases of methane studied have their maximum d-spacing inside the 4 Å limit of the higher resolution mode.

ILL, in contrast to ISIS, is a reactor source and produces a constant stream of neutrons at 50 MW. There is a variety of diffraction beam lines, optimised for may different purposes, but to date no dedicated high-pressure beamline exists at ILL. Currently the Paris-Edinburgh press can be used on two diffraction beamlines; D9 a single crystal instrument and D20 a powder instrument. In the course of these studies beam time was applied for and granted at D20, the results of which are presented in Chapter 6.

The D20 powder instrument, Figure 3.19, was built to be a versatile high-

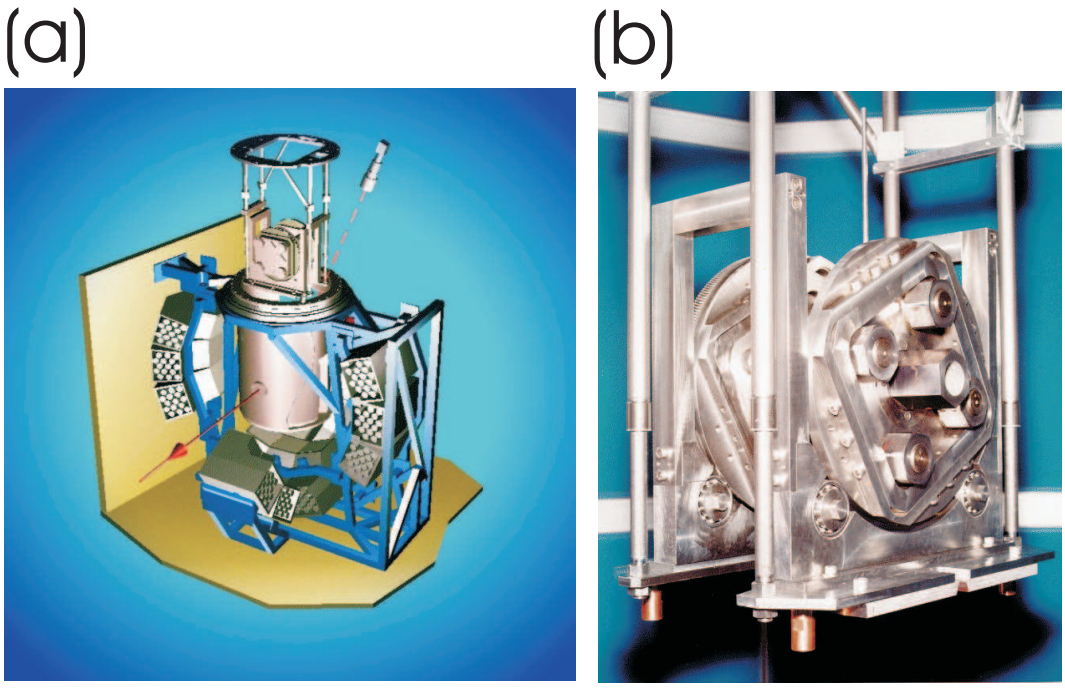

Figure 3.18: Showing the PEARL/HiPr instrument and how the Paris-Edinburgh press is mounted into it. (a) shows a representation of the instrument itself, the red arrow indicates the directions of neutrons through the instrument. There are two banks of detectors, the first is in a traverse geometry and the second in a longitudinal geometry. The press is centred into the instrument in a two staged process. The first of this is the vacuum jacket tank, and then a cradle which fits into the tank. (b) shows a Paris-Edinburgh press in place on a cradle. The press is fitted with centring rings which allow the sample to be rotated, usually to avoid obscuring by the cell tirods.

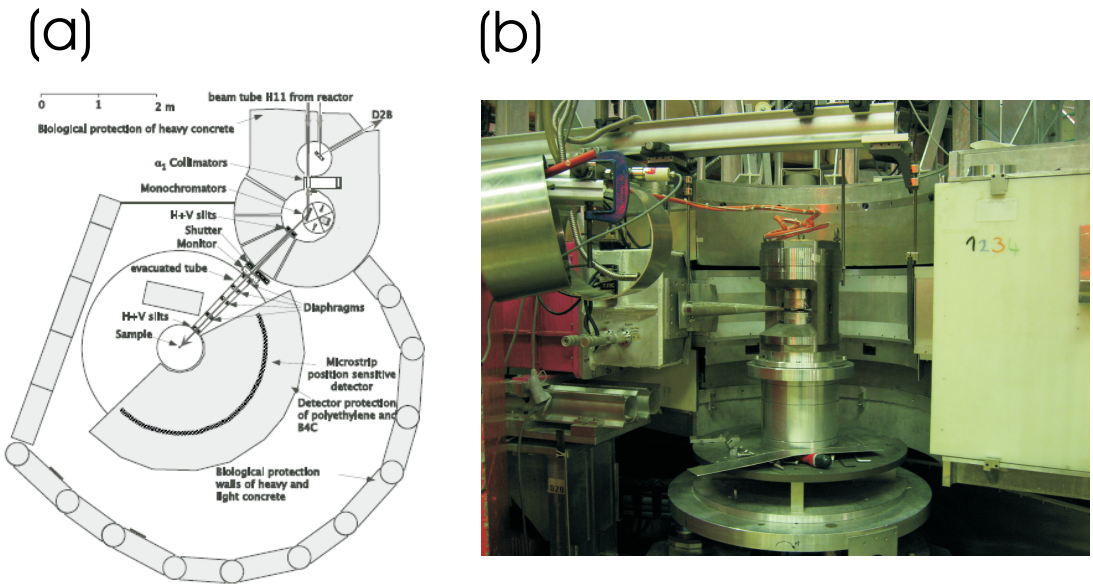

Figure 3.19: (a) taken from [Hansen 08] showing a plan view of D20. The whole sample stage can be moved round the monochromator to adjust the take off angle. (b) shows the the Paris-Edinburgh press (VX variant) in place on D20. To the left of the press is the Cd nozzle for colimation. The orange lead at the top is connected to the high-pressure hydraulic line. Great care must be taken to minimise the torque this line is subjected to, as there is a small risk of rapidly unloading the cell. Behind the press can be seen the area detector.

intensity diffractometer. It is a monochromatic angle dispersive diffractometer with an area detector and the ability to rotate the sample in ω. Different combinations of monochromators and take off angle provides a wide choice of wavelength, resolution and flux, with the highest resolution setting offering a $\Delta d/d \sim 2$ x 10^{-3} [Hansen 08]. D20's fast counting statistics result from the microstrip detector, which covers 153.6°. This is a capacity perhaps wasted on the Paris-Edinburgh press, the VX variant's horizontal angular aperture is 140°. Because of the size of the sample stage, there are very few modifications that need to be made to collect data. A Cd nozzle is fitted to the beam pipe, which can be seen in Figure 3.19(b). This collimates the neutrons onto the sample, limiting background signal. If the sample needs to be rotated in ω (as was the case for methane) care must be taken to not hit this nozzle, and also not to unscrew the hydraulic pressure line fitted on the top. A screen of aluminium was placed between the cell and the detector. Although this cut the sample signal that could be collected, it proved very useful in protecting the €1,000,000 detector.

Data corrections and reduction

For neutron powder data collections many of the corrections referred to in Section 3.2.3 are applied as part of Rietveld refinement. When using the Paris-Edinburgh press at ISIS in transverse mode, the incident beam is passed through the anvils before reaching the sample. Both the anvils, sintered diamond and the gasket materials are highly absorbing of neutrons, which modifies the incident beam before diffraction. This absorption by the press assembly needs to be corrected for. A simple absorption correction, such as that applied as part of the GSAS package, is not appropriate for studies where structural details (such a location of hydrogen) are being refined. Attenuation corrections for the Paris-Edinburgh press in transverse mode can be calculated with the ATTEN program [Marshall 99]. An example of the correction, which is divided from the raw collected pattern, can be seen in Figure 3.20.

The use of the Paris-Edinburgh press on the D20 instrument at ILL is a relatively new technique and efforts to apply appropriate corrections to the data are on-going. Neutron diffraction at ILL is a constant wavelength technique and the geometry of the sample set up is that the beam only passes through the gasket before diffraction. These factors mean that the effect is less severe or complex compared to the ISIS PEARL/HiPr case. In all the studies conducted at D20, as described in Chapter 6, the aim was for phase identification and indexing, rather than for a detailed structural study. For illustration, effect of the cell upon the raw data collected on D20 is illustrated in Figure 3.21.

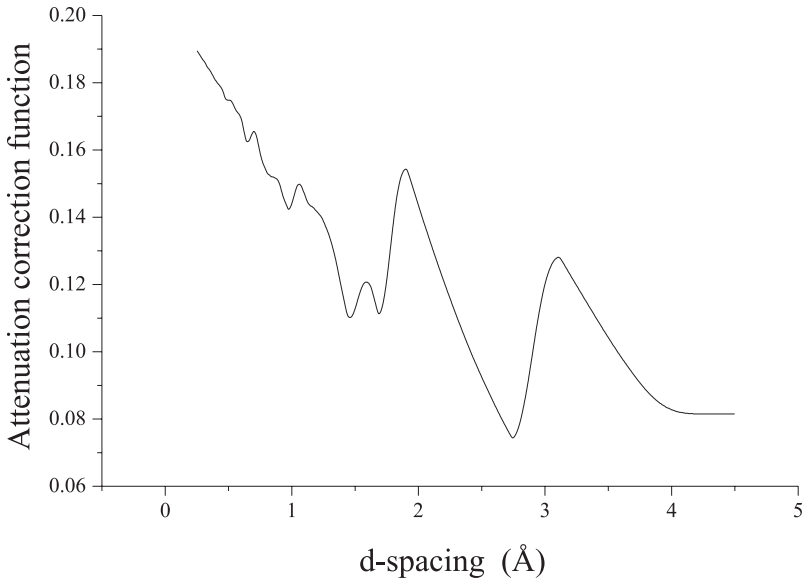

Figure 3.20: The attenuation correction for a toroidal sintered diamond anvil, Ti:Zr gasket and 1-mm anvil separation calculated by the ATTEN program [Marshall 99].

3.4.2 X-ray powder diffraction instruments

In the course of these studies x-ray powder diffraction data have only been collected at ID09a, ESRF, Grenoble. The studies conducted were on methane phase B, detailed in Chapter 5, and work on methane hydrates discussed in Appendix A. Station 9.5 HPT, located at SRS, Daresbury, was set up as a powder diffraction beamline but towards the end of its operating time (SRS closed in August 2008) the station was adapted by the Edinburgh CSEC group to collect single crystal data. Consequently, data collected for this thesis from station 9.5 has only been single crystal collections, so the station will not be described here. However, the set up for collection of power diffraction data from diamond anvil cells on stations ID09a and 9.5 are very similar.

The instrument set up of ID09a is described in Figure 3.22. Placing a diamond anvil cell on a beamline is a relatively straight forward procedure. Because of their small size and weight they can be placed easily on conventional sample stages. To collect meaningful data the small sample size necessitates precise x-ray optics and cell centring techniques. Samples are rarely more than 100 μm in diameter, and if the beam hits that gasket material this contributes an additional powder diffraction pattern. One of the many advantages of using synchrotron sources is the ability to tightly collimate the beam. On ID09a the beam at sample is $\sim$30μm. The small beam size also allows the sample to be rotated slightly in the ω axis during data collection (to reduce textual effects) without adding contamination to the pattern from the gasket.

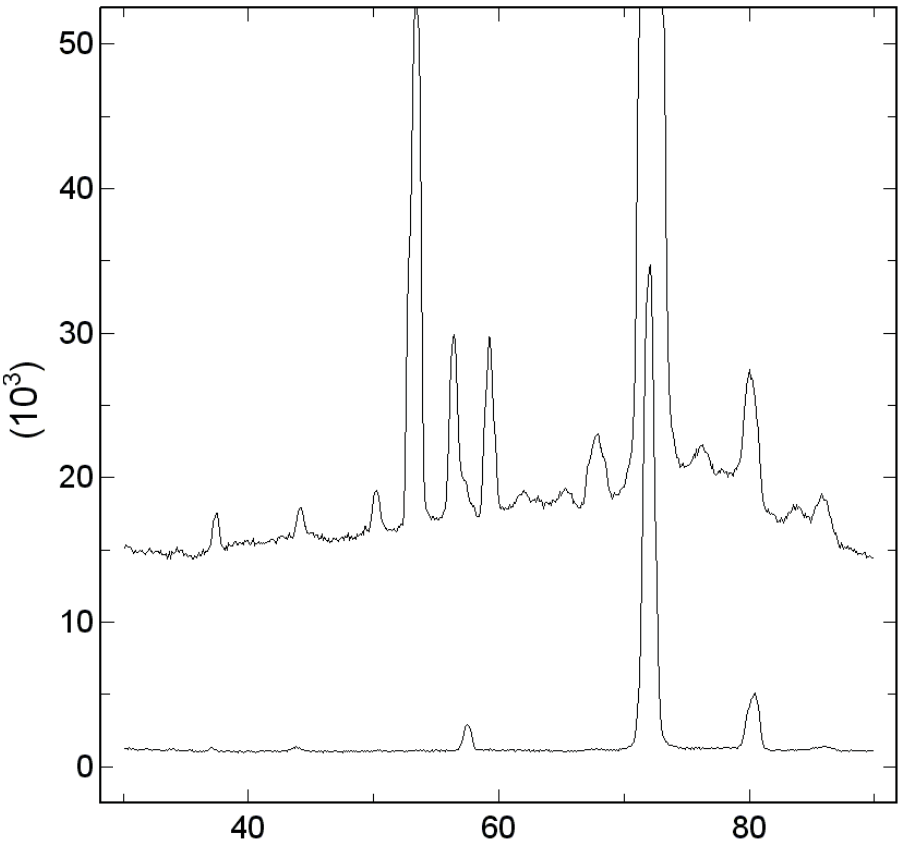

Figure 3.21: Data collected before (top pattern) and after (bottom pattern) a blow out from a Paris-Edinburgh press of a methane sample. This illustrates the background contribution of the cell to the collected pattern.

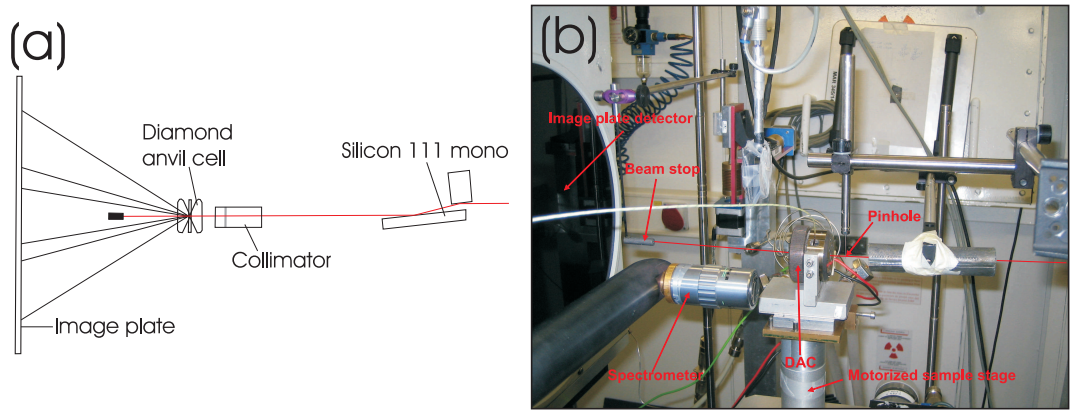

Figure 3.22: The powder diffraction set up on ID09a. (a) is a schematic illustrating the key components and geometry of the system. (b) a picture of the set up with some additional details. The spectrometer, located out of the beam is moved up to examine the cell and collect ruby fluorescence for pressure calibration. The motorised sample stage is key for the alignment procedure.

The alignment procedure is conducted using the beam itself. A diode is place between the cell and the detector, and the signal received is charted as the cell position is varied by moving the sample stage motors horizontally parallel to the detector (usually defined as y axis). This gives a characteristic shape with a maximum plateau signalling the width of the gasket hole (the sample area). This can then be centred, and the procedure repeated in the vertical direction parallel to the detector. To align the sample in the x direction (defined as the direction along the beam) two y axis collections at x and $x+\Delta x$ are taken, and any displacement between these is corrected for.

Data reduction

One of the characteristic features of a raw image plate of diamond anvil cell powder diffraction data is the large, often saturated, spots that are often recorded with the data. These are single crystal diffraction spots from the two diamonds that surround the sample, Figure 3.23(a). These are easily masked from integration using available software, such as Fit2D [Hammersley 97]. Using calibration data, such as that illustrated in Figure 3.6, the raw image plate can be integrated to a single $x-y$ profile, Figure 3.23(c). The pattern is then truncated to alleviate the effects of the edges of the image plate and the beamstop, before a polynomial can be fitted to the rest of the data to account for the Compton scattering from the diamonds. Other corrections are applied as part of the refinement process, described in Section 3.2.4.

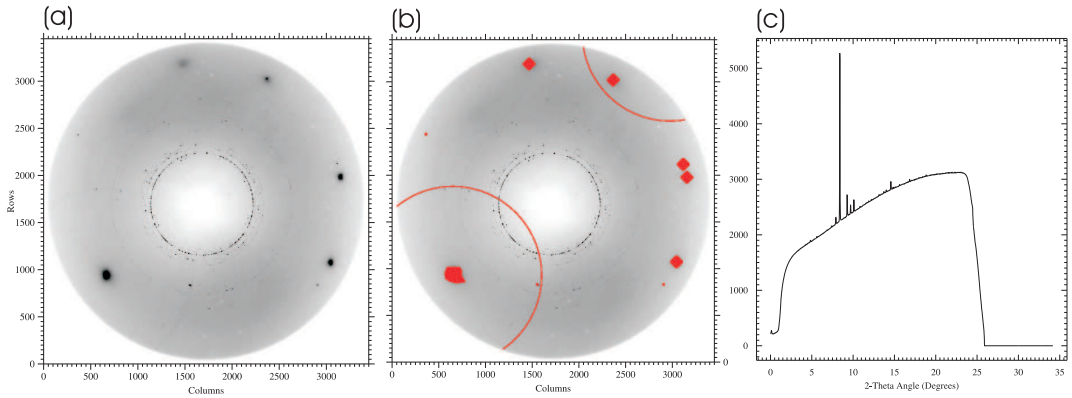

Figure 3.23: The stages of data powder data reduction from a diamond anvil cell. (a) shows a raw image from a MAR345 image plate in full 3450 resolution mode. The signal from the sample is towards the centre of the image, the large spots towards the edges are from the diamonds. The next stage, illustrated in (b), is to mask out unwanted contributions, such as that from the diamonds. Next the Fit2D [Hammersley 97] software is used to integrate the data reducing it to a single line, as in Figure 3.6. (c) shows a typical powder profile from a diamond anvil cell. Compared to Figure 3.6, this pattern has a significant background. At low angles this comes from the beam stop and the sharp drop at 25° 2θ is from the edge of the image plate. The large background underneath the main pattern is from Compton scattering from the diamonds.

3.4.3 X-ray single crystal diffraction instruments

Similar to the x-ray powder data collection, the single crystal data for this thesis was collected with monochromatic sources. Unlike the powder diffraction, which has a largely fixed geometry, to collect single crystal data from a monochromatic source the sample needs to be rotated, preferably about more than one axis. This change must be finely controlled and reproducible for accurate data collection. Data 'shots' are collected in steps as a function of angle between the radiation source and sample. For each 'shot' the sample is exposed to the beam for a constituent period of time. The exposure time will vary depending on the goals of data collection. For a good integration, and a subsequent data set for input into direct methods, it is important that strong sample reflections are not saturated. If the aim of the experiment is to characterised weaker reflections, or diffuse scattering, then the exposure time will be increased and some reflections may saturate. Step sizes are usually between 0.2-0.5° depending of the quality of the crystal sample. Across sweeps of 50° this can mean up to 250 shots are collected as part of a single collection. Consequently, single-crystal data sets are large, and experimenters must carefully design collecting procedures to maximise information whilst minimising collection time. This is even more important for high-pressure data collection where collection procedure must be designed to minimise shielding from the

body of the cell.

During this study two different single crystal collection set ups have been used. The first, which is similar to both the in house diffractometer and station 9.8, SRS, Daresbury, is a Bruker SMART three-circle goniometer fixed χ, with an APEX CCD detector, as illustrated in Figure 3.24. Accompanying this set-up is the Bruker SMART software which is used for data reduction [Bruker 98]. With this geometry it is especially important to design collection with the shielding from the cell in mind. The alignment procedure for this experimental set up is conducted optically with a fixed microscope. The sample is centred so that it does not move when rotated about ϕ angle.

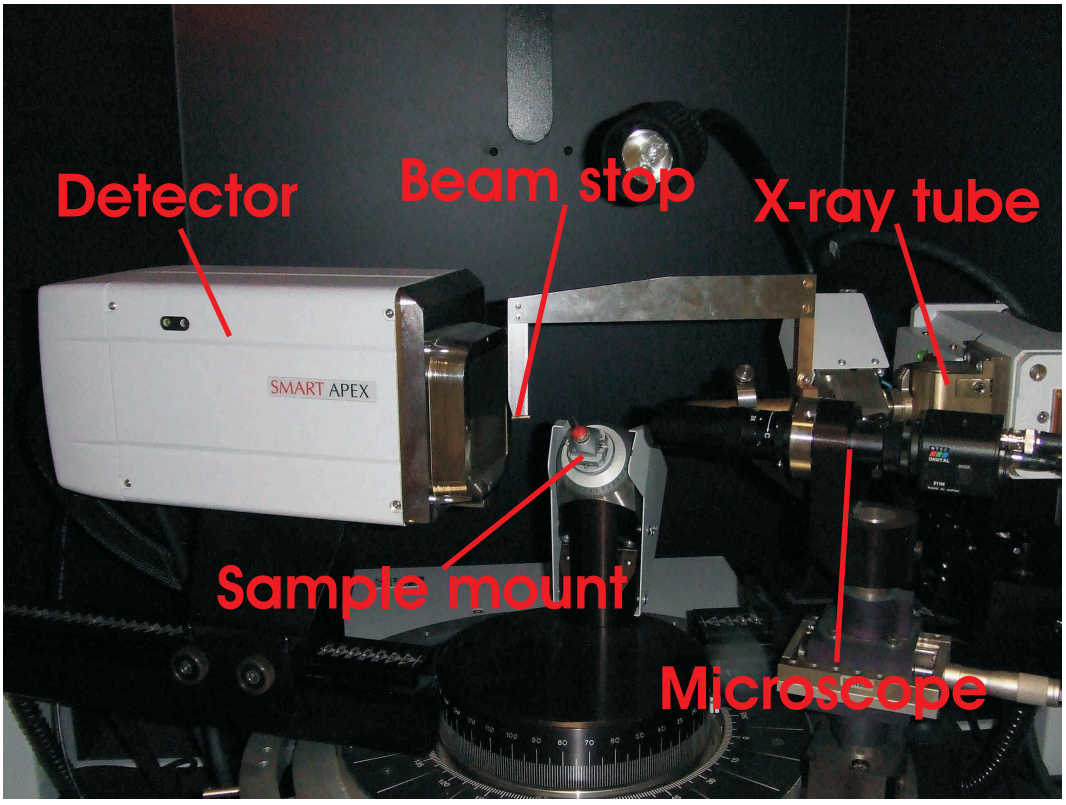

Figure 3.24: An image of the in-house diffractometer belonging to the physics high-pressure group, University of Edinburgh. The main components of the system are labelled, and are all contained within a hutch to provide shielding from the x-rays.

The second set up, used at stations ID09a and ID27, ESRF and 9.5, SRS is identical to that in Figure 3.22 and was developed by the Edinburgh CSEC group [Lundegaard 08]. Here the motors in place to rotate the sample about the ω axis (usually used to alleviate textual effects in powders) are used to their full. The data is collected in steps as a function of ω, and for a Böhler-Almax backed Merrill-Bassett cell this can be up to $\pm 35^{\circ}$ before the sample is shielded by the backing disk. The sample is

centred in the set-up with the same procedure described in Section 3.4.2. Although the detector type used at each station varied, ID09a and 9.5 use a MAR345 detector and ID27 an Oxford instruments CCD detector, the data were routinely converted to Bruker SMART format. This ensured compatibility, ease of comparison and analysis between all the data sets. Collecting single-crystal data with this, second set up, has a number of advantages over the more 'conventional' apparatus of the in house diffractometer. At a synchrotron source the incident beam can be tightly focused to lie within the small gasket holes of high-pressure samples. Only varying the data collection along one axis results in very high stability. This high stability is complemented by the alignment procedure (identical to that explained in Section 3.4.2). Lastly the used of the large MAR345 image plate detectors means that a complete data set can be obtained in two sweeps, cutting down on collection times.

The small characteristic wavelengths of stations 9.8, 9.5 ($\sim$0.7 Å), ID09a ($\sim$0.4 Å) and ID27 ($\sim$0.3 Å) are ideal for studies where angular access to the sample is limited. As described in Section 3.3.1, this is only of value if the sample studies sample scatters to a $\sin\theta/\lambda$ that can be observed.

Data reduction

Integration procedures for single-crystal data are very different to the process described for powder data. Instead of the entire pattern being processed, for single crystal data each individual reflection is integrated over the number of frames which it is observed. The final product of the data is quite different to the $x-y$ plot outputted from powder collection. The aim of single crystal data collection is to produce a list of hkl's each with an observed intensity and error, σ, on that intensity. With information on a structures symmetry this can then be outputted as a list of structure factors, F and σF ready for input to direct methods, or refinement against a pre-existing model.

The first stage of this process is to assign the pattern a unit cell and index the reflections. Conventionally this is achieved with a 'harvest' of reflections over a defined intensity threshold, computed from all the inputted frames. Because of the large background and diamond peaks this is not always successful for high-pressure data collections and the reflections are often picked by hand. The 'harvested' or picked reflection are then inputted into a reciprocal lattice viewer, this study used RLATT part of the Bruker suite of programs [Bruker 98]. This is a good aid for visual examination of the quality of crystal. Ideally a lattice structure will be evident in the reflections, but sometimes outliers from background and diamonds, will need removing. The filtered reflections are inputted back into the SMART software for indexing. The data frames can be viewed with the indexed lattice overlain, and the fit to the data can be assessed.

Before proceeding with integration it is vital that the indexing and orientation matrix accurately predict the reflection positions.

As part of the integration, the SAINT integration software, assesses the background contribution to each reflection. It is important to ensure that this is being adequately modelled and described by the program. For high-pressure data collections part of the area detector is usually obscured by the cell body. This can interfere with the calculation of the background, and effect the quality of the integration. The solution is to generate masking frames which cut out the shielded regions of the area detectors. A further contribution which can affect the quality of the integration is the beam decay of the synchrotron. This is accounted for by monitoring the status of the beam at each data point and then normalising the average counts over the whole data collection.

$$R_{\text{int}} = \frac{\sum \mid F^2_{\text{obs}} - F^2_{\text{obs}}(\text{mean}) \mid}{\sum \mid F^2_{\text{obs}} \mid} \tag{3.21}$$

The beam decay corrected frames, the indexing, orientation matrix and masking frames are all inputted into the SAINT software for integration. There are a number of variables that can be adjusted depending of the quality and type of data. Principally, these centre about which reflections are used to build the peak shape model and how this is then applied to the remaining reflections. The assumed symmetry of the crystal phase is also an input of the software and the quality of the data is assessed with that basis. Using Equation 3.21 the symmetry equivalents of each reflection are averaged and compared to each reflection. A high R_{int} usually signifies a bad quality data set, but can also result if the wrong symmetry applied. If appropriate, the data can be absorption corrected with the SADABS program before final file preparation (for input to a refinement program such as SHELX) is proceeded with XPREP.

3.5 Sample synthesis and growth

This section details the more practical aspects undertaken during this study, loading, preparation and growth of samples.

3.5.1 Gas loading techniques

Methane is a gas at room temperature and as such is highly compressible. This makes loading a sufficient amount of sample within the confines of a pressure cell very challenging. There are two main methods for loading methane and other similar gaseous samples. The first is to load the cell within a pressure chamber surrounded by the sample gas. The sample gas needs to be at a sufficient pressure so that when the cell is closed, there is enough sample contained within it. There are a variety of technical

challenges associated with this method of loading. One is having the capability to close and seal the pressure cell within the chamber. For the smaller diamond anvil cells this has been overcome [Couzinet 03] and previously very difficult samples, such as hydrogen, can now be loaded with relative ease. For larger cells, such as the Paris-Edinburgh press, this technicality has yet to be overcome.

An alternative to loading the sample whilst in the gaseous state is to load it within the liquid state cryogenically. This technique has been used throughout this thesis. The cell and sample must be cooled to below condensing conditions of the sample gas. Then, once the sample is in its liquid state, and can flow into the sample chamber of the pressure cell, the cell is sealed. This method has been used for both the Merrill-Bassett diamond anvil cell and the Paris-Edinburgh press.

Merrill-Bassett cryogenic loading

The cell is prepared as for a conventional loading. The diamonds must be aligned accurately, so that on contact between each anvil no interference fringes are observed. A rhenium gasket is indented to the pressure that the cell is intended to achieve. This is monitored by placing a ruby between the gasket and the diamond and charting the non-hydrostatic ruby florescence with indentation. This stage prevents the gasket hole from collapsing, especially important with highly compressible gaseous samples. Next a hole is drilled in the centre of the indent with a spark eroder. Placing the hole to the centre of the indent maximises the support for the sample area at high-pressure. The next stage is to clean the diamond anvils culets and gasket extremely well, to avoid any contamination. The cell is constructed prior to loading by securing the gasket to the lower culet with blu-tac connected to the cell itself. A small sample of ruby dust is then placed upon the upper anvil, and on closing the cell the ruby must lie within the sample space. The screws of the cell are then tightened so that the cell is only just closed. This is monitored with interference fringes between the gasket and the diamond. The last stage of cell preparation is to place a small steel spring between the gap of the cell body. This is to ensure that when the screws of the cell are opened later, the sample chamber is also opened. Friction in the guide pins can sometimes prevent this.

The closed cell is then placed within the cryogenic loading apparatus described in Figure 3.25. As the Merrill-Bassett is quite small the chamber of the apparatus is filled with aluminium blocks. This cuts down on the amount of sample gas that is used. It also brings the cell closer to the top of the container, which makes proceeding steps easier. The perspex lid of the apparatus is then placed on to sample chamber and the sealed. Before cooling the whole container is flushed with the sample gas, again to minimise the possibility of any contaminants. Next the whole apparatus is

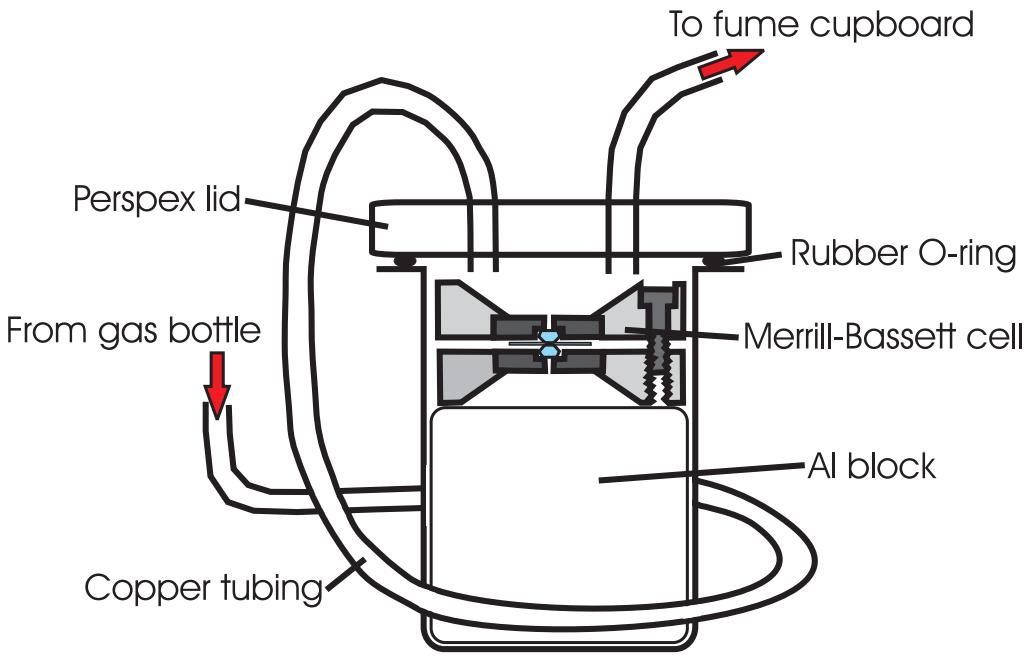

Figure 3.25: A cross sectional diagram of the diamond anvil cell cryogenic loading apparatus.

put into a polystyrene box and surrounded with liquid nitrogen. The sample gas is flowed through the apparatus to initiate condensation. The flow of gas is maintained until the container has a level of liquid sample that covers the diamond anvil cell. The container is kept in the liquid nitrogen bath whilst the lid of the chamber is taken off, to allow access to the screws of the cell. Extra long Allen keys are used to first loosen the cells screws (to allow the surrounding sample to flow into the sample area) and then tightened (to seal the sample within the cell). Then the cell is removed from the apparatus and warmed to room temperature. The presence of a sample and a ruby pressure calibrant is checked by Raman spectroscopy. Because the dust originally placed on the upper anvil is usually moved or washed out during loading, it is a difficult to obtain a characteristic λ_o for the ruby fluorescence. A standard value of 692.32 nm is used as R_1 (the largest and higher wavelength spectra peak) for these loadings.

Paris-Edinburgh press cryogenic loading

Unlike the Merrill-Basset cell, condensing sufficient sample to cover the Paris-Edinburgh press is not an option. Instead the cryogenic loading method is to contain the sample in an area about the anvils. For this an aluminium ring with inner diameter 20 mm and outer diameter 25 mm is drilled with two holes with $\sim 45^\circ$ angular separation, Figure 3.26(a). Capillaries with gas connection fittings, are secured into the holes with

Sty-Cast adhesive. A ring of indium wire, 0.25 mm diameter, is placed around the top and bottom of the aluminium ring to be a low temperature seal. The press is then assembled as outlined in Figure 3.17(b), but with a few modifications. As part of the preparation the outer ring and bottom cup of the SME gasket are glued to the bottom anvil, and the top part glued to the top anvil. This ensures that the gasket does not close before the cell is loaded and prevent gas condensing into the sample space. The ring of cadmium shielding is decreased, so that the inner diameter exceeds 25 mm and will not be damaged when the aluminium ring is removed after loading. The aluminium ring is then placed between each of the anvils. The breach of the press is then tightened to align the anvils and to create a seal between the aluminium ring and the anvils with the indium. The breach is not tightened fully, this is so as not to break the ring and to maintain a 1 mm gap between the top and bottom gaskets now confined inside the loading ring. The assembly at this point can be seen in Figure 3.27(a).

Once the seal on the aluminium ring is leak tested the press can itself be prepared for cryoloading. Figure 3.27, shows the layers of insulation that are placed about the ring and the capillariaries. In addition the capillaries are secured to the press itself. This prevents them from dangling into the liquid nitrogen later, creating blockages. The press is inverted so that the hydraulic inlet is on the top of the cell and the whole assembly is placed inside a bucket, Figure 3.26(b).

The hydraulic fluid inlet is fitted with a heater to prevent blockages in the pentane used to apply load to the cell. The capillaries are connected to a gas regulating system which in turn is connected to the sample gas. The ring is flushed with the sample gas, to removed the chance of contamination. Once all is prepared the bucket is filled with liquid nitrogen until the level is over the bottom stand of the press. With this system a pressure of up to 10 bar can be confined within the aluminium ring. Knowledge of the vapour pressure curve of the sample gas gives a target temperature needed, this is monitored with a thermocouple attached to the loading ring. Condensation of the sample gas can be observed with the gas regulating system, signalled by a sharp decrease in pressure in the sealed system before resting at the vapour pressure at the temperature of the press. Once the condensation process is complete a load of 25 tonnes is applied to the piston with the pentane pressure medium to seal the SME gasket. The press is removed from the liquid nitrogen and allowed to return to room temperature slowly. Once the press is at ambient temperature and the load of the press is steady, the aluminium ring is drilled off and any remnant indium carefully removed.

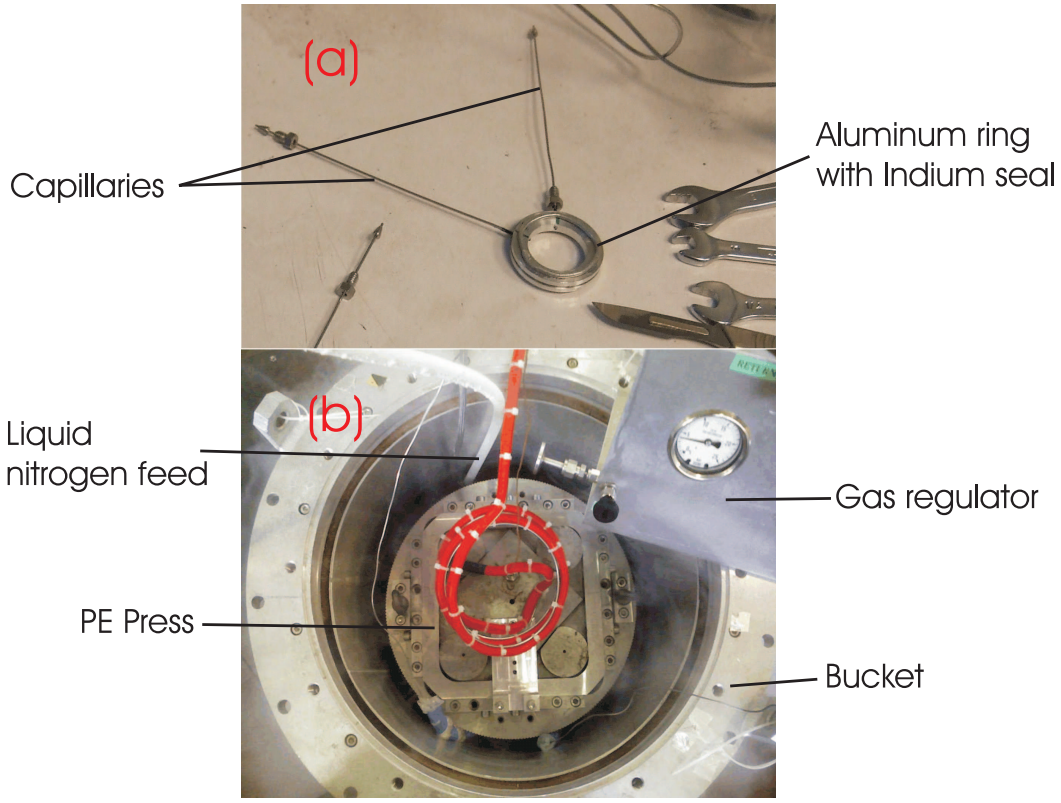

Figure 3.26: The equipment needed for cryogenic loading of the Paris-Edinburgh press. In (a) the construction of the Al loading ring is shown. The ring of 25 mm outer diameter is drilled with two holes to fit capillaries, which are secured in place with Sty-Cast adhesive. Indium wire is placed on the ring to make a low-temperature seal. (b) shows the press in place for cryogenic loading. The gas regulator allows control and monitoring of the pressure inside the ring. The bucket is a container for the liquid nitrogen. The temperature of the cell is monitored separately with a thermocouple. In picture (b) a press with pentane as its hydraulic fluid is being loading. The red cord is a heater that prevents blockages in the hydraulic line. When loading a cell with helium as the hydraulic fluid blockages are not a problem.

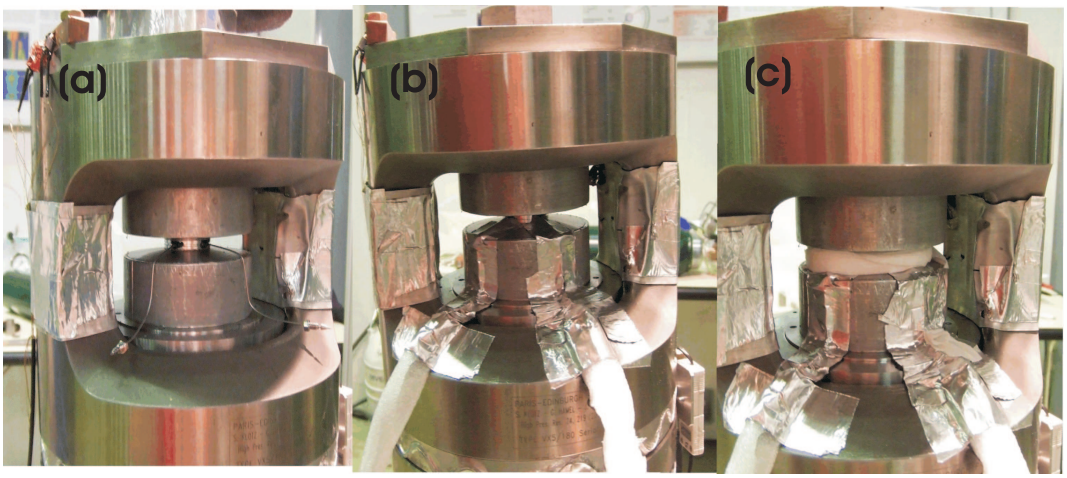

Figure 3.27: Three stages in insulating the cell before cryogenic loading. (a) shows the Al ring in place and the capillaries are bent to follow the cell body to maintain warmth and away from the liquid nitrogen (the cell is inverted for loading). (b) the capillaries are insulated and then attached to the cell body with Al tape. Lastly in (c) the Al ring is insulated. This process was necessary to minimise blockages during loading.

3.5.2 Clathrate sample synthesis

The importance of studying clathrates have been outlined. Although these studies do not appear in the main body of this thesis, they are outlined in Appendix A. Two methods of clathrate sample synthesis were undertaken. The first forms clathrate structures *in situ* by loading their constituent into the pressure cell and the second forms the sample within an autoclave for later loading into a pressure cell.

In situ clathrate growth

Growing clathrate structures *in situ* invariably involves loading water and an additional gaseous sample component. The difficulty arises in containing both of these within the sample space in sufficient quantities to make up a complete loading. The method described in this section was developed for a diamond anvil cell. A similar technique could be developed for the Paris-Edinburgh press, although the control on the amount of water contained in the sample would be more difficult.

A Merrill Bassett type diamond anvil cell is prepared in the normal fashion. Water is placed into the gasket along with some ruby and the cell closed. Next the cell is slowly opened to allow some of the water to escape. Careful control of this means that the proportion of water in the gasket hole can be constrained. Once the amount of water has decreased to the desired amount as in Figure 3.28, it is then closed to prevent any further water escaping. The next stage of the process is to cryo-load the

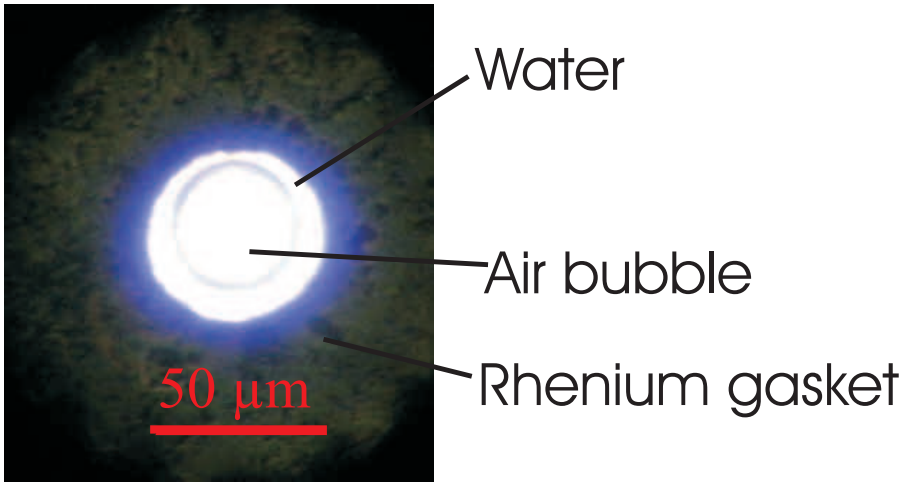

Figure 3.28: Partial filling of the sample gasket as first loading stage for *in situ* clathrate growing techniques. The water will be frozen when cryo-loading commences.

cell as described in Section 3.5.1. During the cooling stage of this process the water is frozen in the sample space, allowing a duel component loading to be achieved.

Autoclave clathrate growth

The second clathrate synthesis technique was developed at the Steichie-Laboratory, National Research Laboratory of Canada, Ottawa. The author travelled to the laboratory to learn the technique and to produce a methane clathrate sample The study of this sample is described in Appendix A.

This technique is a reliable method of synthesising ultra-pure clathrate samples, for experimental use in all types of high-pressure cells. The sample is made in an autoclave which also contains steel rods, Figure 3.29. The first part of the process is to place 10 cc of distilled water into the autoclave, which has a volume of 380 cm^3, then seal the vessel. The autoclave is then placed into a liquid nitrogen bath to freeze the water before using a compressor to pump the air out of the system. The gaseous sample is then pumped into the autoclave creating an over pressure for clathrate formation. For example at 270 K methane clathrate forms at 300 MPa (0.03 GPa), so the vessel is pressurised to 800 psi ($\sim$5.5 MPa, 0.055 GPa).

The formation process takes place over five days, this length of time ensures that all the ice reacts to form clathrate and the resultant sample is a pure. During the five days the autoclave is kept in a freezer and rotated constantly, Figure 3.30. The temperature of the freezer is kept as close to 270 K as possible to maximise the kinetics of the clathrate formation. The rolling motion means that the rods inside the autoclave constantly break up the ice. This exposes any unreacted surface and speeds up the

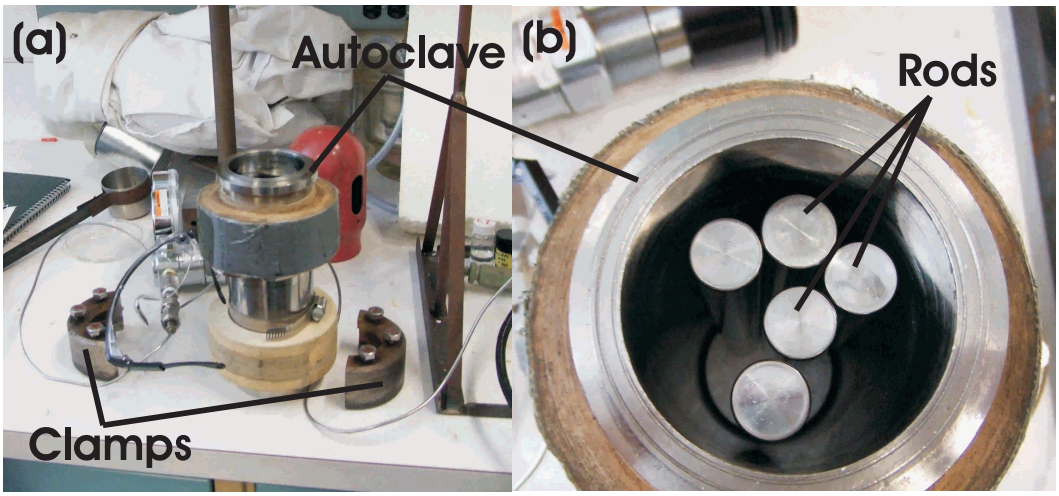

Figure 3.29: The autoclave equipment used for clathrate synthesis at NRC, Canada. (a) shows the autoclave itself with the clamps used to ensure the Teflon seal is leak tight. (b) shows the steel rods that are placed inside the vessel and grind the sample ensuring a larger surface area on the ice for clathrate formation.

reaction by keeping a large surface area for the reaction to take place. Once every 12 hours the whole autoclave vessel is shaken vigourously to aid this process.

During the five days under close monitoring on two occasions the freezer's temperature is brought to above 270 K. Under these conditions the remaining ice will melt whilst the methane clathrate remains stable. When the autoclave returns to below 270 K, the water will more readily react with the excess methane in the system. The pressure of the autoclave is charted during the five days. The pressure drops steadily over the five days but plateaux once the clathrate synthesising process is complete.

The sample is recovered by first placing the autoclave into a liquid nitrogen bath. Once the pressure of the autoclave drops to zero the vessel can be opened and the sample removed for storage in a nitrogen Dewer.

3.5.3 Single crystal growth

Single crystals are often grown by cycling a material about its melting temperature. This process can also be exploited within pressure cells to grow crystals *in situ*. Single crystals grown in this way are often of excellent quality as growing them *in situ* can release the effects of non-hydrostatisity that build when the crystal is compressed from ambient pressure. Growing the crystals at the melt line, once at pressure, also removes the risk of it breaking. The principal of this type of growth is demonstrated in Figure 3.31. Temperature is closely controlled towards the melting temperature. In ice, the example shown, crystal boundaries that are not apparent at room temperature become

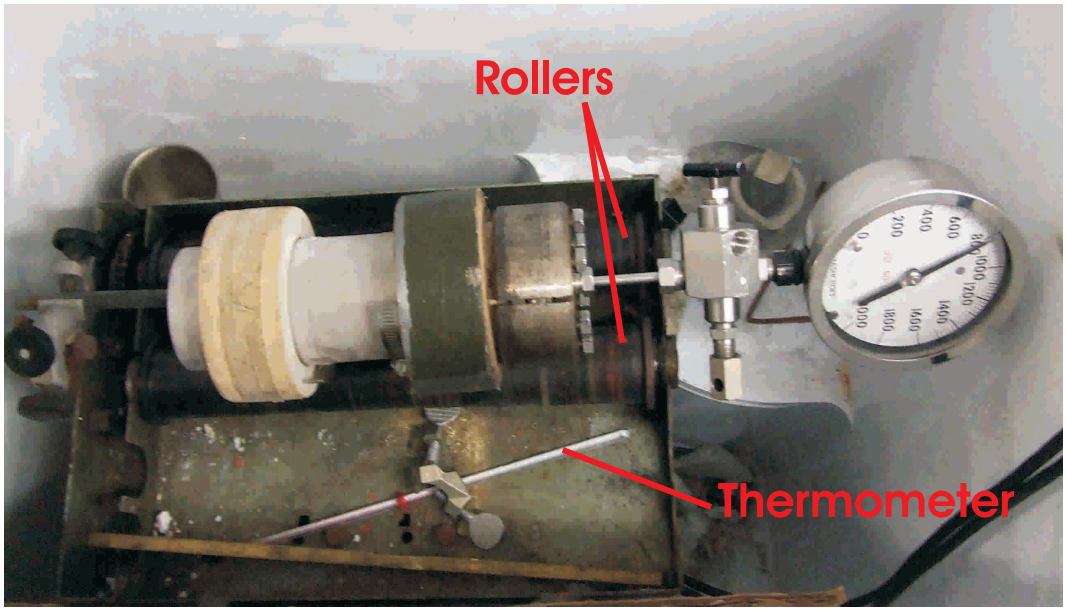

Figure 3.30: The autoclave in place on a roller within a freezer. The thermometer was used to monitor and regulate the temperature, the pressure was noted from the manometer dial.

clear close to the melting temperature, Figure 3.31(A). As the crystallites melt usually a larger one persists longer than the others, Figure 3.31(B) and (C). This becomes the seed crystal and the temperature of the cell is lowered to allow this to grow and fill the gasket.

During these studies there has been a steady development of equipment for single-crystal growth. The original equipment used, shown in Figure 3.32, was quite basic and only allowed for real-time observation of the sample growth and no pressure monitoring. Recording of images was also quite primitive, the pictures shown in Figure 3.31 were taken with a mobile phone. The maximum temperature of this set up was also limited to ∼550 K, as there was no provision for a cooling base.

Figure 3.33 is an image of the final single-crystal growing equipment. Based on a simple optical set up, the image of the sample is very much improved and allowed for more detailed observations, as discussed in Section 4.4.1. The addition of a recording DVD player also meant that every growing run could be recorded, and then later reviewed. The laser and spectrometer enable the user to monitor the ruby fluorescence over the crystal growth, giving an estimation of the sample pressure. This sample set up also has the room to fit a cooling base. With a cooling base much higher sample temperatures can be reached, only limited by the type of pressure cell that is used.

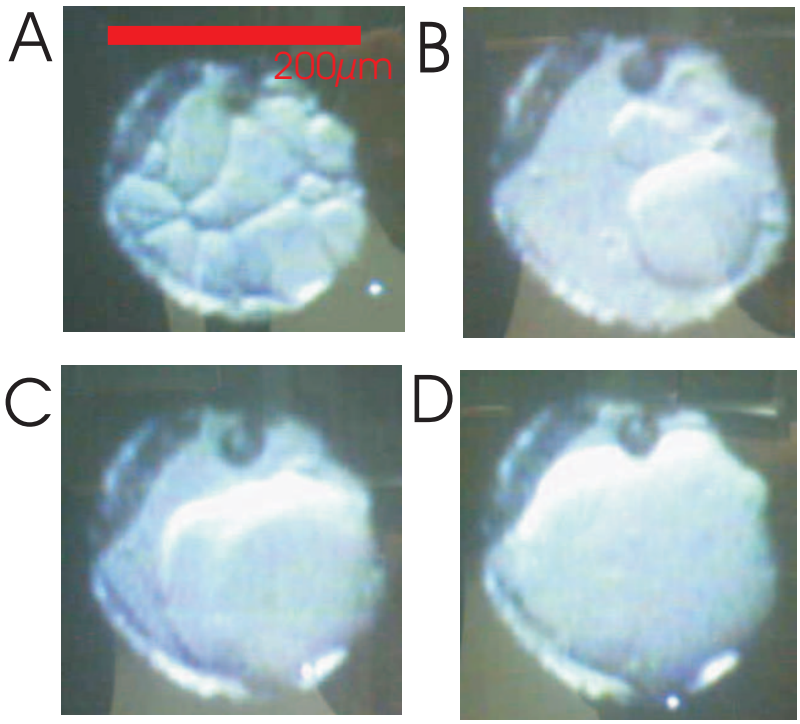

Figure 3.31: Stages in growing a single crystal of ice VII. A) the sample is heated to near it's melting temperature and develops a texture where separate crystallites can be visualised; B) as heating continues the crystallites melt; C) at the point where only once crystallite is left the heating is switched off and the diamond anvil cell cooled; D) further cooling encourages this single crystallite to grow and fill the gasket, becoming a single-crystal.

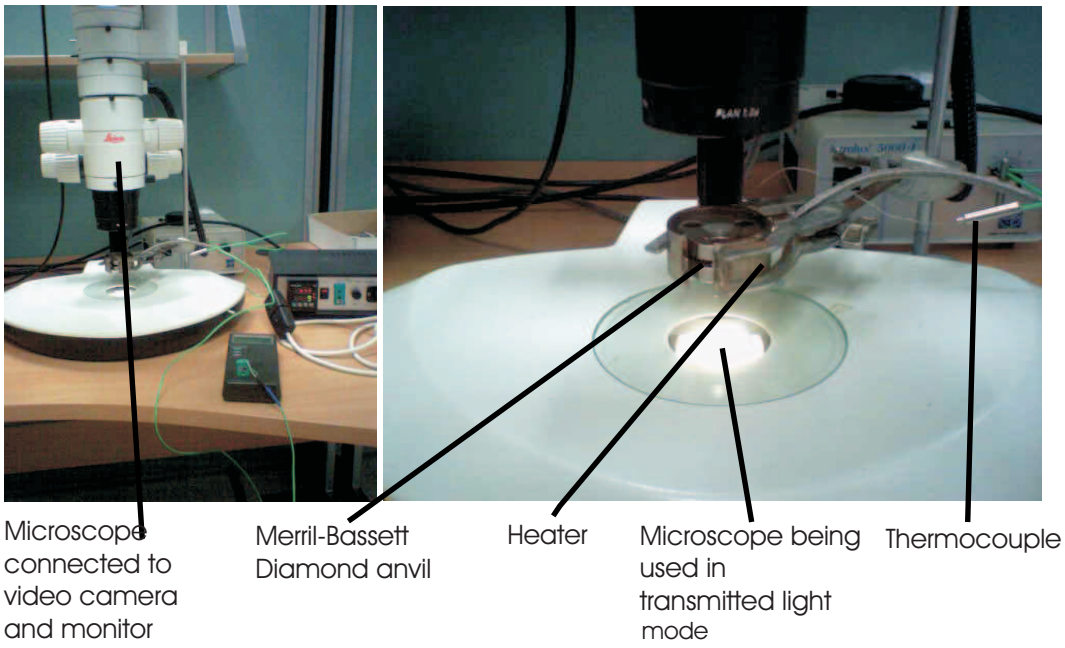

Figure 3.32: The original equipment used for single crystal growth. The Merrill-Bassett cell was held within a resistance heater with a clamp. The cell was mounted under a microscope to allow for visual monitoring of single crystal growth.

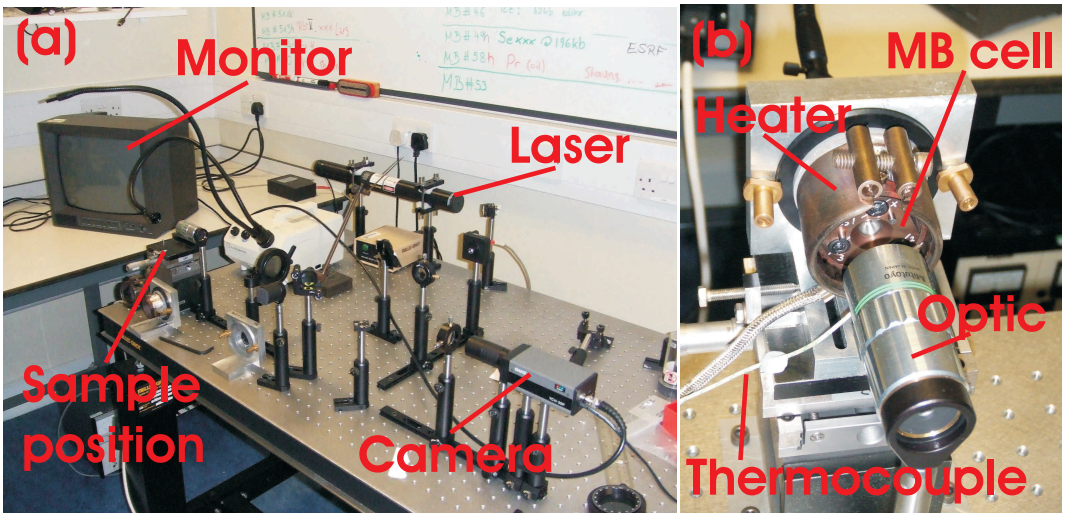

Figure 3.33: The revised equipment for single crystal growth. This has many advantages over the original equipment. Firstly the more secure positioning of the sample allowed for better visual observation of the growing process. The steadier picture also allowed the growing to be recorded with a video camera. The other advantage of this equipment is the integration of a laser spectroscopy system which allows the sample pressure to be monitored as well.

3.6 Summary

It has not been the aim of this thesis to develop new techniques for the study of the outer solar system mineralogy. Rather, to take a large base of techniques that can be used to physically characterise these systems. As all the components; water, ammonia and methane, are hydrogen based there is a real need to take integrated experimental approach to their study. Consequently this chapter has detailed the large number of existing or recently developed techniques that have been used to achieve the results presented subsequently in this thesis. New methods of crystal growth have had to be developed, but these are outlined in Section 4.4.1.

Chapter 4

Studies of methane, Phase A

4.1 Introduction

This introduction will continue the theme of Section 2.5 but with a focus on methane's phase A. The aim of this section is to clarify previous research and nomenclature on the methane phase diagram, as well as review previous research on phase A. A similarly detailed review of phase B will be completed within the introduction to Chapter 5.

Significant polymorphism in the methane phase diagram by first identified in a series of papers by Fabre *et al* [Fabre 82, Thiery 85]. Previous to these studies only the ambient pressure phases I and II were known. As described in Section 2.5, the structures of these phases had already been solved and extensively studied [Press 72]. Fabre *et al*'s series of studies [Fabre 82, Thiery 85] explored methane and deuterated methane up to 1.2 GPa using a piston-clyinder optical cell and Raman spectroscopy. They used low temperatures to induce the solid phases of methane, as at room temperature methane does not solidify to 1.3 GPa. The results from these two studies are summarised in Figure 4.1; four phases of methane were identified in addition to the original phases I and II. The new phases were distinguished by monitoring both the intra-molecular vibration bands; ν_1, ν_2 and ν_3. The lattice band frequencies of methane were observed to have discontinuities with pressure at 0.05, 0.19, 0.49 GPa and 0.90 GPa, marked by red dots on Figure 4.1. These changes were taken to be indicators of phase boundaries from phase II to III, III to IV, IV to V and V to VI respectively. In contrast, the intra-molecular bands changed very little with pressure. From this, and the similarities of site assignments, Fabre *et al* concluded that all of these phases would have tetragonal symmetry. They proposed that all the phase transitions would be initiated by modifications in the hydrogen ordering [Fabre 82].

The room temperature section of the methane phase diagram was originally constructed by Hebert *et al* [Hebert 87], again using Raman spectroscopy. This work

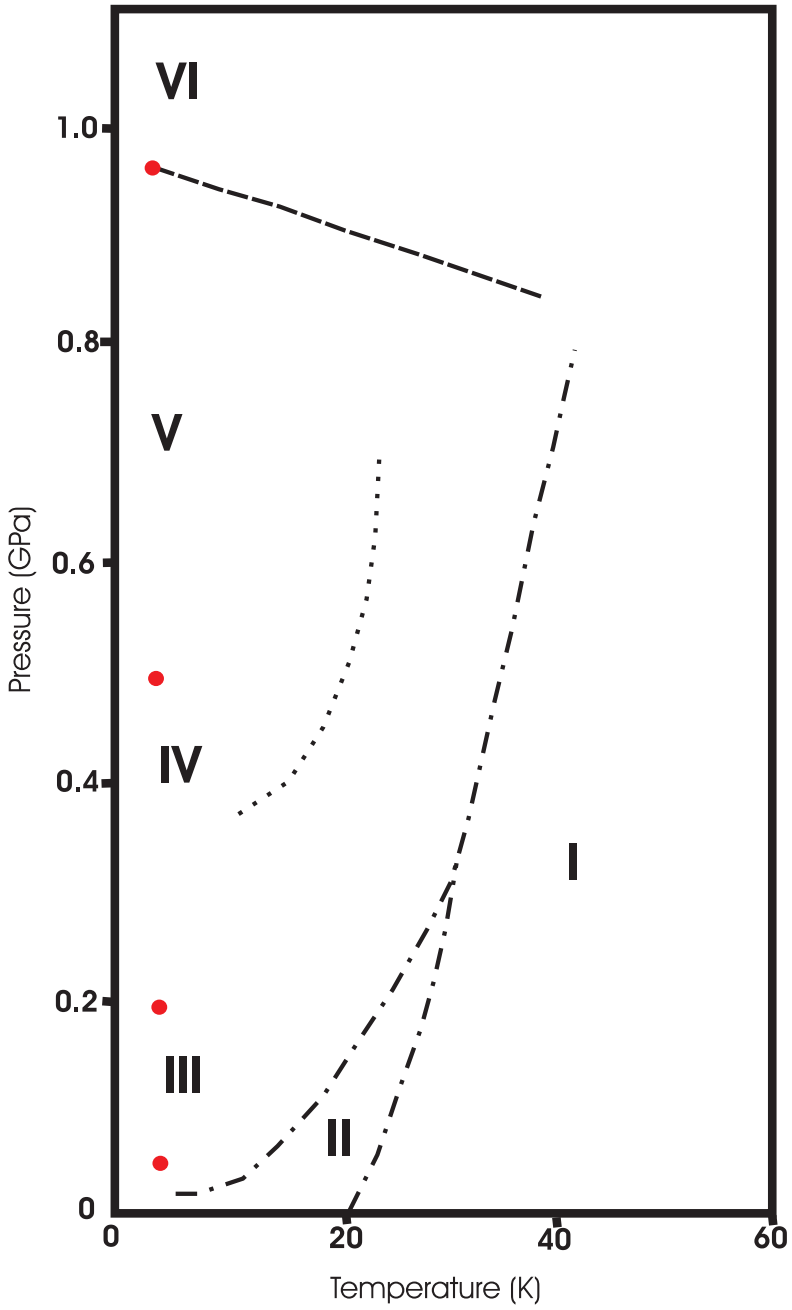

Figure 4.1: Taken from [Thiery 85] and summarises the phase relations of methane known at the time from a variety of sources, with speculative phase boundaries drawn. The red markers indicate point where the spectra from methane was seen to change, and interpreted to be a phase transition [Fabre 82, Thiery 85].

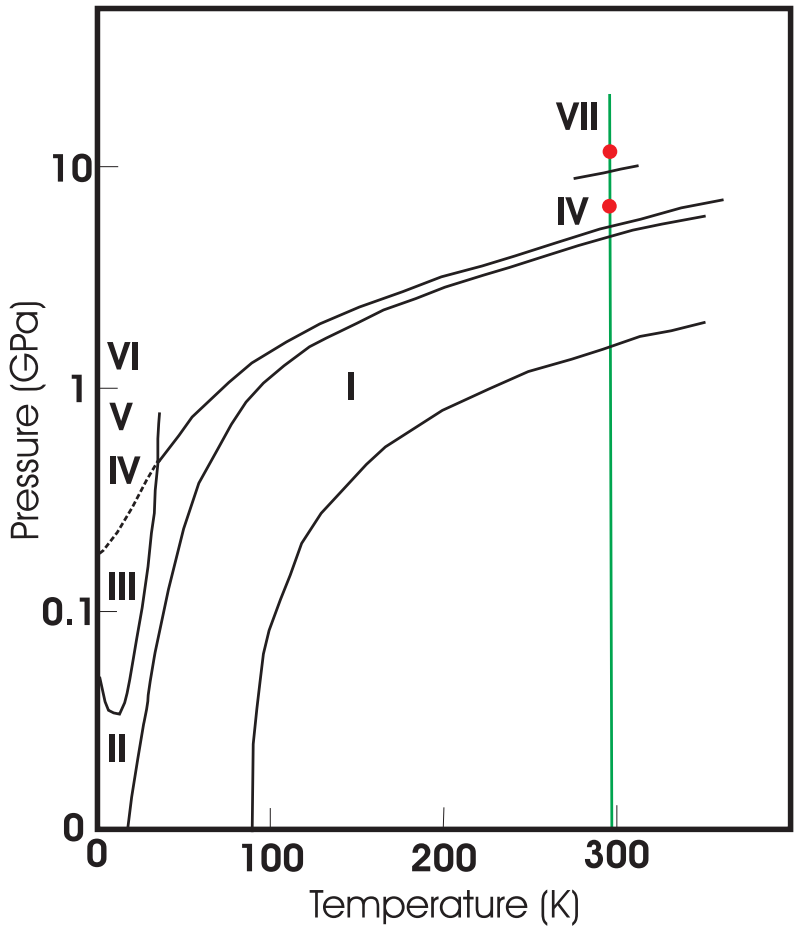

Figure 4.2: The proposed phase diagram on a semi-lograthmic scale taken from [Hebert 87] with the green line showing the path of their experiment. The red markers indicate the onset of phase VII with increasing pressure and its disappearance with decreasing pressure. This marks the first observation of a large hysteresis between phases A and B.

was complemented by Brillouin spectroscopy and measurements of the refractive index. From the combination of these techniques, Hebert *et al* concluded that the transition at 5.2 GPa was to the same phase IV as that observed at low temperature by Fabre *et al* [Fabre 82]. On further compression Hebert *et al* noted that the ν_1 and ν_3 bands changed their behaviour, a phenomena which was time dependent. The change in Raman spectra was interpreted to be a phase transition to a new phase, denoted phase VII. Hebert *et al*'s results are summarised in the phase diagram in Figure 4.2.

As previously described in Section 2.5, methane solidifies at 1.3 GPa to the face centred cubic (fcc) phase I. In this phase each individual molecule is completely rotationally disordered, and can be treated as spheres. The fcc structure of methane

phase I is analogous to solids formed by the rare gases, neon, argon, etc. As a result of this analogy methane's higher pressure behaviour was discussed in terms of a 'bad' rare gas model [Hebert 87, Bini 97]. This lead to an assumption that methane will adopt a hexagonal-closed packed (hcp) structure at higher pressures, which the rare gas solids were predicted to [Loubeyre 88].

Hebert *et al* [Hebert 87] were the first to discuss methane structure evolution with pressure. They took two points of view, the first as introduced above, methane as a 'bad' rare-gas, with all anisotropy in its interactions neglected. The other extreme they discussed was the methane's affinity to the ammonia molecule. Compared to methane, ammonia has one of its hydrogen atoms replaced by an electronic doublet (lone pair). Evolution of ammonia's solid phases could therefore be analogised to methane molecules with larger anisotropic interactions. Despite the differences in the two analogies, both suggest structural transitions in methane will be to a hexagonally close packed (hcp) structure. However, Hebert *et al* state that the transition from the spherically disordered state, to a different structural phase would be induced by anisotropy . This is evident from free-energy calculations that state that pure pair potentials would never undergo a fcc to hcp transition [Loubeyre 88]. At the time, ammonia was thought to undergo a fcc-hcp transition at 3.5 GPa. This transition pressure, lower than the 5.2 GPa of the I to IV transition in methane, was consistent with the greater anisotropy inherent in the ammonia system.

Hebert *et al* coupled their discussion that methane would adopt an hcp structure on transformation from phase I with evidence from their experimental studies [Hebert 87]. The similarities in the ν_1 mode between phase I and phase IV, with no discontinuity over the transition, indicated that the crystal field of both structures would be similar. With Brilliouin scattering they observed the I-IV transition to be first order. In addition they only observed one Raman line for each mode in phase IV, as also seen in phase I, furthering assumption of the subtle fcc-hcp transition. Hence, Hebert *et al* conclude that phase IV would take up a hcp plastic (disordered) structure.

As already discussed in Section 2.4, the structural progression of ammonia with pressure was later shown to be more complex than a fcc-hcp transition [Loveday 96]. It would have been expected that this finding for ammonia would have motivated research on methane. As shown above, all assumptions of structural transitions in methane had at this point stemmed from an analogy to ammonia's behaviour.

It was stated by Bini *et al* [Bini 95] that there was no experimental evidence that related the low temperature and room temperature parts of the methane phase diagram. Subsequently the room temperature phases IV and VII, that were investigated by [Hebert 87], were renamed to be phases A and B. Bini *et al* [Bini 95] used infra-red spectroscopic techniques alongside Raman to probe the structures of A and B, and to

characterise the transition between them. They confirmed Hebert *et al*'s [Hebert 87] findings that phase A showed strong similarities in Raman spectra to phases III, IV and V at low temperatures, but disputed previous claim that it would form a hcp plastic crystal. Bini *et al* observed a split in the ν_1 band frequency, which excluded the previous hcp structural model. They tentatively proposed that the structure of phase A would be centrosymmetric, based on the specific assignment of ν_1. They additionally mapped phase A to phase V at low temperature, as well as B to VI. This was based on a similar 'sluggish' transition between V and VI, and A and B.

In a later study Bini *et al* [Bini 97] monitored the ν_1 mode to investigate the coupling between the room temperature and low temperature phase diagram. Again they used infra-red spectroscopy, but this time with a diamond anvil cell attached to cryogenic equipment. This allowed them to probe the methane phase diagram between 1 to 30 GPa and from 20 to 300 K. The study confirmed their earlier assertion that phases A and B were distinct from their low temperature counterparts, showing discontinuities in the ν_1 on cooling. They also discovered a new phase of methane, named 'hexagonal phase' (HP). Bini *et al* proposed that this was the final ordered state of methane. The results of their study are summarised in Figure 4.3. Bini *et al* also suggested, contrary to previous work, that phase A would adopt a tetragonal symmetry similar to that of phase III.

In the later paper, Bini *et al* [Bini 97], described an overall picture of the known structural evolution of methane. They summarised that methane's crystal structure evolves from fcc (phases I and II) to a hcp closed packed single site structure (phase HP). Methane achieves this through intermediate multisite tetragonal (phases III, IV and possibly A) and hexagonal (phases V, VI and B) modifications. Despite this comprehensive body of work, they advised that structural knowledge would not be complete until diffraction studies were undertaken.

To date there has been only one diffraction study on phase A, an x-ray powder-diffraction study in a diamond anvil cell by Nakahata *et al* [Nakahata 99]. Instead of a tetragonal or hcp structure, they reported that phase A has a rhombohedral unit cell with $a = 8.643(1)$ Å and $\alpha = 89.40(2)°$. Nakahata *et al* had insufficient data to assign a space group. They noted that there were strong similarities between this unit cell and the high-pressure phases of CCl_4 and CF_4 [Koga 75, Fitch 93]. Nakahata *et al* briefly describe a possible transformation process between phases I and A. They point out that in the hexagonal setting of the rhombohedral indexing the c-axis is 15.126 Å. This is close to three times the lattice constant observed in phase I ($a \sim$5.2 Å). It was then expected that the [111] direction of the rhombohedral lattice to coincide with the [001] direction of the fcc lattice in phase I. However, Nakahata *et al* observe that phase A could not be reached by a distortion of the fcc lattice. This is because the

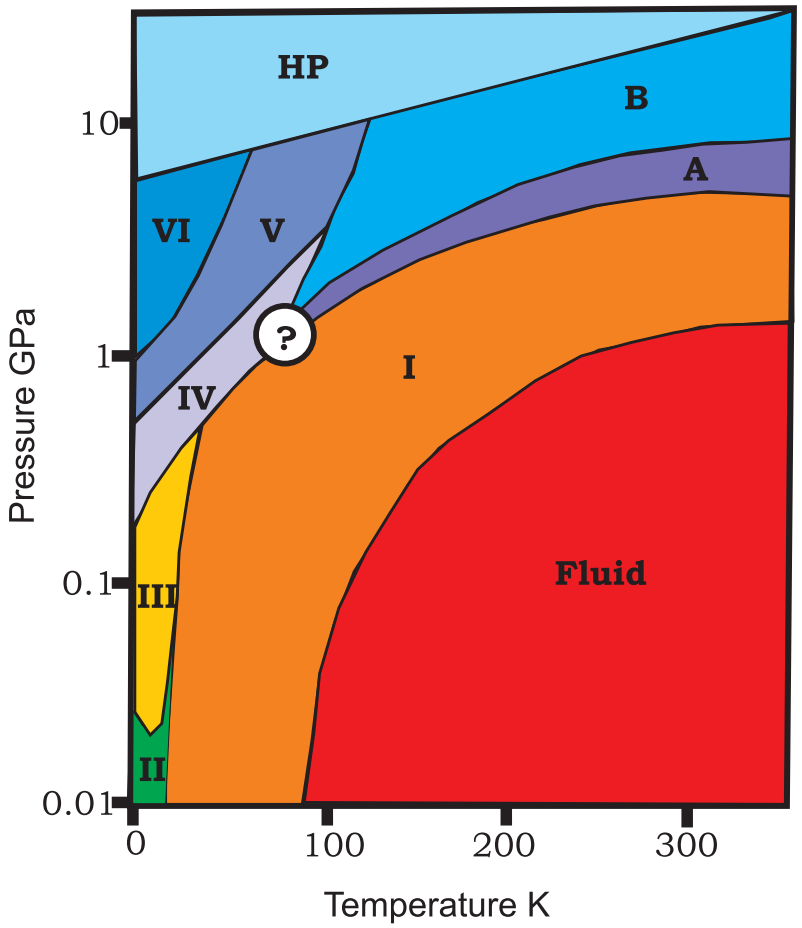

Figure 4.3: Current phase diagram of methane after [Bini 97]. The area marked with the question mark indicates where the boundaries have not yet been determined and are the source of debate. The phases coloured in blue colours are those within unknown structures. Of note is the fact that beyond 1 GPa and above room temperature the melting line of methane is unknown.

symmetry about the [111] axis in the rhombohedral space group will be different to that found about the [001] within the cubic fcc lattice. From this, they conclude that the phase I to phase A transition involves a significant re-arrangement of the molecules. They estimated that the unit cell of this phase would contain 21 molecules, based on similarities with the CCl_4 and CF_4 systems and volume constraints. Nakahata *et al* point to five possible space groups ($R3, R\bar{3}, R32, R3m$ and $R\bar{3}m$) on the basis that these space groups can accommodate 21 molecules within the unit cell.

This was the first evidence that methane does not adhere to the expected structural progression of fcc to hcp. As outlined in Chapter 2, knowledge of this kind is key to our detailed understanding of outer solar system planetary systems. Experiment verification is needed to determine the symmetry, molecular content and positions of molecules within the phase A structure. It is the scope of this chapter to provide this by charting how understanding of phase A and the structural evolution of methane with pressure has progressed as a result of these studies.

4.2 Powder diffraction study

The first stage in determining the structure of methane phase A was to confirm the indexing of Nakahata *et al* [Nakahata 99] and that this unit cell does contain 21 molecules. A further aim was to determine a space group for the structure. The assignment of a rhombohedral unit cell by this group was contrary to all expectations of the symmetry of phase A and the high-pressure evolution of methane structures. Their powder patterns, Figure 4.4, were obtained on beamline BL10XU at the SPring-8 synchrotron, Japan at a wavelength of 0.4373 Å with a very similar set up to that described in Section 3.4.2.

A key point for this study is the observation by a number of authors [Hazen 80, Bini 97, Fabre 82] that methane samples have a tendency to form bad single crystals or textured powders upon compression. During their study on phase I, Hazen *et al* [Hazen 80] noted that on each pressure increase the methane sample grew into a new crystal with a different orientation. However, their study was halted on the transformation at 5.2 GPa (to phase A) as the single-crystal became a textured polycrystalline sample.

In Figure 4.4 the indexing of phase A is clearly shown, and the persistence of the structure between 7.0 and 12.9 GPa is illustrated. Unfortunately Nakahata *et al* do not discuss the quality of the powder sample, and as such the relative intensities of the reflections cannot be relied on. This also could affect the indexing if reflections are not observed because of the texture in the powder. To confirm Nakahata *et al*'s indexing an archive experimental pattern was used. The pattern, Figure 4.5, was collected in

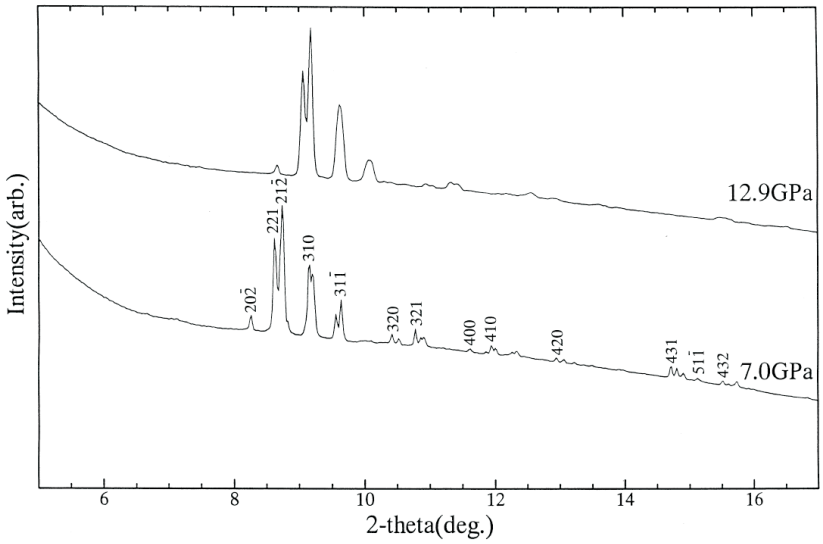

Figure 4.4: The powder profiles used by Nakahata *et al* [Nakahata 99] to index phase A.

1996 at ID09a, ESRF at a wavelength of 0.4664 Å, by an experimental team led by J.S. Loveday (CSEC, University of Edinburgh). To obtain a good powder, the sample was pressurised to 30 GPa and on decompression formed a good powder. Unfortunately, access to the raw image of this pattern is not available for inclusion in this thesis. An image from the original lab book was sufficient for the author to be convinced of the quality of the sample. The pattern to be analysed was collected at a pressure of 7.6(2) GPa.

The pattern was refined with the LeBail method, as described in Section 3.2.4. Two fits are shown in Figure 4.5. The first stage of LeBail refinement is to determine the correct lattice parameters. This was done by first manually fitting the lattice parameters to the pattern before allowing the program (in this case Jana2000 [Petricek 00]) it to refine it. Jana2000 does not allow rhombohedral settings to be input, so the cell was refined with a hexagonal setting to $a = 12.0731(3)$ Å and $c = 15.0262(4)$ Å. This transforms to an rhombohedral cell of $a = 8.583$ Å and $\alpha = 89.38°$.

The pattern was first fitted with the space group $P3$, shown in Figure 4.5(a). This is the lowest symmetry trigonal space group. If any peaks are not described by this then the structure would not be trigonal or a subset, rhombohedral. Tick marks below the pattern indicate where a peak could be found. The fit with the $P3$ space group

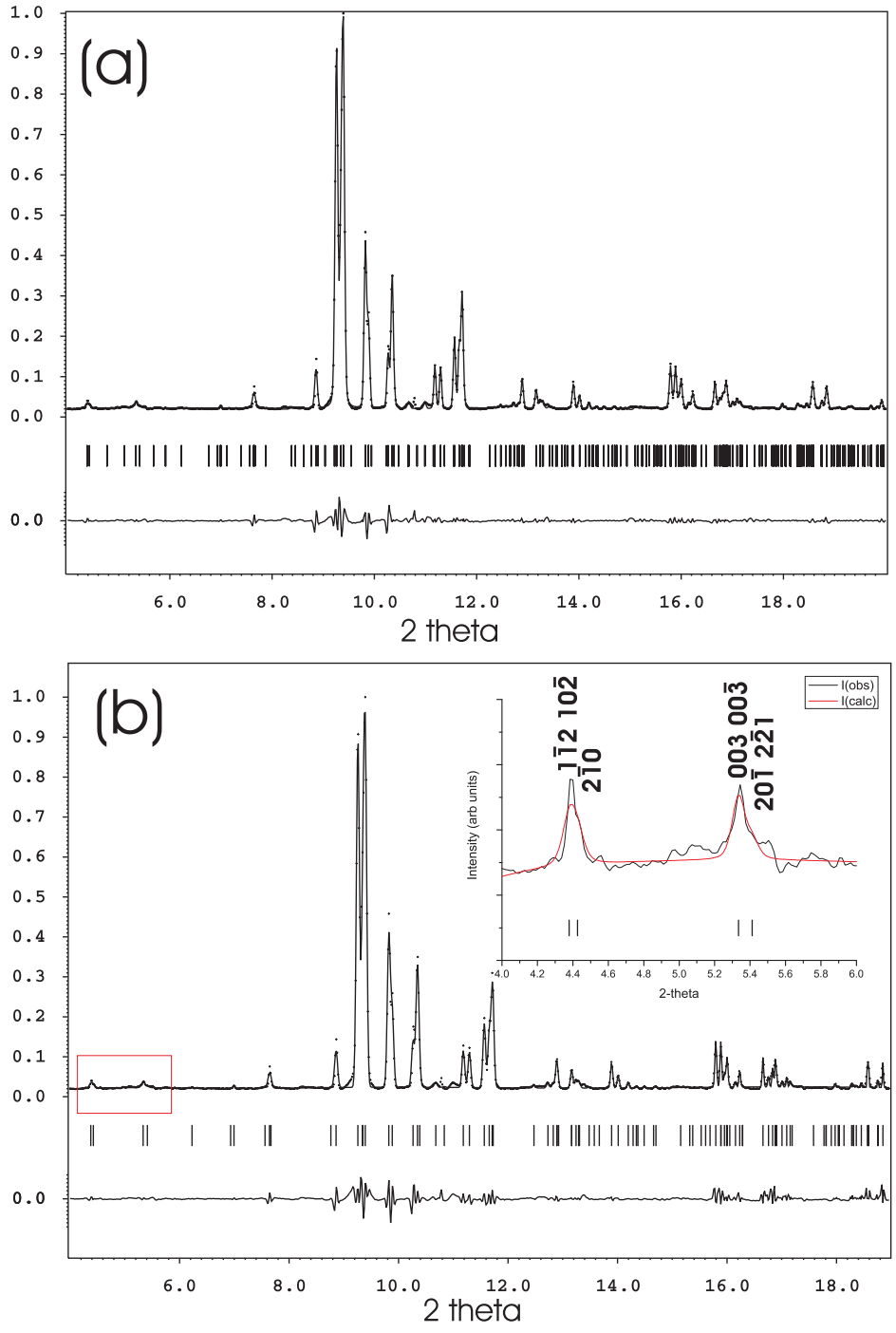

Figure 4.5: Two LeBail fits of the methane phase A data, collected at a pressure of 7.1(2) GPa, the wavelength of these data is $\lambda = 0.4664$ Å. The lines underneath the pattern are tick marks which mark the positions of symmetry generated reflections, and the line beneath this is a difference curve between the data and model. The first (a) is with $P3$ symmetry and the second (b) has been fitted with $R\bar{3}m$. Inset of (b) is a magnification of the section of the patter marked by the red box. This shows the observation of the [003] and [00$\bar{3}$] reflections that violate space groups $R3c$ and $R\bar{3}c$.

shows that all of the observed reflections are indexed to a trigonal lattice. The next stage is to confine the symmetry further, to a rhombohedral unit cell. The pattern in Figure 4.5(b) shows the experimental data fitted with the $R\bar{3}m$ space group, the highest symmetry of the five space groups postulated by Nakahata *et al.* All reflections are indexed with this symmetry.

Comparing Figures 4.4 and 4.5 shows the quality of the archive data from 1996 is better than that published by Nakahata *et al.* As a result many more peak assignments could be made and the unit cell assigned with more confidence. There are seven rhombohedral space groups, and two ($R3c$ and $R\bar{3}c$) can now be ruled out from reflection conditions. For these two space groups to conform when indexed with hexagonal axes, $[h\bar{h}l]$: $h+l = 3n$ and $l = 2n$ also $[00l]$: $l = 6n$ [Prince 04]. In the pattern in Figure 4.5(b) there is a lot of peak overlap and, for instance, the $(5\bar{1}1)$ reflection (labelled in Figure 4.5(b)) cannot be used to rule out $R3c$ or $R\bar{3}c$ as it overlaps with the $(10\bar{5})$. However, the (003) and $(00\bar{3})$ reflections, illustrated inset of Figure 4.5(b), violate the reflection conditions for $R3c$ and $R\bar{3}c$ space groups. Unfortunately, there are no reflection conditions that can tell the remaining five space groups ($R3, R\bar{3}, R32, R3m$ or $R\bar{3}m$) apart.

Attempts were made to solve the structure using the Fullprof [Rodriguez-Carvajal 93] simulated annealing function. None were successful, probably due to the complexity of this phase. This necessitated the extra information that could be obtained from single crystal diffraction.

From this powder study the indexing of phase A with a rhombohedral unit cell of $a \approx 8.6$ Å and $\alpha \approx 89.5°$ (subject to pressure) was confirmed. The symmetry was confined to the $R3, R\bar{3}, R32, R3m$ or $R\bar{3}m$ space groups. The results presented here are consistent with Nakahata *et al* conclusions, but further confined the symmetry of phase A.

4.3 Validation study on Phase I

4.3.1 Data collection

As part of the single-crystal investigation of phase A, a validation study was carried out upon phase I. As methane is a weak scatterer of x-rays this was to determine what extent of detail could be resolved by x-ray diffraction. Descriptions of the method of crystal growth and data collection on station 9.5, SRS, Daresbury are given in Sections 4.4.1 and 3.4.3. After growing, the pressure of the sample was 3.8(2) GPa, within the boundaries of phase I. The crystal was grown in a Böhler-Almax (BA) backed Merrill-Bassett diamond anvil cell and then collected at station 9.5, as explained in Section

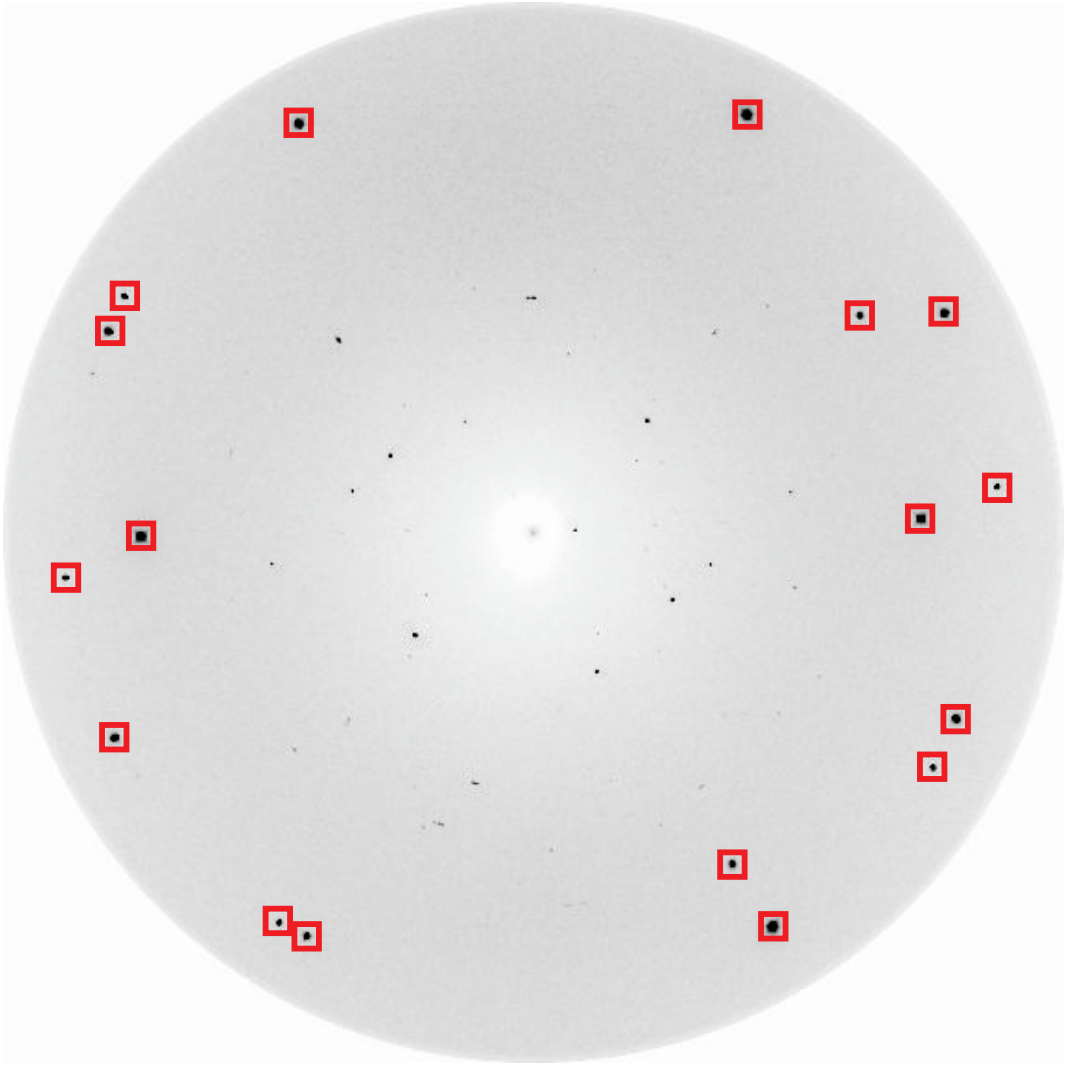

Figure 4.6: A single shot image of a methane phase I crystal collected for 3 minutes whilst being oscillated ±15°. The grey circle area is the surface area of the MAR image plate detector, the reflections marked in red boxes are from the diamonds that surround the sample. Methane reflections towards the centre. They are all point like and show no smearing characteristic of a bad quality crystal (as illustrated in Figure 3.5).

3.4.3. Before the data collection was started, the quality of the crystal was checked with a single shot image. This test shot was collected over 3 minutes whilst the cell was oscillated around ω by $\pm 15°$ and the resulting image is shown in Figure 4.6. From this image it was identified the reflections were point-like and there was no evidence of multiple crystals. Subsequently, the data were collected in 241 steps of 0.25°. The step size was chosen to adequately collect the reflections, which characteristically had a rocking curve of 0.5°, Figure 4.7(b). The data set was cut a little short by the refilling of SRS, and only 232 raw data frames were available to be reduced.

4.3.2 Results

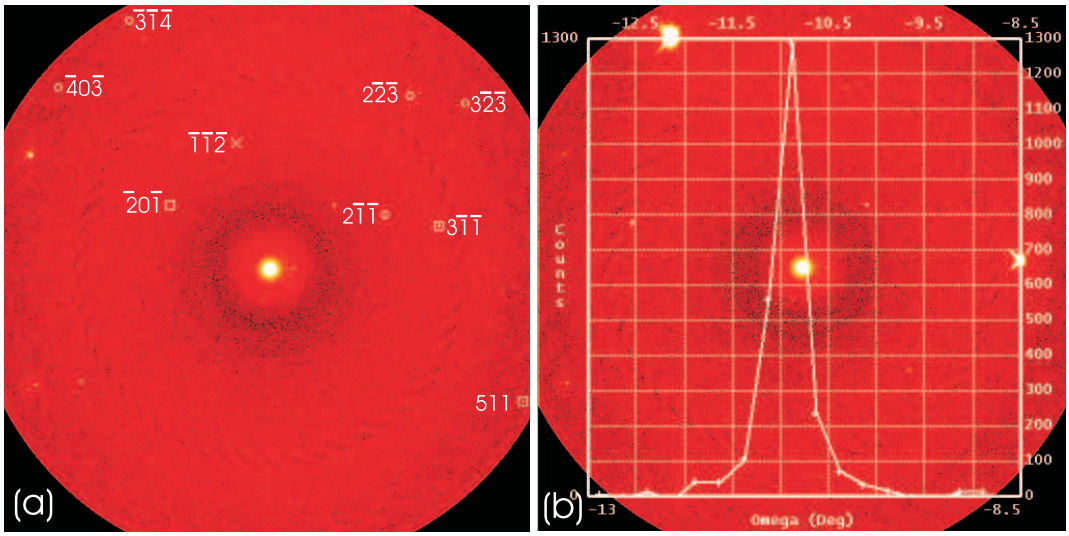

Figure 4.7: Raw image files from the phase I data collection on 9.5, SRS, Daresbury. (a) shows frame 143 of the series at ω=-5.50° and demonstrates the assignment of face centred cubic symmetry to the cubic index. The data has been indexed with a cubic unit cell with a = 5.17(1) Å and marked by the white symbols. All reflections which are observed conform to the all even or all odd *hkl*s expected in fcc symmetry. Those with a mixture of even and odd *hkl*s are not observed. The data is being displayed with the Bruker SMART software. This program designates boxes (as seen around the $[3\bar{1}\bar{1}]$ reflection) to reflections that are centred on this particular frame. Crosses mark reflections that are entering the frame and circles mark reflections which are not centred on the frame but could be visible. (b) shows the rocking curve for the $[3\bar{1}\bar{1}]$, with a FWHM of 0.5°. This demonstrates the quality of the crystal.

Figure 4.7 demonstrates the quality of the phase I crystal that was collected. The crystal was indexed to a face centred cubic cell with a = 5.17(1) Å. On integration the data gave a R_{int} value of 0.12. Data was cut off during integration at 1 Å. This was because integration statistics suggested all reflections with *d*-spacings less than 1

Å gave a σ/Iσ ratio of more than 2/3. The R_{int} value was quite poor, when compared to later data collections, but this can be attributed to the low number of reflections collected. There are only 33 integrated reflections in the collated raw data. However, application of an absorption correction using the SADABS program, lowered the R_{int} to 0.05. Subsequent data preparation and merging (R_{merge} of 0.04) resulted in a .hkl file with nine reflections detailed in Table 4.1.

h	k	l	mean I	mean σI	Hazen *et al* designation*
1	1	1	1483.22	12.29	vs
2	0	0	1076.38	28.45	s
2	2	0	207.86	12.43	ms
2	2	2	60.12	1.90	ms
3	1	1	93.96	2.24	m
3	3	1	13.58	1.39	vw
4	0	0	44.08	8.62	w
4	2	0	19.26	1.53	vw
4	2	2	8.35	1.29	NO

Table 4.1: The observed and integratable reflections from the phase I crystal, compared to the previous work of Hazen *et al* [Hazen 80]. *vs, very strong; s, strong; ms, moderately strong; m, moderate; w, weak; vw, very weak; NO, not observed.

Table 4.1 shows that the integrated results compare very favourably to the work of Hazen *et al* [Hazen 80]. This previous study represents the only single crystal study on methane at pressure published in the literature. Hazen *et al* were unable to integrate their reflections, hence the qualitative interpretation. The results of this study confirm the relative intensity assignment of Hazen *et al*, with the addition of a weak reflection not observed before. The current study was able to use these results for further refinement.

These data were refined against the structure originally determined by Press [Press 72] from ambient pressure neutron diffraction of CD_4 at 77 K. This study found the space group of phase I was found to be $Fm3m$ with the centre of the tetrahedra (carbon positions) located at $(0, 0, 0)$ resulting in four molecules within the unit cell. Press demonstrated that until the transition to phase II at 20.4 K the molecular orientation, and hence hydrogen positions, remained completely disordered.

4.3.3 Methane scattering factors

Similar to atomic scattering factors, explained in Section 3.1.1, the diffraction response of a rotating molecule can be described by a molecular scattering factor. Each scattering factor curve, like those illustrated in Figure 3.1, can be analytically described as a

exponential series, Equation 4.1 [Prince 04]. The terms a_1, a_2, a_3, a_4, b_1, b_2, b_3, b_4 and c are required for input into SHELX.

$$f(\sin\theta/\lambda) = \sum_{i=1}^{4} a_i \exp(-b_i \sin^2\theta/\lambda^2) + c \tag{4.1}$$

There have been several attempts to determine the scattering factor of a rotating methane molecule, taking different theoretical approaches. The five studies compared here are Downs and Finger [Downs 96], Buckingham *et al* [Buckingham 41], Bernal *et al* [Bernal 53] and two studies by Mills [Mills 58, Mills 61].

The only paper that quotes the scattering factor curve in terms of Equation 4.1 was that of Downs and Finger [Downs 96]. The remaining curves were fitted to Equation 4.1 with Microsoft Excel's solver routine. The parameters later used in refinement for each curve are shown in Table 4.2. In addition SHELX requires information on the anomalous scattering f' and f'', linear absorption μ, covalent radius r and the atomic weight. For hydrogen the anomalous scattering is of negligible quantity at the energy of used, so the values for carbon were inputted (although these are very small at these energies). μ was set to zero, as similarly at these x-ray wavelengths the absorption of the sample is negligible. For the covalent radius, the C-H bond distance in methane was used, 1.084 Å. The atomic weight was set to 10.000 a.m.u. These scattering factor curves are displayed in Figure 4.8 with carbon and neon for comparison, and along an axis which demonstrates their differences in Figure 4.9.

The scattering factor of a rotating, disordered, methane molecule Figure 4.9 shows that beyond 0.42 $\sin\theta/\lambda$ the scattering for all the models, is less than that of a carbon atom. The calculations suggest that carbon atom is being 'shielded' from diffraction by the disordered hydrogen atoms surrounding it. This effect is analogous to that shown in Figure 3.1(a), the contribution from the 'valence' hydrogen atoms is shown to dominate over the 'core' effect from the carbon.

4.3.4 Refinement

A number of refinements to the data were undertaken. The R-factor was charted for each step and the values are summarised in Table 4.3. The first stage was to refine a carbon only model against the data with only the scale factor refined. Second was to refine the isotropic thermal parameter, U_{iso}. This lowered the R-factor significantly, but the value of U_{iso} increase to 0.1316. This 'blowing up' of the thermal parameter was the model trying to account for the absence of electron density contribution of the disordered hydrogen.

Next the SFAC commands in the SHLEX input file were altered. Instead of reading

Curve	χ^2	a_1	a_2	a_3	a_4	b_1	b_2	b_3	b_4	c
Downs and Finger (1996)	n/a	1.544	-0.514	6.181	2.574	0.581	3.995	13.797	36.111	0.215
Buckingham *et al* (1994)	0.062	-0.541	1.009	2.027	7.890	13.765	5.035	0.246	34.540	-0.494
Bernal *et al* (1953)	0.004	1.625	-0.665	3.834	4.979	0.612	5.960	16.437	39.750	0.213
Mills (1958)	0.032	-0.606	0.871	1.613	8.075	12.157	4.705	0.386	29.934	-0.015
Mills (1961)	0.032	-0.732	0.813	1.578	8.232	12.216	4.554	0.421	29.685	0.045

Table 4.2: The values obtained by fitting Equation 4.1, all fitted with Microsoft Excel's solver routine with the exception of Downs and Finger [Downs 96] who quoted the values within their paper. The χ^2 fit of the parameters to the curve is also quoted, to indicate that all fitted well.

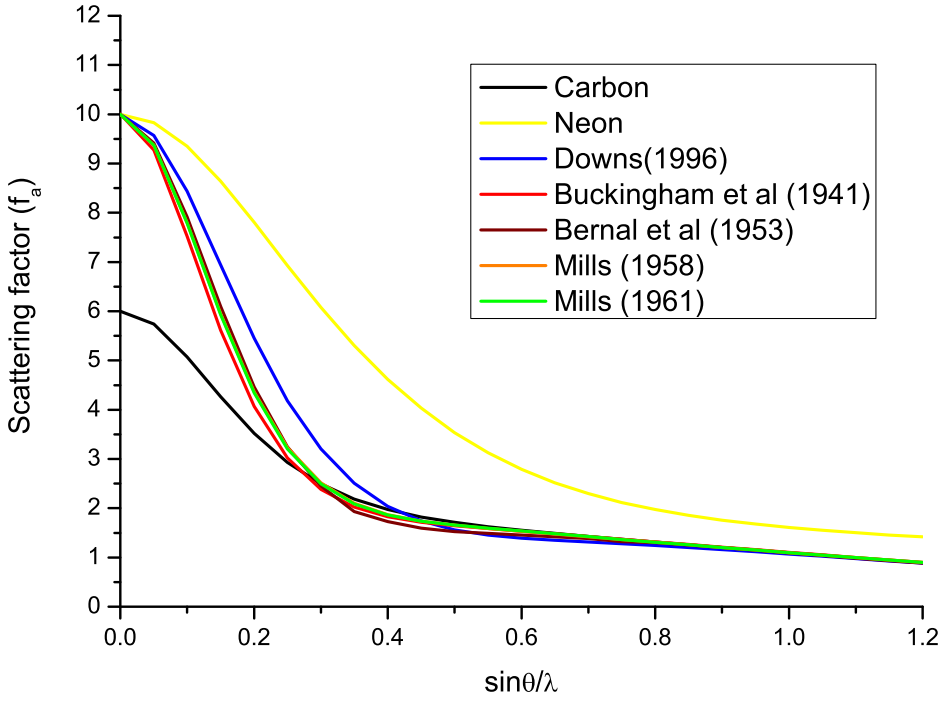

Figure 4.8: Comparisons of the five different scattering factor curves for methane discussed in this section compared with neon and carbon (values taken from [Prince 04]).

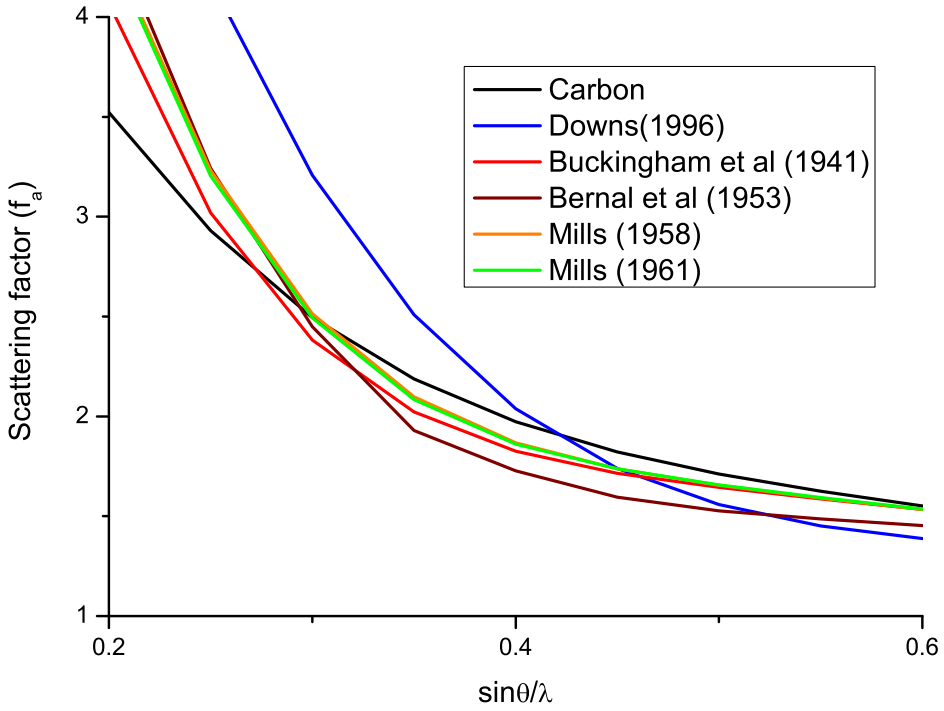

Figure 4.9: A close up of the five different scattering factor curves discussed in this section, compared to carbon (value taken from [Prince 04]. This illustrates the large differences calculated even at ambient pressure.

values for carbon and hydrogen, the values from Table 4.2 were used for each scattering factor model. During these refinements, the U*iso* was allowed to refine which now would reflect the methane molecule as a whole.

The last stage was to input hydrogen directly into the refinement, to serve as a comparison to the molecule scattering factors. A hydrogen atom was positioned the general position $(x, 0, 0)$ at a distance of 0.8 Å, $x = 0.1545$. This generated six hydrogen positions surrounding each carbon, but the site occupancy factor (s.o.f.) was reduced to two thirds to effectively model the correct number of hydrogen per carbon. For this refinement the U_{iso} was fixed on the carbon and hydrogen to the default value of 0.025 as well as fixing, x, the position. This had the effect of reducing the R-factor relative to the first stage (carbons only input) of refinement, as it accounted for some of the electron density surrounding the carbon. The next stage refined the U_{iso} on both the carbon and hydrogen. This lead to a dramatic fall in the R-factor to 2.3 %, giving values of 0.088 and 0.102 for the U_{iso} for carbon and hydrogen respectively. The results of this stage refinement procedure are summarised in Table 4.3.

The last refinement was a surprising result, that the $(x, 0, 0)$ model of hydrogen disorder would give a lower R-factor to that of the theoretically determined scattering factors. Because of the low number of observations, the changes in R-factor must be statistically examined to determine whether or not the change is meaningful. For this a Hamilton R-factor test was used [Hamilton 65]. This test uses F ratios tabulated in volume C of the International Tables of crystallography [Prince 04]. The F_{read} value from the international tables is compared to a F_{calc} value which is obtained with Equation 4.2. Here R_{c} is the R-factor of the constrained model, R_{u} is the R-factor of the unconstrained model. ν_1 is calculated by subtracting the number of parameters in the constrained model, q, from the number of parameters in the unconstrained model, p. ν_2 is the number of observations, n, subtracted by p, the number of parameters in the unconstrained model. For this test, the best fitting SFAC of Mills (1961) was used which gave the smallest R-factor of all the scattering factor models, 0.058, to compare the hydrogen $(x, 0, 0)$ model of 0.023.

$$F_{\text{calc}} = (\nu_2/\nu_1)[(R_{\text{c}}/R_{\text{u}})^2 - 1] \tag{4.2}$$

Table 4.4 displays the results from the Hamilton R-factor test applied to the R-factor drop between the methane SFAC models, and one with hydrogen in a $(x, 0, 0)$ model. In each case $n = 9$, as displayed in Table 4.1. If the F_{read} is less than the F_{calc} value then the drop in R-factor is a meaningful result. As shown in Table 4.4, $F_{\text{read}} < F_{\text{calc}}$ and so drop in R-factor between the two models is real and not an artefact of the greater amount of freedom in the unconstrained model.

Parameters	Refined	Carbon U_{iso} (Å^2)	Methane U_{iso} (Å^2)	Hydrogen U_{iso} (Å^2)	Hydrogen s.o.f.	R factor
1	Carbons input	0.025	n/a	n/a	n/a	0.395
2	Carbon U_{iso}	0.13(1)	n/a	n/a	n/a	0.072
2	Downs and Finger SFAC	n/a	0.091(9)	n/a	n/a	0.064
2	Buckingham *et al* SFAC	n/a	0.103(6)	n/a	n/a	0.064
2	Bernal *et al* SFAC	n/a	0.059(8)	n/a	n/a	0.059
2	Mills (1958) SFAC	n/a	0.097(6)	n/a	n/a	0.058
2	Mills (1961) SFAC	n/a	0.097(6)	n/a	n/a	0.058
1	Carbon and hydrogen input	0.025	n/a	0.025	0.0833	0.259
3	Carbon and Hydrogen U_{iso}	0.088(3)	n/a	0.10(2)	0.0833	0.023

Table 4.3: Charting the refinement as each stage is progressed. The thermal parameters at each stage are noted and where applicable the occupancy factor, s.o.f., is noted for hydrogen as well. Where a value is coloured red, this indicates that it was fixed during refinement.

R_c	R_u	q	p	ν_1	ν_2	F_{read}	F_{calc}
0.058	0.023	2	3	1	6	4.20	13.397

Table 4.4: The Hamilton R-factor test applied to the drop from modelling the methane molecule with the scattering factor of Mills (1961)(R_c) to modelling this with hydrogen at a $(x, 0, 0)$ orientation, (R_u).

4.3.5 Conclusion to the section

The purpose of this study was to show that meaningful results can obtained from limited data on methane. Despite the low scattering of methane by x-rays, a model with hydrogen in a $(x, 0, 0)$ orientation has been refined to a R-factor of 0.023. The difference between a carbon only model with a 'blown up' thermal parameter (U_{iso}) and one with carbon and hydrogen refined can be distinguished, with the latter model being a significant improvement. The fact that the calculated scattering factors of a disordered methane molecule, presented in Figure 4.8, do not improve the fit relative the the $x, 0, 0$ model of hydrogen about the carbon is surprising. If it is considered that these scattering factors were determined for methane under ambient conditions, perhaps the result is less surprising. It is evident from the results presented here that these scattering factors are not appropriate to describe the scattering of the disordered methane molecule under pressure.

As already indicated by Nakahata's study [Nakahata 99] the unit cell of phase A is rhombohedral, with 21 molecules. This departure from the expected hexagonal closed packed structure or tetragonal already suggests that phase A is more complex than analogous structures in ammonia. Hence, the realisation of fine detail in the structure, such as disorder within the hydrogen, is key to understanding methane structures.

4.4 Single crystal x-ray study

Given the limited amount of information that could be obtained from the powder data, it became clear that additional information from single-crystal data was needed to solve the structure of phase A. The validation study on phase I, Section 4.3, showed that, despite the low scattering of methane and the small sample sizes inherent for high-pressure diffraction, valid experiments on methane could be conducted. The study on phase A was aided by the significant advancements in high-pressure single crystal techniques that occurred during this thesis. One of these was the use of Böhler-Almax seats in the Merrill-Bassett diamond anvil cell, as explained in Section 3.3.1. This was in addition to the development of single crystal data collection on specialist high-pressure

diffraction beamlines at synchrotron sources, discussed in Section 3.4.3.

4.4.1 Sample preparation

All crystals were grown in Merrill-Bassett type diamond anvil cells (MB-cell) described in Chapter 3. Initially it was hoped to take advantage of methane's tendency to form larger crystallites, and to simply anneal the crystals with an oven. Methane and a ruby pressure calibrant were loaded into MB-cell with the cryogenic loading method described in Section 3.5.1. After this the pressure of the cell was put to 8 GPa (monitored with the ruby fluorescence technique [Mao 78]) and placed into the oven. For the first run the temperature was simply ramped to 570 K and then switched off. At this point in the study only beryllium-backed MB-cells were being used, which limited the maximum temperature that the cell could be heated to 570 K. After cooling the cell's pressure was checked, and had always lost 3-4 GPa. On subsequent heating the pressure loss was much less. This is a consistent observation for MB-cells upon heating. Hence, it became necessary to 'pre-heat' the MB-cells for them to maintain pressure. After pre-heating, the cell was put back to 8 GPa before heating again. During this, second heating, the temperature would be put to 570 K, and the stepped back very slowly to ambient temperature ($\sim$5 K/hour). It was hoped that the slow cooling would anneal the sample into a single crystal. This method was only partially successful. After heating each sample was checked with the in-house SMART diffractometer. If it had grown to a crystal, of sufficient quality, it could then be taken to a synchrotron for data collection.

Using the method described above only two crystals of good quality were produced, and so another strategy for crystal growth was undertaken. The original crystals were still used for preliminary studies, these results are described in the subsequent Section 4.4.2. One of the conclusions of the preliminary studies was that Böhler-Almax (BA) backing disks were needed, instead the beryllium-backed ones. These BA backing disks have two main advantages for this study. First the absence of background diffraction from beryllium would greatly improve the quality of the integration of the reflections. Secondly, because these cells now did not contain the toxic beryllium, they could be heated to 670 K more readily accessing the melting line of methane.

It was decided to apply a method of *in situ* crystal growth used before on high-pressure ice crystals. This method had been outlined in Section 3.5.3. There were concerns as to the possible effectiveness of growing crystals in this fashion, because of the lack of knowledge on the melting curve. The current phase diagram of methane, Figure 4.3, is truncated at 300 K where experimental studies on the melting curve cease. Hence the melting curve of methane was only charted to 1.3 GPa where it intersect

room temperature. The assumption at the time was that the methane melting curve would be, by 5 GPa, beyond that accessible by resistance heating a MB cell (i.e. above 670 K). Despite this it was reasoned that there was no reason why, if the method can be applied to ice crystals, it could not for methane.

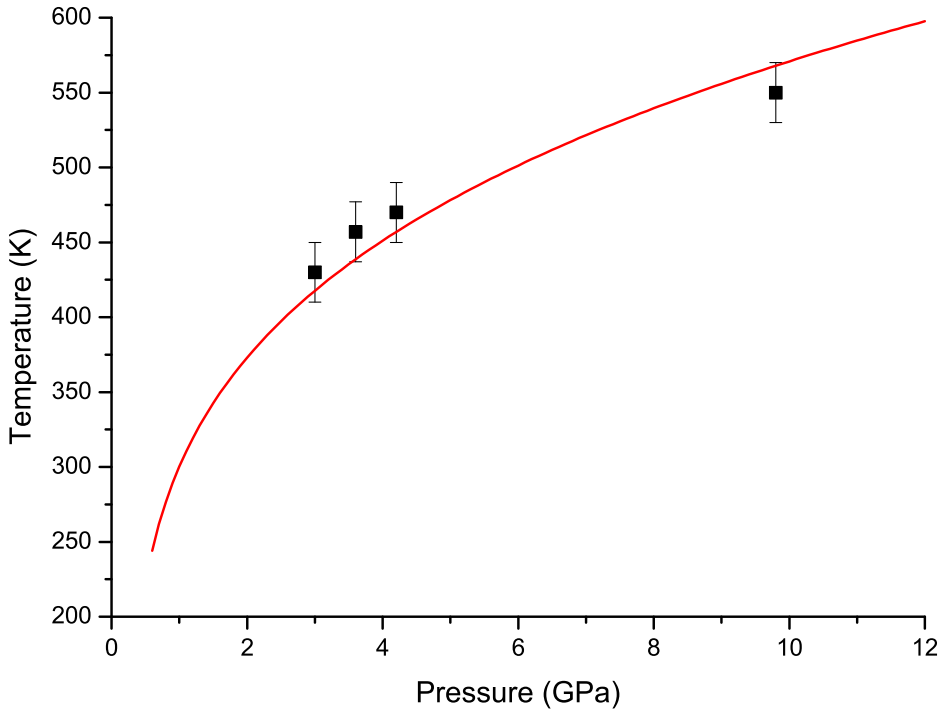

Figure 4.10: A guide melting curve for methane, constructed during attempts of growing single crystals. For all points melting was visually observed, with the sample behaving as shown in Figure 4.11. The curve has been fitted with a Simon-Glatzel [Simon 29] equation where $T = T_o[1 + (P - P_o)/a]^{1/c}$. $T_o = 300$K and $P_o = 1.2$ GPa. The parameters a and c were fitted with Microsoft Excel's solver routine to be $a = 0.697$ GPa and $c = 4.092$.

The method of crystal growth described in Section 3.5.3 was remarkably successful, but had to be revised for the methane system. The standard procedure for methane samples, when growing single crystals of phase A, was first to raise the pressure of the MB cell to between 8 and 10 GPa. Then, similarly to the previously described method, the cell would need to be 'pre heated' before growing could proceed to prevent significant pressure loss. But even during these 'pre heating' runs the cell was monitored visually, as it enabled a rough mapping of the melt line. The points of melting observed during this study, and an approximate melting curve, have been drawn in Figure 4.10.

Observation of melting was very clear, as shown in Figure 4.11.

Once the MB cell had been 'pre-heated' it was then raised back to an appropriate pressure for crystal growth. To grow phase A the pressure of the cells was increased to 7 GPa and then heated at a rate of 10 K/minute until close to the melting temperature. Once the pre-cursors of melting were observed, Figure 4.11(a), the heating rate was decreased, to allow for better control of the samples temperature.

The behaviour of methane samples upon melting was very different to that seen in ice. In contrast to Figure 3.31(c) obtaining methane in a state of discrete solid and liquid within the gasket proved very challenging. Instead, an annealing temperature had to be maintained and the growth of one crystallite over the others had to be encouraged. This was achieved by introducing a temperature 'sink', such as a cold Allen key, at one point on the cell. This would induce a slight temperature gradient within the gasket. This encouraged crystal growth, as shown in Figure 4.11. It was rare to obtain a crystallite that completely filled the gasket, so after each crystal growth a sketch was made of the crystal boundaries. A sketch was necessary because as the temperature was decreased the contrast of the crystal boundaries would disappear, in line with similar observations in ice.

After cooling all the crystals were checked on the in-house SMART diffractometer to assess their quality. Disappointingly this method of crystal growth on the melt line did not yield the quality of crystal hoped for. Despite visual observations to the contrary, diffraction revealed multiple large crystallites within the sample chamber. A number of crystals were sent to synchrotron sources for collection, but the quality of these were still inadequate for the anticipated study. The reason for this degradation in crystal quality was discovered from visual observation during heating at a moderate rate (5 K/minute). With the cell at 7 GPa, at $\sim$370 K a steady crystal growth that took over the whole gasket was seen. In contrast to the melting observation, Figure 4.11, this transformation was subtler, Figure 4.12. The crystal facets growing were much sharper than those grown at the melt. The transition shown in Figure 4.12 was interpreted to be a result of a solid to solid phase transition taking place in methane. The resultant phase is discussed further in Chapter 6. It was clear that this solid-solid phase transition at $\sim$370 K was responsible for breaking the crystal grown at the melt line.

A method of growing crystals at this solid-solid phase boundary was devised. Introducing a small temperature contrast with a cold Allen key, was very effective. The whole crystal growing process was a lot slower as it occurred at a much lower temperature than the melting growing. As a result the growth could be controlled more accurately, but did require more patience of the experimenter.

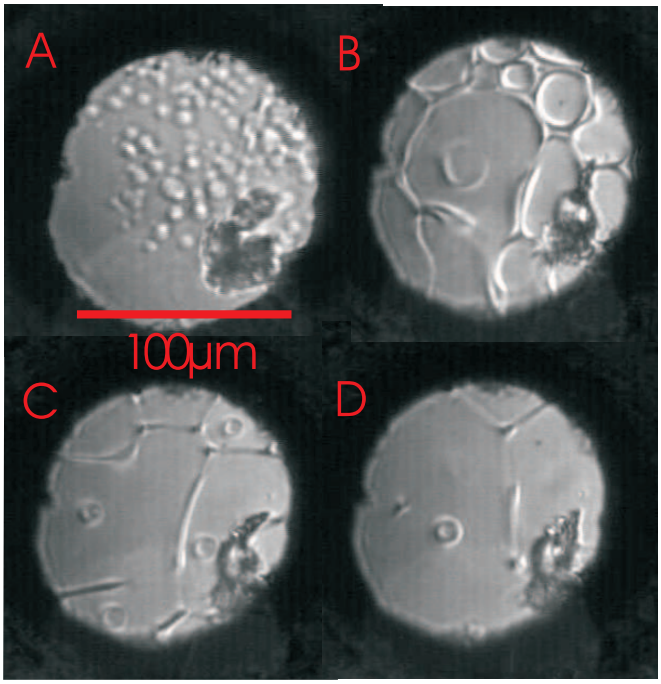

Figure 4.11: Illustrations of growing methane crystals at the melting line. In all these images the sample was at 10 GPa. A, as the sample approaches the melting temperature (∼650 K) textures develop until in, B, where individual crystallites can be made out. The temperature is controlled and cycled to favour the growth of a few crystallites, C and D. The focusing of the beam at stations 9.5 and ID09a is such that individual crystallites can be picked to obtain good single crystal data.

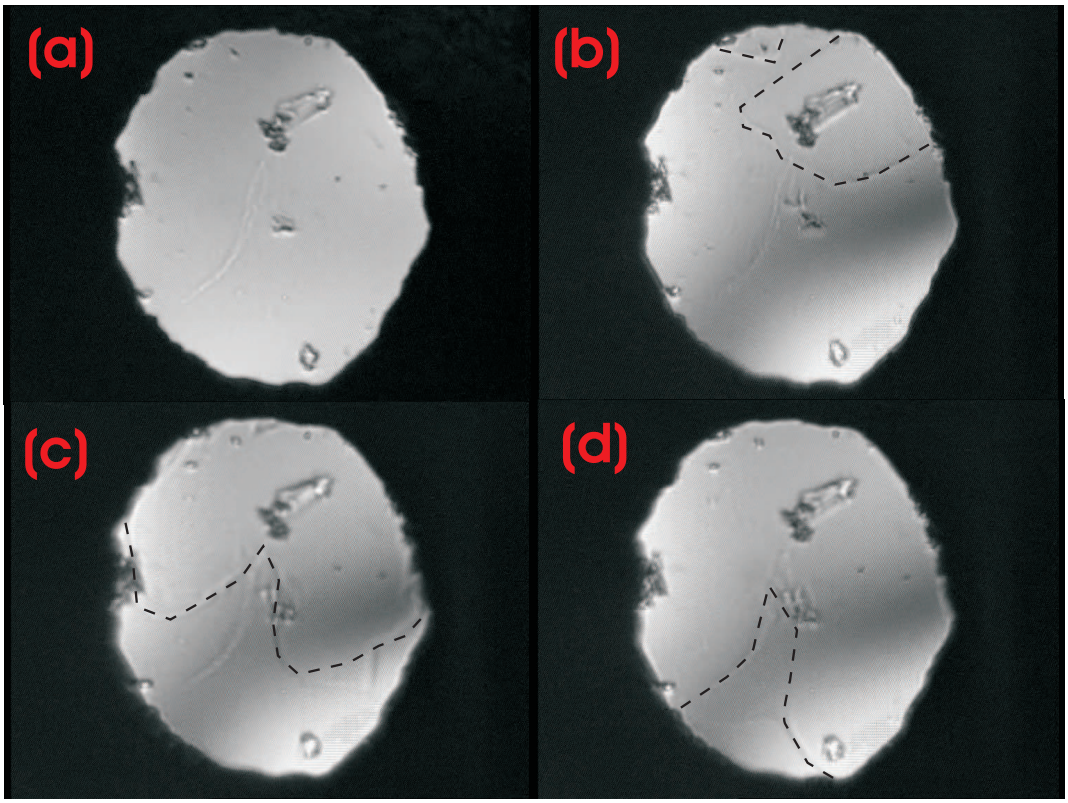

Figure 4.12: The progress of crystal growing at a solid-solid transition in methane. In all images the sample is at 9.3(2) GPa. (a) is at highest temperature, 410 K as the crystal is grown by slow cooling. A thermal sink is created on one side of the cell, to help create a seed crystal. In (b) at 400 K the seed crystal is growing from the top of the gasket and (c) and (d) charts the crystal's progress in growing.

4.4.2 Preliminary data collection

Preliminary data were collected at station 9.8, SRS, Daresbury on a set up described in Section 3.4.3. Data were collected from a single crystal grown with the first method described above. The collection strategy for a Merrill-Bassett diamond anvil cell is detailed in Table 4.5, based on that developed for the in-house SMART diffractometer. The cell is stepped in a negative direction in ω, with the user choosing the collection time for each frame and the ω step size for each frame. Once a particular scan is complete, the diffractometer is programmed to drive to a new start position in ω and ϕ to begin the next set of collections. The collection strategy outline in Table 4.5 ensures that the x-rays always have access to the sample and are not obscured by the steel cell body. The distance from the detector to the sample is at all times set to 70 mm, to prevent a collision between the cell and the detector.

Set	$2\theta(^\circ)$	$\omega(^\circ)$	$\phi(^\circ)$	Sweep$(^\circ)$
1	-28.00	-10.00	0.00	30.00
2	28.00	40.00	0.00	50.00
3	-28.00	-10.00	180.00	30.00
4	28.00	40.00	180.00	50.00
5	-28.00	-170.00	0.00	50.00
6	28.00	-140.00	0.00	30.00
7	-28.00	-170.00	180.00	50.00
8	28.00	-140.00	180.00	30.00
9	-40.00	-170.00	0.00	20.00
10	-40.00	-200.00	180.00	20.00
11	0.00	12.00	0.00	32.00
12	0.00	-160.00	0.00	32.00

Table 4.5: Data collection strategy for a Merrill-Bassett diamond anvil cell used on the SMART diffractometer set up at station 9.8. SRS, Daresbury and in-house. This ensures that at any point in the collection x-rays have access to the sample and are not obscured by the steel cell body. The 2θ, ω and ϕ columns give the starting position of the cell for each collection. The sweep column charts how much in ω the cell is rotated during collection.

The first crystal was collected at a wavelength of 0.6911 Å with 1 s frame exposure time, 0.2° frame steps and 4 mm of attenuation in the beam to prevent the reflections from saturating. The pressure of this sample was 7.5 GPa. On initial inspection the data were satisfactory, with the area detectors collecting many discrete single crystal reflections. However, there were a limited number of reflections beyond 1.8 Å. After the data collection reflections were individually picked from sets 1, 3, 11 and 12, the sample was indexed to a rhombohedral unit cell with $a = 8.60(9)$ Å and $\alpha = 89.1(7)^\circ$.

On closer inspection many of the reflections were smeared, and there was no consistent peak shape. There were also a number of reflections that were not described by the stated unit cell. This data collection had shown that it was possible to obtain single crystal diffraction from methane phase A. At this point there was a confidence that the crystal quality could be improved, so there was no attempt to integrate these data.

The second sample, also grown with the first 'oven' method. This sample was collected over four runs, detailed in Table 4.6. The multiple runs were designed to be able to extract the maximum information from the sample. Attenuation of the beam was varied by placing a piece of aluminium of stated thickness in front of the sample. The more strongly attenuated data set, with 1 mm of aluminium, contained no saturated reflections. To provide information on the weaker reflections the aluminium was removed, allowing some of the stronger reflections to saturate. The step size was varied to provide a balance between more detailed information on the peak shape and the time for collection.

Collection	Exposure time (s)	ω step size (°)	Thickness of Al (mm)
1	1	0.30	0.25
2	1	0.20	1.00
3	1	0.20	0.00
4	1	0.15	1.00

Table 4.6: The four collections carried out on the methane phase A, all collected with a wavelength of 0.6911 Å.

Figure 4.13(a) is a characteristic data frame from the second collection run, frame 103, $\omega = -30.4°$ of set 1 (see Table 4.5). It can be seen that even in this run, with the maximum amount of beam attenuation the background is still very high. Contributions can be identified to be from the beryllium backing disk and the rhenium gasket where the counts exceed even the strongest methane reflection. The sample was at a pressure of 7.7 GPa and indexed to a rhombohedral unit cell with $a = 8.56(2)$ Å and $\alpha = 89.5(6)°$. Because of the high counts from the beryllium and rhenium scattering integration in these areas would prove impossible as they would contribute to non-observed reflections and alter the shape of the observed ones. These data were integrated, but restricted to a minimum d-spacing of 2.20 Å. This is within the first diffraction peak of beryllium (2.10 Å/19° 2θ) and rhenium (1.66 Å/23.4° 2θ) and ensured that all the peaks integrated were background free. Restricting the integration in this way heavily reduces the number of reflections that can be extracted.

The integration of run 2 (all sets) yielded 161 reflections, with an R_{int} of 0.09. Analysis with the XPREP software agreed with the group of space groups

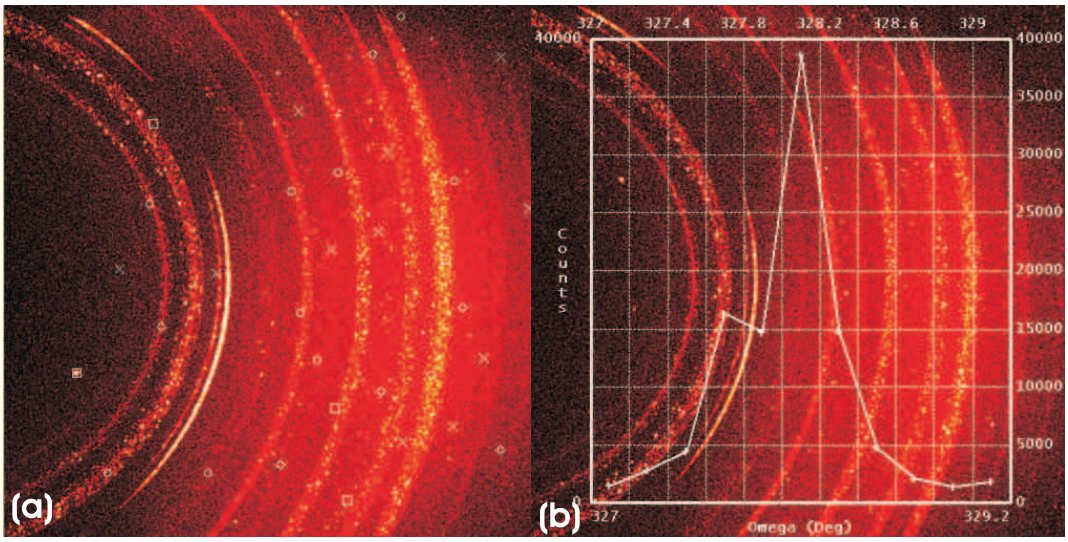

Figure 4.13: (a) An example of data obtained from preliminary studies at station 9.8, Daresbury, frame 103, $\omega = -30.4°$ of set 1. This shows the level of background that is present even in the highly attenuated data set. The inability to focus the beam size means that on top of scattering from the beryllium backing disk, the rhenium gasket is also contributing to the background. (b) shows the rocking curve from the $[2\bar{4}\bar{3}]$ reflection, characteristic to the peak shape from reflections from this crystal. The shoulder that can be seen on the left side of the reflection suggests the crystal is not of good quality as it may be slightly split, either as a twin or into two crystallites.

previously suggested, ($R3, R\bar{3}, R32, R3m$ and $R\bar{3}m$) [Nakahata 99]. In addition from the distribution of reflection intensities XPREP indicated that $R3$ and $R\bar{3}$ ($\bar{3}$ Laue class) space groups were a more favourable fit to these data . Attempts were made to to solve the structure with these data through direct methods. Cutting the integration to 2.20 Å meant that some of the strongest reflection were cut off. For visualisation of this effect, it would be similar to cutting the reflection profile in Figure 4.5 at 11.5°2θ. As outlined in Section 3.1.4, direct methods works by phasing a subset of reflections. For this the programs pick the strongest reflections as these are deemed the most well determined. Omitting the strongest reflections will make the results of direct methods unreliable or nonsense. Because of the restricted d-spacing integration direct methods did not return a viable structure for phase A.

From the preliminary studies, the symmetry of phase A had been confined to $R3$ or $R\bar{3}$ space groups. To further the structural realisation of this phase, data of a much better quality of data would have to be collected. In addition, the ability to integrate reflections at d-spacings lower than 2.10 Å would be essential. New growing techniques, as described in Section 4.4.1, would drastically improve the standard of crystal. These new crystals were also to be grown in MB cells with Böhler-Almax diamonds and backing disks. This would remove the background on the area detectors from the beryllium backing disks. Also at this point in the study there was a move to collecting single crystal data from previously powder-diffraction only beamlines [Lundegaard 08]. Collection from these beamlines, 9.5 at SRS Daresbury and ID09a, ID27 at ESRF is outlined in Section 3.4.3. The chief advantage for this study of collection at these sections was the ability to tightly collimate the beam on sample at these stations. This would hopefully also cut the gasket contribution to the background, and result in a background free area detector images to integrate.

4.4.3 Data collection

The aim was to use the extra information obtained with single-crystal x-ray diffraction to determine the positions of the carbons within the methane phase A structure.

During the course of this study, 12 separate data collections were made on phase A between station 9.5, SRS, Daresbury and ID09a and ID27, ESRF, Grenoble. Many of these were collected as test crystals during the development of high-pressure single crystal techniques on these originally powder diffraction stations. Because of the developmental nature of these experimental runs, data in most of the collections were of not sufficient standard to be solved. Details on each collection can be viewed in the inventory of single crystal synchrotron data collected in Appendix B. There are a number of data sets where the strongest reflections were saturated, making them

unsuitable for input into direct methods. There is also a data set where the beam has been attenuated too much. In this, only the 5 strongest peaks are observed. This proved to be insufficient information for direct methods to phase and solve the structure. Achieving a balance in the beam intensity was one of the biggest obstacles in collecting a detailed enough data set on methane phase A. The beam needed to be not so strong as to saturate the largest reflections, but also strong enough to provide enough intensity to define the smaller reflections.

In this section only two data sets will be discussed, from station ID09a, ESRF and station 9.5, SRS. The first to be discussed was collected from a crystal of phase A at a pressure of 13.6 GPa. This was higher than normal, and the reason for this will be discussed in Chapter 5. Despite the pressure the crystal was still of excellent quality and indexed to a unit cell of a = 8.23(1) Å $\alpha = 89.5(1)^\circ$. There were a number of short preparation data sets collected to check that none of the the strongest reflections were saturating, and that the there was enough intensity to resolve the smaller reflections. Because of the high flux of the ESRF synchrotron, rather than shortening to frame collection times to a point where the shutter would be inaccurate, the undulator feeding station ID09a was tuned down. This provided a low enough flux to collect the methane data without saturating it. The data set was collected in 0.33332° steps in ω from -30° to 30° collecting for 5 seconds at each point. The quality of the data is illustrated in Figure 4.14. These data integrated well, with $R_{\text{int}} = 0.03$, and as such was judged good enough to not require an empirical absorption correction. There were 1025 independent reflections integrated. An initial observation from these data, was how well the crystal scattered, to a *d*-spacing of 0.8 Å. This suggests that hydrogen in the crystal structure will be ordered to some degree, as the scattering is to $\sin\theta/\lambda = 1.25$, beyond the decrease that is seen the methane scattering factor, Figure 4.8.

Data from this run were consequently prepared for inputting into direct methods in the two space groups identified in Section 4.4.2, $R3$ and $R\bar{3}$. For input to direct methods, the programs require, in addition to a unit cell, that a space group is specified. If it not clear that the structure is described by a particular space group at this stage, then the data should be prepared in all of the potential space groups. After preparation of the input files in to $R3$ and $R\bar{3}$, they were run through the SHELXS direct methods program part of the SHELX suite [Sheldrick 08] discussed in Section 3.4.3.

4.5 Results

Both input files, in $R3$ and $R\bar{3}$, gave a viable output structure, only suggesting locations for carbon atoms. The viability of the carbon structure was assessed with the carbon to carbon distances, and the number of carbons within the unit cell. At 5.12 GPa, Hazen

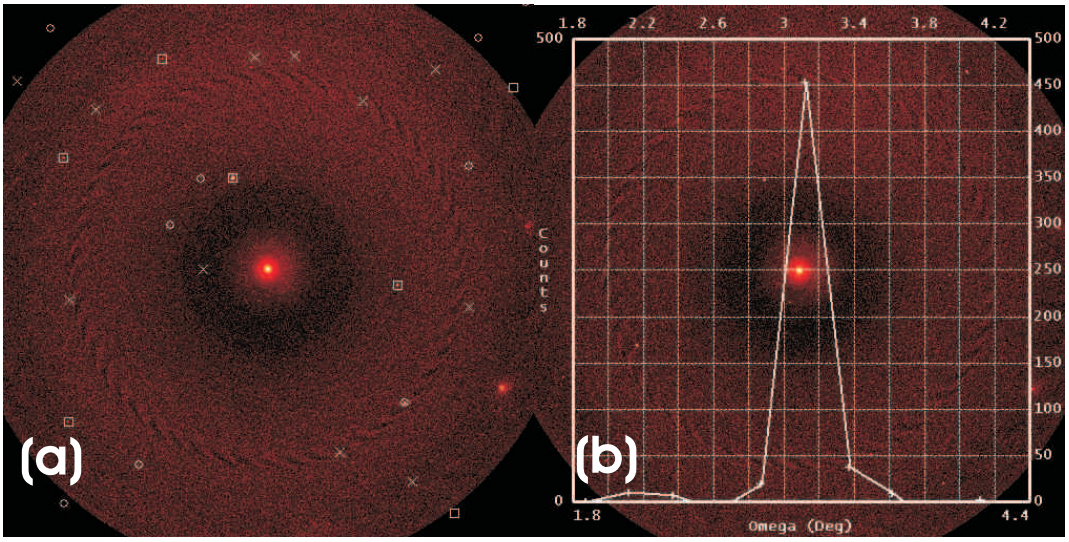

Figure 4.14: (a) is an example frame collected from station ID09a, ESRF. Compared to previously collections on phase A (Figure 4.13) it shows a significant reduction in the background. (b) is the characteristic rocking curve of this data set, 0.15° at FWHM.

et al [Hazen 80] indexed the unit cell of phase I to be 5.095 Å. This implies a carbon to carbon distance of 3.64 Å. This distance is for a fully disordered rotating methane molecule, and would be too large if applied to the potentially ordered tetrahedra of methane phase A. A structure that gave carbon to carbon distances of less than 2.8 Å was judged to be unrealistic (accounting for the abnormally small unit cell of this data set given the high pressure). Although Nakahata *et al* [Nakahata 99] had stated that phase A should contain 21 molecules, structures with 22 and 20 molecules would also be considered.

Both the $R3$ and $R\bar{3}$ structure solutions were deemed viable by the criteria stipulated above, and as such both were refined against the data. Both of the discovered structures contain 21 carbon atoms. The refined structures from this data set are described in Table 4.7 for the $R3$ structure and Table 4.8 for the $R\bar{3}$ structure. Figure 4.15 and 4.16 shows views of the structures. For completeness, there was an attempt to solve the structure in the other space groups proposed by Nakahata *et al*, $R32, R3m$ and $R\bar{3}m$) but none of these yielded viable solutions. This is in agreement with the preliminary results of this study which showed that $R3$ and $R\bar{3}$ space groups would be favoured because of intensity distributions.

Both the $R3$ and $R\bar{3}$ structure solutions have no carbon to carbon distances that are less the 2.95 Å. On close inspection it can be shown that they are in fact both the same structure. Figure 4.17 is of eight unit cells of each structure viewed along the [010] direction. This clearly shows that the $R3$ structure can be described by translating the

Carbon	Wyckoff	x	y	z	U_{iso} (Å^2)
C1	1a	0.578(4)	0.578(4)	0.578(4)	0.04(1)
C2	1a	0.947(4)	0.947(4)	0.947(4)	0.07(2)
C3	1a	1.187(2)	0.187(2)	0.187(2)	0.02(1)
C4	3b	0.842(2)	0.310(2)	0.711(2)	0.002(4)
C5	3b	0.455(7)	0.343(8)	0.852(8)	0.12(2)
C6	3b	0.707(6)	0.613(6)	0.963(6)	0.10(2)
C7	3b	0.517(3)	0.200(3)	0.424(3)	0.019(7)
C8	3b	0.954(6)	0.090(6)	0.426(7)	0.10(2)
C9	3b	1.213(2)	0.096(2)	0.719(2)	0.001(4)

Table 4.7: Carbon positions and thermal parameters of the phase A solution in $R3$ symmetry. The figures in brackets are the estimated standard deviations (esd). This structure refined to an R-factor of 0.147.

Carbon	Wyckoff	x	y	z	U_{iso} (Å^2)
C1	1a	0.000(0)	0.000(0)	0.000(0)	0.015(8)
C2	2c	0.613(2)	0.613(2)	0.613(2)	0.04(1)
C3	6f	-0.272(2)	0.131(2)	0.256(2)	0.027(4)
C4	6f	0.382(2)	0.145(2)	0.053(2)	0.036(5)
C5	6f	0.493(1)	0.858(2)	0.371(1)	0.028(4)

Table 4.8: Carbon positions and thermal parameters of the phase A solution in $R\bar{3}$ symmetry. The figures in brackets are the estimated standard deviations (esd). This structure refined to an R-factor of 0.198.

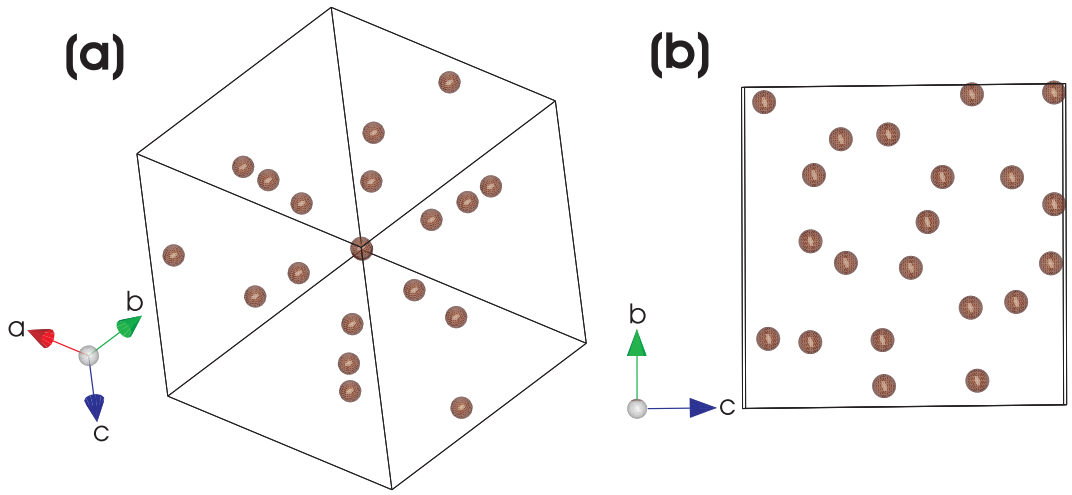

Figure 4.15: (a) A view down the [111] direction of the $R3$ candidate phase A structure and (b) is a view along the [100] direction. This structure refined to an R-factor of 0.147.

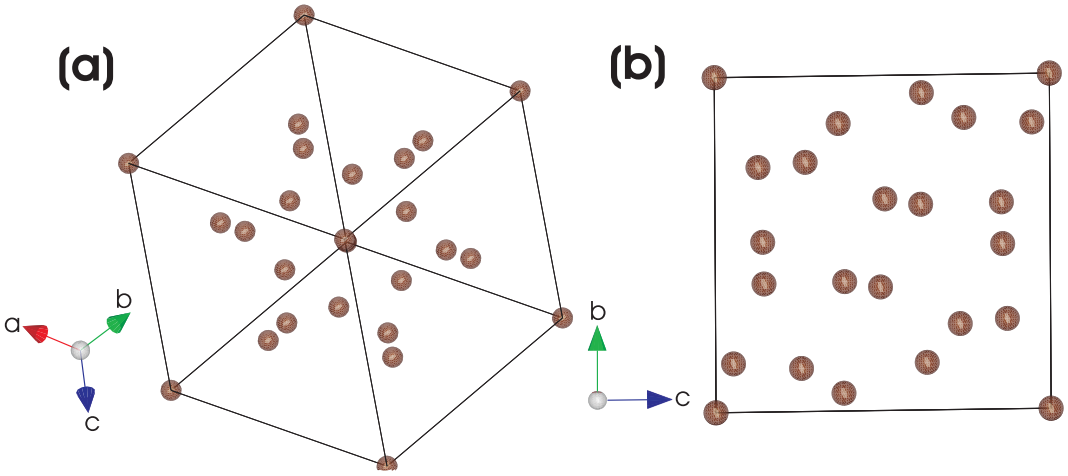

Figure 4.16: (a) A view down the [111] direction of the $R\bar{3}$ candidate phase A structure and (b) is a view along the [100] direction. This structure refined to an R-factor of 0.198.

$R\bar{3}$ structure. But which is the correct way of describing the structure?

Examining the R-factors of the structure refinement begins to answer the question posed above. The $R3$ structure refines to $R = 0.144$ and the $R\bar{3}$ structure refines to $R = 0.198$. This could be an artefact of the extra freedom that the $R3$ space group allows the structure, and the thermal parameters that $R3$ resolves are not all realistic, Table 4.7. A Hamilton R-factor test was undertaken to determine whether the drop in R-factor between these two models is a real change, or just a reflection of the extra freedom of the $R3$ space group. The result of this test is shown in Table 4.9.

R_c	R_u	n	q	p	ν_1	ν_2	F_{read}	F_{calc}
0.198	0.144	1025	16	31	15	994	1.676	57.077

Table 4.9: The Hamilton R-factor test applied to the drop from confining the structure in $R\bar{3}$ (R_c) to $R3$ (R_u).

The test was carried out as explained in Section 4.3. Similarly to the previous test, the $F_{read} < F_{calc}$ stating that the drop in R-factor is significant. This means that the $R3$ space group is the more appropriate way of describing the structure of methane phase A.

This assertion was confirmed by a second data set. Collected on station 9.5, SRS this data was from a sample grown separately at a pressure of 9.1(2) GPa. These data were collected from $-30°$ to $30°$ in $0.25°$ steps in ω with 15 second exposure for each frame. These data indexed to a unit cell of $a = 8.80$ Å and $\alpha = 89.4°$, and integrated to a value of $R_{int} = 0.04$. This resulted in 591 symmetry equivalent reflections. These

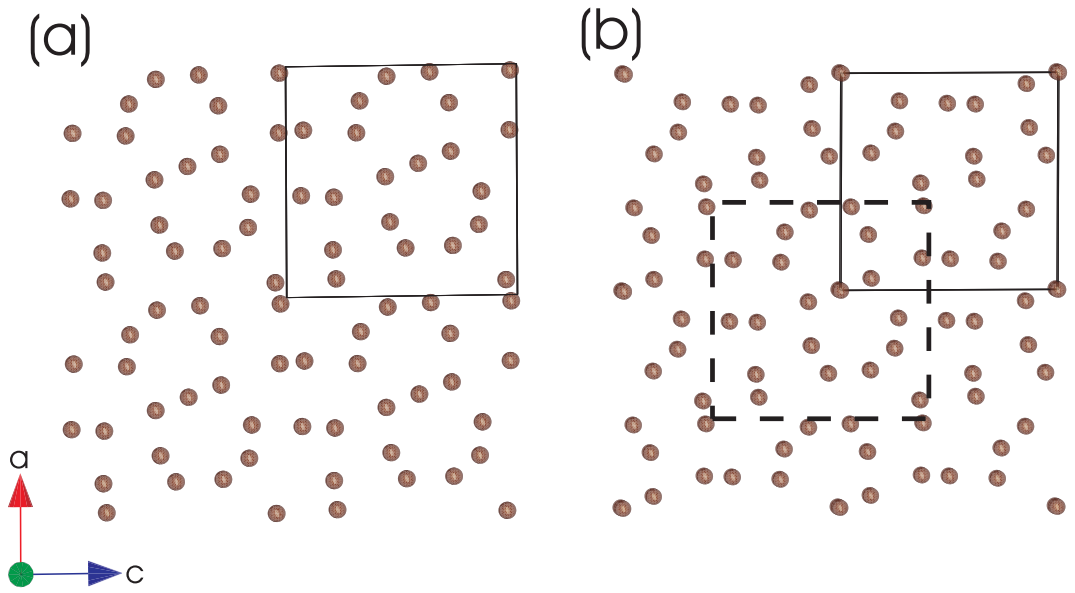

Figure 4.17: Comparing the $R3$ (a) and $R\bar{3}$ (b) structure solutions by viewing them both over eight unit cells along the [010] direction, with the unit cells marked. From this it can be seen that the contents of the $R\bar{3}$ structure is a translation from the contents in the $R3$ unit cell as indicated by the dashed box.

data were refined with both the $R3$ and $R\bar{3}$ structural models yielding R-factors of 0.09 and 0.34 respectively. The structure parameters of phase A from this data set are given in Table 4.10

The variation in thermal parameters, shown in Tables 4.7 and 4.10 perhaps suggests that there may be different states of order to the hydrogen within phase A. The $R3$ model positions in Table 4.10 will be used to move forward the structural realisation of phase A.

4.6 Discussion of the molecular structure

As stated in the introduction, the original expectations for the transitions of methane structure with pressure were that it would become a hexagonally close packed structure [Hebert 87]. This was later challenged, and it was proposed that phase A would form a tetragonal 'transition' phase (between face centred cubic and hexagonally close packed structures) [Bini 97]. The indexing of phase A to a rhombohedral unit cell [Nakahata 99] was a departure from all these expectations.

The essential symmetry elements for a cubic unit cell is that it has three 3-fold axes that pass through each diagonal. The rhombohedral unit cell, in contrast to a tetrahedral unit cell, has more affinity to the cubic cell of phase I, but with only one

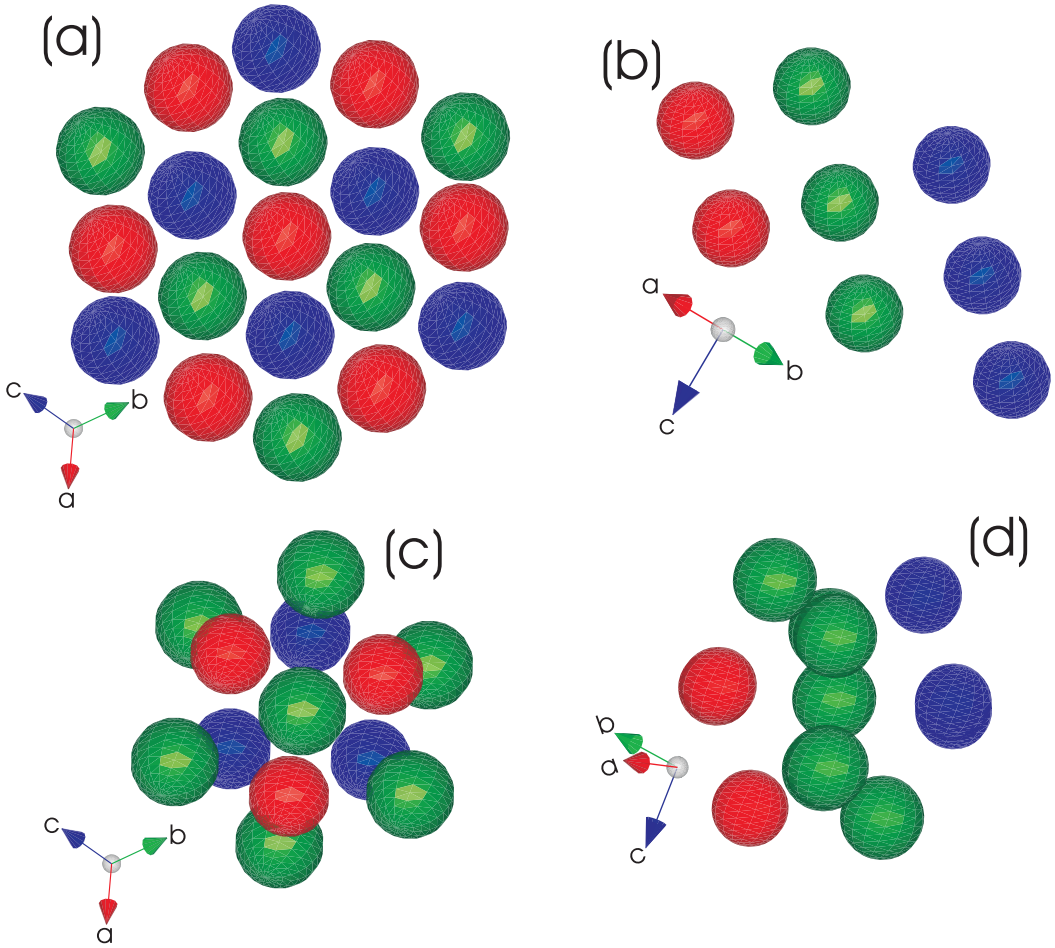

Figure 4.18: Comparison of the cubic closed packed structure of methane phase I with the molecular (carbon) structure of phase A. A 'space filling' drawing of the carbon atoms has been used to make the relationships clearer. The carbons in each layer are coloured the same to differentiate them from other layers. (a) and (b) are both of the ideal cubic closed pack structure, as taken by phase I viewed along a [111] and [110] direction respectively. (c) and (d) are views of the structure of phase A, which takes a 'distorted' cubic closed back structure. The carbons that show this are highlighted in red, green and blue. When viewed along a [111] direction, (c), the three layers can be seen to stack. When viewed on (d) the blue atoms show the nature of the distortion in the layers. This distortion lowers the symmetry along the other diagonals of the cell, what would have been the other trigonal axis if the cell was cubic. This also enlarges the repeat of the structure, resulting in a larger unit cell.

Carbon	Wyckoff	x	y	z	U_{iso} (Å^2)
C1	1a	0.576(4)	0.576(4)	0.576(4)	0.07(1)
C2	1a	0.971(2)	0.971(2)	0.971(2)	0.04(1)
C3	1a	1.210(4)	0.210(4)	0.210(4)	0.18(4)
C4	3b	0.833(2)	0.311(2)	0.704(2)	0.010(4)
C5	3b	0.438(5)	0.310(4)	0.858(6)	0.16(2)
C6	3b	0.720(3)	0.640(3)	0.970(4)	0.07(1)
C7	3b	0.531(3)	0.205(3)	0.436(3)	0.07(1)
C8	3b	0.945(3)	0.057(3)	0.447(3)	0.107(1)
C9	3b	1.201(3)	0.072(3)	0.730(4)	0.08(1)

Table 4.10: Carbon positions and thermal parameters of the phase A solution in $R3$ symmetry refined from the second data set collected at station 9.5, SRS. In brackets are the estimated standard deviations (esd). This structure refined to an R-factor of 0.09.

3-fold axis. The packing of the spheres in the phase I structure is routinely referred to a face centred cubic (fcc). It can also be described as cubic close packed (ccp) with a 3-layered repeat structure. This is illustrated in Figure 4.18(a) and (b) with the red, green and blue spheres each belonging to a different layer. Figure 4.18 compares the structure of phase A with the idealised cubic closed packing of phase I. There are some similarities, phase A exhibits an 3-layer repeat structure. But, as shown in Figure 4.18(d) this is distorted enough to lower the symmetry along the other two diagonals of the cell.

The molecular (carbon) structure reveals that phase A has a 'distorted' cubic close packed structure. This is probably a result of a partial loss of complete spherical disorder in the hydrogen that surround the carbon in each molecule. The validation study on phase I suggested that this process is already apparent by 3.8(2) GPa. By becoming partially or fully ordered the tetrahedral methane molecules can pack more efficiently. This agrees with the suggestion of Hebert *et al* [Hebert 87] that transformations in the solid phases of methane would be induced by anisotropy of the molecule. To confirm this, the location of hydrogen within the structure must be identified, 84 atoms in all. This is where the limit of single crystal x-ray diffraction is reached. The low scattering of the hydrogen atom, having only one electron, means that it is impossible to determine the position of this number of atoms. Hence, the experiments for this study moved to powder neutron diffraction.

4.7 Neutron powder diffraction

As outlined in Chapter 3, it is the aim of this thesis to take an integrated approach to the structural realisation of outer solar system mineralogy. As all the possible minerals are composed of light elements; carbon, nitrogen and hydrogen, neutron diffraction is an obvious tool to probe their structures. As shown in the previous section x-ray diffraction can only directly resolve the carbon positions of methane phase A. This only accounts for 60 % of the electron density of the methane structure. It had already been established that the structure of phase A is too complex to be solved by powders alone, Section 4.3.5. But, the use of neutron powder diffraction in conjunction with results from the single crystal x-ray diffraction could reveal new information. As outlined in Section 3.2.2 neutrons, unlike x-rays, scatter off the nucleus rather than the electron cloud of an atom. For diffraction from hydrogen this means that the intensity of the scattering is not a function of the number of electrons and hence measurable. The caveat is that hydrogen scatters incoherently and for crystallographic studies must be substituted for deuterium. The effect of deuteration upon methane at high pressure and room temperature is expected to be small and not to influence the crystal structures. Similar studies from water and ammonia have indicated that it is valid to substitute deuterium and hydrogen in this way [Loveday 99, Klotz 99, Fortes 04, Besson 94].

4.7.1 Experiment

As explained in Section 3.3.2 the difficulty of high-pressure neutron diffraction lies in obtaining a large enough sample to diffract from. This intrinsically limits neutron diffraction to 30 GPa with the Paris-Edinburgh press. To obtain phase A, pressures in excess of 5.2 GPa are needed at room temperature, well within the capabilities of the Paris-Edinburgh press.

This study aimed to use the heavy atom structure determined in Section 4.5 as input for Fourier difference refinement against neutron powder diffraction. Any positive peaks left in the electron density should indicate deuterium (hydrogen) positions.

Deuterated methane was cryo-loaded into a V3 Paris-Edinburgh press, as explained in Section 3.5.1, with pentane as the hydraulic fluid to drive the ram. The loading ring was tested to hold 10 bar of pressure, so the cell was cooled to 145 K. For neutron diffraction studies of phase A a single toroid SME gasket was used, to maximise the amount of sample. The data presented in this section were collected at PEARL/HiPr at the ISIS facility, Section 3.4.1, in a transverse geometry. Because of the nature of the loading, and the goal of structural characterisation, no pressure calibrant was added to the sample. Comparison with x-ray powder patterns, such as Figure 4.5 enabled the sample transformation to be identified.

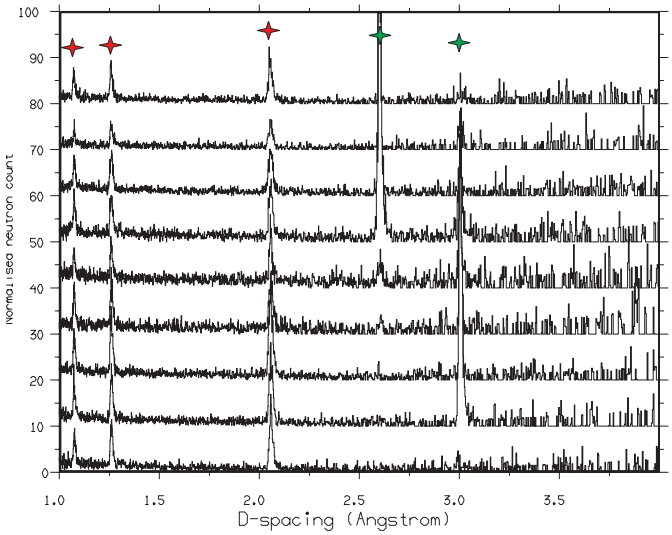

Figure 4.19: A ring plot of methane phase I within a Paris-Edinburgh press at 48 tonnes, from the transverse geometry detectors on PEARL/HiPr, ISIS. Each profile is the pattern received at a separate detector, the normal procedure is to sum these to acquire the final profile. The red stars indicate reflections from the sintered diamond anvils, and green stars indicate positions of the main methane phase I reflections. This shows that this sample of phase I is very textured, close to being a single crystal. Ideally the intensity from reflections should be spread evenly through the detectors, or at least present in more than one of them.

As stated previously in this chapter, methane samples have a tendency to form textured powders or bad single crystals in diamond anvil cells. It was not clear if this would also be the case for the large volume Paris-Edinburgh press. Figure 4.19 is a plot of multiple patterns from each of the separate detectors at 90° 2θ to the sample, designated a ring plot. In this figure the deuterated methane sample is at 48 tonnes, still in the cubic structure of phase I. Figure 4.19 shows that the sample at this point has formed a very textured powder.

Fortunately, on further compression and the subsequent transformation to phase A, the methane sample formed a better averaged powder. Figure 4.20 shows a similar plot to that in Figure 4.19, but in contrast the sample has become a fair powder. These data in Figure 4.20 were collected at 110 tonnes, for collection to perform Fourier difference analysis the sample was cooled from this point to 110 K. This was to minimise the effect of thermal motion upon the deuterium.

4.7.2 Fourier difference analysis

Figure 4.22 shows the subsequent powder profile that was used for Fourier difference analysis. These data were refined in GSAS [Larson 94] with the structure outlined in

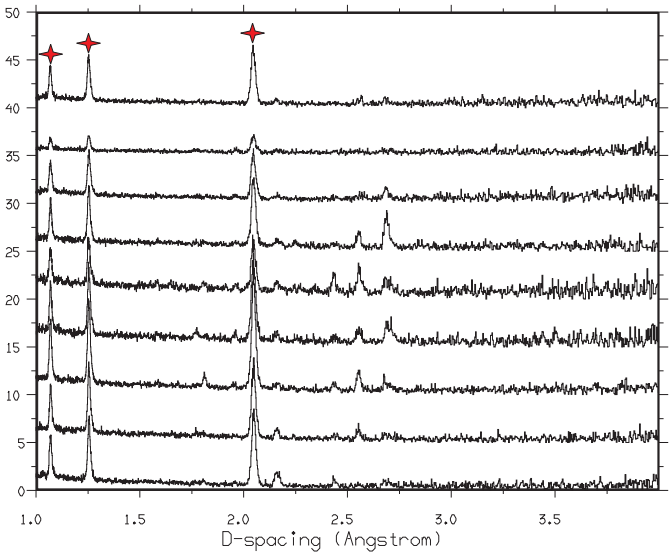

Figure 4.20: A ring plot, similar to Figure 4.19 but from the sample at 110 tonnes in a Paris-Edinburgh press. The red stars indicate the reflections from the sintered diamond anvils. Other reflections present are from the methane sample which has taken the phase A structure. Unlike Figure 4.19 sample reflections are present in most of the detectors, those at the top being shielded remnant indium from the loading process. Summation of these patterns would relieve any subsequent textual effect and result in a good powder pattern.

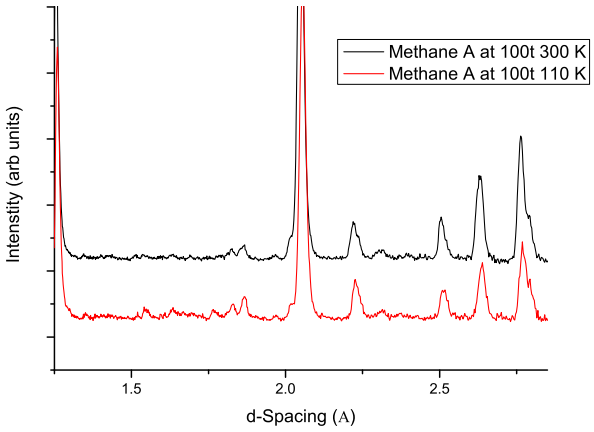

Figure 4.21: Comparing the neutron powder patterns from methane phase A at 110 tonnes and 300 K (red line) and at 110 tonnes and 110 K (black line). The reduced thermal motion at the lower temperature means that the peaks between 1.5 and 2.0 Å become better resolved. Subsequently the low temperature pattern was used to locate hydrogen atoms.

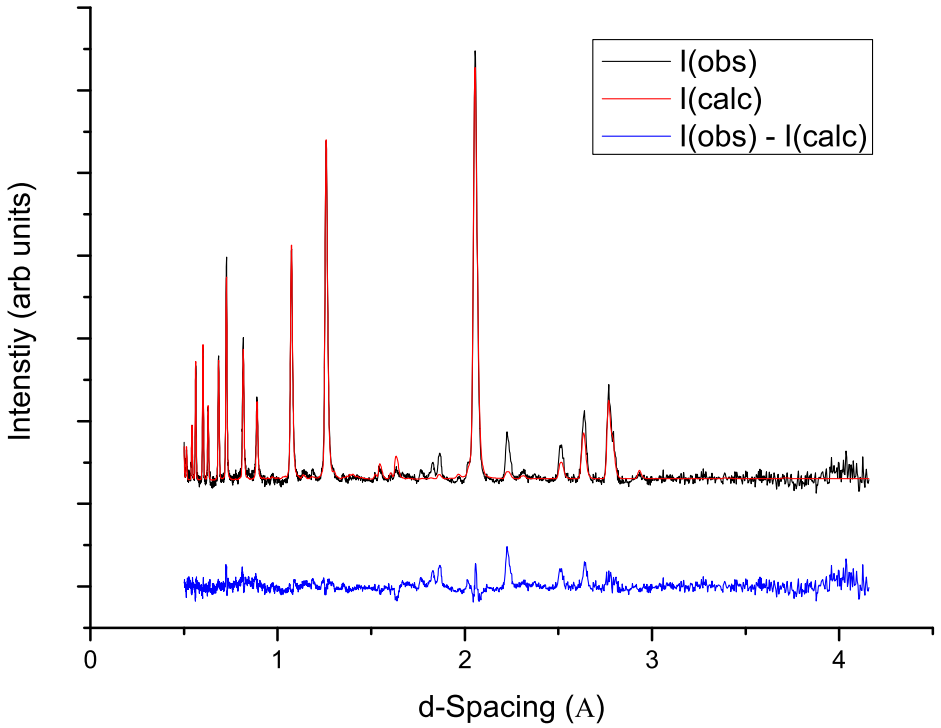

Figure 4.22: The powder profile of methane at 110 tonnes and 110 K fitted with the structure determined in Section 4.4.3. This fitted with χ^2 = 5.56 and wRp = 0.083. There are a number of peaks that are not well described by the carbon only structure, indicating the suitability of this pattern for Fourier cycling to locate deuterium (hydrogen) atoms.

Table 4.7, but setting all the U_{iso} values to a standard value of 0.025 Å^2. This was to remove any contribution that the thermal parameter may be giving to the electron density. This model fitted the pattern with $R_{wp} = 0.083$ and $\chi^2 = 5.42$. Compared to the x-ray diffraction pattern, Figure 4.5, the neutron diffraction pattern of phase A shows more prominent reflections at low d-spacings. The pre-determined carbon structure poorly fits the intensity of these peaks, Figure 4.22. This indicates that the intensity contribution to these peaks is mainly from the deuterium atoms.

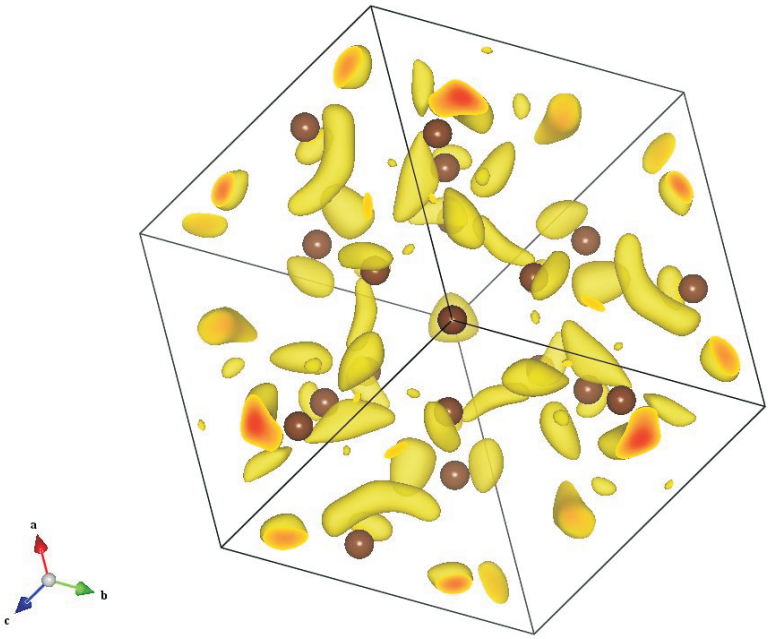

Figure 4.23: The resultant Fourier map from the data presented in Figure 4.22, viewed along the [111] direction. This has been drawn to shown only the significant positive electron density.

The observed structure factors were extracted from this refinement in Figure 4.22, and used in a Fourier difference ($F_{obs} - F_{calc}$) calculation, within the GSAS suite [Larson 94]. This was set up to encompass a whole unit cell, and calculated at 169 points along each axis. Any residual positive peaks in the map could indicate the positions of deuterium (hydrogen) atoms. A three dimensional plot of the subsequent Fourier map is shown in Figure 4.23. As an example a more detailed view of the arrangement of residual electron density about the C2 carbon can be seen in Figure 4.24. Encouragingly Figure 4.24 shows a carbon with tetrahedrally co-ordinated 'blobs' of residual electron density surrounding it. The discrete nature of these 'blobs' indicate

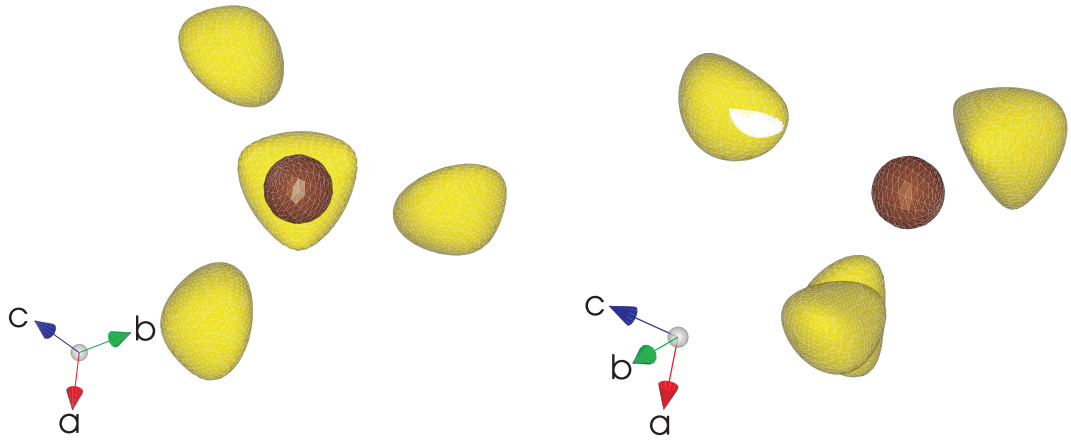

Figure 4.24: A more detailed view, only showing the residual electron density that surrounds the C2 carbon position. The residual electron density is tetrahedrally co-ordinated and suggest that the C2 carbon is part of an ordered methane molecule.

that the deuterium that surround the C2 carbon are ordered.

From this start point, a routine of Fourier cycling was implemented. Spurious peaks and 'real' deuterium peaks were disseminated by using the crystal structure visualisation program VESTA [Momma 06]. Deuterium positions were identified and then inputted into the structural model for further Fourier cycling. After three cycles 34 positions, generating 69 out of the 84 expected hydrogen were found. The fit of this structure to the data is shown in Figure 4.25.

Once 34 hydrogen positions had been generated every carbon molecule had either 3 hydrogen atoms defined about it or was sitting on the 3 fold axis of the unit cell. This enabled the rest of the hydrogen to be inferred from geometric considerations. Table 4.11 lists the positions of atoms within the methane phase A structure inferred by this study

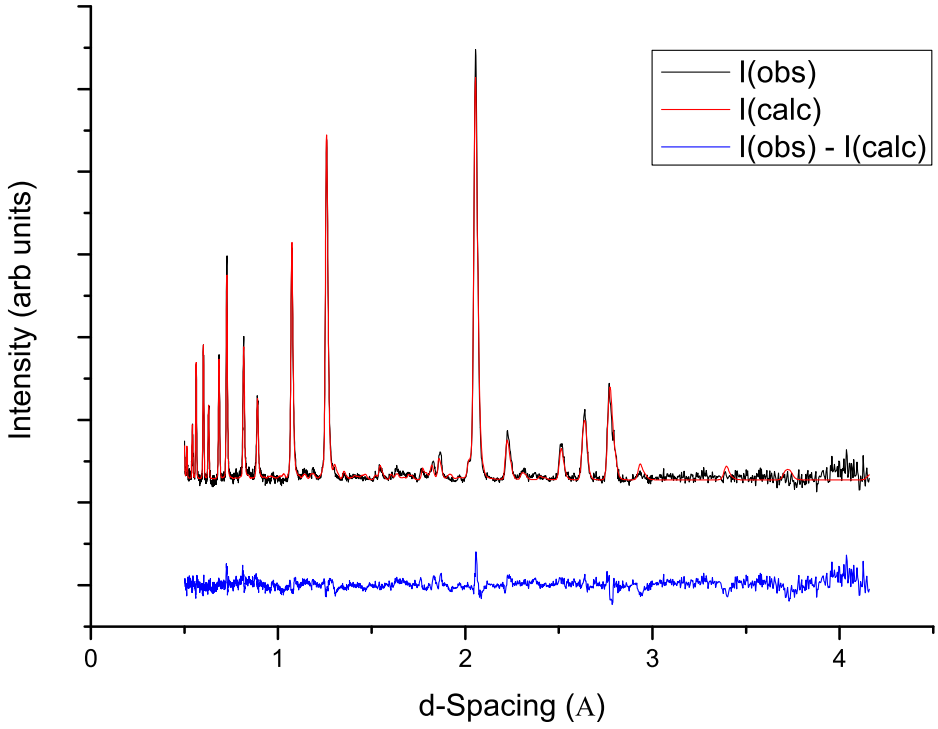

Figure 4.25: The powder profile of methane at 110 tonnes and 110K fitted with the structure determined in Section 4.4.3 and the hydrogen found by Fourier cycling. The blue difference curve indicates how much the fit has improved, with a $\chi^2 = 3.615$ and $wRp = 0.069$ with 69 out of 84 hydrogen inputted. Only the scale factors, lattice parameters and instrument parameters are being refined to the data. The small amount of residual intensity also meant that further Fourier analysis is difficult.

Atom	Wyckoff	x	y	z	U_{iso} (Å^2)
C1	1a	0.576(4)	0.576(4)	0.576(4)	0.07(1)
D11	1a	0.523	0.523	0.523	
D12	3b	0.670	0.590	0.550	
C2	1a	0.971(2)	0.971(2)	0.971(2)	0.04(1)
D21	1a	0.890	0.890	0.890	
D22	3b	0.900	0.027	0.06	
C3	1a	1.210(4)	0.210(4)	0.210(4)	0.18(4)
D31	1a	0.280	0.280	0.280	
D32	3a	0.140	0.090	0.245	
C4	3b	0.833(2)	0.311(2)	0.704(2)	0.010(4)
D41	3b	0.379	0.658	0.922	
D42	3b	0.246	0.694	0.765	
D43	3b	0.353	0.805	0.796	
D44	3b	0.250	0.750	0.940	
C5	3b	0.438(5)	0.310(4)	0.858(6)	0.16(2)
D51	3b	0.400	0.890	0.490	
D52	3b	0.520	0.246	0.801	
D53	3b	0.398	0.301	0.728	
D54	3b	0.279	0.942	0.356	
C6	3b	0.720(3)	0.640(3)	0.970(4)	0.07(1)
D61	3b	0.900	0.706	0.620	
D62	3b	0.862	0.742	0.573	
D63	3b	0.050	0.757	0.687	
D64	3b	1.030	0.660	0.550	
C7	3b	0.531(3)	0.205(3)	0.436(3)	0.07(1)
D71	3b	0.330	0.510	0.290	
D72	3b	0.423	0.528	0.111	
D73	3b	0.524	0.599	0.210	
D74	3b	0.410	0.240	0.423	
C8	3b	0.945(3)	0.057(3)	0.447(3)	0.107(1)
D81	3b	0.045	0.494	0.861	
D82	3b	0.000	0.178	0.450	
D83	3b	0.053	0.308	0.921	
D84	3b	0.950	0.440	0.980	
C9	3b	1.201(3)	0.072(3)	0.730(4)	0.08(1)
D91	3b	0.082	0.700	0.326	
D92	3b	0.200	0.980	0.660	
D93	3b	0.259	0.034	0.809	
D94	3b	0.120	0.160	0.681	

Table 4.11: Table of atomic positions for the structure of methane phase A. The carbon positions and thermal parameters and esds were determined from the single crystal data collection described in Section 4.4.3. The deuterium positions, the majority determined by Fourier difference cycling, but the positions in red were determined geometrically. Fits of this structure to data are shown in Figure 4.26.

The limitations of the positions determined by this method are illustrated by Figure 4.26. In this figure it is shown that fitting the full structure degrades the fit to the powder profile. But this model is more realistic including four hydrogen for every carbon, unlike the model fitted in Figure 4.25. It also has to be considered that no atomic parameters are being refined in these fits, because of the number of parameters that this would entail. Figure 4.20 shows that the sample was not an ideal powder and textural effects would prevent more accurate determination of deuterium positions.

Under ambient conditions methane molecules form tetrahedral with a C-H distance of 1.09 Å and an ideal tetrahedra angle of 109.5° between each of the hydrogen. The deuterium structure that the Fourier peaks infer did not produce ideal tetrahedra about the carbons. This is a fault with the data as there is no other evidence that at this pressure the methane molecule itself would have been modified. There is no split in the ν_1 C-H vibron reported in the previous literature on phase A [Hebert 87, Bini 97, Nakahata 99] so the expectation is that the molecular environment would remain the same throughout the structure.

Despite the limitations of the data set, the non-ideal hydrogen tetrahedra reveal why the molecular structure is a 'distorted' cubic closed packed structure as described in Section 4.6. The Fourier difference location of hydrogen atoms suggest that these atoms are to some extent ordered. As such, to increase the density at this pressure and improve the efficiency of the molecular packing the molecules 'slot' together. This is evident from the full structure where no carbon-deuterium bond is seen to directly oppose another. The fitting of the tetrahedra causes the distortion of the cubic closed packed layers and results in the observed structure. There is still, within this fitted tetrahedra model, room for the molecules to be partially disordered. There is some evidence for this from the final residual Fourier difference map about the C8 carbon, Figure 4.28.

Figure 4.28 shows that the molecule centred about the C8 position is probably disordered as there are positive peaks in the residual electron density surrounding it. Because of the discrete nature of the residual density it is shown that the molecule is no longer completely spherically disordered as they are in phase I. It is likely that the molecule is moving between two positions, a step towards complete order. Partial-disorder in the hydrogen positions would also explain the non-ideal tetrahedron positions that the Fourier difference map determined in some of the molecules.

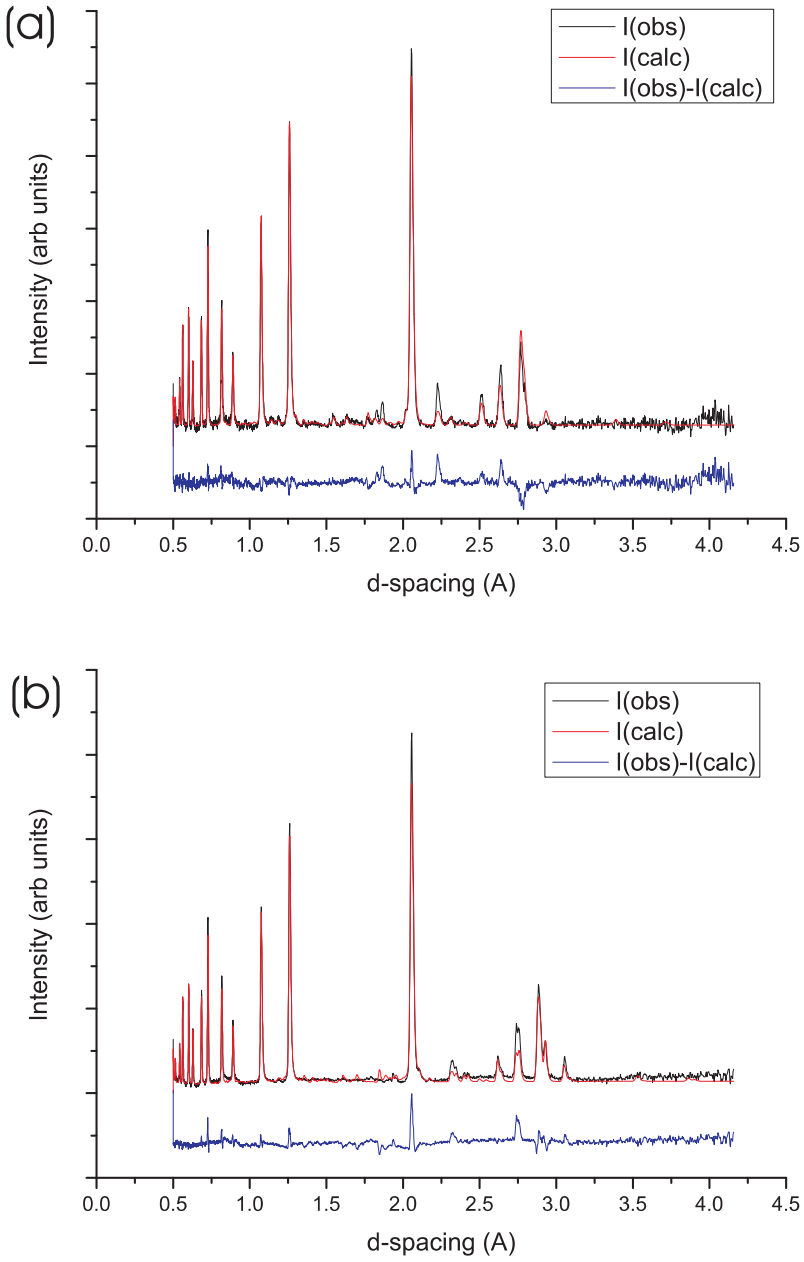

Figure 4.26: Two fits of the structure in Table 4.11 to neutron powder data. (a) is the fit to the same profile as Figure 4.25 at 110 tonnes and 110 K, $R_{\mathrm{wp}} = 0.077$ and $\chi^2 = 4.247$. (b) is a fit to neutron powder data at 70 tonnes and 300 K, $R_{\mathrm{wp}} = 0.105$ and $\chi^2 = 0.954$. In both these patterns, only the scale factors, lattice parameters and instrument parameters are being refined.

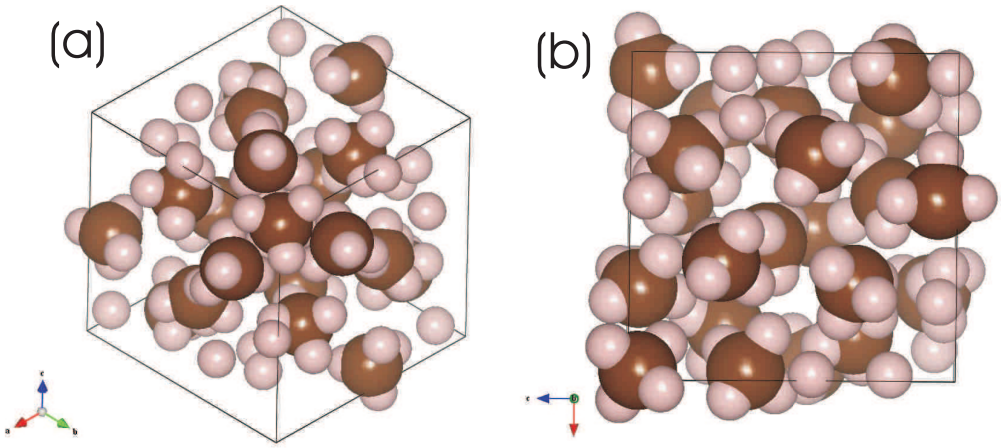

Figure 4.27: Images of the structure of methane phase A, along the [111] axis (a) and the [010] axis (b). The positions of hydrogen about the carbon, despite not rigidly conforming to tetrahedra, do not at any point oppose a hydrogen from another molecule. In this sense the methane tetrahedra 'slot' together throughout the structure.

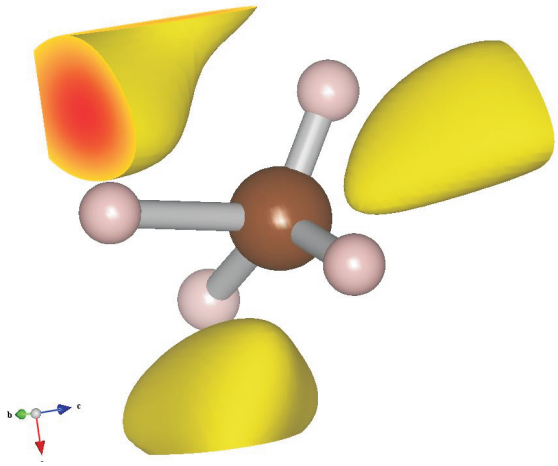

Figure 4.28: Image of the residual electron density from the final Fourier cycle about the C8 carbon and its hydrogen. The yellow positive peaks indicate that there is still some electron density unaccounted for by the determined structure. This is most probably because of some disorder of this molecule. The discrete nature of the residual electron density suggests that the molecule is not completely spherically disordered but moving between two orientations.

Vector x	y	z	Corresponding atom
0	0	0	Carbon
1	1	1	Deuterium
-1	-1	1	Deuterium
-1	1	-1	Deuterium
1	-1	-1	Deuterium

Table 4.12: Vectors used to define a rigid methane molecule for refinement in GSAS. The vector was given a magnitude of 0.575 with resulted in a C-H bond length of 1 Å.

4.7.3 Rigid body analysis

An alternative method of locating the hydrogen in the methane A structure is to carry out a refinement with a rigid body, in place of the individual atoms. As there is no evidence that at these pressures the methane has departed from its molecular state, it is appropriate to refine this structure with the atoms input as complete molecules. To achieve this in GSAS the atoms of a rigid body are defined with vectors relative to one central atom. In this case the carbon is chosen to be the central atom, and the deuterium placed around it in accordance with the vectors described in Table 4.12.

A Rietveld refinement was progressed with the profile used in Section 4.7.2. The central carbon atoms were located at the sites described in Table 4.10. During refinement the defined molecules were allowed to rotate. The only other modification to the model was that the deuterium surrounding C1, C2 and C3 had to be set to an occupancy of $\frac{1}{3}$ as these molecules are sited on the 3-fold axis of the structure. The resultant fit of this model can be seen in Figure 4.29.

Figure 4.29, encouragingly, is a better fit to the data than the profiles described in Figure 4.26. Additionally, because this model is more realistic (describing all the deuterium present in the structure), the result of this method of deuterium positioning has been more successful than that shown in Figure 4.25.

Tables 4.13 and 4.14 give the positions of the carbon and deuterium atoms determined in the rigid body refinement. These are also displayed in Figure 4.30. Similarly to the resultant structure from Fourier difference analysis, Figure 4.27, the rigid body refinements reveals a structure that confirms the molecular structure determination in Section 4.6. Again, no deuterium atoms are seen to oppose each other, and allowing the density of the structure to increase.

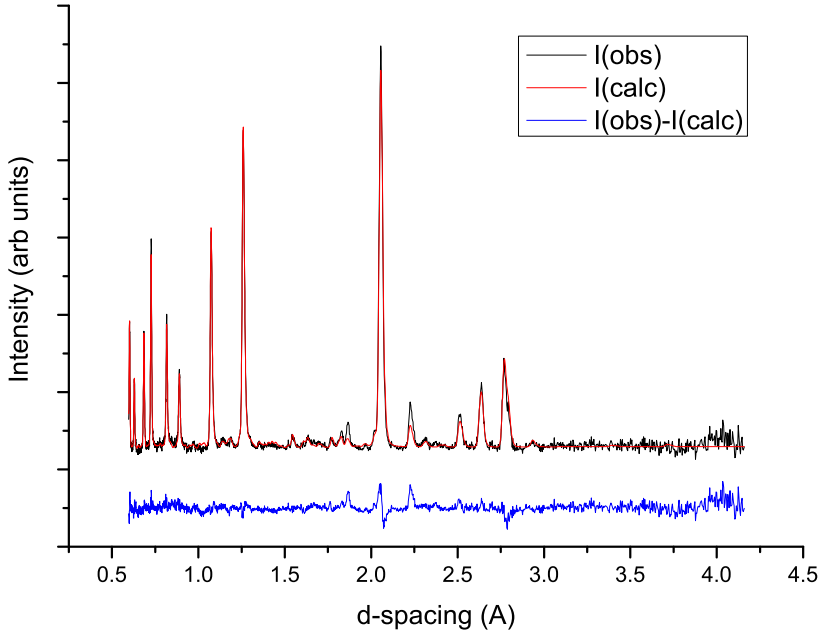

Figure 4.29: Fit of methane A structure constrained with rigid body methane molecules. The structure has been refined against the same profile as Figure 4.25 at 110 tonnes and 110 K, $R_{\mathrm{wp}} = 0.072$ and $\chi^2 = 3.686$.

Atom	Wykcoff	x	y	z	U_{iso} (Å^2)	Occupancy
C1	1a	0.576(4)	0.576(4)	0.576(4)	0.07(1)	1.0000
D11	3b	0.57(2)	0.62(2)	0.68(2)		0.3333
D12	3b	0.46(2)	0.53(3)	0.55(1)		0.3333
D13	3b	0.60(2)	0.65(2)	0.49(1)		0.3333
D14	3b	0.65(3)	0.48(1)	0.57(2)		0.3333
C2	1a	0.971(2)	0.971(2)	0.971(2)	0.04(1)	1.0000
D21	3b	0.88(2)	0.95(2)	1.05(2)		0.3333
D22	3b	1.04(2)	0.872(2)	0.963(2)		0.3333
D23	3b	0.91(2)	0.99(1)	0.864(1)		0.3333
D24	3b	1.03(3)	1.06(1)	1.00(2)		0.3333

Table 4.13: The table of atom positions in methane phase A generated with rigid body constraints. The carbon positions and thermal parameters and esds were determined from the single crystal data collection described in Section 4.4.3. Fits of this structure to data are shown in Figure 4.29

Atom	Wykcoff	x	y	z	U_{iso} (Å^2)	Occupancy
C3	1a	1.210(4)	0.210(4)	0.210(4)	0.18(4)	1.0000
D31	3b	1.24(1)	0.27(2)	0.12(2)		0.3333
D32	3b	1.17(2)	0.10(1)	0.16(2)		0.3333
D33	3b	1.28(2)	0.19(2)	0.30(2)		0.3333
D34	3b	1.11(1)	0.26(2)	0.24(2)		0.3333
C4	3b	0.833(2)	0.311(2)	0.704(2)	0.010(4)	1.0000
D41	3b	0.765(7)	0.262(9)	0.61861)		1.0000
D42	3b	0.761(5)	0.359(8)	0.788(7)		1.0000
D43	3b	0.901(9)	0.225(8)	0.753(8)		1.0000
D44	3b	0.903(9)	0.396(6)	0.655(8)		1.0000
C5	3b	0.438(5)	0.310(4)	0.858(6)	0.16(2)	1.0000
D51	3b	0.492(7)	0.367(8)	0.947(6)		1.0000
D52	3b	0.518(6)	0.241(7)	0.798(7)		1.0000
D53	3b	0.350(6)	0.240(6)	0.903(7)		1.0000
D54	3b	0.390(7)	0.390(7)	0.782(7)		1.0000
C6	3b	0.720(3)	0.640(3)	0.970(4)	0.07(1)	1.0000
D61	3b	0.769(6)	0.541(5)	1.018(6)		1.0000
D62	3b	0.786(5)	0.675(7)	0.875(5)		1.0000
D63	3b	0.608(3)	0.615(6)	0.933(6)		1.0000
D64	3b	0.715(7)	0.727(4)	1.051(6)		1.0000
C7	3b	0.531(3)	0.205(3)	0.436(3)	0.07(1)	1.0000
D71	3b	0.541(7)	0.302(4)	0.365(7)		1.0000
D72	3b	0.437(4)	0.139(8)	0.400(7)		1.0000
D73	3b	0.631(5)	0.138(6)	0.428(8)		1.0000
D74	3b	0.513(7)	0.239(8)	0.5492)		1.0000
C8	3b	0.945(3)	0.057(3)	0.447(3)	0.107(1)	1.0000
D81	3b	1.024(4)	0.143(5)	0.467(8)		1.0000
D82	3b	0.905(8)	0.012(8)	0.551(2)		1.0000
D83	3b	0.852(4)	0.1026)	0.385(7)		1.0000
D84	3b	0.97(7)	-0.030(4)	0.383(7)		1.0000
C9	3b	1.201(3)	0.072(3)	0.730(4)	0.08(1)	1.0000
D91	3b	1.128(6)	-0.021(3)	0.727(7)		1.0000
D92	3b	1.297(3)	0.048(9)	0.662(6)		1.0000
D93	3b	1.145(7)	0.170(6)	0.687(7)		1.0000
D94	3b	1.234(6)	0.090(7)	0.843(1)		1.0000

Table 4.14: Continuation of Table 4.13

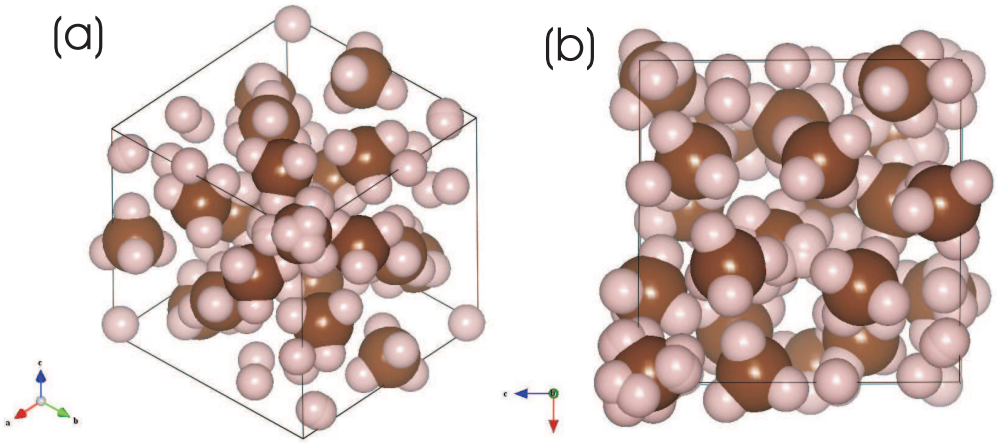

Figure 4.30: Images of the structure of methane phase A described in Table 4.13 and 4.14, along the [111] axis (a) and the [010] axis (b). Similarly to the arrangements determined in Section 4.7.2 the hydrogen do not at any point oppose a hydrogen from another molecule. Again the methane molecules are seen to 'slot' together lowering the closed packed symmetry relative to phase I.

4.7.4 Conclusion

This study has stretched what can be determined from high-pressure neutron powder diffraction. Because of the amount of deuterium atoms, a coherent approach to any further refinement is difficult. The possibility of partial-disorder to all or some of the nine molecular positions, revealed in Section 4.7.2, only compounds this. It is believed what has been achieved here is the limit of what can be reasonably implied about the phase A structure from these data collected. One further complementary technique could be employed to further refine the model, single crystal neutron diffraction. The extra information that individual reflections would afford to realising this structure, would be the only way in which the hydrogen (deuterium) positions could be completely resolved. To date collecting this kind of data collection at pressure has proved an extraordinarily challenging process. This would be the further direction for any more experimental work on this phase.

4.8 Summary

Within this section the structure of methane phase A has been determined to the best ability of current high-pressure diffraction techniques. The first stage was to determine whether the proposed unit cell within the literature adequately described the structure. The rhombohedral unit cell found by Nakahata *et al* was confirmed to describe the structure, and a group of space groups were identified to be candidates to describe the symmetry of phase A. As attempts to solve the structure from the powder diffraction data were futile, the next course of experimentation identified was to carry out single crystal x-ray diffraction.

Before the single crystal data collection on phase A was discussed, a validation study on the preceding phase I was described. This set out what could validly be said about methane structures from high-pressure single crystal data. Attempts to grow a samples of phase A were described, and preliminary data sets confined the symmetry to $R3$ or $R\bar{3}$ space groups. The molecular structure was determined and its affinity to the cubic close pack structure of phase I was explored. The validity of the molecular structural determination was tested from refinement against two separate data sets from different crystals, collected at different synchrotrons.

To locate the hydrogen within the structure powder neutron diffraction data were collected. Combined with Fourier cycling, this revealed the position of 69 out of the 84 expected hydrogen atoms. The rest of the hydrogen were placed in the structure with geometric considerations. The overall structure was discussed and the possibility of residual partial disorder in some of the molecular positions was shown.

This study on methane phase A has exhausted the available high-pressure diffraction techniques. The result, with both carbon and hydrogen positions, illustrates the wealth of information that can be harvested from these incomplete data sets. The evidence of disorder can only be discussed at this stage, and would require single crystal neutron diffraction data to fully quantify it.

Chapter 5

Studies of methane, phase B

5.1 Introduction

The development of the methane phase diagram was previously discussed in Section 4.1. This section will instead concentrate on the literature relating to phase VII or B as it was later renamed. The phase was first identified as a distinct structure of methane by Hebert *et al*, [Hebert 87] who sequentially named it phase VII. It was identified as a separate phase from the preceding phase IV by monitoring of the internal Raman modes, ν_1 and ν_3. Upon the transition to phase VII the response of these modes to pressure changed to a lesser gradient, and shoulders appeared on the low energy side of both peaks. Hebert *et al* demonstrated, from Brillouin scattering, that the transition between IV and VII was 'sluggish' and completed only at 25 GPa. The appearance of shoulders to the ν_1 and ν_3 peaks in the Raman spectrum (ν_4 being obscured by a spectral peak from diamond), was thought to indicate that the transition between IV and VII is an orientational one. It was also observed that on decompression phase VII did not transform back to phase IV until $\sim$6 GPa. Hebert *et al* proposed a hexagonal closed packed (hcp) structure for phase VII, justified by the arguments set out in Section 4.1.

Phase VII, was renamed as phase B by Bini *et al* [Bini 95] in the same work in which they renamed IV to be phase A. This was justified by the lack of information that coupled the low temperature phases (IV, V and VI) to the room temperature phases (henceforward referred to as A and B). The study by Bini *et al* probed methane with infrared spectroscopy, complementing their work with Raman measurements. They confirmed the previously discussed findings of Hebert *et al*, that phase B is a distinct phase of methane that appears from $\sim$10-12 GPa. In this paper [Bini 95] it is reported that phase B is stable to 30 GPa. In this paper [Bini 95] Bini *et al* also begin to discuss the symmetry that phase B may adopt, confining to the $4/mmm$, $6/mmm$, $m\bar{3}$ or

$m\bar{3}m$ point groups. The $4/mmm$ point group was excluded at this stage because of the assumption that phase B would take up a close packed structure. The suggested similarities of methane to ammonia and the rare gas solids led Bini *et al* to state that phase B would adopt a hexagonally close packed structure, $6/mmm$. Like Hebert *et al*, Bini *et al* concluded that phase B would be a fully ordered, single site crystal structure [Bini 95].

In later work, Bini *et al* [Bini 97] proposed a further phase transformation in methane from phase B to a modification they denoted 'hexagonal phase' or HP. The change in the ν_1 components that were observed at 300 K are shown in Figure 5.1. Bini *et al* commented that across the B to HP transition the number of ν_1 and ν_3 components are preserved. They proposed this as evidence that the structure transition is because of a site change or reduction in symmetry between phases, B and HP. In contrast to Hebert *et al*'s findings that the transition to B is only concluded at 25 GPa, Bini *et al* conclude that phase B is a distinct crystal modification that is stable up to this pressure. They modified their earlier claims [Bini 95] that phase B would have have ordered single site structure, in light of the discovery of the HP phase. However, to exhibit the number of ν_1 components observed from phase B, Bini *et al* state that the structure must adopt a unit cell of high symmetry. From all considerations Bini *et al* concluded that methane phases B and HP would adopt a common hcp based structure, but with different local molecular symmetry [Bini 97].

Similar to phase A, only one significant diffraction study exists in the literature on phase B, again, an x-ray powder diffraction study. The work was carried out by the same Japanese group who undertook the indexing of phase A discussed in Section 4.1. Umemoto *et al* proposed that the unit cell of phase B would be cubic with a lattice parameter of $a = 7.914$ Å at 16.9 GPa [Umemoto 02] . In this study, x-ray diffraction patterns were collected to 37 GPa, alongside Raman spectroscopy measurements. The Raman spectra show the same change at 25 GPa than that Bini *et al* had observed [Bini 97]. Umemoto *et al* report that a cubic unit cell is maintained to 37 GPa. The similarity in lattice parameter between this unit cell and that proposed for phase A, $a = 8.64$ Å and $\alpha = 89.6°$ suggested that the phase transformation was a result of deforming the cell of phase A into a cubic one for phase B. As a result the structures of phase A and B were proposed to be relatively similar [Umemoto 02]. In Umemoto *et al*'s paper only the x-y profiles of the data were shown, and there are no comments on the quality of the sample collected. As previously discussed in Section 4.2, methane has been widely reported to form bad powders and it is curious that this is not discussed.

Phase B occupies a large part of phase diagram of methane, as shown in Figure 5.2. It is the stable phase of methane at room temperature and 20 GPa. The boundary of the middle ice layer of Uranus and Neptune is calculated to begin at 20 GPa 2000

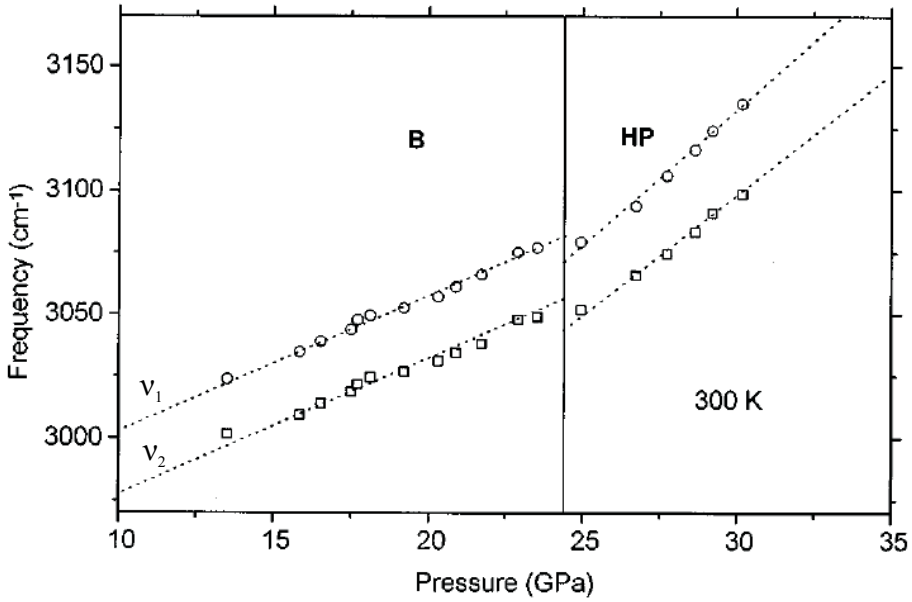

Figure 5.1: Taken from [Bini 97], this figure shows the frequency variation of the ν_1 component of methane at 300 K up to 30 GPa. Bini *et al* attribute the change of behaviour at ∼25 GPa to be the result of a phase transition from phase B to a new phase HP [Bini 97].

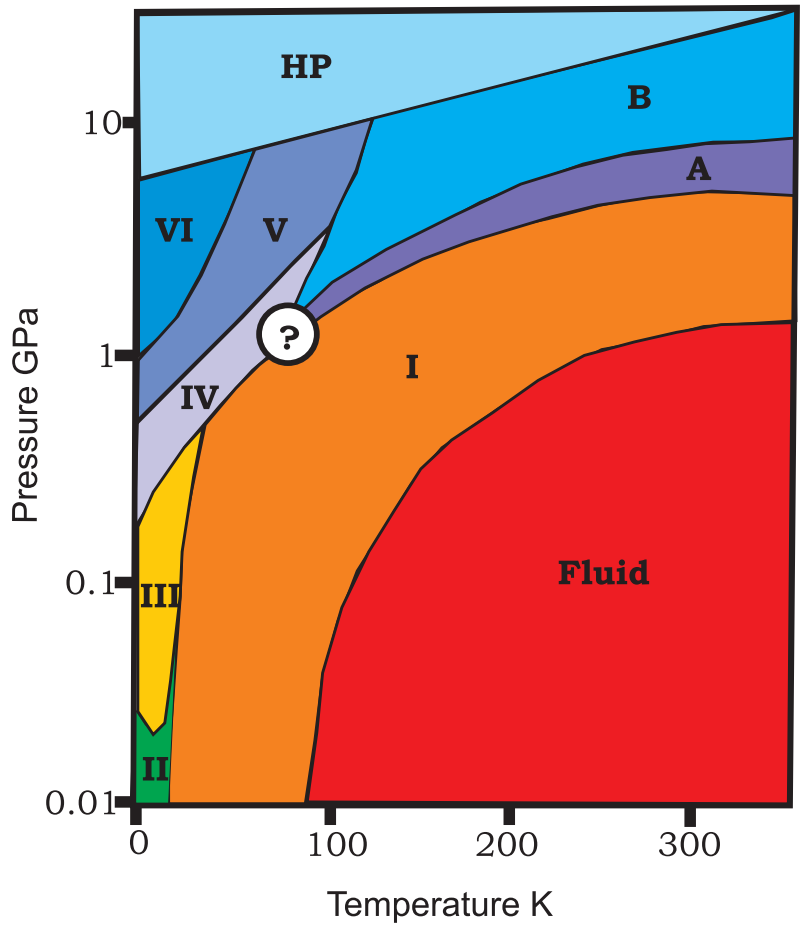

Figure 5.2: Current phase diagram of methane after [Bini 97].

K [Guillot 95], making phase B the starting structure for methane simulations of this layer. As previously outlined in Chapter 2, detailed structural knowledge of the high-pressure behaviour of fundamental molecules, such as methane, is necessary to further probe the interior if these giant planets and others. Structural details (accurate unit cell, atomic positions) from experimental studies allow for better determination of molecular potentials that can be used for computing more extreme behaviour. The aim of the studies within this chapter are to constrain the structural details of methane phase B.

5.2 Powder diffraction

To achieve the aims set out in Section 5.1 a similar line of investigations was followed to that undertaken for phase A in Chapter 4. The first stage was to confirm the unit cell proposed by Umemoto *et al.*

A sample of methane was loaded into a Merrill-Bassett diamond anvil cell, using the method described in Section 3.5.1. The sample was contained within a rhenium gasket with a small chip (10-15 μm) of ruby for pressure calibration. As already described, previous workers have reported that it is difficult to get a good powder from a methane sample, noting its tendency to form textured or poorly averaged powders [Hazen 80]. A good powder of methane B was obtained by this study, first by rapid compression to $\sim$20 GPa. Then the sample was decompressed to 8.3(2) GPa, within the down-stroke stability field of phase B. The powder sample that resulted from this process was collected at station ID09a, ESRF with the set up described in Section 3.4.2. The raw image plate data, demonstrating the quality of the sample, and can be seen in Figure 5.3.

Figure 5.4 shows a comparison between the data reported by Umemoto *et al* and that integrated from the data presented in Figure 5.3. The profiles in both instances exhibit the same main features but the extra details in the data collected for this study are apparent.

In their paper Umemoto *et al* graph their results charting molecular volume response to pressure. This equation of state was used to project their unit cell (determined at 16.9 GPa) to the pressure of the pattern of the data presented in Figure 5.3. Umemoto *et al*'s unit cell would become approximately $a = 8.377$ Å at 8.3 GPa. This cell was used as an input parameter for a primitive cubic cell which was then LeBail refined against the data collected for this study with Jana2000 [Petricek 00]. The unit cell of Umemoto *et al*, whilst fitting the stronger peaks, did not fit some of the additional weak peaks observed, Figure 5.5. This showed that this pre-determined unit cell was not a correct description of methane phase B. The positions of these unindexed reflections relative to the other reflections suggested that the unit cell would still be cubic, but

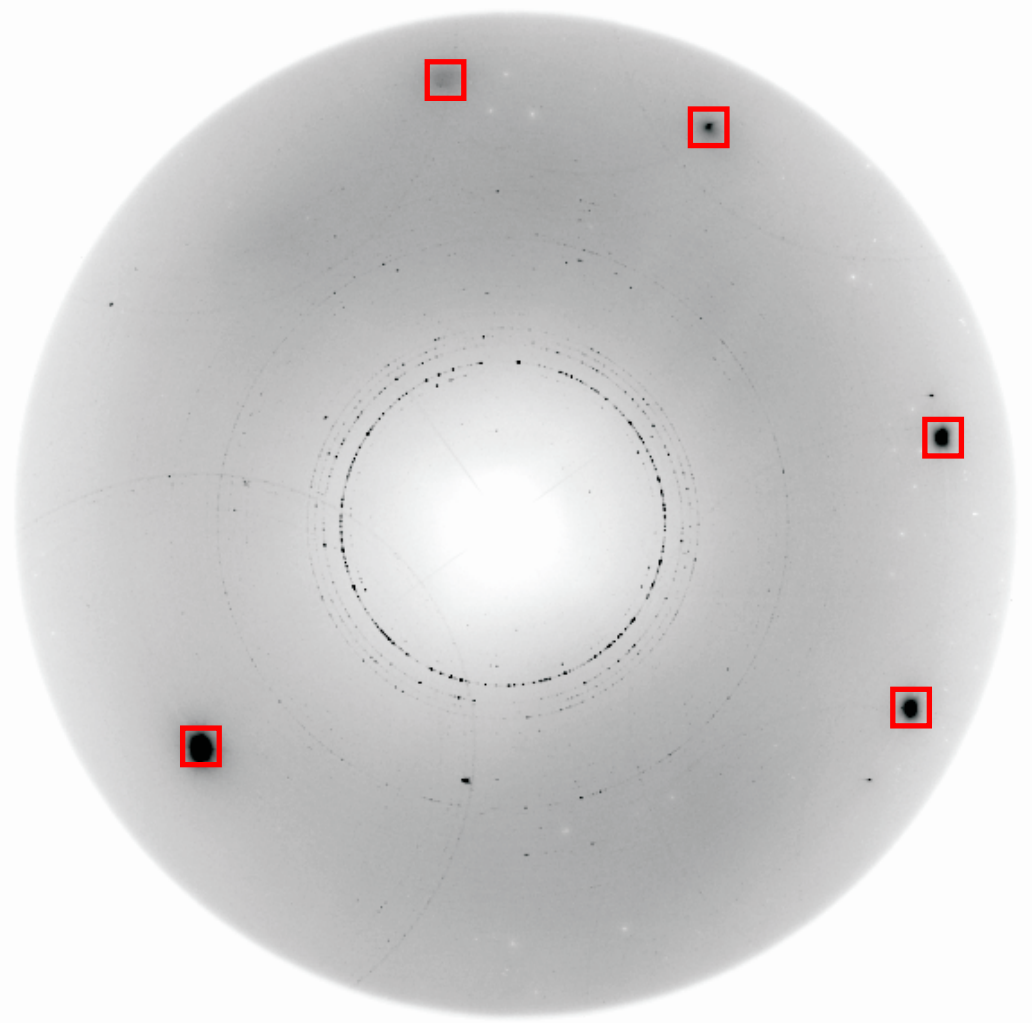

Figure 5.3: Raw image plate image of phase B at 8 GPa. Although the pattern is slightly spotty, there is a near complete Debye-Scherer ring indicating the quality of the powder. The large single crystal diffraction spots from the diamond, marked by red boxes, were masked before integration of the pattern.

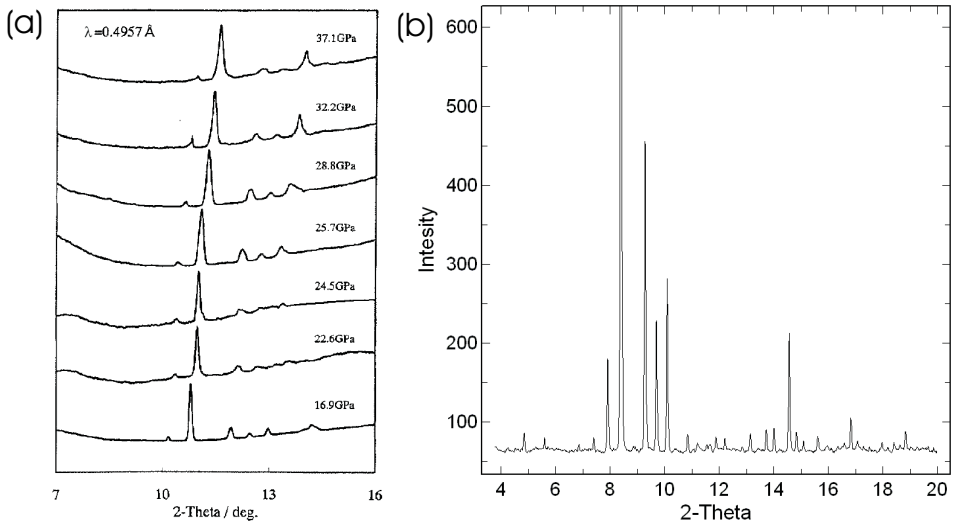

Figure 5.4: Comparison of Umemoto *et al*'s profile (a) compared to the data collected as part of this study (b). The wavelength of collection for (a) was $\lambda = 0.4957$ Å and for (b) was $\lambda = 0.4138$ Å, accounting for the shift in 2θ.

would have to be larger to encompass the additional reflections. Subsequently this study determined a larger cubic cell of $a = 11.87(1)$ Å at 8.3(2) GPa, $\sqrt{2}$ bigger than the original indexing.

In contrast to their group's study on methane phase A, Umemoto *et al* made no assertions about the possible space group of phase B. The conformity of the reflections observed in this study to $h + k + l = 2n$ indicated that the unit cell would be body centred cubic. Other systematic absences, indicated that the space group of this phase would be one of $I23$, $I2_13$, $Im\bar{3}$, $I432$, $I\bar{4}3m$ or $Im\bar{3}m$. From density considerations the number of molecules within this unit cell were estimated to be between 56 and 64. The confinement of symmetry to a body centred cubic unit cell was confirmed by a Le Bail refinement, Figure 5.6.

The large number of molecules coupled with the limited amount of information that can be taken from a powder profile meant that is was not possible to solve phase B from the current data set. At this point, similar to the phase A investigation, it was decided to exploit the tendency for methane to form very textured powders and attempt to grow a single crystal.

This powder diffraction study had been remarkably successful, re-assigning the unit cell and constraining the symmetry of phase B to be one of six space groups. The departure of this phase from the expected hexagonal closed packed structure was not entirely unexpected. As explained in Section 5.1 Bini *et al* [Bini 97] had even previously

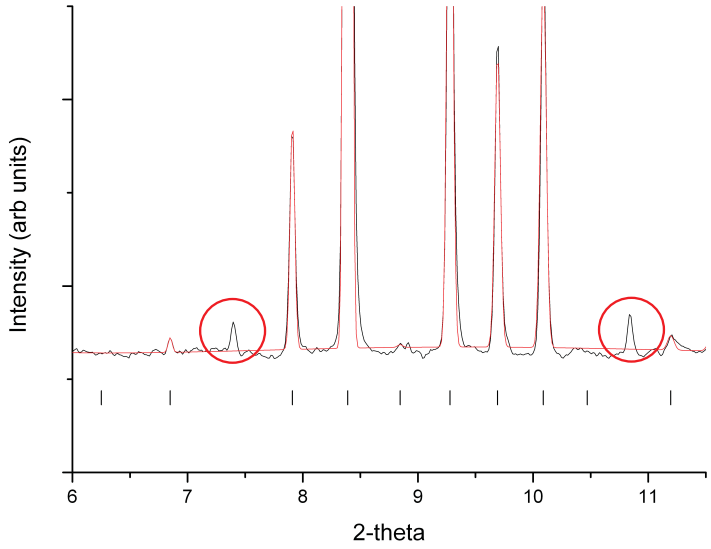

Figure 5.5: Powder diffraction profile of phase B at 8.3(2) GPa fitted with a Le Bail refinement to the projected unit cell proposed by Umemoto et al [Umemoto 02]. The black line is the data, whilst the red line is the Le Bail refinement fit. The tick marks under the profile shown the expected positions of peaks. The circles highlight two weak peaks that are unexplained by Umemoto *et al*'s unit cell and led to a revised indexing of $a = 11.87(1)$ Å for this pressure.

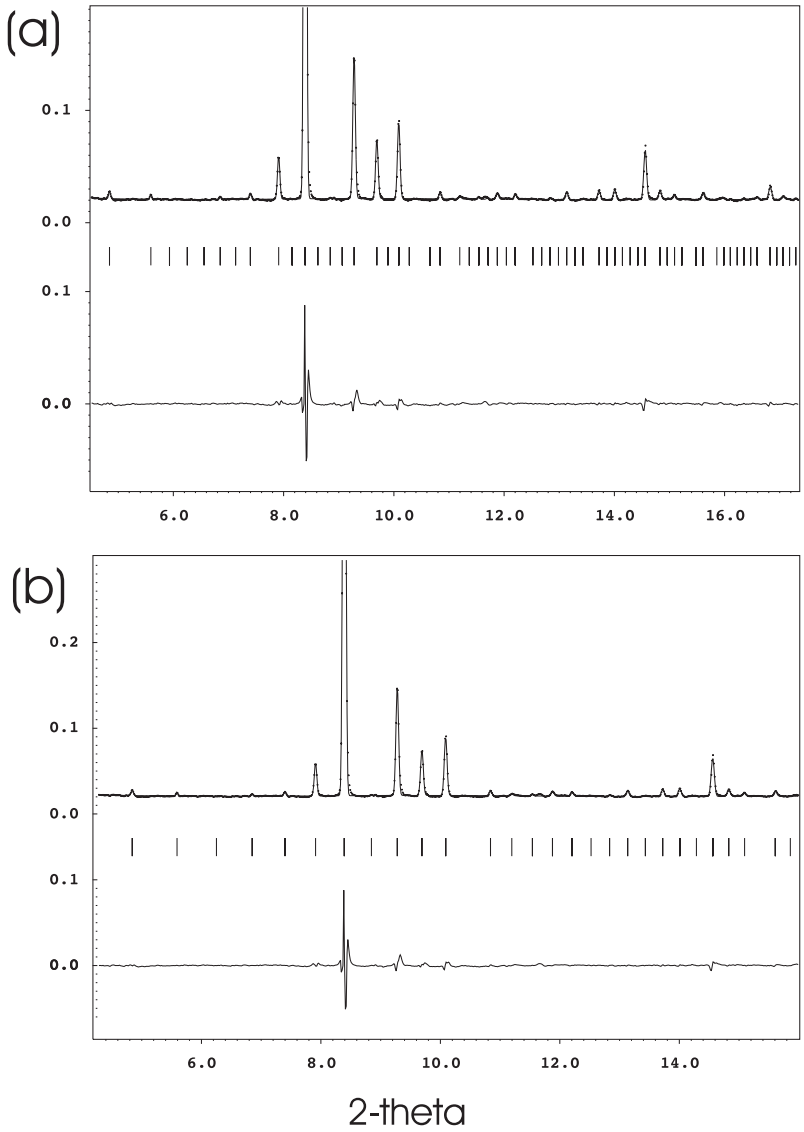

Figure 5.6: Phase B data LeBail refined with (a) a primitive unit cell ($P23$) and (b) a body centred unit cell ($Im\bar{3}$). Overlain the data profile is the refined model profile, the difference between these is shown by the difference curve at the bottom of each graph. Like in Figure 5.5 the tick marks indicate expected positions of peaks. The large number of absent reflection in (a) indicated a higher symmetry. Observation that the reflections conformed to the $h+k+l = 2n$ conditions led to the assigning of a body centred cell to this phase.

suggested that phase B could take up $m\bar{3}m$ or $m\bar{3}$ point group symmetry. However, the size of the assigned unit cell was surprising at nearly 12 Å. This is a significant departure from the single site model put forward by most previous work on phase B [Hebert 87, Bini 95, Bini 97]. It is clear that a phase of this complexity can only be solved with the extra information provided by single crystal diffraction.

5.3 Single crystal diffraction

The first single crystal of phase B was grown whilst attempting to grow a phase A crystal. A Merrill-Bassett (MB) diamond anvil cell was loaded with methane using the method described in Section 3.5.1. The only departure from the stated procedure was that the cell was pre-cooled in liquid nitrogen before being placed into the condensed liquid methane. Using the ruby calibrant that was placed into the cell, the pressure was raised to 10 GPa. Following the method set out in Section 4.4.1 a single crystal was grown at the boundary of the solid-solid transition, already discussed. This transition took place at 460 K, reflecting the higher pressure of the cell relative to that in Section 4.4.1. The cell was cooled and the pressure after crystal growth was found to be 8.3(2) GPa. The crystal quality was checked with the in-house SMART diffractometer (described in Section 3.4.3), and found to be a good quality crystal and indexed to have a cubic unit cell of 11.85(2) Å. This indicated that the methane sample had taken up phase B rather than the desired phase A. At the time it was thought that a pressure increase and improved kinetics on heating had caused the sample to transform at a slightly lower pressure than expected. It was decided to keep the phase B sample for the subsequent study.

5.3.1 Collection at station 9.5

Data were collected from the crystal, at 8.3(2) GPa on station 9.5 at SRS Daresbury on apparatus explained in Section 3.4.3. The quality of the crystal is demonstrated in Figure 5.7, which the crystal exhibiting a characteristic rocking curve of 0.5° FWHM. Data were collected from the crystal in two runs, both collecting ±25°, with 0.2° steps in ω. The first data collection was collected with 10 s exposure for each frame. A second data collection was collected with a 20 s exposure and a larger beam size. The higher intensity of the second data collection was designed to characterise the weaker reflections for later refinement.

From this data collection a total of 176 symmetry equivalent reflections were obtained, with an $R_{\text{int}} = 0.08$. An initial analysis with the XPREP software suggested the symmetry would be described by space group $I\bar{4}3m$ from the distribution of

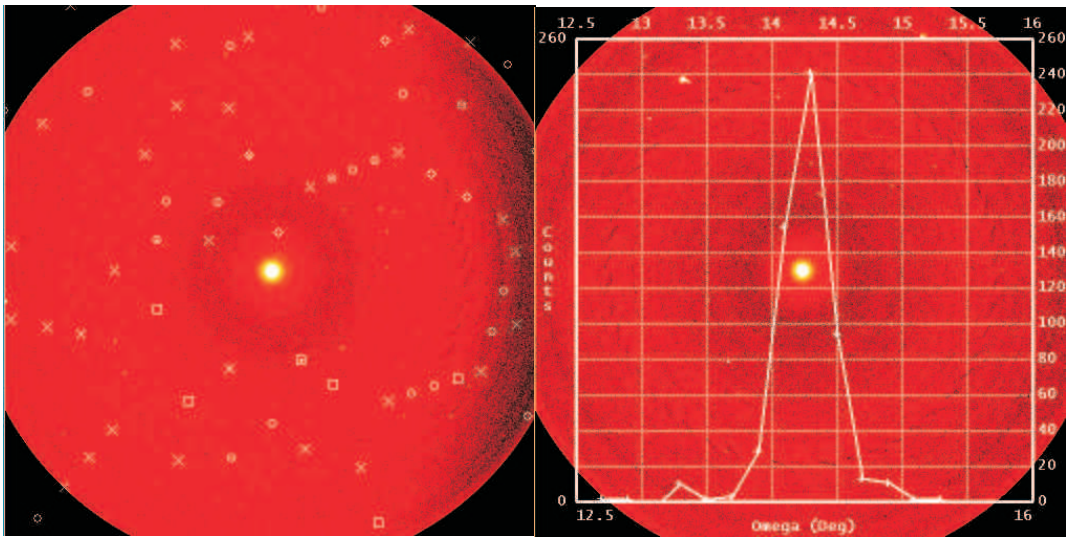

Figure 5.7: Showing the quality of the crystal used to determine the structure of phase B. The left image is frame 17, $\omega = 21.8°$ with reflection from the determined unit cell marked with white shapes. The right image is of the characteristic rocking curve of the crystal, 0.5° at FWHM.

	Wykcoff	x	y	z	U_{iso} (Å^2)
C_1	2a	0.000(0)	0.000(0)	0.000(0)	0.15(7)
C_2	24g	0.091(1)	0.278(1)	0.091(1)	0.092(7)
C_3	8c	0.319(2)	0.319(2)	0.319(2)	0.09(2)
C_4	24g	0.535(3)	0.145(2)	0.145(2)	0.11(1)

Table 5.1: Positions of the centre of methane tetrahedra (carbons) within the methane phase B structure as determined from a first data collection, from 9.5, SRS. This refined to a R-factor of 0.09.

intensities. At the time of this data collection a method of beam decay correction had not been determined. This meant the quality of initial data reduction was such that direct methods could not yield a viable structure. The carbon atom positions were, in this case, determined by a trial and error Fourier difference approach. This was possible because of the graphical user interface of the Crystals refinement package [Betteridge 04]. This allowed trial carbons to be inputted then a Fourier difference map ($F_{obs} - F_{calc}$) calculated and the resultant q peaks assessed in relation to the parts of the structure already determined. The final result was a four site structure, which gave 58 molecules within the unit cell. Table 5.1 gives the positions determined for phase B. This structure refined against the data to give a R-factor of 0.09.

Like the study of phase A, the structure was checked with a separately grown crystal. This was collected on station ID27, ESRF. This crystal, was grown in the same cell as

	Wykcoff	x	y	z	U_{iso} (Å^2)
C_1	2a	0.0000(0)	0.0000(0)	0.0000(0)	0.117(13)
C_2	24g	0.0901(5)	0.2783(7)	0.0901(5)	0.094(3)
C_3	8c	0.3192(7)	0.3192(7)	0.3192(7)	0.103(7)
C_4	24g	0.5344(8)	0.1435(6)	0.1435(6)	0.099(3)

Table 5.2: Positions of the centre of methane tetrahedra (carbons) within the methane phase B structure as determined from a second data collection from ID09a, ESRF. This refined to an R-factor of 0.09.

the previous crystal, was phase B crystal at 7.2(2) GPa. On integration, the extracted data gave an R_{int} value of 0.05 with 255 symmetry equivalent reflections. Refinement resulted in the positions given in Table 5.2 and an R-factor of 0.09.

5.4 Discussion of the molecular structure

Unlike the structural result on phase A, Chapter 4, there was no ambiguity of space group determination. The structure solution was progressed with $I\bar{4}3m$ because XPREP statistics had narrowly favoured this space group. Later attempts to solve the structure in the remaining space groups did not result in viable solutions. The structure basis outlined in Tables 5.1 and 5.2. is an arrangement molecules on Wykcoff positions 2a, 8c and two on 24g. In $I\bar{4}3m$ there are no further reflection conditions imposed by the special positions. These positions can be translated into space group $I23$, from translating the xxx (8c) positions from $I\bar{4}3m$ to xyz positions. There is no reduction in R-factor through doing this and any movement in the refined positions is negligible when compared to the esds. Hence the assignment of the higher symmetry $I\bar{4}3m$ is correct in this case. The remaining space groups that had been identified ($I2_13, Im\bar{3}, I432$ and $Im\bar{3}m$) do not allow for the determined arrangement of carbon atoms.

At 8.3(2) GPa the determined molecular structure implies an average molecular volume of 28.95 Å^3. Because of the anomalous low pressure of growth this can be compared directly to one of the crystals of phase A grown at a pressure of 8.5(2) GPa. This phase A crystal implied an average molecular volume of 30.48 Å^3 at this pressure. With this information the volume change between phase A and B found to be 5 %. When compared to the 1 % drop between phase I and phase A this is very large, indicating a significant structural re-arrangement.

Figure 5.8 is an illustration of the molecular structure of phase B determined by this study. The study of Umemoto *et al* had already shown that the structure of phase B departed from the original expected behaviour discussed in Section 5.1. Instead of

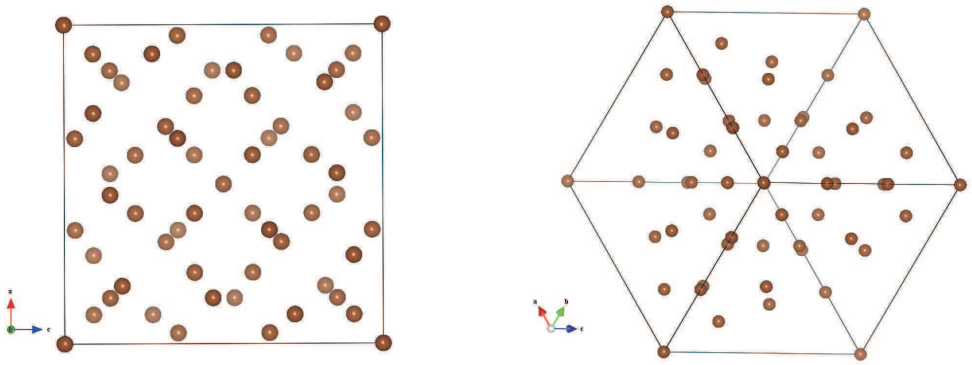

Figure 5.8: Illustrations of the molecular structure of phase B determined by this study, viewed along a [001] direction (left) and a [111] direction (right).

the expected hexagonally close packed arrangement [Hebert 87, Bini 97], the structure of phase B had been indexed to be cubic. The original assumptions of methane's evolution with pressure had been based on a 'bad rare gas' model. This proposed that the behaviour of methane would fall between that of the rare gases (fcc to hcp) and ammonia (fcc to orthorhombic(distorted hcp)).

Examining the local co-ordination of the C_2 and C_4 positions it is seen that each of these carbons have 12 nearest neighbours, a number indicative of a close packed arrangement, Figure 5.9. This is in contrast to the C_1 and C_3 positions which have 16 nearest neighbours - a capping atom upon a four-member ring, over-topped by a six-member ring chair arrangement that is capped by a triangle. If fact closer examination of the C_2 and C_4 co-ordination spheres show large 'cavities' where the close packing has been distorted to allow for the larger 16 member cage to be constructed.

Another observation of the structure is the variety of molecular distances (expressed as carbon to carbon distances) that it exhibits. The distance shown in Table 5.3 are calculated from the structure in Table 5.2, sample at 7.2 GPa. They range from 3.058 to 3.918 Å. The smaller distances are between the the carbons which have 12 nearest neighbour, with the larger distances between the 16 co-ordinated carbons. This binary segregation into the 16 co-ordination 'cage-like' structures and the tighter packed 12 co-ordinated close packed carbons could account for a segregation of ordered and disordered molecules. In any case the range of carbon to carbon distances suggest a range of molecular environments within the structure, agreeing with spectroscopy studies [Hebert 87]. The structure of phase B is a departure from close packing, hexagonal or otherwise, indicating the limitations of assuming a 'bad rare gas' model for methane structure evolution.

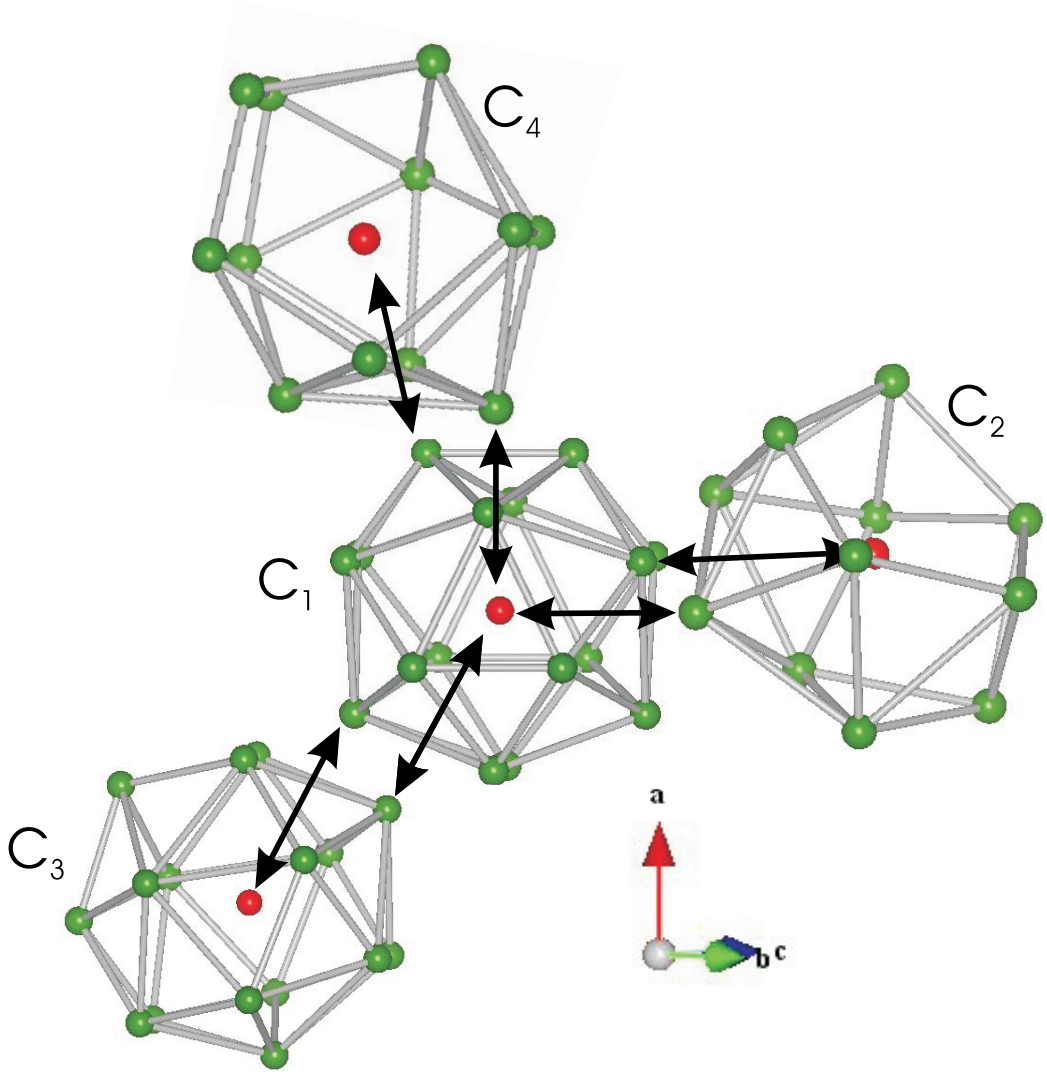

Figure 5.9: The four co-ordination spheres of the carbon atoms and how these correlate to form the structure. The arrows indicated where the central atom of each cage lies within its neighbours co-ordination sphere.

Carbons	Distance (Å)
C_1 - C_2	3.673
C_1 - C_3	3.758
C_2 - C_2	3.194
C_2 - C_2	3.058
C_2 - C_3	3.622
C_2 - C_4	3.204
C_2 - C_4	3.649
C_2 - C_4	3.398
C_3 - C_1	3.758
C_3 - C_2	3.918
C_3 - C_2	3.622
C_3 - C_4	3.944
C_3 - C_4	3.475
C_4 - C_4	3.541
C_4 - C_4	3.578

Table 5.3: Details of carbon to carbon distance in the phase B structure determined by this study. The values were determined from the positions given in Table 5.2

5.5 Contaminants

Further attempts to grow a single crystal in a separate high-pressure cell sparked concerns. The crystals studied in Section 5.3 were grown in a cell identified as MBΔ9. The cell used for determination of the phase A structure was MBΔ1. As discussed in Section 4.4.3 the crystal of phase A used to first determine its structure was at an anomalous high pressure of 13.6(2) GPa. This was because the original intention for this cell, MBΔ1, was to grow a single crystal of phase B. Despite following the same path initially as that described in Section 5.3, the result in cell MBΔ1 was always crystal of phase A. At the time it was thought that the differing pressure performance of this cell could describe its contrasting behaviour. So the attempt of growing a phase B crystal was repeated at higher pressures. Despite attempts of growing at 10 GPa and 14 GPa (resulting in crystals at 9.1(2) GPa and 13.6(2) GPa) all became good single crystals of phase A. This behaviour is in stark contrast to that of the cell used for the study within this chapter which had grown a phase B crystal at 8.3(2) GPa, and later re-grown at 7.2(2) GPa. Whilst this behaviour is not inconsistent with the literature (phase A has been observed to 15 GPa previously and similarly phase B had been observed to exist to 7 GPa [Nakahata 99, Hebert 87]), the differences in the behaviour of the cells would have to be investigated.

One difference identified was a detail mentioned on the process of loading the cells. MBΔ1 was sealed within the cryo-loading loading apparatus from the start of the

procedure. In contrast, MBΔ9 was loaded in conjunction with another cell, and was pre-cooled in liquid nitrogen before being placed into the pool of condensed methane. Although the cell was closed when place in the liquid nitrogen, there is a danger that this could have introduced a nitrogen contaminant into cell MBΔ9. This contaminant could be producing the difference in behaviour between the cells. To test for the presence of nitrogen (or indeed any other contaminant) the LABRAM Raman spectroscopy system, normally used for monitoring ruby fluorescence, was used. A detailed description of Raman spectroscopy is beyond the scope of this chapter, and indeed this thesis. Briefly it is a technique which uses lasers to excite molecules to higher energy states, and then observes the energy shifts as the molecule returns to its ground state. The energy shifts result in spectra which is characteristic to the environment of the molecule/atom which is present. For the purposes of this study it is an way of quickly identifying what molecular species exist within the sample area.

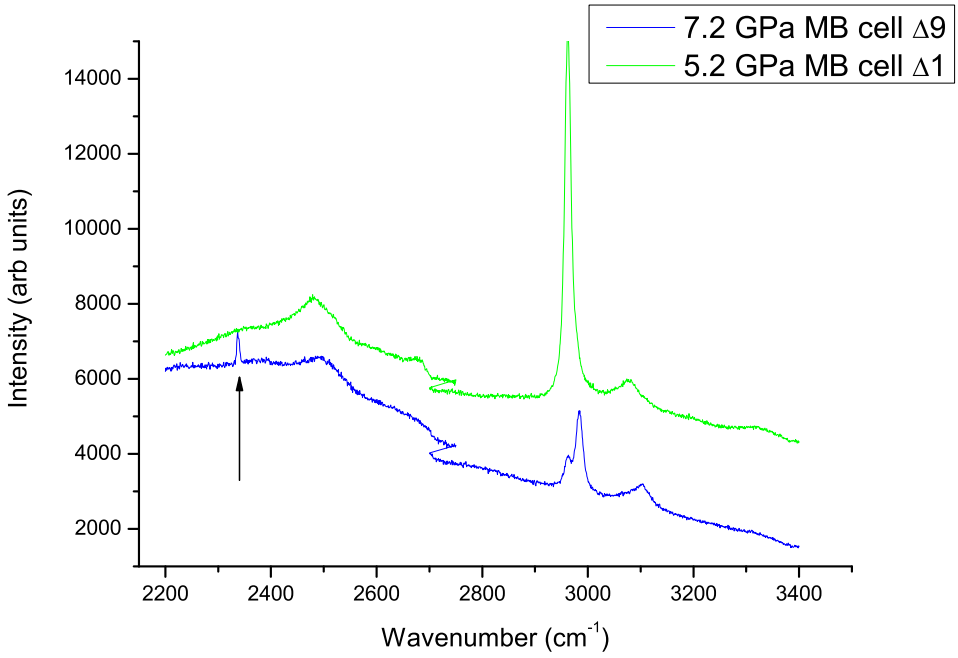

Figure 5.10: Raman spectra from the two Merrill-Bassett cells used during this study. The peak at $\sim$2350 cm^{-1} marked by the arrow in the lower blue spectra is from the triple bond between nitrogen molecules. The spectra from the methane itself can be seen about 3000 cm^{-1}. The split in the larger peak(seen in the blue line) is a characteristic feature of phase B [Hebert 87].

Figure 5.10 compares Raman spectra from the two cells. In both spectra the

characteristic ν_1 and ν_2 peaks from methane are observed (about 2980 cm^{-1} and 3075 cm^{-1} respectively). In the spectra from MBΔ9 (blue line) a peak can be seen at $\sim$2350 cm^{-1}. This energy is characteristically from triple bonded nitrogen within its molecular environment and confirms that nitrogen is present in the sample space. In an attempt to try and determine the extent of the contamination a micro-Raman study was carried around the sample area of MBΔ9, with the results presented in Figure 5.11.

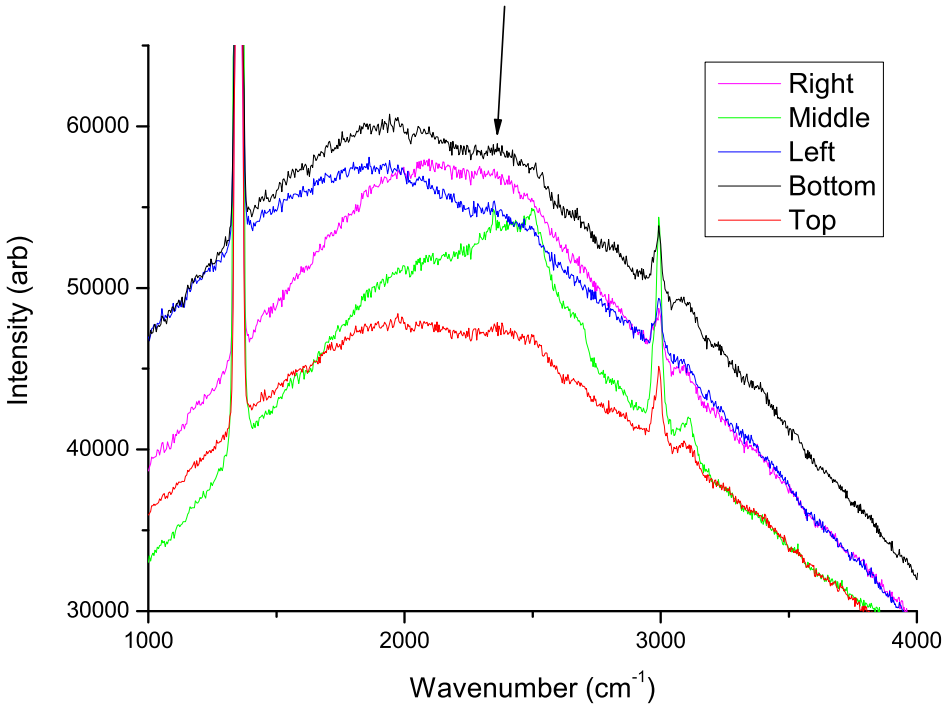

Figure 5.11: Spectra taken from different locations about the sample space of MBΔ9. It is taken over a wider spectral range than Figure 5.10 to show that there are no additional contaminants. The black arrow points to the location of the nitrogen peak, which can be seen in the spectra from the middle of the cell (green) and the left of the cell (blue). This shows that nitrogen is not present throughout the sample space, but methane is.

Taking advantage of the small size of the LABRAM laser spot (9-10 μm) compared to the size of the gasket (100 μm) molecules present at a range of localities within the sample space could be identified. Figure 5.11 shows that nitrogen is not present throughout the sample space, whereas methane is. This suggests that the amount of nitrogen contamination would be less than 10 % of the sample.

The fit of molecular structure outlined in Table 5.2 to the powder diffraction data

in Section 5.2 is shown in Figure 5.12. Unfortunately the loading that produced this pattern was no longer available for checking for contaminant. But as a reason for the presence of nitrogen in MBΔ9 was identified, it would be reasonable to suggest that nitrogen was not present in any other loading. The agreement of the structure to the powder data and the chemical neutrality of nitrogen suggests that the nitrogen is not combining with the methane to form a new material. But it does seem to be exacerbating the hysteresis between phases A and B.

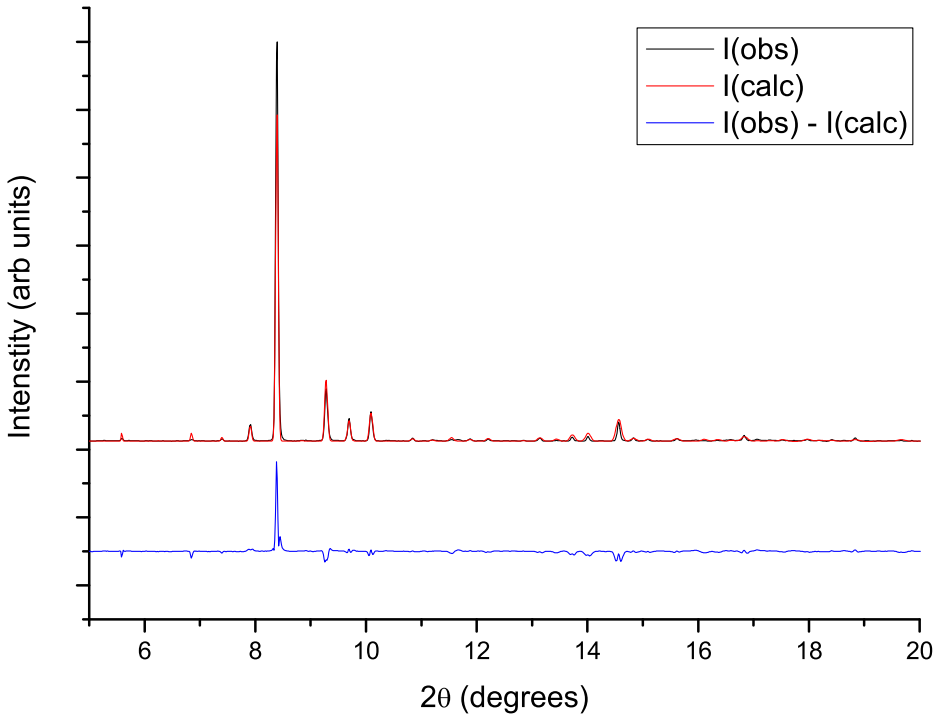

Figure 5.12: Rietveld refinement fit of the structure determined in Section 5.3 against the data collected as part of the study in Section 5.2. The structure fitted with χ^2 = 1.088 and wRp = 0.11. The difference curve indicates that the fit could still be improved. This could be a result of textural effects, and the fact that the structure was refined with carbon positions only (i.e. not including hydrogen).

There has been no previous reporting on the effect of nitrogen or any other contaminants on methane structures in the literature before. There are a number of methods described for loading methane. Of the seven diamond anvil cells studies described in Section 4.1 and 5.1 only two studies were identified to have a risk of contamination on loading [Nakahata 99, Umemoto 02]. The method these described

involves spraying methane gas to be condensed on a gasket kept at liquid nitrogen temperature. With this method there is a high chance of significant contamination. The phase A part of this study is known to have no nitrogen contamination, and the indexing of the cell agrees with the possibly contaminated work [Nakahata 99].

The contamination in this study can reasonably only be attributed to the MBΔ9 cell, used for the single crystal experiment. This was the only successful loading where the 'pre-cooling' method was used. All of the other loadings in a diamond anvil cell, for the powder diffraction study of phases A and B and the single crystal study of B, can be reasonably assumed to be contaminant free. With this is mind, and the agreement in unit cell and structural determination between the studies, the presence of nitrogen can be assumed to be having no effect on the crystal structures of methane under pressure. The effect upon the transition between phases A and B of nitrogen is intriguing. How significant is the effect? Does this finding potentially question the existence of phase B as a distinct phase of methane? These questions are explored further in the later Section 5.7.

5.6 Neutron diffraction

Similar to the previous study in Chapter 4 the next logical step in the structural determination of phase B was to perform powder neutron diffraction. This study was conducted with the Paris Edinburgh press on PEARL/HiPr at the ISIS neutron facility using sintered diamond anvils in a V3-pentane Paris-Edinburgh press with either single toroid or double toroid gasket assemblies. The sample was loaded in to the press with the method described in Section 3.5.1. A description of each of the loading, and how the sample was studied is detailed in Table 5.4. Because of the desire for the maximum signal from the sample no pressure calibrant was loaded into the sample space for each attempt. The pressure of the sample was approximated from the methane diffraction pattern using the equation of state determined in [Nakahata 99]. This has been fitted with a Birch-Murnaghan equation of state giving $V_o = 45.9$ Å^2, $K_o = 7.9$ GPa and $K'_o = 4$. The unit cell volume of the sample at every pressure was obtained by Rietveld refinement in GSAS [Larson 94] with the carbon structure determined in Section 5.3. This was then divided by the number of molecules in the unit cell (21) to determine an average molecular volume for the methane molecules.

Three different pressure - temperature routes were followed in an attempt to form a sample of methane phase B. The first route followed to form phase B was to pressurise the sample to approximately 10 GPa (molar volume of 27.43 Å^3) and to leave the sample for two weeks. The time dependance of formation of phase B had previously been reported, [Bini 97, Hebert 87]. It was hoped this would enable formation of phase

Loading	Date	Gasket	Comments
1	15/09/06	Single toroid	Taken to 110 tonnes, left for 57 days. Then cooled to 110 K. Load increased to 160 tonnes at 200 K.
2	26/11/06	Double toroid	Load put to 65 tonnes, no sample.
3	28/11/06	Double toroid	Put to 80 tonnes, no sample.
4	06/12/06	Single toroid	No sample.
5	07/12/06	Double toroid	Leak of pig tail, loading lost.
6	08/12/06	Double toroid	Stepped to blow-out at 200 tonnes. All collections at room temperature.
7	09/12/06	Double toroid	Anvils closed up, no sample.
8	08/02/08	Single toroid	Stepped to 109 tonnes then heated to 100°. Then put to 130 tonnes and heated to 90°.

Table 5.4: Details of the methane loadings at ISIS for the study of high-pressure deuterated methane

B at a relatively low pressure. This was desired as the lower pressure would dictate that the anvils would have a larger separation and more diffraction signal could be collected from the sample. This would allow for better characterisation of phase B with neutron diffraction. Unfortunately, this method did not yield phase B

The second method, to obtain phase B at a modest pressure for the reasons described above, was to compress at 200 K. It was hoped to take advantage of the lower transition boundaries at lower temperatures, Figure 5.2. Again this did not work, and phase A was retained.

The last method to attempt to form phase B was to compress until either a transformation or a blow out. Unfortunately the sample blew-out before transformation reproducibly upon compression from a load of 190 tonnes to 200 tonnes. A pattern was collected at 190 tonnes which gave a volume of 22.56 $Å^3$, using the equation of state [Nakahata 99] this equated to a pressure of 19.1 GPa.

The failure to obtain phase B in a deuterated methane sample again throw doubt on phase B's existence. Despite undertaking a number of pressure-temperature routes to obtain the phase, the sluggishness of the transition prevailed and phase A was obtained at all conditions. The absence of phase B could be a result of the deuterated sample. Transitions to phase B from phase A have been reported up to pressures of 14 GPa [Bini 97]. This would imply a deuteration effect on transition of $\sim$5 GPa, much larger than than reported for other hydrogenous systems an itself should be investigated further. Coupled with other observations in this chapter, suggests that there is much still unconstrained on the phase A to B transition. In the absence of a neutron powder pattern of phase B the hydrogen positions could not be determined by Fourier difference cycling.

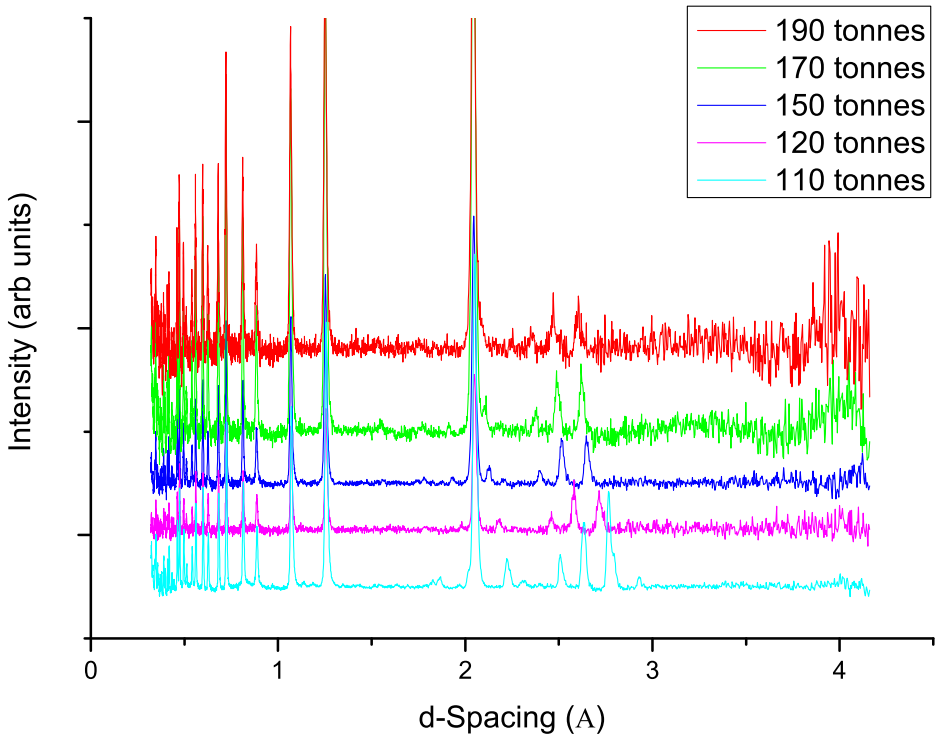

Figure 5.13: Powder patterns of deuterated methane collected at 100 to 190 tonnes on the PEARL/HiPr diffractometer at ISIS. The signal of the sample gets worse as load is increased because the anvils obscure the sample from the detectors. The sample is seen to maintain phase A at all conditions.

5.7 Phase B to HP transition

As previously discussed in Section 5.5 the formation of Phase B at lower pressure would seem to be an artefact of nitrogen contamination, as a non-contaminated cell did not form phase B even at 13.6(2) GPa. Whilst this is not inconsistent with the literature (phase B can exist between 7 and 14 GPa [Hebert 87, Bini 97]) the lack of reproducibility was perplexing. The added nitrogen contamination would seem only to be exacerbating the phase A to B transition. But the added evidence from deuterated methane not being able to form phase B under a range of conditions also questions the existence of B as a distinct structure.

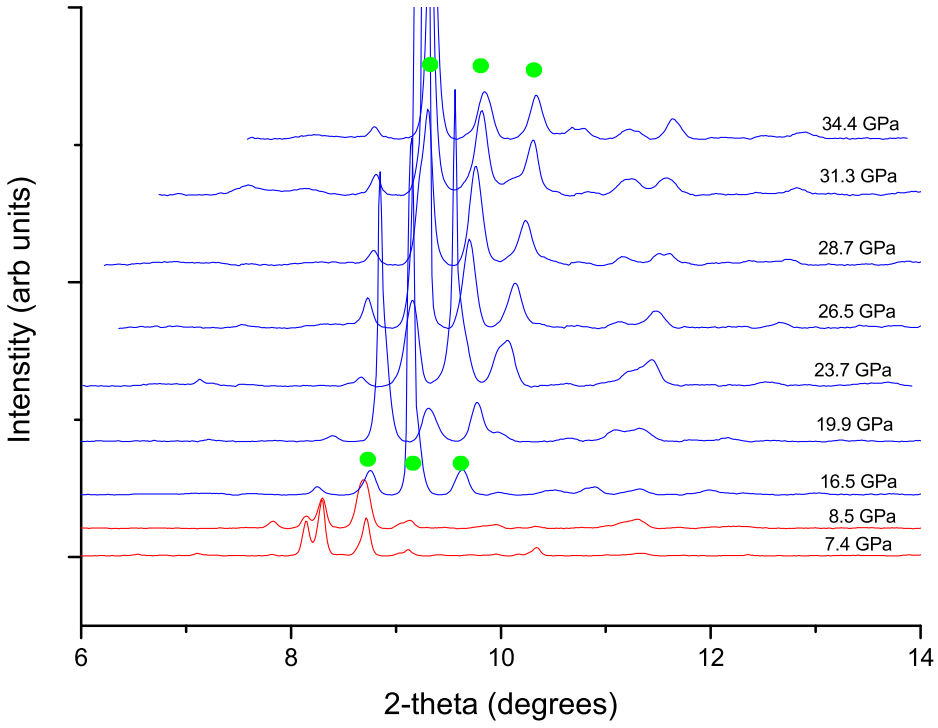

Figure 5.14: Powder diffraction patterns collected from ID09A, stepping through the B to HP transition. The profiles in red index to the phase A unit cell and those in blue index to the phase B unit cell. The reflections charted in Figure 5.15 are marked with a green circle. These data were collected at a $\lambda = 0.4130$ Å.

To determine whether or not phase B is a distinct phase a study was conducted at higher pressures. At 25 GPa at room temperature phase B has been reported to become the 'hexagonal' or HP phase [Bini 97]. This was assumed to be the final ordered

state of methane. Comparisons between the two phases, B and HP, show that their spectra are very similar and the differences between them were postulated to be a result of hydrogen ordering. Previous diffraction of methane collected from 16.9 to 37.1 GPa had reported a very slight anomaly in volume at 25 GPa, but their evidence was inconclusive [Umemoto 02].

A powder diffraction study was undertaken at ESRF, station ID09a on methane in a bevelled diamond anvil cell. The bevelled design of the diamond anvils is to compensate for the deformation of the diamonds under pressure exceeding 50 GPa. The original intention of the study was to reach megabar pressures but it was soon clear that the loading would not achieve this. As a result the pressure was stepped down from 32.2 GPa until it back transformed to phase A at 8.5 GPa, these data are shown in Figure 5.14.

The textured powders prevented any detailed refinement on each pattern. But instead the *d*-spacing of three reflections which were present in each pattern were charted as a function of pressure. The results of this are presented in Figure 5.15. It shows a discontinuity in the *d*-spacings between the patterns at 23.6 and 23.7 GPa.

This discontinuity is attributed to the transition between phase B and HP, which has been effected by a down stroke hysteresis. Despite the change in volume, there is no major change in the diffraction pattern. These data show that there is a transition between B and HP, and as such phase B is a distinct phase of methane. With little change in the major features of the diffraction pattern, phase HP probably retains the molecular structure of phase B but increases the ordering of the hydrogen.

5.8 Discussion

Because of the similarities in diffraction pattern between B and HP, and separate reports on the similarity of their Raman and IR spectra this study proposes that methane phase B and HP have the same molecular structure. The similarities between the B and HP powder diffraction pattern that this and previous work shows [Umemoto 02] suggest that this transition involves little change in the tetrahedron (carbon) positions and any differences could be because of ordering and change of the local symmetry of the hydrogen. It also raises doubts as to whether the preceding HP phase is the 'final' ordered structure as stipulated in [Bini 97], and there is now some experimental evidence supporting these doubts [Hirai 08].

This recent study presented the possibility of a time dependent pre-B structure and further post-HP structures in methane [Hirai 08]. As none of the studies for this thesis were undertaken in the time scales that is proposed for pre-B, no comment on this phase can be made. The post-HP transitions that they propose are from Raman

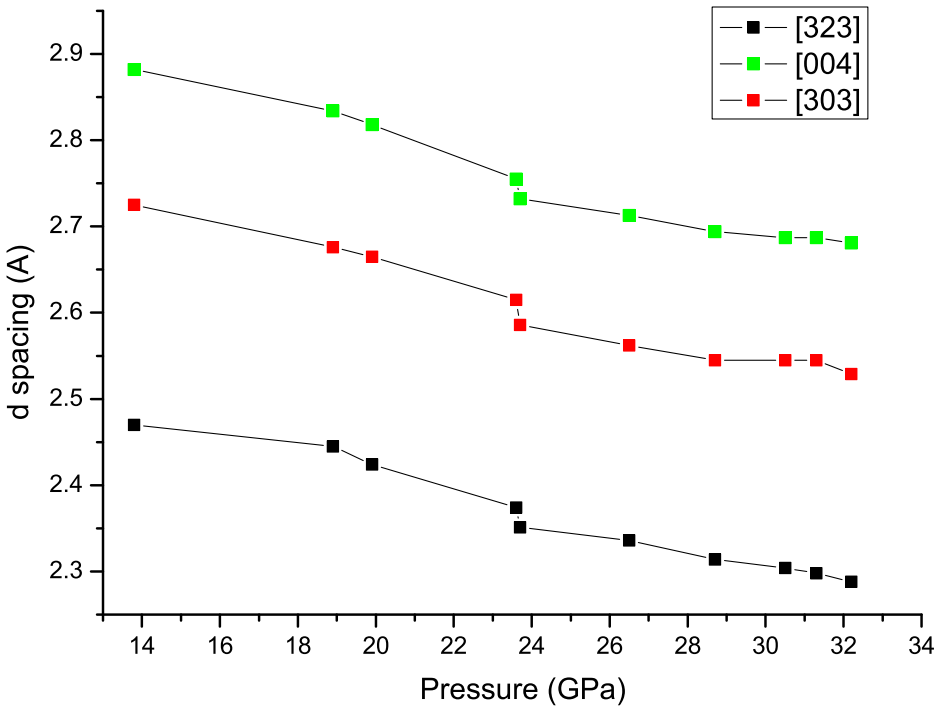

Figure 5.15: Charting three reflections present in each of the patterns shown in Figure 5.14 as a function of pressure. The discontinuity shown in all the reflections between 23.6 and 23.7 GPa is attributed to the transition between phase B and HP.

studies with x-ray diffraction to 81.0 GPa. There is little change on compression in the diffraction patterns, and pattern is indexed with the smaller unit cell existing in the literature [Umemoto 02]. The Raman spectroscopy that is presented in Hirai *et al*'s study is more convincing, with the ν_1 and ν_2 shown to split at 35.0 and 65.0 GPa. These results suggest that the molecular structure that this study believes is common to B and HP is retained to higher pressures. Further this, the post-HP transitions suggest that HP is not the 'final' ordered state of methane and that these later transitions are further ordering ones.

Doubts were raised on whether or not phase B was a distinct structure of methane. These were because of the similarities of the diffraction pattern between B and HP, and the behaviour of non-contaminated and deuterated samples described in Sections 5.5 and Section 5.6. This evidence suggest that phase B is a metastable transition phase, intermediate between A and HP. Nitrogen contamination could be seen to be exacerbating the A to B hysteresis, enabling phase B to be formed at anomalously low pressures. As part of this study the volume change of the A to B transition was constrained to 5 %, and a further volume contraction was observed at 23 GPa on pressure decrease. The volume change at transitions from A to B and B to HP do suggest that it is a distinct phase. It is clear that much is still to be understood about the nature of the high-pressure transitions of methane. Knowledge of the molecular structure is a sure step towards this understanding.

5.9 Summary

This chapter describes the first, in depth structural study of methane phase B, including a range of diffraction techniques. Along similar lines to the study of phase A in Chapter 4, the study began with a powder diffraction study to confine the unit cell and symmetry. Unlike the phase A study, the unit cell was indexed to be different from that existing within the literature, still cubic but with a lattice parameter that is $\sqrt{2}$ bigger. The symmetry of phase B was shown to be body centred, one of $I23$, $I2_13$, $Im\bar{3}$, $I432$, $I\bar{4}3m$ or $Im\bar{3}m$.

The distribution of intensities from the single crystal data implied that the symmetry was described by the $I\bar{4}3m$ space group. Fourier difference refinement revealed the molecular (carbon) structure which refined to an R-factor of 0.09 from separate crystals collected at different synchrotrons. The molecular structure was discussed, and shown to have some features of a close packed arrangement. The variety of carbon to carbon distances that the structure exhibiting was proposed to be evidence that some of the molecules are still disordered.

The inclusion of contamination within the cell that determined the molecular

structure, meant that the meaningfulness of the structure it yielded had to be carefully justified. The behaviour of the sample in each loading is consistent with the literature, but the lack of reproducibility between the cells was frustrating. As this cell was reasoned to be the only one that had been subject to contamination, comparisons with other studies within the literature and this work, were used to justify the validity of the molecular structure.

Similarly to the previous study on phase A, attempts were made to conduct a neutron diffraction study on phase B. Unfortunately, despite a number of different pressure-temperature paths explored, the phase B was not formed in deuterated methane.

The validity of phase B as a distinct structure of methane was supported by the stepped x-ray powder diffraction study. Upon decompression the *d*-spacings of the profile were seen to undergo a discontinuous shift between 23.7 and 23.6 GPa. This feature close to the upstroke transition between B and HP at 25 GPa, was attributed to the back transition between these phases. The sample was very textured, and did not allow for detailed refinement. But it was observed that there was little change in the main features of diffraction pattern. From this it was postulated that the molecular structure is retained across phases B and HP.

Chapter 6

Further studies of the phase diagram

6.1 Introduction

This chapter will first describe two investigations on the high-pressure behaviour of methane. Rather than detailed structural investigations the two studies to be described explored the phase diagram of methane. One of the most prevalent questions raised during the previous chapters was the coupling of the low and room temperature phase diagram of methane. The first investigation to be described, was a bid to determine the relationship between the room-temperature and low-temperature phase diagrams. The second investigation set out to characterise the transition observed during methane crystal growth, Section 4.4.1.

6.2 Low temperature neutron diffraction

As set out in Section 4.1 the first investigations into the room temperature phases of methane beyond 5.2 GPa suggested that phase IV existed from low to room temperatures. Bini *et al* [Bini 95] pointed out that there was no experimental evidence to couple the room temperature and low temperature phase diagram. As a result the room temperature phase previously denoted phase IV was renamed to phase A. In a later study Bini *et al* [Bini 97] confirmed the separating of the phase diagram with a spectroscopy study that spanned 20-300 K, 0.2 - 30.0 GPa. The phase boundaries that were set out by charting the ν_1 mode with infra-red spectroscopy are shown in Figure 6.1.

The spectra of phases IV, V and VI were characterised by experiments which compressed at low temperature (below 125 K). The transitions between these low

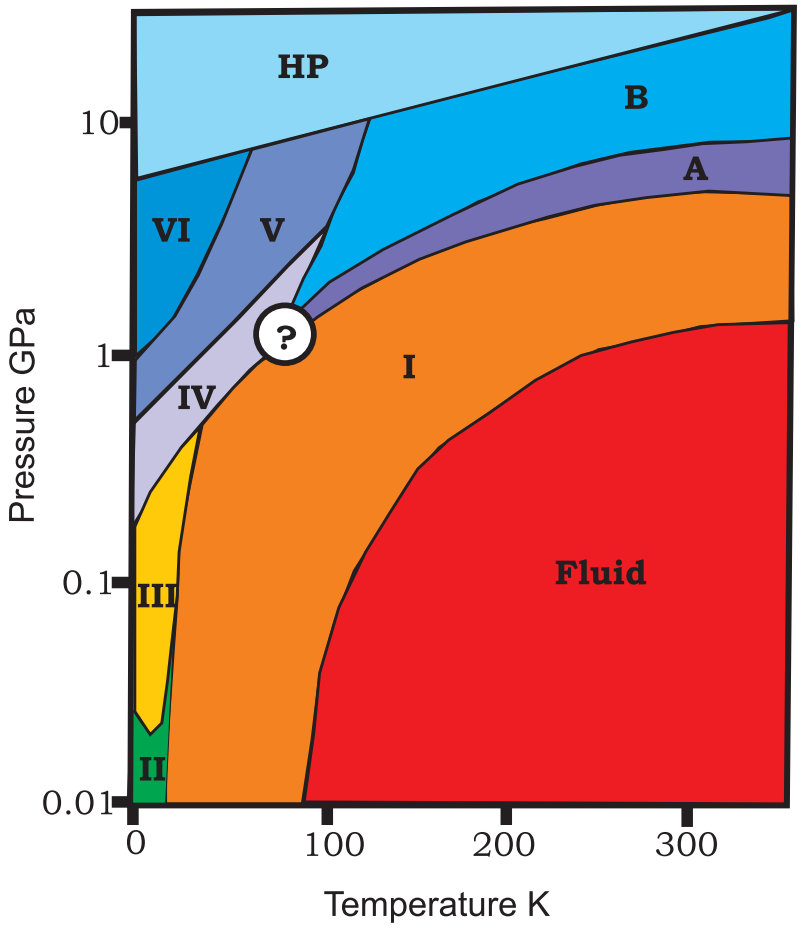

Figure 6.1: The phase diagram of methane after [Bini 97].

temperature phases and the room temperature (A, B and HP) were characterised by separate isobaric cooling experiments. The spectra obtain from these were poorly resolved and no appreciable change was seen, other than slight shift in the ν_1 position. In Section 5.7 it was shown that despite a change in the pressure response of the ν_1 between phases B and HP, there is no major change in the diffraction pattern. Hence obtaining diffraction patterns at high-pressure and low temperatures would enable a better characterisation of any structural transitions at low temperatures.

In their paper Bini *et al* describe that the spectra between phase IV and V are very similar, but on the basis of arguments explained in Section 4.1 they assign the structure of phase IV to a tetragonal symmetry and V to a hexagonal one. Later discussions in the study mapped phase IV to A and V to B. As has been shown in Chapter 5, the structure of phase B is not hexagonally close packed (hcp), but instead cubic with some distorted hcp features. Would the low temperature phases take up similar structures?

In Figure 6.1 Bini *et al* show that at 100 K and 2 GPa methane should exists as phase B. The failure to form phase B during the room temperature neutron diffraction study, Section 5.6, makes the opportunity of synthesis at low temperatures an inviting one. To attempt this, and to answer some of the points posed above, beamtime was applied for and granted on the D20 instrument at ILL.

6.2.1 Experiment

The D20 instrument has been previously described in Section 3.4.1. Time was applied on this instrument as its versatility extends to collection of *in situ* high-pressure low temperature data sets. This is because the VX5 Paris-Edinburgh press owned by ILL has a specially adapted closed cycle refrigerator (CCR) which enables it to potentially reach temperatures of 3 K.

To ease loading and to cut down on wastage of beamtime there was an attempt to pre-load the sample before the experiment. This could be achieved using a special clamp that been designed at IMPMC, Paris. The clamp and its use is demonstrated in Figure 6.2. The clamp was loaded in Paris a month before the experiment was to commence. The clamp was loaded using the cryo-loading method described in Section 3.5.1. As well as enabling pre-loading of the sample, the smaller size of the clamp meant that loading was much quicker, as it did not take as long to cool as the whole press.

The attempt of loading the clamp in Paris was not successful, and no sample was contained in the gasket. A second attempt to load the clamp at ILL was successful, and data from D20 revealed a good liquid signal. However, despite increasing the load, the sample would not crystallised. The pressure of the sample would not increase, and the sample was downloaded. The reason for this failure of pressure increase was revealed

Figure 6.2: Images of the sample clamp for the Paris-Edinburgh press. The parts that make up the apparatus are illustrated in (a), there are two anvils, two backing disks, two plugs and a holding ring that fit inside the body of the clamp. The apparatus is assembled in (b). Load is applied to the upper plug and pressure is generated at the sample. One the load is applies the holding ring (which has a thread to attach it to the clamp body) is screwed to hold the pressure in the clamp. The plugs on both the top and bottom of the clamp means that one the clap is placed into the Paris-Edinburgh press (c) further load can be applied to the sample.

when the clamp was taken apart. Figure 6.3 shows some of the cracks that were found in the clamps components. It is thought that the failure of the clamp occurred during the loading process.

Figure 6.3: The top plug of the clamp which was damaged during the ILL experiment.

Because of the damage to the clamp a similar re-loading was not possible. Loading instead had to be completed with the entire cell, with the method described in Section 3.5.1. This was complicated somewhat as the CCR had to be attached, as in Figure 6.4, during this process. Nevertheless, a successful loading was achieved, but by this time one day of beamtime had been lost.

The press was loaded with a single toriod SME gasket and used sintered diamond anvils. Unlike the loadings described in Chapters 4 and 5, a curl of lead was placed into the gasket before the methane loading. Because of the aim of the study was for phase identification, rather than previous structure determination aims, there was a need for a pressure calibrant. The lattice parameter of lead from Rietveld refinement could be used for this, but the equation of state would need correcting for low temperatures. There was an additional hope that the lead would prevent significant single-crystal growth. The equation of state of lead [Mao 90] was adjusted for volume thermal expansivity (α_v = 8.1 x 10^{-5} K^{-1}) from 300 K. At some points the lead peaks were obscured by

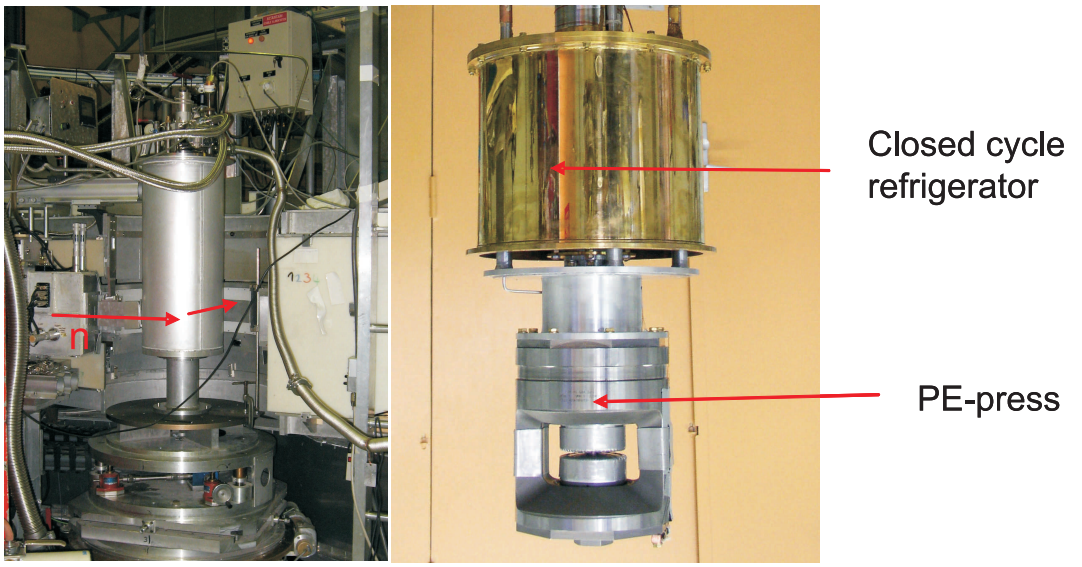

Figure 6.4: The Paris-Edinburgh press mounted on D20. The image of the left shown the whole assembly in place on D20 incased in a vacuum tank. This tank could be filled with liquid nitrogen to speed up the cooling process. The right image shows the assembly within the tank, with the VX5 Paris-Edinburgh press suspended beneath the closed cycle refrigerator.

the sample pattern, decreasing the accuracy of the pressure determination.

Figure 6.4 shows the press mounted on the instrument. The data were collected on D20, ILL with a wavelength of 2.413 Å, high flux, medium resolution mode. The press was rotated in ω by 60° to mitigate against the texture that methane samples adopted. The profiles were then averaged to obtain a better representation of the intensities. By rotating the cell an additional problem was encountered. The VX variant Paris-Edinburgh press, as an improvement for angle dispursive diffraction, has only two tirods whereas its predecessor has four. When the cell is rotated the tirod will obscure part of the detectors from the sample and impact on the collected pattern. This is demonstrated in Figure 6.5. To mitigate against this a script was written to cut the obscured part of each pattern out, and sum the result to one profile. This gave very bad patterns from the point the tirod obscured, and the end result was that each collection had to be truncated at this point.

A thermocouple placed close to the sample space detached during cooling. Instead the temperature of the sample had to be determined from other thermocouples. The temperature was measured at two points, one at the CCR itself attached to the top of the cell and another at the bottom of the press. The thermocouple at the bottom of the press corresponded to the maximum temperature of the sample, and the thermocouple at the CCR to the minimum. Figure 6.6 shows the progression of the temperature

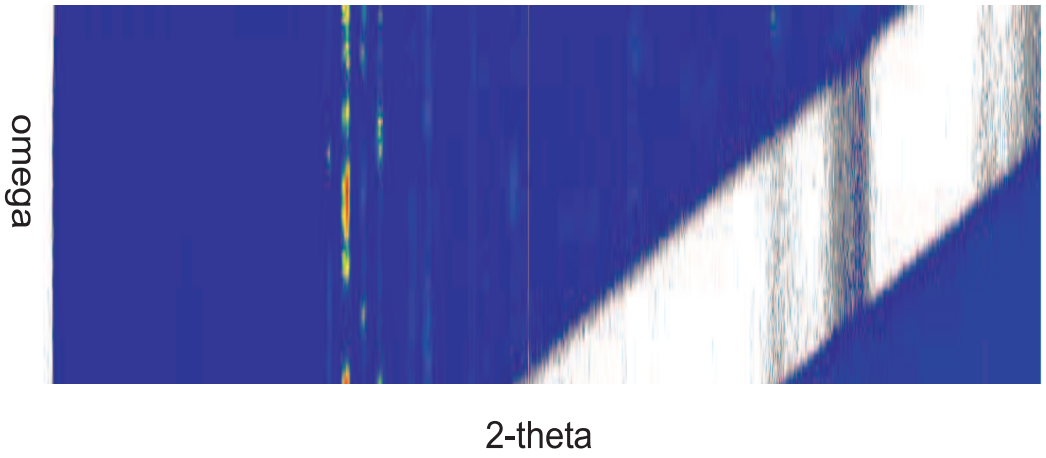

Figure 6.5: A characteristic data collection from during the low temperature neutron diffraction experiment at ILL, The effect of the tirod on the patterns collected can be seen, scoring though the ω scans. This image also demonstrates the texture of the sample. An ideal powder would give constant vertical lines, corresponding to a refection being observed at every step in ω. This is not the case for the deuterated methane sample. Taking an average over the scans would alleviate the texture problems.

across the experiment. This shows how the sample temperature lagged behind that of the CCR. The lag is a result of the large mass of metal that makes up the press. It was important to wait for the temperature to stabilise before data collection. Unfortunately this added to the time of the experiment and restricted the coverage of the phase diagram.

The experimental path was designed to follow Bini *et al*'s [Bini 97] pressure temperature paths in a hope to form phases V, VI and B. Because of the danger of solidifying the helium pressure medium at low temperatures the load on the cell can only be applied at about 80 K. From 80 K (temperature of the CCR) the cell was cooled and heated to other temperatures to increase the coverage of the phase diagram. The experimental path was as follows: the sample was initially compressed to 1.5 GPa at room temperature to form phase I. The press was then cooled, the sample formed phase A at 120 K 1.5 GPa, to 25 K. After a collection at 25 K collection the press was warmed to 80 K to increase the load to 2.5 GPa. At this pressure the press began to leak. The leak was thought to come from the lead seal on the piston. To try and fix the leak the press was warmed to 120 K and data collected then (a regulating system on the compressor was able to stabilise the load to the press). As the press was still leaking slightly the load was increased to 3.6 GPa, which finally sealed it. At this load the press was again cooled to 25 K, collected at this point, before warming to 100 K to increase the load to 5.4 GPa. Once at 5.4 GPa, the sample was once again cooled to 25 K for the last low-temperature data collection.

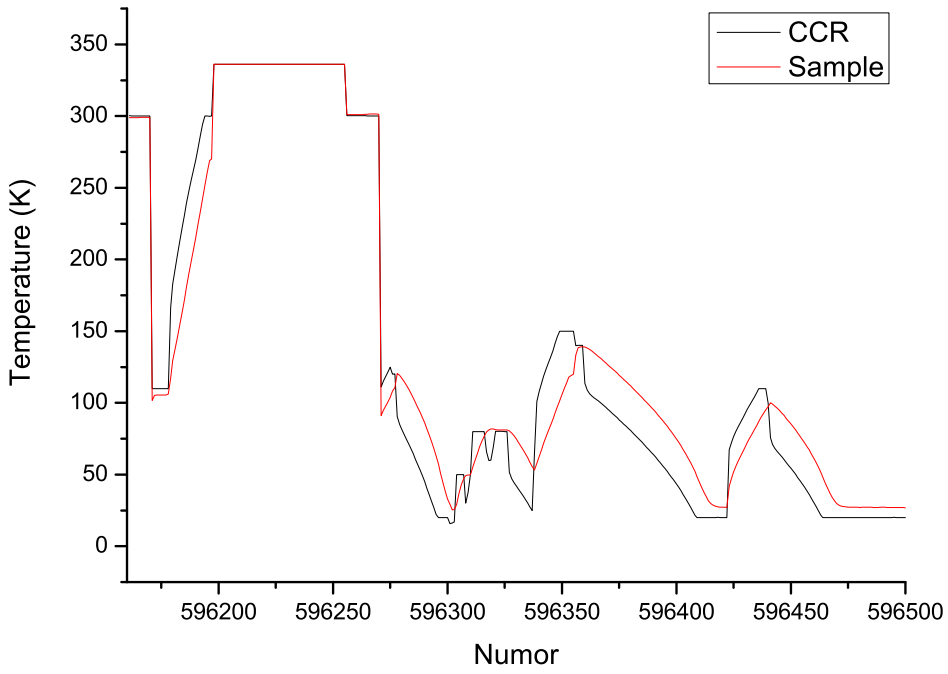

Figure 6.6: A log of the sample and CCR temperatures across the whole low temperature experiment. Numors are designated to each data collection, but the time of these vary. The sample temperature lags behind the temperature of the CCR because of the mass of the Paris-Edinburgh press that surrounds it.

6.2.2 Results

Averaged profiles were obtained from the sample at 27(2) K at three different pressures up to 5.6(2) GPa. Additional average profiles were taken at four different pressures (again up to 5.6(2) GPa), but a variety of temperatures (100-140 K). All averaged profiles described indexed to be rhombohedral, with lattice parameters a $\approx$ 9.0 Å and $\alpha \approx 89.3(2)^\circ$. This is the same indexing as that noted for the room-temperature phase A [Nakahata 99]. The behaviour of unit cell volume across the stated conditions is shown in Figure 6.7.

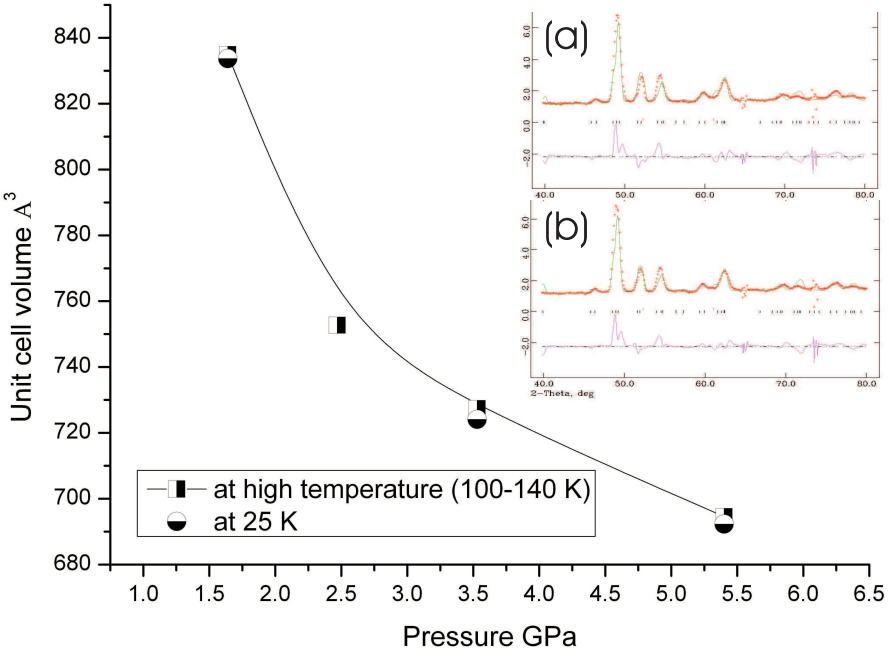

Figure 6.7: The changes of unit cell volume of methane with pressure and low temperatures. The two types of data points, at high and low temperature, show that there is little difference in the structure over this temperature range.

The averaged profiles were refined against the carbon structure for A, predetermined in Chapter 4. All profiles fitted well ($R_{wp} \approx 10$ %) to the structure of phase A. As no phase transformation from the phase A structure was observed, the results question the segregation of low and high temperature phases of methane. The results instead suggest that the rhombohedral room-temperature structure, phase A, is the dominant phase at low temperatures, above 0.5 GPa. On heating to 140 K at 3.5 GPa there was no transformation to phase B, as would have been expected

from the boundaries drawn in the phase diagram, Figure 2.11. It is clear from these measurements that further characterisation is required to accurately chart structural phase boundaries of methane at high-pressure and low-temperatures.

Potentially, the contrast of these measurements to the results of Bini *et al* could be a deuteration effect. According to the phase diagram of this work [Bini 97] Figure 2.11, the experimental path taken should have intersected at least three phase boundaries. This experiment only observed one transition, from phase I to the phase A structure at 1.5 GPa ∼100 K, in line with the boundary proposed by Bini *et al*. This suggest that there is very little effect from the deuteration of the sample, in line with what is observed for water and ammonia. However, to fully answer this question the experiment should be repeated with a hydrogenous sample.

6.3 High temperature single crystal diffraction

In Chapter 4, it was explained that the growth of single crystals for the studies on phase A and B was complicated by the observation of a transition in the sample. The transition, illustrated in Figure 4.12 occurring at 9.3 GPa and 410 K, was interpreted to be between two solids phases as melting has been observed at higher temperatures. As has already been explained, knowledge on the complete phase behaviour of methane is needed to facilitate better modelling of planetary systems. With this motivation the subsequent experiment was designed to characterise the phase after the observed transition at high temperatures. A further advantage of charting the transition visually, was the observation that the sample had a tendency to form a single crystals on transformation. This made the choice of a single crystal experiment very clear.

6.3.1 Experiment

The aim of the this experiment was to collect single crystal data from a methane sample at high-pressure and high-temperature. To characterise the phase above the transition, data would have to be collected at a pressure of ∼7 GPa and a temperature of ∼400 K. This experiment was undertaken as part of a long term project on station 9.5 HPT, SRS, Daresbury laboratories. The set up was modified from that described in Section 3.4.2 to include a resistive heater. This modification of equipment is explained in Figure 6.8. Unfortunately, the set up of the equipment was such that the sample could not be monitored visually, nor the pressure determined during heating. Choosing this set-up, without a cooling base, meant that there was limited time to collect the single crystal data whilst at high temperature.

The sample was loaded cryogenically, as described in Section 3.5.1. Like all the

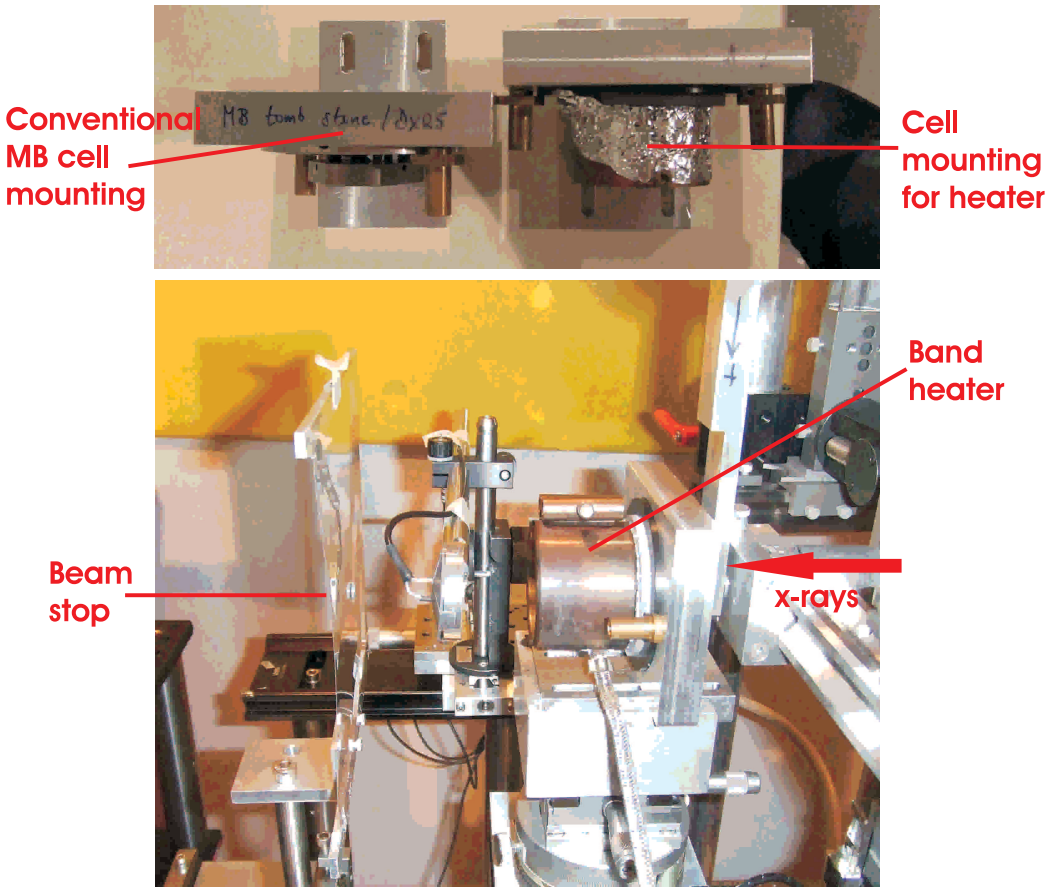

Figure 6.8: The heating apparatus set up on station 9.5, SRS. The top picture shows the change in position for mounting a MB diamond anvil cell to incorporate a band heater. The bottom picture shows the set up on the beamline. Because of the moderate temperatures investigated there was no need for cooling water apparatus.

previous methane samples, research grade methane gas from Sigma Aldrich (99.99%) was used. This was loaded into a 400 μm culet beryllium backed Merril-Basset diamond anvil cell. The cell was pressurised into phase A at 7.7(2) GPa. Before this experiment the cell had been through several heating runs. With this annealing procedure it was hoped to minimise the chances of pressure drops during heating.

6.3.2 Preliminary results

The cell was heated and single-crystal data set was collected once the cell had reached a constant 400 K and again once the cell had returned to room temperature. The pressure measured after heating with ruby fluorescence to be 7.7(2) GPa. At temperature single-crystal data were collected had been collected by rotating about ω -15° to +15° the maximum angular aperture allowed by the beryllium seats within the cell. As an extra precaution, to allow for thermal expansion of the set up, the sample was centred every 5°.

The data collected at 400 K indexed to rhombohedral cell, a = 8.39(3) Å and α = 89.9(6)°, suggesting that methane had been retained in phase A. The closeness of the α value to 90° meant that at this stage the phase could not be ruled out as cubic, and the pattern could also be indexed to a cubic cell with a = 8.39(2) Å. To determine the correct symmetry the data were integrated, the rhombohedral cell gave a R_{int} = 0.12, compared to the cubic cell R_{int} = 0.46. This indicates that the absences and distribution of intensities of the pattern imply that the methane at these conditions is still the rhombohedral phase A. It was concluded that the transition had not been reached and the experiment would need to be repeated.

6.3.3 Results

As a modification to the previous method it was decided to heat up in steps and collect data at each step. This would mean that the sample could be monitored for any significant changes. In the absence of a cooling system there were limitations for how long data could be collected for. As a result extended single crystal collections at each temperature could not be achieved. Instead, 'one-shot' images were collected. Similar to the process of collecting powder data the cell is rocked about an angle in ω whilst the sample is exposed to the beam. The collected image will retain d-spacing information that can be used to characterise the structure at each point.

The sample was contained in the same cell used during the preliminary experiment, before heating the pressure was 7.7(2) GPa and the cell returned to 7.0(2) GPa after the experiment. The temperature was increased with steps of power provided to the resistance heater. The actual temperature was determined with a thermocouple

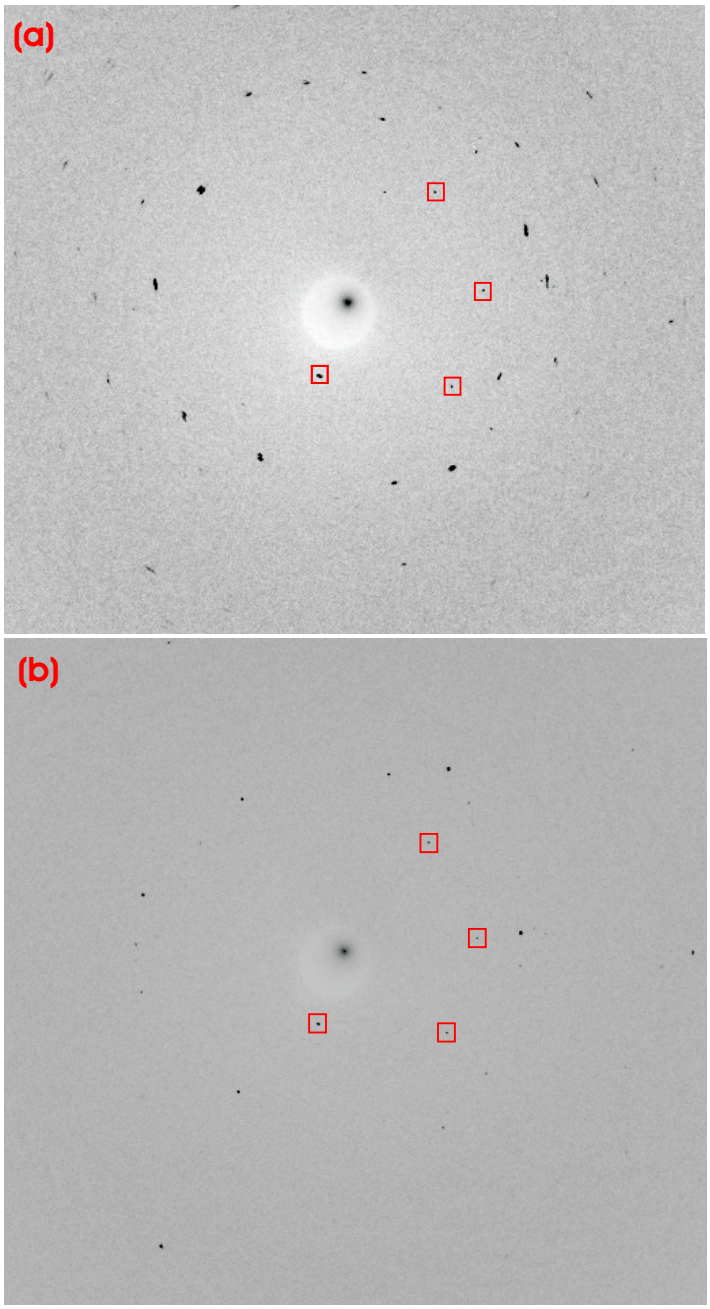

Figure 6.9: Two area detector images of methane, (a) 400 K ∼7 GPa and (b) 416 K ∼7 GPa. The red boxes mark background reflections that are present in each frame and subsequently masked out. There is a clear change in the character and arrangement of the reflections between the data collections, interpreted to indicate that the sample has undergone the transformation observed in Chapter 4.

attached externally to the cell. At each step, the power to the heater was increased and one the temperature had stabilised data were collected. The cell was rocked ±5° in ω for an exposure time of 5 minutes.

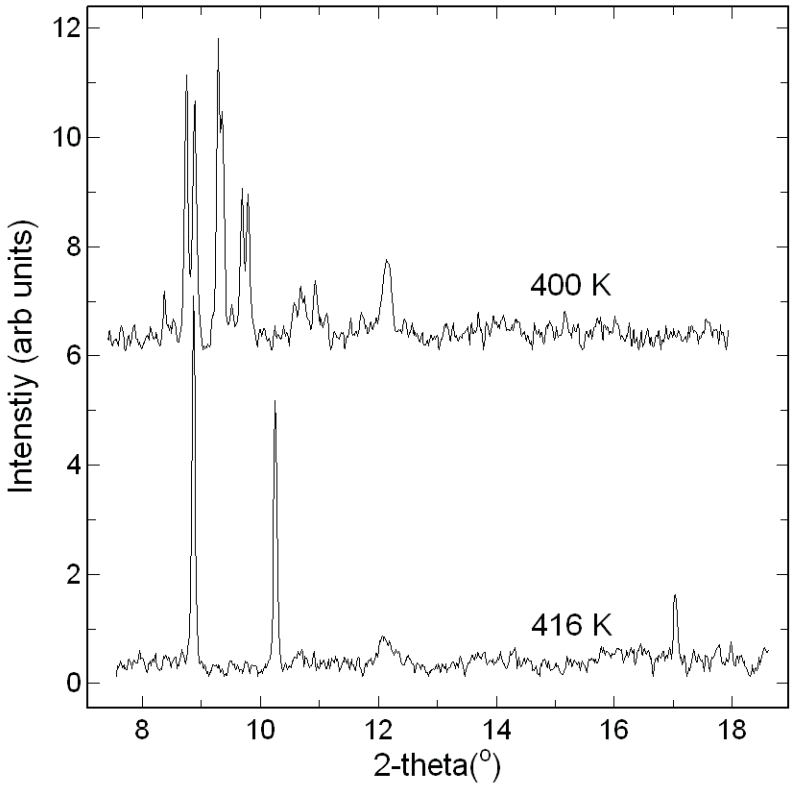

Figure 6.10: Integration of the images shown in Figure 6.9. This more clearly demonstrates change of character of the sample.

During this experiment a transition was observed between steps of 400 and 416 K. Because of the weak scattering of the sample, displaying this is difficult, Figure 6.9. To show the transition clearly, the raw data were integrated to 'powder' patterns. The patterns, Figure 6.10, cannot be viewed as powder patterns as the relative intensities between each reflection will be wrong. However, the positions of the reflections can give insight to the unit cell of methane at these conditions.

The image in Figure 6.9(b) indexes to a face-centred cubic cell of 4.99(2) Å, indicating that the sample has back-transformed to phase I (5.17 Å at 300 K and 3.8(2) GPa). This is perhaps unsurprising as it shows that methane is similar to other molecular crystals in forming a cubic structure directly from the liquid.

Using the observations collated during crystal growth, and the melt line established in Chapter 4, the high-pressure phase diagram of methane can be tentatively determined above 300 K, Figure 6.11. The trend line drawn for the phase A to I transitions indicates that it will intersect with the melt line, creating a triple point approaching 17 GPa ~625 K. The implication of this is that the cubic structure of phase I would not be able to exist at conditions beyond this point in pressure and temperature.

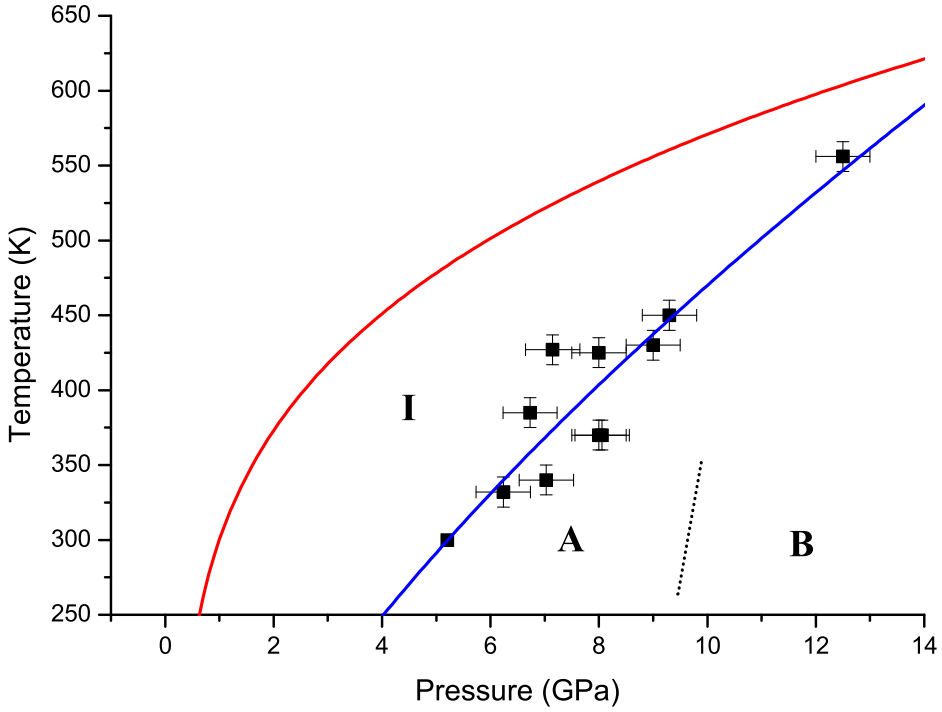

Figure 6.11: The high-pressure phase diagram of methane above 300 K. The black squared points of transition (with associated uncertainties of the measure value) observed during growing single crystals described in Chapter 4, the the blue trend line fitted between them. The red line is the melt line presented in Figure 4.10.

This investigation has shown that phase characterisation at high-temperature high-pressures with single-crystal diffraction of low scattering molecules is possible. Having stated this, the quality of collected data could be radically improved with some adaptation of equipment. One such improvement would be the inclusion of a cooling base enabling the sample to be kept at temperature for full single-crystal collections. Despite these limitations, this characterisation of methane at high-temperature and high-pressure has enable inferences to be made on its phase diagram.

6.4 Summary

These two, accessory studies, have increased on current knowledge on the methane phase diagram. The first low temperature experiment demonstrated that the previous segregation of the phase diagram at this point is incorrect, and to 5 GPa and 20 K the rhombohedral phase A of methane is stable. The second study showed that the cubic phase I, extends to a higher temperature and pressure regime than previously thought, suggesting that phase A is itself a 'buried' phase. The trends in transition and melt curves suggest that a triple point will exist in the methane phase diagram at $\sim$17 GPa and $\sim$625 K.

Chapter 7

Conclusions

The two main outcomes from this body of work are the structure solutions for methane phases A and B, described in Chapters 4 and 5 respectively. These results could only be achieved by the integration of a variety of high-pressure diffraction techniques. As with all investigations, other avenues of interest were established. Chapter 6 was written to describe the investigations that had been undertaken on methane aside from its structural characterisation at high-pressure. Alongside the main investigation on methane the author has completed studies on other outer solar system minerals, as introduced and reviewed in Chapter 2. These studies, which are briefly outlined in Appendix A, further show the successful application of the techniques learnt during this thesis.

Perhaps what astonished the author on the approach to this subject was the lack of structural information on methane. This absence of information is stark when compared to similarly fundamental molecules, for instance carbon dioxide, water and ammonia. Nothing was known on the atomic arrangement of methane beyond 5.2 GPa. It is more perplexing when it is considered in the context of planetary observations. Chapter 2 reviewed the current knowledge of the interiors of the icy gas giants of our solar system, Uranus and Neptune. As part of this, it was explained how models of gas giant interiors have been constrained by the observations of passing spacecraft. In a following section in Chapter 2, water, ammonia and methane were discussed, describing experimental studies of relevance to the interiors of Uranus and Neptune. It is concerning to note that there has to date been little effort to tie the results of these experimental studies to the interior modelling that was discussed. Of particular note are the respective observations by Lin *et al* [Lin 05] and Ninet *et al* [Ninet 08] that the water and ammonia melting curves are projected to intersect the isentropes of Uranus and Neptune. The prospect of solid stratification within the interiors of the icy gas giants would change the energetics and processes within interior models dramatically. Methane, along with water, has now

been identified to be present within the atmosphere of a Jupiter-sized planet 63 light years away [Swain 08]. This is a first indication that methane could be a component of gas giants beyond our solar system.

The work of this thesis does not have immediate implications for models of the interiors of Uranus and Neptune. However, high-pressure structural characterisation of methane is a necessary step towards full understanding of these environments. Better knowledge of molecular behaviour at experimentally accessible conditions will allow theoretical studies to probe inaccessible conditions with greater accuracy. It is hoped that the structures determined within this thesis will be used in this way.

The structures determined by this thesis have shown that previous assumptions on the structural behaviour of methane at high pressure were wrong. These assumptions had concluded that methane's high pressure structures would be described by single site models and would have a basis of hexagonal close packing. The determined structures of phases A and B shown that this is not the case for methane, with phase A described by nine molecular sites and phase B four. Phase A does take up a packing structure which is a distortion of the face centred cubic (cubic close packing) of phase I. This is perhaps could be thought of as an intermediary step towards a more simplified packing regime. But the structure of phase B, disputes this idea, as it exhibits a larger structure, with a distorted close packed structure. This result, coupled with the demonstration of no large scale structural transformation between phase B and HP, suggest that the methane structures will remain large and multi-sited to much higher pressures.

Both of the structures presented are key evidence that the methane molecule is no longer 'spherical' at pressures greater than 5.2 GPa. This assumption stemmed from the structure of phase I which was thought to be fully rotationally disordered. A preliminary study on phase I showed that calculated structure factors did not refine well against this model when compared to refinement of a separated carbon and hydrogen model. This suggests that even within phase I, the effect of pressure is the loss of methane's spherical nature. This result would begin to explain the differences in observed and calculated behaviour of methane, if calculations are based on methane having a spherical potential. If the conditions of Uranus and Neptune's interiors are to be effectively re-created details such as the potential of a methane molecule and its high-pressure behaviour need to be well established.

The low temperature study described within Chapter 6 concluded that, to 5 GPa at 20 K, there are no structural transformations from phase A. This result disputes the work of Bini *et al* [Bini 97] which describes three additional phases under these conditions, IV, V and VI. These phases were identified from shifts and splittings in the main ν_1 spectra, observed with Raman and infra-red spectroscopy. The interpretation of this behaviour to be a result of phase transformation was based on the assumptions

of a single site model of phase A. In fact, as this thesis has established, the structure of phase A needs nine sites for a full description. The number of modes that this complex arrangement would result in could account for the subtle shifts that Bini *et al* observed.

There are a variety of implications of this work on the wider studies of methane and simple molecular systems. One such implication is to theoretical work investigating the possibility of chemical pre-compression initiating superconducting behaviour in hydrogen. Although methane has not been postulated to display this behaviour its analogues silane (SiH_4) and germane (GeH_4) have [Feng 06]. The results of this thesis suggest that simplified structure assumptions are far from adequate when modelling methane and this could apply to its analogues. Recent calculations used a variety of single site models to predict the onset of metallic behaviour in methane at 520 GPa [Martinez-Canales 06]. In light of the results of this thesis these calculations should be run again. It re-asserts the point that firm knowledge on crystalline structures are vital for accurate modelling of conditions that are unable to be accessed experimentally.

Without the combinations of diffraction techniques the full structural determination of phase A (carbon and hydrogen positions) would not have been possible. When collecting high-pressure data there is always a compromise in the quality of the data that can be achieved because of the environment of the sample. It proved very important to tailor each experiment and the instrument used to the type of data that was desired. The sequence of techniques followed in both Chapters 4 and 5 demonstrated how the strengths of each experimental technique were utilised. The x-ray powder diffraction study served to make a preliminary characterisation of the unit cell of each structure, and also allowed some confinement of the structure's symmetry. This information could then be confirmed by the single-crystal study, from which atomic positions of the central carbons were determined. In the case of phase A, the carbon positions were confirmed by neutron powder diffraction, and Fourier difference analysis gave insight to the hydrogen positions. A natural extension to this flow of techniques would be to carry out single-crystal neutron diffraction on the methane phases studied. This would potentially allow refinement of the hydrogen positions, and reveal any remnant disorder in the methane molecules. This thesis has demonstrated the effectiveness of combining different diffraction techniques to the study of hydrogen-dominated materials at high-pressure. Other workers may consider approaching further studies to minerals of the outer solar system in a similar way.

It is realised that the work of this thesis is by no means the end of high-pressure investigations on methane and the minerals of the outer solar system. In reality, it is hoped, that this work will be a beginning.

Appendix A

Studies of other hydrogen dominated systems

This appendix has been included to illustrate the wide variety of studies that have taken place in conjunction with the other work of this thesis. The studies presented here represent the path that the author has taken to becoming an experienced researcher. For all these projects, with the exception of the work on amorphous ice, the author was the principal investigator.

A.1 Amorphous Ice

The advent of high-pressure studies upon the ice phase diagram revealed a further 'weirdness of water'; its exhibition of polyamorphism. Water can be super-cooled to as low as 231 K before crystallisation begins and has been known for some time to exhibit strange properties in this region. This is shown by the coefficients of thermal expansion, isothermal compressibility and pressure constant specific heat capacity projected to diverge at 288 K [Speedy 76]. At ambient pressure, below a glass transition temperature of 130 K glassy water or more commonly named amorphous ice is produced. Although amorphous ice is a solid, it exhibits a disordered liquid-like arrangement of its molecules [Mishima 84]. Amorphous ice has also been observed in a variety of distinct forms which inhabit their own 'stability' fields. There are to date three known 'phases' of amorphous ice, low density amorphous (LDA), high density amorphous (HDA) and very high density amorphous (VHDA), ice. Diffraction patterns from HDA and VHDA can be seen in Figure A.1. It has been observed that amorphous ice, like crystalline ice, can undergo 'polyamorphic transitions' between these phases. An interesting example is the LDA to HDA transition which is accompanied by a 20% volume change [Mishima 98]. This is significant as it would suggest that between LDA and HDA is first order

transition rather than a continuous transition that would have been expected between two amorphous phases.

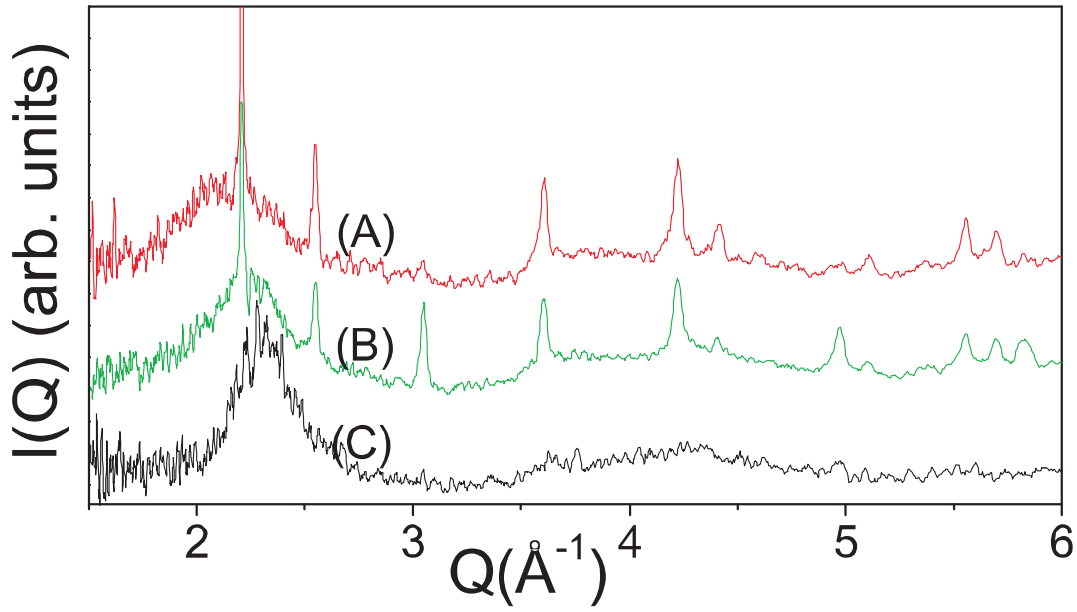

Figure A.1: Diffraction patterns of HDA recovered to ambient pressure at 80(2) K after annealing at 1.7 GPa for (A) ∼78 minutes and (B) 60 hours. For comparison (C) is a pattern of VHDA at 80(2) K after isobaric formation, warming HDA to 135 K at 1.7 GPa. Sharp peaks are from the lead pressure calibrant and sintered diamond anvils. The inset illustrates how the positions of the amorphous peaks are fitted with a Lorentzian function.

Much of the focus of early PEARL/HiPr beamtime at the ISIS facility was towards continuing the group's investigations into amorphous ice. This work involved studying the change in position (relaxation) of the amorphous peak of HDA as a function of time, at pressure and at low temperatures. This relaxation is thought to be a manifest of structural changes and was discovered to occurs *in situ* at pressure and low temperature (<80 K). This change is in addition to relaxation that occurs when the HDA samples are recovered and left at ambient pressure, adding another term of complexity to studying amorphous ice.

To produce HDA samples, 99.9% D_2O is loaded with a curl of lead (as a pressure calibrant) into a V3 type Paris-Edinburgh cell adapted for working at low temperatures. This is sealed with three tonnes of load, before being cooled to 220 K. At this point the sample is put in the PEARL/HiPr instrument to check that the sample is clean ice Ih (no contamination from Ice II or XII). Then the sample is further cooled to 130 K before 10 tonnes are applied to seal the piston, and then the temperature of the sample is further dropped to ∼80 K. Once this is achieved the sample is compressed in steps of

10 tonnes until it fully amorphises, at pressure of ∼1.7 GPa. From this point a variety of investigations were conducted in a bid to characterise the relaxation behaviour of HDA both at pressure and when recovered back to ambient pressures.

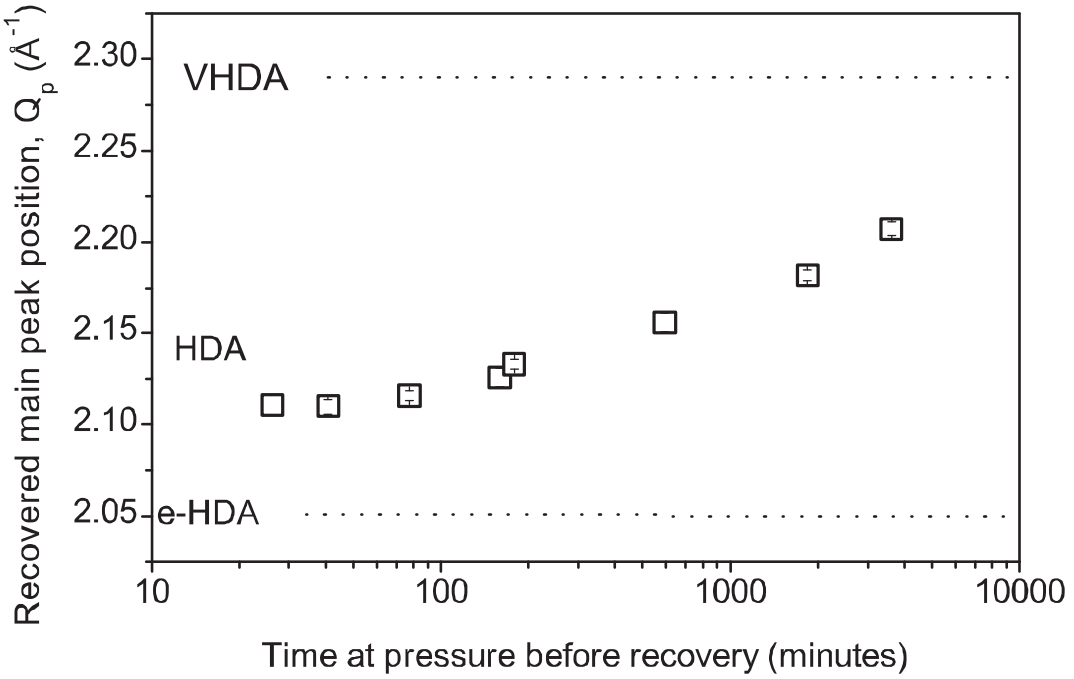

Figure A.2: Main amorphous peak of HDA at 80(2) K and ambient pressure as a function of length of time held at pressure. The dotted lines mark the main amorphous peak values for fully annealed (e)HDA and VHDA.

One of the key findings have been that the ambient pressure recovered position of the first diffraction peak of HDA changes with time that the sample is held at the pressure of 1.7 GPa and 80 K. Figure A.1 and A.2 illustrates this point and shows that as the sample is held at pressure for increasing time its final position tends towards that of VHDA. This relaxation is seen to be seven times faster than a similar effect observed at ambient pressure of recovered HDA towards that of LDA whilst still at 80 K. This work is significant in that it shows that is it important to take into account possible relaxation effects in all three forms of amorphous ice throughout production and experimentation.

A current experiment on HDA has been to observe the effect of doping with HCl. Doping of crystalline ice allows a 'speeding up' of the ordering process, revealing the ordered ice phases [Tajima 82, Salzmann 06]. It is possible that the relaxation effects in HDA would be influenced by an 'ordering' of the water molecules, reducing their co-ordination. By doping the HDA samples a 'final' state of the amorphous phase could be produced. Characterisation of this phase would be significant as the 'final' state of

HDA is likely to be prevalent in the far outer solar system, especially within icy Kuiper Belt objects.

A.2 Methane hydrate III, a powder x-ray study

As already described in Chapter 2, the structure of MHIII is extremely stable. It is as yet to be experimentally observed to decompose under pressure [Hirai 08, Machida 06], but is calculated to do so at pressures approaching 100 GPa [Iitaka 03]. Hirai *et al* undertook a x-ray powder diffraction study of methane hydrate to 86 GPa [Hirai 06]. They presented evidence that the MHIII structure underwent a structural phase transition at 40 GPa. For this experiment, Hirai *et al* had initially loaded the cubic MHI, which has a methane:water ratio of 5.6:1. It has been previously observed that when compressing MHI on transformation to other, more methane rich, methane hydrate structures the samples 'throws' the addition water to form ice VII [Loveday 01a]. The ice VII in the gasket obscures the, more subtle, diffraction from the MHIII. Hirai *et al* also observed this, and state it as the reason for being unable to solve or refine their data on the 'transformed' MHIII [Hirai 06].

One aim of this experiment was to study a pure sample of MHIII, overcoming the limitation encountered by Loveday *et al* and Hirai *et al*. This would be achieved by loading a sample of approximately the desired 2:1 water methane composition and growing samples of MH-III *in-situ* at pressure. The method of loading this sample was described in Section 3.5.2. This procedure was only partially successful. In order to grow the desired phase, fine control of pressure (on the order of a kilobar) is imperative. Directly from the loading the sample formed MHI at 0.47(20) GPa, Figure A.3. This transformed to MHII on increasing pressure to 1.61(20) GPa. Over time the MHII was seen to grow along with methane, Figure A.3. At the transformation to MH-III the water expelled from the MH-II structure did not react with the excess of methane and the resultant sample was left containing methane, ice VII and MH-III. Figure A.4 shows the diffraction patterns collected from this sample with increasing pressure, to the maximum reached 46.6 GPa. As is shown, methane itself undergoes phase transitions increasing the complexity of the diffraction results. The experiment did confirm Hirai *et al*'s findings that MH-III has a very wide range of stability, but the patterns were not of suitable quality to study the structural pressure dependence of MH-III or its transition behaviour.

This experiment did mark a significant breakthrough as it was the first loading of methane and water as separate species resulting in the growth of MH-II *in-situ* in a diamond anvil cell. In subsequent tests it was found that it is possible to also grow MH-III directly by modest heating of the cell. Using this procedure it would

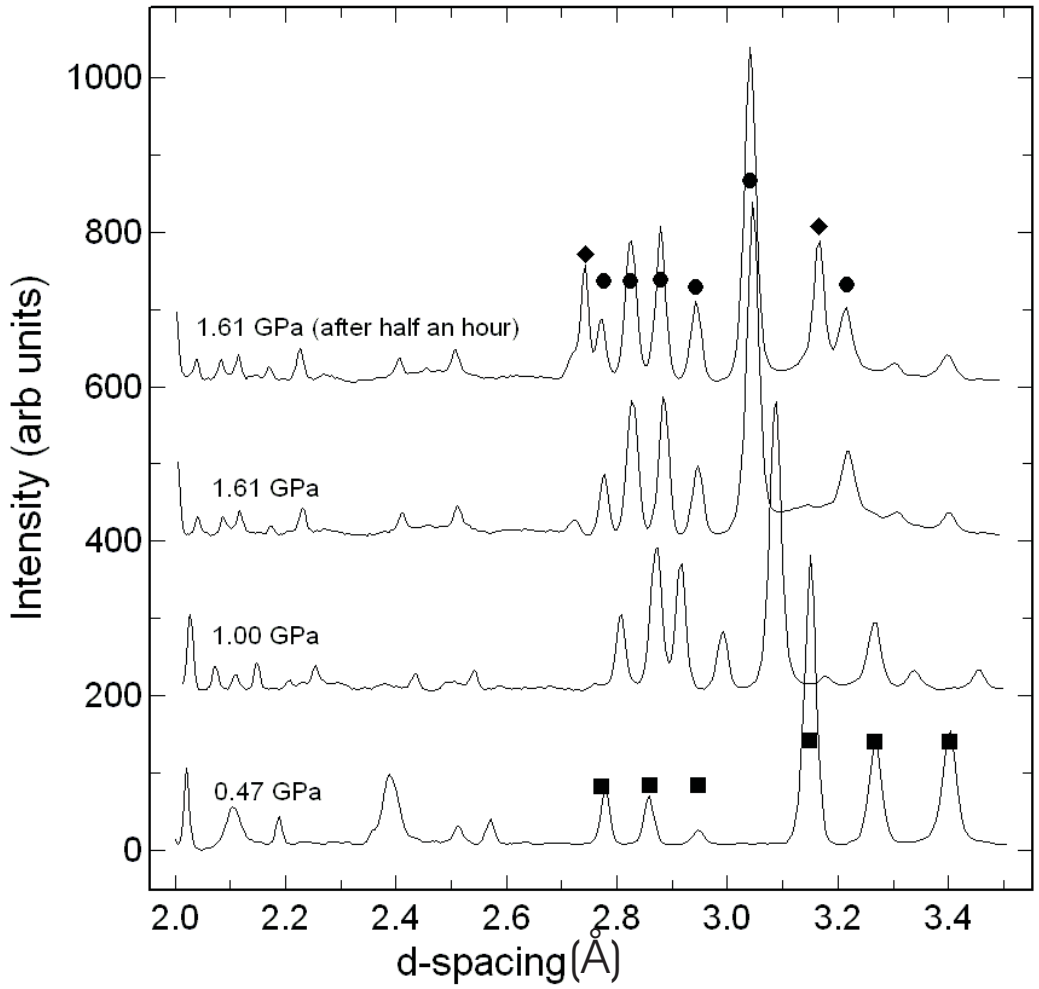

Figure A.3: Diffraction patterns showing the progression of the sample from MHI (indicated by squares) towards MHII (circles) with solid methane I (diamonds) growing.

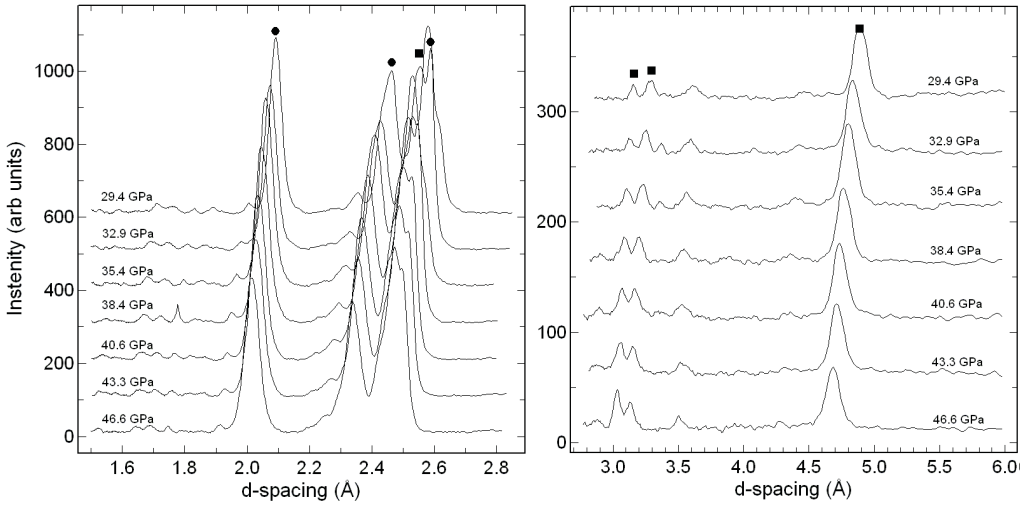

Figure A.4: The large methane peaks (indicated by circles) unfortunately obscure the weaker methane clathrate (squares) and prevented us from observing the possible phase transition that begins at ∼40 GPa [Machida 06]. However, elsewhere in the pattern we see no discernible change (above background values) like the ones reported in Machida's paper

potentially be possible to grow a sample which is almost completely MH-III and to carry out measurements of the structural pressure dependence and investigate the phase transitions at 40 GPa.

A.3 Single-crystal studies of methane hydrate

Although the structure of methane hydrate II (MHII) has been attributed to the sH hexagonal structure of clathrate hydrates [Loveday 01a] there are still some questions regarding the specific structural details. The characteristic feature of the sH structure is the large central that is exhibits, as shown in Figure A.5. There is debate as to the location of methane molecules within MHII, and Raman studies have suggested a transition in the occupancy of the larger cage with pressure [Kumazaki 04]. To resolve this question and to further probe the structure of MHII a single crystal study of this phase was started.

It was decided to attempt to grow MHII from an initial loading of pure MHI. A sample of pure MHI was synthesised on a trip to NRC, Ottawa, with a process that is described in Section 3.5.2. The sample was then shipped cryogenically back to Edinburgh where it was loaded into a diamond anvil cell using the procedure shown in Figure A.6. Loading a powdered MHI sample is more complex than conventional

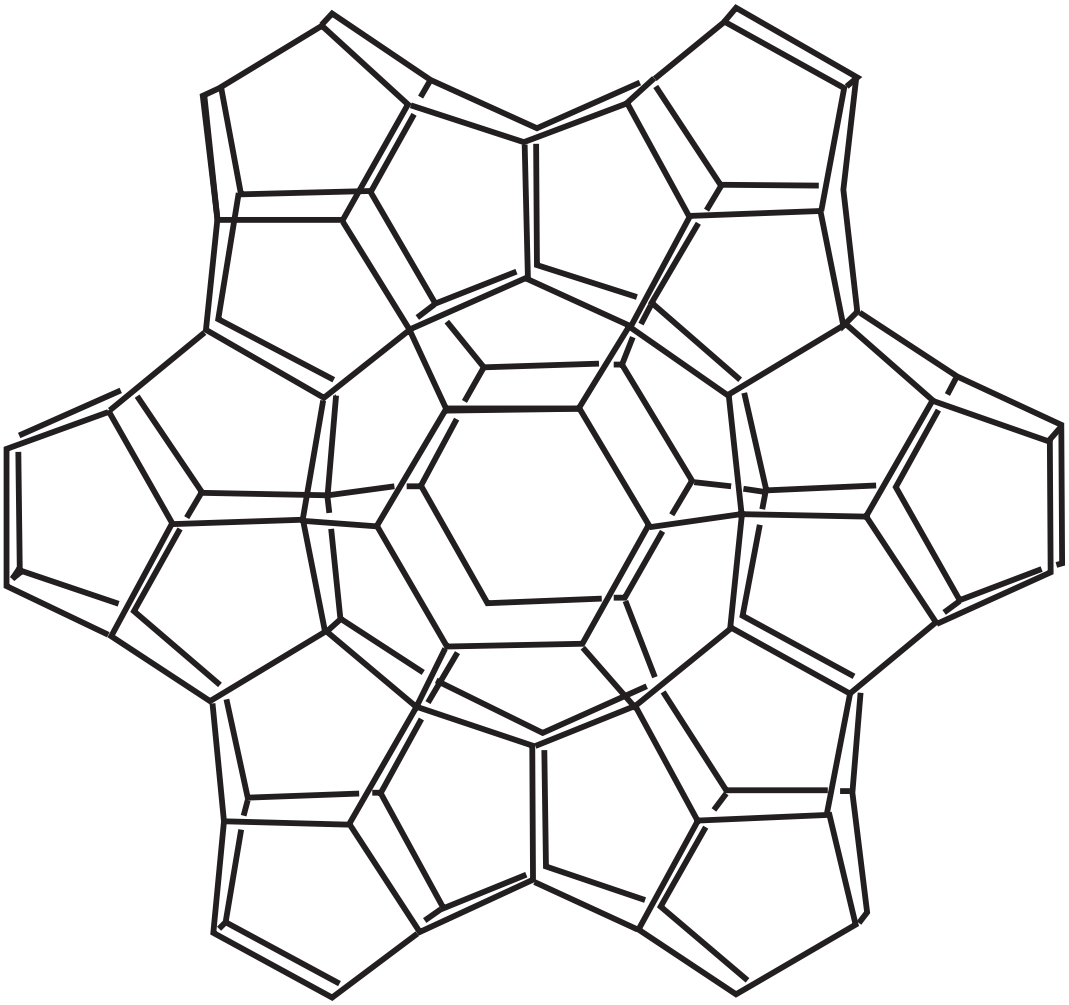

Figure A.5: Image of the packing in the sH clathrate hydrate structure taken from [Kirchner 04]. The larger icosahedron cage is surrounded with six smaller dodecahedron cages.

samples as it needs to be kept significantly below 268 K to prevent any decomposition.

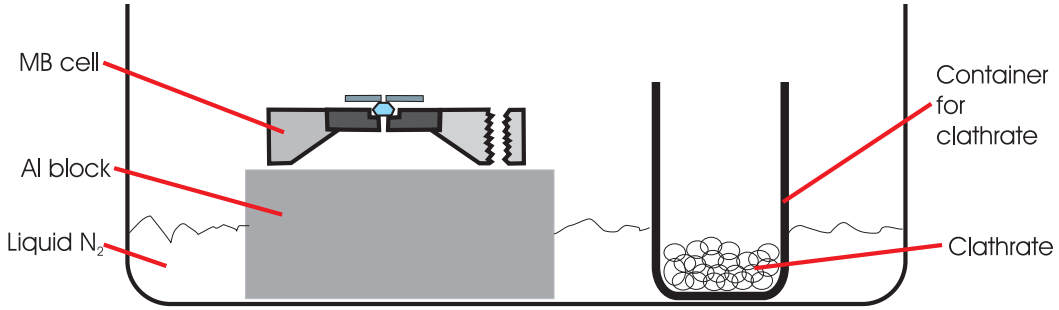

Figure A.6: Details of the procedure to load clathrate samples into a diamond anvil cell. The bottom half of the diamond anvils cell (in this case a Merrill-Bassett type cell) is shown placed on an aluminium block which is sitting in liquid nitrogen. This will cool the cell significantly below 268 K and prevent the sample from decomposing on contact. The container with the clathrate is place next to the cell, also in the liquid nitrogen. The boiling liquid nitrogen additionally provides an atmosphere of N_2 to prevent atmospheric water from condensing on to the apparatus. A pre-cooled implement is used to transfer the clathrate from the container to the gasket. The top of the cell would be cooled next to the bottom half, so that when it is placed on top and sealed the sample does not decompose.

The clathrate was loaded into a beryllium-backed Merrill-Bassett cell (MB cell) with 800 μm culet-sized diamonds. The large culet size (400 μm is more conventional) limits the maximum pressure that can be achieved but gives much greater control of pressures in the region 0.5-2 GPa (5-20 kbar). MHI is reported to transform to MH II at 0.9 GPa [Hirai 01], and MHII to MHIII at 2 GPa [Loveday 01b]. The speculated occupancy transition within MHII has been proposed to occur at 1.3 GPa [Kumazaki 04], hence the ability to control pressures in this region for this investigation is essential. Hence it was also important to take a characteristic Raman spectra of the ruby calibrant at ambient pressure, as describe in Section 3.10. This increase the accuracy of the pressure determination to $\pm$0.1 GPa.

As a preliminary stage of this investigation a MHI crystal was grown. The pressure of the cell was raised to 0.8(1) GPa and using the crystal growing apparatus described in Section 3.5.3 the crystal was annealed into form between 310-320 K. The resultant crystal is picture in Figure A.3(a). Data collection from this crystal will be describe later in this section.

Later attempts to grown a single crystal of MHII were of only limited success. The first crystal, pictured in Figure A.3(b), was grown from the initial crystal of MH I by pressurising it to 0.9(1) GPa. After pressurising the the sample was annealed with the

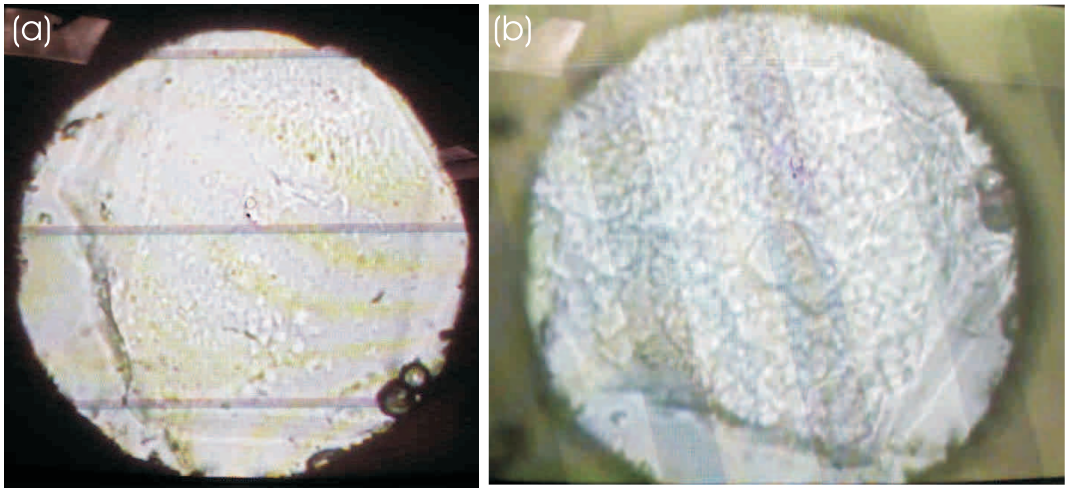

Figure A.7: Two images of methane hydrate crystals grown during this study. (a) shows a MHI crystal at 0.6(1) GPa and (b) shows the later grown MHII crystal.

crystal growing apparatus. The crystal produced was not of good quality, and attempts to integrate data collected from it failed. A variety of further techniques were employed to attempt the growth of a better quality MHII single crystal, but to date none of these have been successful.

Figure A.3 illustrates the quality of the crystal picture in Figure A.3(a). Data were collected on station ID27, ESRF from a set up described in Section 3.4.3 at a wavelength of 0.3738 Å. The collection was in steps of 0.25° over an ω range of ±30°. The data indexed to have a primitive cubic unit cell with $a = 11.71(1)$ Å, agreeing with previous indexing of MHI (a sI clathrate structure) at ambient conditions [Kirchner 04]. With this indexing the data were integrated, $R_{\text{int}} = 0.07$. From absences and intensity distribution the spacegroup of the diffraction pattern was assigned to $Pm\bar{3}n$. Using the MHI model described by Kirchner *et al* [Kirchner 04], the oxygen and carbon atoms of the structure were refined against the data, the resultant values can be viewed in Table A.1. Before the refinement the (222) group of reflections had to be removed as these had saturated during data collection.

Data were collected from the MHII crystal shown in Figure A.3 at station 9.8 with a set up described in Section 3.4.3. Using the same collection strategy described in Table 4.5, data were collected at $\lambda = 0.6884$ Å. As Figure A.3 shows, the quality of the crystal was such that the data could not be integrated. However, the crystal could be indexed which enabled the identification of the phase. The pattern was described by a hexagonal unit cell, $a = 11.94(1)$ Å and $c = 10.01(1)$ Å.

The assigned indexing of the MHII crystal compares favourably with the only other previous single-crystal diffraction study of MHII. Chou *et al* [Chou 00] collected energy

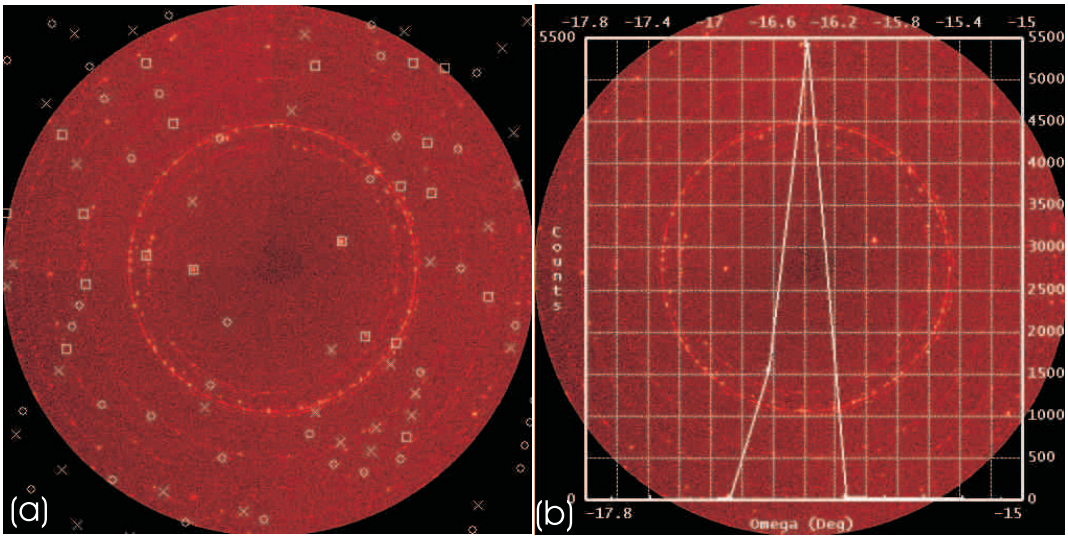

Figure A.8: Images showing the quality of data collected from the MHI crystal pictured in Figure A.3(a). (a) is frame 55 of the data collection taken at ω = -16.5°. The powder diffraction lines that can be seen are from the beryllium backing disk of the MB cell. The white marks indicate expected reflections from a primitive cubic indexing, a = 11.71(1) Å, which the pattern conforms to. (b) is a rocking curve from a characteristic reflection (in this case the [12$\bar{3}$]). The FWHM of this is 0.2° illustrating the excellent quality of this crystal.

	Wyckoff	x	y	z	s.o.f.	U_{iso} (Å^2)
O_1	24*k*	0.0000(0)	0.3092(5)	0.1169(6)	0.5000	0.055(5)
H_1	24*k*	0.0000(n/a)	0.3250(n/a)	0.0510(n/a)	0.2500	0.044(n/a)
H_2	48*l*	0.0510(n/a)	0.2710(n/a)	0.1340(n/a)	0.5000	0.044(n/a)
H_3	24*k*	0.0000(n/a)	0.3600(n/a)	0.1500(n/a)	0.2500	0.044(n/a)
O_2	16*i*	0.1830(6)	0.1830(6)	0.1830(6)	0.3333	0.058(5)
H_4	16*i*	0.2160(n/a)	0.2160(n/a)	0.2160(n/a)	0.1667	0.043(n/a)
H_5	48*l*	0.1620(n/a)	0.1280(n/a)	0.2200(n/a)	0.5000	0.043(n/a)
O_3	6*c*	0.0000(0)	0.5000(0)	0.2500(0)	0.1250	0.063(7)
H_6	24*k*	0.0000(n/a)	0.4470(n/a)	0.2110(n/a)	0.2500	0.044(n/a)
C_1	2*a*	0.0000(0)	0.0000(0)	0.0000(0)	0.0416	0.039(18)
H_7	24*k*	0.0000(n/a)	0.0490(n/a)	0.0860(n/a)	0.1650	0.078(n/a)
C_2	6*d*	0.2500(0)	0.5000(0)	0.0000(0)	0.1250	0.134(15)
H_8	12*g*	0.2986(n/a)	0.5000(n/a)	0.0687(n/a)	0.2500	0.170(n/a)
H_9	12*g*	0.2014(n/a)	0.5000(n/a)	0.0687(n/a)	0.2500	0.170(n/a)

Table A.1: Refined positions of the MHI structure from the high-pressure single crystal data collected as part of this study using a structure described in [Kirchner 04]. The hydrogen atoms were fixed as the data were not of sufficient quality to refine them. Values in brackets are the estimated standard deviations (e.s.d.) of each value. This refined to an *R*-factor of 0.03.

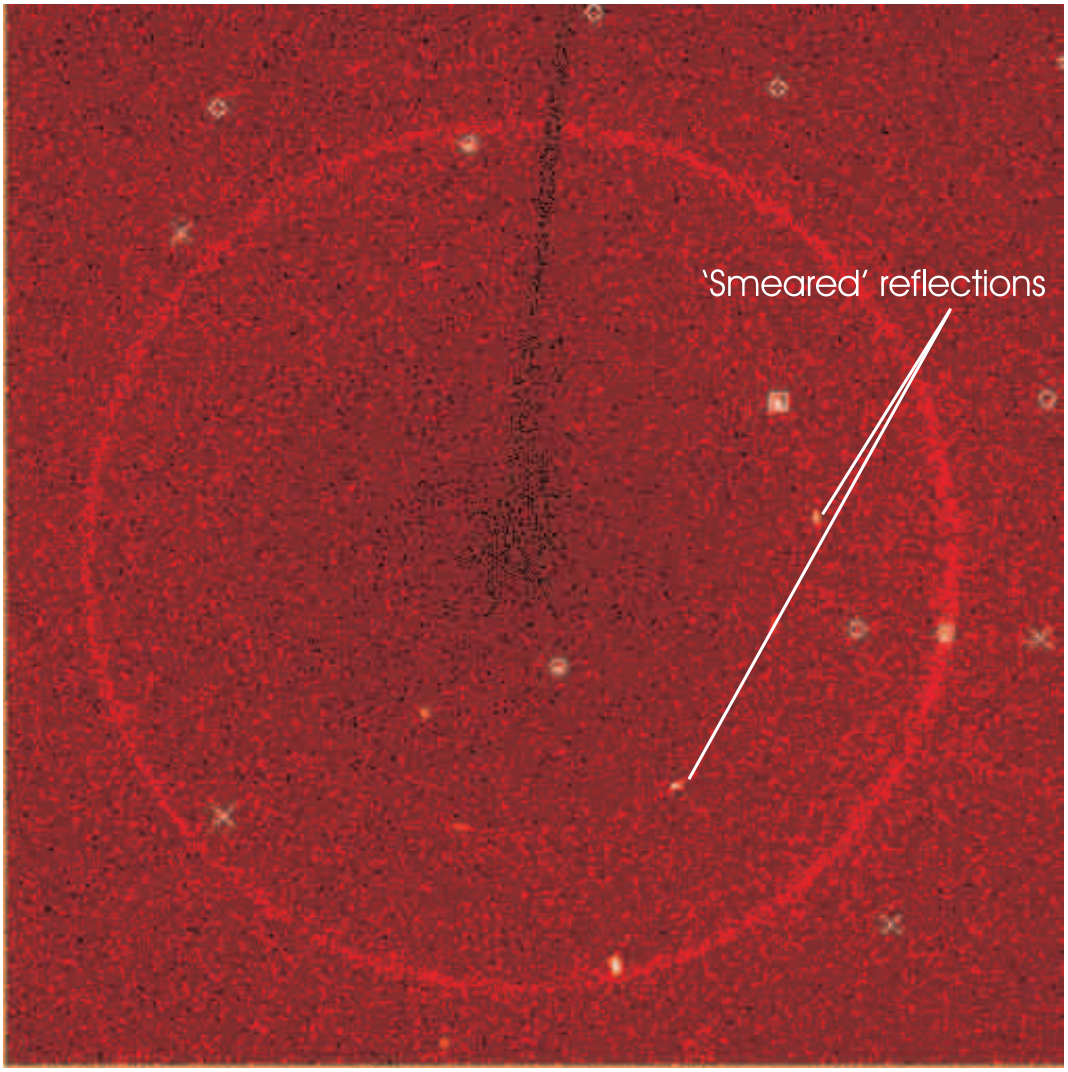

Figure A.9: Shows the poor quality of diffraction data collected from the MHII crystal picture in Figure A.3(b). The individual reflection are very broad, in contrast to that shown from the MHI crystal in Figure A.3. In addition this image shows that some of the reflections are 'smeared' toward powder rings (like demonstrated in Figure 3.5).

dispursive diffraction on a MHII crystal at 0.6 GPa, obtaining a unit cell of a = 11.980(2) Å and c = 10.17 Å. Unlike the study of Chou *et al* the angular-dispersive diffraction of this study had the potential of integrating reflection intensities, which would have potentially enable the location of methane molecules within the clathrate cages. Unfortunately the crystal that was grown was not of sufficient quality to attempt this.

In contrast to Chou *et al*'s study on methane hydrate at lower pressures this study found no evidence of the sII clathrate structure. This face-centred clathrate variant is thought to be metastable when formed in the methane hydrate system. The indexing of the first crystal as primitive cubic, with a = 11.71 Å, clearly identifies this crystal as the sI, MHI phase. Further studies of the methane occupation in MHII and the relative stability of a sII clathrate structure are vital for detailed understanding of Titan's sub-surface interactions [Tobie 06].

A.4 Ammonia hydrates

The background of these investigations has already been discussed in Section 2.6.2. During this thesis two high-pressure neutron diffraction experiments upon ammonia hydrates were conducted on loadings of ammonia dihydrate (ADH) composition. The first was to recreate the high pressure phases observed by Fortes *et al.* [Fortes 04]. The second was to discover what phases would be produced upon continued compression of an liquid of ADH composition along the room temperature isotherm. The study was undertaken at the PEARL/HiPr instrument at the ISIS facility, UK, using a Paris-Edinburgh press. Neutron diffraction is vital to the detailed study of this phase because of the proliferation of hydrogen within the structures of ADH.

The sample was synthesised from deuterated water and ammonia into a 33 wt% solution, by mixing the substances within a pressurised condenser. It was important to minimise exposure of the user to the ammonia and for the volatile mixture to remain contained to maintain the right composition. Loading of the resultant liquid into the Paris-Edinburgh press was complicated by the need to keep the liquid below 268 K to prevent phase separation. The solution to this problem was to place the entire cell within the cold room at ISIS, cooling it (and the experimenter!) to close to 258 K enabling loading of the ammonia dihydrate in a stable environment.

The first pressure-temperature path followed was to cool to ∼120 K before warming up upon adding the load. With this pressure/temperature path, it was hoped to re-creates the evolution conditions of the interior of Titan. Following this route, ADH phases were formed that were distinctive to those of ammonia mono-hydrate (AMH) under similar conditions. The intentions of this data was to further characterise the

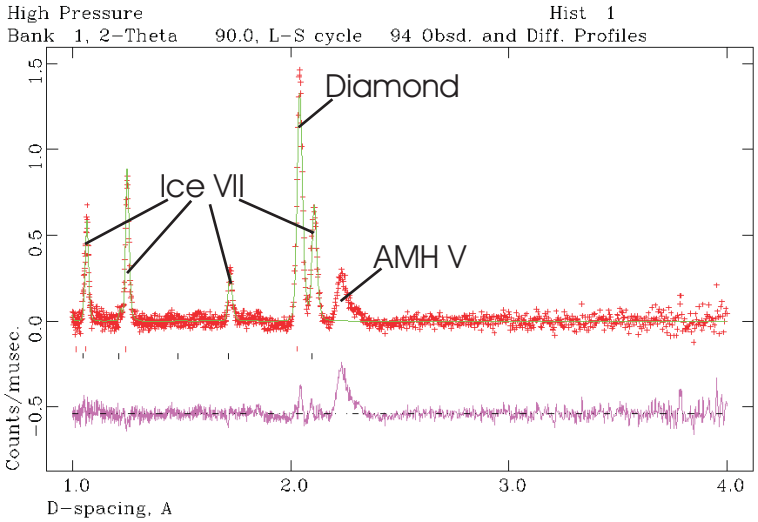

Figure A.10: Neutron diffraction data of AMH V at 200 tonnes, showing rietveld fits of the Diamond (from the anvils) and ice VII peaks. The AMH V peaks are unfitted as the structure is unknown. The lattice parameter of ice VII found from this is $a = 2.971(1)$ Å which implies a pressure of ∼27 GPa

ADH phases that were first identified by [Fortes 04].

The second route taken was to compress at room temperature in a bid to form the ADH phases observed before directly from the liquid. Along this path no ADH phases were formed, and from a load of 35 tonnes the monohydrate, AMH V, was formed. It was of interest to probe how stable this structure is, and as such the load was stepped up to a maximum of 200 tonnes generating a pressure of 27 GPa (determined from the excess ice VII present). Figure A.4 presents the data from the sample at 200 tonnes, with a Reitveld fit of the ice VII peaks. To this point AMH V was stable with no evidence of ionisation under compression that had been previously calculated to occur at 12 GPa [Johnson 88], a result that could have implications for modelling of the interiors and magnetic fields of the icy gas giants.

A.5 Carbon dioxide clathrates

This project was to investigated any possible high pressure transformations of CO_2 clathrate. Like MHI, at moderate pressure (0.2 GPa) carbon dioxide clathrate forms with a sI cubic clathrate structure [Udachin 01]. This was the first study to probe the high-pressure, room temperature behaviour of this gas clathrate phase.

The sample was prepared and loaded with similar apparatus to that detailed in

Figure A.6. The sample was first prepared by grinding solid CO_2 with deuterated ice in a pestle and mortar contained in a liquid nitrogen environment. The resultant powder was then piled into the sample space in an anvil. Another, pre-cooled, anvil was placed on top of the sample and the two anvils were clamped together with a bolt. The anvil assembly was then placed inside a pre-cooled Paris-Edinburgh cell and sealed with 3 tonnes of load. The experiment was repeated later with a pure clathrate sample synthesised using the method described in Section 3.5.2. This gave the same results as the sample that was formed into clathrate within the pressure cell.

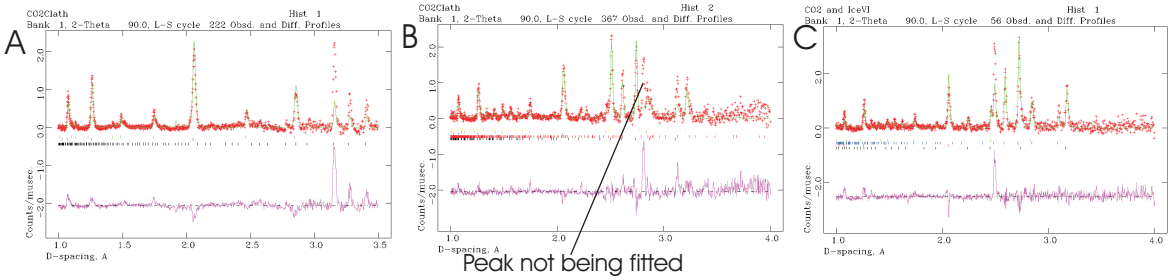

Figure A.11: Three stages of compression experiment of CO_2 clathrate ~270 K. A) Clathrate present with some liquid not used at this point (removed with background) shows a fit with the structure as determined by [Udachin 01]($\chi^2 = 2.900$). B) Mixed transition pattern, here is being fitted with solid CO_2, ice VI, and the sH clathrate structure but a 'mystery' peak remains unfitted.($\chi^2 = 4.527$) C) Pattern on further compression showing clean solid CO_2 and ice VI, d_{111} lead gives the pressure at this point to be 1 GPa.($\chi^2 = 2.551$)

CO_2 clathrate was compressed at two different temperatures, ~300 K and ~270 K, At both temperatures the sI clathrate structure was observed to decompose as the pressure increased. However, at the cooler temperature there was some evidence of a phase transformation before decomposition, but any phase at this point will have a very small stability field, Figure A.5.

Appendix B

Single crystal data collected

Summary of the single crystal synchrotron data collected on methane during this study. Information is given on; the date of collection, the instrument collected on (see Section 3.4.3 for more details), the run number of the collection, the wavelength of the collection, the name of the data set, the cell the crystal was in, the pressure of the sample and the indexing. Then there is information on the R_{int} on the data integration and lastly comments on the data collection.

Date	Instrument	Run	λ (Å)	Set	Cell	Pressure	χ	Index (Åand °)	R_{int}	Comments
29/07/2008	ID09a	hs3090h	0.4138	sxm	MBΔ9	6.9 GPa	0°	a = 12.038	0.04	Top five peaks saturated
28/07/2008	ID09a	hs3090h	0.4138	sxh	MBΔ1	13.6 GPa	90°	a = 8.23 α = 89.5	0.03	refil between frames 065 066
27/07/2008	ID09a	hs3090h	0.4138	sxc	MBΔ1	13.6 GPa	0°	a = 8.23 α = 89.5	0.03	Good crystal
23/07/2008	9.5	EQ	0.4439	sxe	MBΔ1	13.6 GPa	0 °	a = 8.23 α = 89.5	n/a	Short data set, 90 frames
22/07/2008	9.5	EQ	0.4439	sxd	MBΔ1	9.1 GPa	0 °	a = 8.51 α = 89.3	0.04	Good data set
21/07/2008	9.5	EQ	0.4439	sxc	MBΔ9	3.8 GPa	0 °	a = 5.17	0.12	Shortend data set, 232 frames
07/07/2008	9.5	EP	0.4439	sxd	MBΔ1	5.2 GPa	0 °	a = 8.80 α = 89.4	0.06	60s exposure
05/07/2008	9.5	EP	0.4439	sxb	MBΔ1	5.2 GPa	0 °	a = 8.80 α = 89.4	0.04	15s exposure
22/04/2008	ID27	hs3090g	0.2647	sxai	MBΔ9	7.2 GPa	90°	a = 11.91	0.05	Saturated
22/04/2008	ID27	hs3090g	0.2647	sxah	MBΔ9	7.2 GPa	90°	a = 11.91	0.11	Too weak
22/04/2008	ID27	hs3090g	0.2647	sxag	MBΔ9	7.2 GPa	0°	a = 11.91		Saturated
22/04/2008	ID27	hs3090g	0.2647	sxaf	MBΔ9	7.2 GPa	0°	a = 11.91		Too weak
19/04/2008	ID27	hs3090g	0.2647	sxl	MBΔ1	6.4 GPa	0°	a = 8.74 α = 89.3	0.06	Saturated
19/04/2008	ID27	hs3090g	0.2647	sxk	MBΔ1	6.4 GPa	90°	a = 8.74 α = 89.3	0.23	Saturated
19/04/2008	ID27	hs3090g	0.2647	sxj	MBΔ1	6.4 GPa	90°	a = 8.74 α = 89.3	0.35	Saturated
19/04/2008	ID27	hs3090g	0.2647	sxi	MBΔ1	6.4 GPa	0°	a = 8.74 α = 89.3	0.06	Saturated
06/10/2007	9.5	EK	0.4439	sxh	MB46	7.7 GPa	0°	a = 8.43 α = 89.9	n/a	Room temperature
06/10/2007	9.5	EK	0.4439	sxg	MB46	7.7 GPa	0°	a = 8.61 α = 89.3	0.07	High temperature
05/10/2007	9.5	EK	0.4439	sxf	MBΔ1	8.5 GPa	90°	a = 8.51 α = 89.5	0.03	Good data
05/10/2007	9.5	EK	0.4439	sxe	MBΔ1	8.5 GPa	0°	a = 8.51 α = 89.5	0.02	Good data
05/10/2007	9.5	EK	0.4439	sxb	MBΔ9	8.3 GPa	90°	a = 11.850	0.09	Good data
05/10/2007	9.5	EK	0.4439	sxa	MBΔ9	8.3 GPa	0°	a = 11.850	0.07	Good data
26/08/2007	ID09a	hs3090d	0.4131	sxe	MBΔ1	7.0 GPa	90°	a = 8.54 α = 89.3	0.04	Saturated
26/08/2007	ID09a	hs3090d	0.4131	sxd	MBΔ1	7.0 GPa	0°	a = 8.54 α = 89.3	0.06	Frames 48 to 64 missing, Saturated
26/08/2007	ID09a	hs3090d	0.4131	sxc	MBΔ9	8.3 GPa	90°	a = 11.876	0.076	Diamond reflection obscurred integration
26/08/2007	ID09a	hs3090d	0.4131	sxb	MBΔ9	8.3 GPa	0°	a = 11.876	0.05	Refill in frame 174
22/07/2007	9.5	EJ	0.4439	sxb	MBΔ9	8.3 GPa	0°	a = 11.85	0.07	Good set 20s plus bigger beam
21/07/2007	9.5	EJ	0.4439	sxa	MBΔ9	8.3 GPa	0°	a = 11.85	0.08	Good set 10s frame

Bibliography

[Adams 79] D. Adams. The Hitchhikers Guide to the Galaxy. Pan Books, 1979.

[Ancilotto 97] F. Ancilotto, G.L. Chiarotti, S. Scandolo & E. Tosatti. *Dissociation of methane into hydrocarbons at extreme (planetary) pressure and temperature.* Science, vol. 275, page 1288, 1997.

[Benedetti 99] L.R. Benedetti, J.H. Nguyen, W.A. Caldwell, H. Lui, M. Kruger & R. Jeanloz. *Dissociation of CH_4 at high pressures and temperatures: diamond formation in giant planet interiors?* Science, vol. 286, page 100, 1999.

[Bernal 53] M.J.M Bernal. *Analytical wavefunctions for methane and the ammonium ion.* Proceedings of the Royal Society of London: Series A, vol. 66, page 514, 1953.

[Besson 92] J.M. Besson, R.J. Nelmes, G. Hamel, J.S. Loveday, G. Weill & S. Hull. *Neutron powder diffraction above 10 GPa.* Physica B, vol. 180, page 907, 1992.

[Besson 94] J.M. Besson, Ph. Pruzan, S. Klotz, G. Hamel, B. Silvi, R.J. Nelmes, J.S. Loveday, R.M. Wilson & S. Hull. *Variation of interatomic distances in ice VIII to 10 GPa.* Physical Review B, vol. 49, page 12540, 1994.

[Betteridge 04] P. W. Betteridge, J. R. Carruthers, R. I. Cooper, K. Prout & D. J. Watkin. *CRYSTALS version 12: software for guided crystal structure analysis.* Journal of Applied Crystallography, vol. 36, page 1487, 2004.

[Bini 95] R. Bini, L. Ulivi, H.J. Jodl & P.R. Salvi. *High pressure crystal phases of solid CH_4, probed by Fourier transform infrared spectroscopy.* Journal of Chemical Physics, vol. 193, page 1354, 1995.

[Bini 97] R. Bini & G. Pratesi. *High Pressure infrared study of solid methane: phase diagram up to 30 GPa.* Physical Review B, vol. 55, page 14800, 1997.

[Block 70] S. Block, C. E. Weir & G. J. Piermarini. *Polymorphism in benzene, naphthalene, and anthracene at high pressure.* Science, vol. 169, page 586, 1970.

[Böhler 04] R. Böhler & K. deHansetters. *New anvil designs in diamond-cells.* High Pressure Research, vol. 24, page 391, September 2004.

[Boone 91] S. Boone & M.E. Nichol. *Ammonia-water mixtures at high pressures: melting curves of ammonia dihydrate and ammonia monohydrate and a revised high-pressure phase diagram for the water rich region.* Proceedings of Lunar and Planetary Science, vol. 21, page 603, 1991.

[Bragg 13] W.L. Bragg. *The structure of some crystals as indicated by their diffraction of x-rays.* Proceedings of the Royal Society of London: Series A, vol. 89, page 248, 1913.

[Bridgman 37] P.W. Bridgman. *The phase diagram of water to 45,000kgcm^{-2}.* Journal of Chemical Physics, vol. 5, page 964, 1937.

[Bridgman 52] P.W. Bridgman. *The resistance of 72 elements, alloys and compounds to 100,000 kgcm^{-2}.* Proceedings of the American Acadamy of Arts and Science, vol. 81, page 167, 1952.

[Bruker 98] S. Bruker. *SMART for windows and IRIX software reference manual.* Technical report, Madison (USA), 1998.

[Buckingham 41] R.A. Buckingham, H.S.W. Massey & S.R. Tibbs. *A self-consistent field for methane and its applications.* Proceedings of the Royal Society of London: Series A, vol. 178, page 119, 1941.

[Cavazzoni 99] C. Cavazzoni, G.L. Chiarotti, S. Scandolo, E. Tosatti, M. Bernasconi & M. Parrinello. *Superionic and metallic states of water and ammonia at giant planet conditions.* Science, vol. 283, page 44, 1999.

[Chou 00] I.M. Chou, A. Sharma, R.C. Burruss, J. Shu, H.K. Mao, R.J. Hemley, A.F. Goncharov, L.A. Stern & S.H. Kirby. *Transformations in methane hydrates.* Proceedings of the National Acadamy of Science, vol. 97, page 13484, 2000.

[Compton 23] A.H. Compton. *Absorbtion meausurements of the change of wavelengh accompanying the scattering of x-rays.* Philisophical Magazine, vol. 46, page 897, 1923.

[Couzinet 03] B. Couzinet, N. Dahan, G. Hamel & J.C. Chervin. *Optically monitored high-pressure gas loading apparatus for diamond anvil cells.* High Pressure Research, vol. 23, page 409, 2003.

[Datchi 06] F. Datchi, S. Ninet, M. Gauthier, A.M. Saitta, B. Canny & F. Decremps. *Solid ammonia at high pressures: A single-crystal x-ray diffraction study to 123 GPa.* Physical Review B, vol. 73, page 174111, 2006.

[dePater 01] I. dePater & J.J. Lissauer. Planetary science. Cambridge Univeristy Press, 2001.

[Downs 96] R.T. Downs & L.W. Finger. *Modeling the thermal motion of freely rotating molecules.* In XVII Congress and General Assembly, pages C–443. International Union of Crystallography, 1996.

[Dubrovinskaia 04] N.A. Dubrovinskaia & L. Dubrovinsky. *Melting of Ice VII from Raman spectroscopy.* Annual report, Bayerisches Geoinstitut, 2004.

[Elachi 05] C. Elachi, S. Wall, M. Allison, Y. Anderson, R. Boehmer, P. Callahan, P. Encrenaz, E. Flamini, G. Franceschetti, Y. Gim, G. Hamilton, S. Hensley, M. Janssen, W. Johnson, K. Kelleher, R. Kirk, R. Lopes, R. Lorenz, J. Lunine, D. Muhleman, S. Ostro, F. Paganelli, G. Picardi, F. Posa, L. Roth, R. Seu, S. Shaffer, L. Soderblom, B. Stiles, E. Stofan, S. Vetrella, R. West, C. Wood, L. Wye & H. Zebker. *Cassini radar views the surface of Titan.* Science, vol. 308, page 970, 2005.

[Eremets 96] M. Eremets. High pressure equipment. Oxford University Press, 1996.

[Fabre 82] D. Fabre, M.M. Thiery & K. Kobashi. *Raman spectra of solid CH_4 under high pressure. II. New high pressure phases below 9 kbar and 4.2 K.* Journal of Chemical Physics, vol. 76, page 4817, 1982.

[Feng 06] J. Feng, W. Grochala, T. Jaroń, R. Hoffmann, A. Bergara & N.W. Ashcroft. *Structures and potential superconductivity in SiH_4 at high pressure: en route to 'metallic hydrogen'.* Physical Review Letters, vol. 96, page 017006, 2006.

[Fitch 93] A.N. Fitch & J.K. Cockcroft. *The structure of solid carbon tetrafluoride.* Zeitschrift fur Kristallographie, vol. 203, page 29, 1993.

[Fortes 03] A.D. Fortes, J.P. Brodholt, I.G. Wood & L. Vočadlo. *Hydrogen bonding in solid ammonia from ab initio calculations.* Journal of Chemical Physics, vol. 118, page 5987, 2003.

[Fortes 04] A.D. Fortes, I.G. Wood, K.S. Knight, W.G. Marshall, J.P. Brodholt, M. Alfredsson & L. Vočadlo. *New high-pressure phases of ammonia dihydrate.* Lunar and Planetary Institute Conference Abstracts, page 1254, 2004.

[Gauthier 88] M. Gauthier, Ph. Pruzan, J.C. Chervin & J.M. Besson. *Raman scattering study of ammonia up to 75 GPa: evidence for bond symmetrisation at 60 GPa.* Physical Review B, vol. 37, page 2102, 1988.

[Goncharov 05] A.F. Goncharov, N. Goldman, L.E. Fried, J.C. Crowhurst, I.W Kuo, C.J. Mundy & J.M. Zaug. *Dynamic ionization of water under extreme conditions.* Physical Review Letters, vol. 94, page 125508, 2005.

[Guillot 95] T. Guillot. *Condensation of methane ammonia and water in the inhibition of convection in giant planets.* Science, vol. 269, page 1697, 1995.

[Guillot 99] T. Guillot. *Interiors of giant planets inside and outside the solar system.* Science, vol. 286, page 72, 1999.

[Guillot 05] T. Guillot. *The interiors of giant planets: models and outstanding questions.* Annual Reviews in Earth and Planetary Science, vol. 33, page 493, 2005.

[Hall 54] T. Hall. *High-pressure, high temperature apparatus: The 15° "belt".* Technical report, General Electrical: Chemistry Research Department, 1954.

[Hamann 69] S.D. Hamann & M. Linton. *Electrical conductivities of aqueous solutions of KCL, KOH and HCl, and the ionization of water at high shock pressures.* Transactions of the Faraday Society, vol. 65, page 2186, 1969.

[Hamilton 65] W.C. Hamilton. *Significance test on the crystallographic R factor.* Acta Crystallographica, vol. 18, page 502, 1965.

[Hammersley 97] A.P. Hammersley. *FIT2D: an introduction and overview.* Technical report, ESRF internal report, 1997.

[Hansen 08] T.C. Hansen, P.F. Henry, H.E. Fischer, J. Torregrossa & P. Convert. *The D20 instrument at ILL: a versatile high-intensity two-axis neutron diffractometer.* Measurement Science and Technology, vol. 19, 2008.

[Hazen 80] R.M. Hazen, H.K. Mao, L.W. Finger & P.M. Bell. *Structure and compression of crystalline methane at high pressure and room temperature.* Applied Physics Letters., vol. 37(3), page 288, 1980.

[Hebert 87] P. Hebert, A. Polian, P. Loubeyre & R. LeToullec. *Optical studies of methane under high pressure.* Physical Review B, vol. 36, page 9196, 1987.

[Hirai 00a] H. Hirai, T. Kondo, M. Hasegawa, T. Yagi, Y. Yamamoto, T. Komai, K. Nagashima, M. Sakashita, H. Fujihisa & K. Aoki. *Methane hydrate behaviour under high pressure.* Journal of Chemical Physics, vol. 104, page 1429, 2000.

[Hirai 00b] H. Hirai, T. Kondo, M. Hasegawa, T. Yagi, Y. Yamamoto, K. Nagashima, M. Sakashita, K. Aoki & T. Kikegawa. *Methane hydrate, amoeba or a sponge made of water molecules.* Chemical Physics Letters, vol. 104, page 490, 2000.

[Hirai 01] H. Hirai, Y. Uchihara, H. Fujihisa, M. Sakashita, E. Katoh, K. Aoki, K. Nagashima, Y. Yamamoto & T. Yagi. *High pressure structures of methane hydrate observed up to 8 GPa at room temperature.* Journal of Chemical Physics, vol. 155, page 7066, 2001.

[Hirai 04] H. Hirai, T. Tanaka, T. Kawamura, Y. Yamamoto & T. Yagi. *Structual changes in gas hydrates and existence of a filled ice structure of methane hydrates above 40* GP*a.* Journal of Physics and Chemistry of Solids, vol. 65, page 1555, 2004.

[Hirai 06] H. Hirai, S. Machida, T. Kawamura, Y. Yamamoto & T. Yagi. *Stabalising of methane hydrate and transition to a new high-pressure structure at 40 GPa.* American Mineralogist, vol. 91, page 826, 2006.

[Hirai 08] H. Hirai, K. Konagai, T. Kawamura, Y. Yamamoto & T. Yagi. *Solid methane behaviours under high pressure and room temperature.* Journal of Physics: Conference Series, vol. 121, no. 102001, 2008.

[Holmes 85] N.C. Holmes, W.J. Nellis, W.B. Graham & G.E. Walrafen. *Spontaneous Raman scattering from shocked water.* Physical Review Letters, vol. 55, page 2433, 1985.

[Hubbard 80] W.B. Hubbard & J.J. McFarlane. *Structure and evolution of Uranus and Neptune.* Journal of Geophysical Research, vol. 85, page 225, 1980.

[Hubbard 95] W.B. Hubbard, M. Podolak & D.J. Stevenson. Neptune and Triton, chapter The interior of Neptune, page 109. Univerity of Arizona Press, 1995.

[Iitaka 03] T. Iitaka & T. Ebisuzaki. *Methane hydrate under high pressure.* Physical Review B, vol. 68, page 172105, 2003.

[Ivanov 60] V.E. Ivanov. Method of obtaining very high pressures to 100,000 atm and above. Technical report, 1960.

[Johnson 88] D.A. Johnson. *The thermochemistry of ammonium compounds and the energy barrier opposing ammonium ion reorientation.* Journal of Chemsitry Society - Dalton Transactions, vol. 2, page 445, 1988.

[Jordan-Sweet 00] J.L. Jordan-Sweet. *Synchrotron x-ray scattering techniques for microelectronics-related materials studies.* IBM Journals of Reserach and Development, vol. 44, no. 4, 2000.

[Khvostantsev 77] L.G. Khvostantsev, L.F. Vereshchagin & A.P. Novikov. *Device of toroidal type for high pressure generation.* High Temperature - High Pressure, vol. 9, page 637, 1977.

[Kirchner 04] M.T. Kirchner, R. Bosse, W.E. Billups & L.R. Norman. *Gas hydrate single crystals structure analyses.* Journal of the American Chemical Society, vol. 126, page 9407, 2004.

[Klotz 99] S. Klotz, J.M. Besson, G. Hamel, R.J. Nelmes, J.S. Loveday & W.G. Marshall. *Metastable ice VII at low temperature and ambient pressure.* Nature, vol. 398, page 681, 1999.

[Klotz 04] S. Klotz, G. Hamel & J. Frelat. *A newtype of compact large-capacity press for neutron and x-ray scattering.* High Pressure Research, vol. 24, page 219, 2004.

[Koga 75] Y. Koga & J.A. Morrison. *Polymorphism in solid CCl_4.* Journal of Chemical Physics, vol. 62, page 3359, 1975.

[Kuiper 44] G.P. Kuiper. *Titan: a satellite with an atmosphere.* Astrophysical Journal, vol. 100, page 398, 1944.

[Kumazaki 04] T. Kumazaki, Y. Kito, S. Sasaki, T. Kume & H. Shimizu. *Single crystal growth of the high-pressure phase II of methane hydrate and its Raman scattering study.* Chemical Physics Letters, vol. 388, page 18, 2004.

[Larson 94] A.C. Larson & R.B. Von Dreele. *General structural analysis system (GSAS).* Technical report LAUR 86-748, Los Alamos National Laboratory, 1994.

[Laue 13] M. Laue. *A quantative examination of the theory for the interference appearances in x-rays.* Annalen der Physik, vol. 41, page 989, 1913.

[Lin 05] J.F. Lin, E. Gregoryanz, W. Shruzhkin, M. Somayazulu, H.K. Mao & R.J. Hemley. *Melting behaviour of H_2O at high pressures and temperatures.* Geophysical Research Letters, vol. 32, no. L11306, 2005.

[Loubeyre 88] P. Loubeyre. *Three-body-exchange interaction in dense rare gases.* Physical Review B, vol. 37, page 5432, 1988.

[Loveday 96] J.S. Loveday, R.J. Nelmes, W.G. Marshall, J.M. Besson, S. Klotz & G. Hamel. *Structure of deuterated ammonia IV.* Physical Review Letters, vol. 76, no. 1, page 74, 1996.

[Loveday 99] J.S. Loveday & R.J. Nelmes. *Ammonia monohydrate VI: a hydrogen-bonded molecular alloy.* Physical Review Letters, vol. 83, page 4329, 1999.

[Loveday 01a] J.S. Loveday, R.J. Nelmes & M. Guthrie. *High-pressure transitions in methane hydrate.* Chemical Physics Letters, vol. 350, page 459, 2001.

[Loveday 01b] J.S. Loveday, R.J. Nelmes, M. Guthrie, S.A. Belmonte, D.R. Allan, D.D. Klug, J.S. Tse & Y.P. Handa. *Stable methane hydrate above 2 GPa and the source of Titan's atmospheric methane.* Nature, vol. 410, page 661, 2001.

[Loveday 01c] J.S. Loveday, R.J. Nelmes, M. Guthrie, D.D. Klug & J.S. Tse. *Transition from cage clathrate to filled ice: the structure of methane hydrate III.* Physical Review Letters, vol. 87, page 215501, 2001.

[Loveday 03] J.S. Loveday & R.J. Nelmes. *High-pressure neutron diffraction and models of Titan.* High Pressure Research, vol. 23, page 41, 2003.

[Loveday 04] J.S. Loveday & R.J. Nelmes. *The ammonia hydrates - model mixed hydrogen-bonded systems.* High Pressure Research, vol. 24, page 45, 2004.

[Lundegaard 08] L.F. Lundegaard. *High-pressure diffraction studies of rubidium, phase IV.* PhD thesis, School of Physics, Univeristy of Edinburgh, 2008.

[Lunine 87] J.I. Lunine & D.J. Stevenson. *Clathrate and ammonia hydrates at high pressure: application to the origin of methane on Titan.* Icarus, vol. 70, page 61, 1987.

[Machida 05] S. Machida, H. Hirai, T. Kawamura, Y. Yamamoto & T. Yagi. *Stability of filled-ice structure of methane hydrate and existence of a post filled-ice structure above 40 GPa.* Proceedings of joint 20th AIRAPT-43th EHPRG meetings, vol. 1, page 15, 2005.

[Machida 06] S. Machida, H. Hirai, T. Kawamura, Y. Yamamoto & T. Yagi. *A new high-pressure structures of methane hydrate surviving to 86 GPa and its implications for the interior of giant icy planets.* Physics of the Earth and Planetary Interiors, vol. 155, page 170, 2006.

[Mao 78] H.K. Mao, P.M. Bell, J.W. Shaner & D.J. Steinberg. *Specific volume meausrements of Cu, Mo, Pd, and Ag and calibration of ruby R1 flurescence pressure guage from 0.06 to 1 Mbar.* Journal of Applied Physics, vol. 49, page 3276, 1978.

[Mao 90] H.K. Mao, Y. Wu, J.F. Shu, J.Z. Hu, R.J. Hemley & D.E. Cox. *High-pressure transition and equation of state of lead to 238 GPa.* Solid State Communications, vol. 74, page 1027, 1990.

[Marshall 99] W.G. Marshall. *ATTEN: An attenuation correction calculation for the Paris-Edinburgh press on the PEARL/HiPr diffractometer at ISIS.* Technical report, ISIS Facility, 1999.

[Marshall 02] W.G. Marshall & D.J. Francis. *Attainment of near-hydrostatic compression conditions using the Paris-Edinburgh press.* Journal of Applied Crystallography, vol. 35, page 122, 2002.

[Martinez-Canales 06] M. Martinez-Canales & A. Bergara. *No evidence of metallic methane at high pressure.* High Pressure Research, vol. 26, page 369, 2006.

[Merrill 74] L. Merrill & W.A. Bassett. *Miniature diamond anvil pressure cell for single crystal x-ray diffraction studies.* Review of Scientific Instruments, vol. 45, page 183, 1974.

[Mills 58] I.M. Mills. *Wave function of the methane molecule.* Molecular Physics, vol. 1, page 99, 1958.

[Mills 61] I.M. Mills. *Errors in the wavefunctions for the methane molecule.* Molecular Physics, vol. 4, page 57, 1961.

[Mills 82] R. L. Mills, D. H. Liebenberg & P. Pruzan. *Phase-diagram and transistion properties of condensed ammonia to 10 kbar.* Journal of Physical Chemistry, vol. 86, page 5219, 1982.

[Mishima 84] O. Mishima, L.D. Calvert & E. Whalley. *'Melting ice' I at 77 K and 10 kbar: a new method of making amorphous solids.* Nature, vol. 310, page 393, 1984.

[Mishima 98] O. Mishima & H.E. Stanley. *The relationship between liquid, supercooled and glassy water.* Nature, vol. 396, page 329, 1998.

[Moggach 08] S.A. Moggach, D.R. Allan, S. Parsons & J.E. Warren. *Incorporation of a new design of backing seat and anvil in a Merrill Bassett diamond anvil cell.* Journal of Applied Crystallography, vol. 41, page 249, 2008.

[Momma 06] K. Momma & F. Izumi. *VESTA.* Comission of Crystollagraphic Computing; IuCr Newsletter, vol. 7, page 106, 2006.

[Nakahata 99] I. Nakahata, N. Matsui, Y. Akahama & H. Kawamura. *Structual studies of solid methane at high pressures.* Chemical Physics Letters, vol. 302, page 359, 1999.

[Nellis 81] W. J. Nellis, F. H. Ree, M. van Thiel & A. C. Mitchell. *Shock compression of liquid carbon monoxide and methane to 90 GPa (900 kbar).* Journal of Chemical Physics, vol. 75, page 3055, 1981.

[Nellis 88] W. J. Nellis, D.C. Hamilton, N.C. Holmes, H. B. Radousky, F. H. Ree, A. C. Mitchell & M. Nichol. *The nature of the interior of Uranus based on studies of planetary ices at high dynamic pressure.* Science, vol. 240, page 779, 1988.

[Nelmes 98] R.J. Nelmes, J.S. Loveday, W.G. Marshall, G. Hamel, J.M. Besson & S. Klotz. *Multisite disordered structure of Ice VII to 20 GPa.* Physical Review Letters, vol. 81, page 2719, 1998.

[Neumann 03] M.A. Neumann, W. Press, C. Noldeke, B. Asmussen, M. Prager & R. Ibberson. *The crystal structure of methane phase III.* Journal of Chemical Physics, vol. 119, page 1586, 2003.

[Ninet 08] S. Ninet & F. Datchi. *High pressure - high temperature phase diagram of ammonia.* Journal of Chemical Physics, vol. 128, page 154508, 2008.

[Oganov 05] A.R. Oganov, G.D. Price & S. Scandolo. *Ab initio theory of planetary materials.* Z. Kristallographie, vol. 220, page 531, 2005.

[Patterson 34] A.L. Patterson. *A Fourier series method for the determination of the components of interatomic distances in crystals.* Physical Review, vol. 46, page 0372, 1934.

[Pauling 39] L. Pauling. The nature of the chemical bond. Cornell University Press, Ithaca, NY, 1939.

[Peterson 56] S.W. Peterson & H.A. Levy. *A single-crystal neutron diffraction study of heavy ice.* Acta Cryst., vol. 10, page 70, 1956.

[Petricek 00] V. Petricek & M. Dusek. *The crystallographic computing system JANA2000.* Technical report, Institute of Physics, Praha, Czech Republic, 2000.

[Piermarini 75] G.J. Piermarini, S. Block, J.D. Barnett & R.A. Forman. *Calibration of the pressure dependance of the R_1 ruby flourescence line to 195 kbar.* Journal of Applied Physics, vol. 46, page 2774, 1975.

[Podolak 90] M. Podolak, R. T. Reynolds & R. Young. *Post Voyager comparisons of the interiors of Uranus and Neptune.* Geophysical Research Letters, vol. 17, page 1737, 1990.

[Podolak 91] M. Podolak & M. Marley. *Interior model constraints on superabundances of volatiles in the atmosphere of Neptune.* Bulletin of the American Astronomical Society, vol. 23, page 1164, 1991.

[Press 72] W. Press. *Structure and phase transitions of solid heavy methane.* Journal of Chemical Physics, vol. 56, page 2597, 1972.

[Prince 04] E. Prince, editor. International Tables for Crystallography - mathematical, physical and chemical tables, volume C. Kluwer Academic Publishers, 3rd edition, 2004.

[Rietveld 69] H.M. Rietveld. *A profile refinement method for nulcear and magnetic structures.* Journal of Applied Crystallography, vol. 2, page 65, 1969.

[Rodriguez-Carvajal 93] J. Rodriguez-Carvajal. *Reacent advances in magnetic structure determination by neutron powder diffraction.* Physica B, vol. 192, page 55, 1993.

[Salzmann 06] C.G. Salzmann, P.G. Radaelli, A. Hallbrucker, E. Mayer & J.L. Finney. *The preparation and structures of hydrogen ordered phase of ice.* Science, vol. 311, page 758, 2006.

[Schwager 04] B. Schwager, L. Chudinovskikh, A. Gavriliuk & R. Boehler. *Melting curve of H_2O to 90 GPa measured in a laser-heated diamond cell.* Journal of Physics: Condensed Matter, vol. 16, page S1177, 2004.

[Sheldrick 08] G.M. Sheldrick. *A short history of SHELX.* Acta Crystallographica, vol. 64, page 112, 2008.

[Simon 29] F.E. Simon & G. Glatzel. *Remarks on the fusion-pressure curve.* Zeitschrift fuer Anorganische und Allgemeine Chemi, vol. 178, page 309, 1929.

[Speedy 76] R.J. Speedy & C.A. Angell. *Isothermal compressibility of supercooled water and evidence for a thermodynamic singularity at -45 °C.* Journal of Chemical Physics, vol. 65, page 851, 1976.

[Stanley 04] S. Stanley & J. Bloxham. *Convective-region geometry as the cause of Uranus' and Neptune's unusual magnetic fields.* Nature, vol. 428, page 151, 2004.

[Stevenson 82] D.J. Stevenson. *Interiors of the giant planets.* Annual Reviews in Earth and Planetary Science, vol. 10, page 257, 1982.

[Swain 08] Mark R. Swain, Gautam Vasisht & Giovanna Tinetti. *The presence of methane in the atmosphere of an extrasolar planet.* Nature, vol. 452, page 329, 2008.

[Syassen 08] K. Syassen. *Ruby under pressure.* High Pressure Research, vol. 28, page 75, 2008.

[Tajima 82] Y. Tajima, T. Matsuo & H. Suga. *Phase transition in KOH-doped hexagonal ice.* Nature, vol. 299, page 810, 1982.

[Thiery 85] M.M. Thiery, D. Fabre & K. Kobashi. *Raman spectra of solid CH_4 under high pressure. III. New high pressure phases in solid CH_4 and CD_4.* Journal of Chemical Physics, vol. 83, page 5165, 1985.

[Thomson 10] J.J. Thomson. *On a theory of the struture of the electric field and its application to Röntgen radiation and to light.* Phillisophical Transactions of the Royal Society, vol. 19, page 301, 1910.

[Tobie 06] G. Tobie, J.I. Lunnie & C. Sotin. *Episodic outgassing as the origin of atmospheric methane on Titan.* Nature, vol. 440, page 61, 2006.

[Udachin 01] K.A. Udachin, C.I. Ratcliffe & J.A. Ripmeester. *Structure, composition and thermal expansion of CO_2 hydrate from single crystal x-ray diffaction measurements.* Journal of Physical Chemistry B, vol. 105, page 7833, 2001.

[Umemoto 02] S. Umemoto, T. Yoshii, Y. Akahama & H. Kawamura. *X-ray diffraction measurements for solid methane at high pressures.* Journal of Physics: Condensed Matter, vol. 14, page 10675, 2002.

[Vinet 87] P. Vinet, J.R. Smith, J. Ferrante & J.H. Rose. *Temperature effects on the univeral equation of state of solids.* Physical Review B, vol. 35, page 1945, 1987.

[Waite 05] H.J. Waite, H. Niemann, R.V. Yelle, W.T. Kasprzak, T.E. Cravens, J.G. Luhmann, R.L. McNutt, W. Ip, D. Gell, V. De La Haye, I. Muller-Wordag, B. Magee, N. Borggren, S. Ledvina, G. Fletcher, E. Walter, R. Miller, S. Scherer, R. Thorpe, J. Xu, B. Block & K. Arnett. *Ion neutral mass spectrometer results from the first flyby of Titan.* Science, vol. 308, page 982, 2005.

[Weir 59] C.E. Weir, E.P. Lippincott, A. VanValkenburg & E.N. Bunting. *Infrared studies in the 1 - 15 micron region to 30,000 atmospheres.* Journal of Research: National Bureau of Standards, vol. 63A, page 55, 1959.

[Wilson 00] C.C. Wilson. Single crystal neutron diffraction from molecular materials. World Scientific, 2000.

[Yung 84] Y.L. Yung, M.A. Allen & J.P. Pinto. *Photochemistry of the atmosphere of Titan: comparison between model and observations.* Astrophysical Journal, vol. 55, page 465, 1984.

[Zharkov 91] V.N. Zharkov & T.V. Gudkova. *Models of giant planets with a variable ratio of ice to rock.* Ann. Geophysicae, vol. 9, page 357, 1991.